Highly Efficient Inductive Power Transfer

Variable Compensation for Misalignment Tolerance and Voltage/Current Doubler for Battery Interoperability

Grazian, F.

DOI
10.4233/uuid:b2d29368-cf59-4c2e-be32-60e794212d0a

Publication date
2023

Document Version
Final published version

Citation (APA)
Grazian, F. (2023). *Highly Efficient Inductive Power Transfer: Variable Compensation for Misalignment Tolerance and Voltage/Current Doubler for Battery Interoperability*. [Dissertation (TU Delft), Delft University of Technology]. https://doi.org/10.4233/uuid:b2d29368-cf59-4c2e-be32-60e794212d0a

Highly Efficient Inductive Power Transfer

Variable Compensation for Misalignment Tolerance and Voltage/Current Doubler for Battery Interoperability

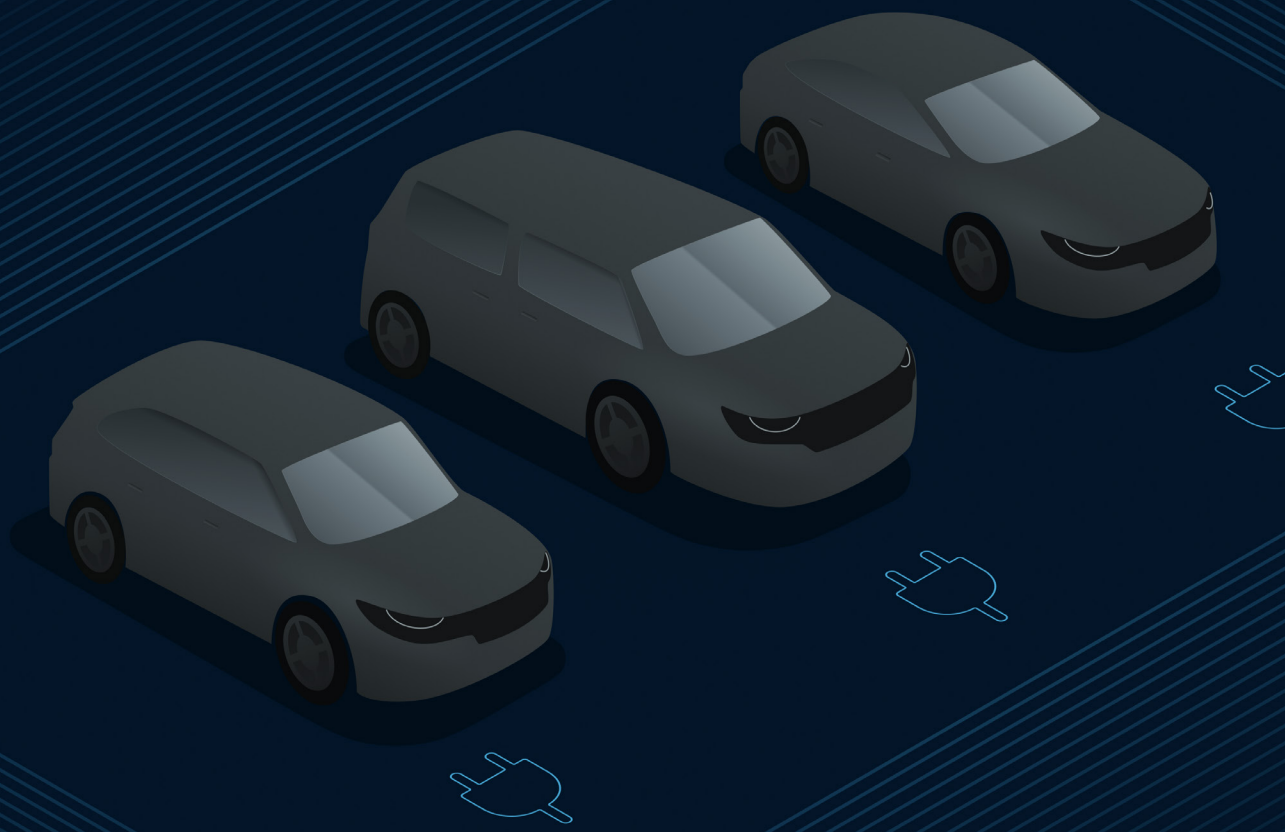

Francesca Grazian

HIGHLY EFFICIENT INDUCTIVE POWER TRANSFER

VARIABLE COMPENSATION FOR MISALIGNMENT TOLERANCE AND VOLTAGE/CURRENT DOUBLER FOR BATTERY INTEROPERABILITY

Dissertation

for the purpose of obtaining the degree of doctor
at Delft University of Technology
by the authority of the Rector Magnificus Prof. dr. ir. T.H.J.J. van der Hagen,
chair of the Board for Doctorates,
to be defended publicly on
Friday 12 May 2023 at 10:00 hours

by

Francesca GRAZIAN

Master of Science in Electrical Engineering, Delft University of Technology,
The Netherlands
born in Prato, Italy

The dissertation has been approved by the promotor.

Composition of the doctoral committee:

Rector Magnificus,	chairperson
Prof. dr. ir. P. Bauer,	Delft University of Technology, promotor
Dr. J. Dong,	Delft University of Technology, copromotor

Independent members:

Dr. Z. Qin,	Delft University of Technology
Prof. dr. A. Neto,	Delft University of Technology
Prof. dr. G. Papafotiou,	Eindhoven University of Technology
Prof. dr. F. Freschi,	Politecnico di Torino, Italy

Other member:

Prof. dr. T. Batista Soeiro,	University of Twente

Printed by Ridderprint

Cover designed by Benedetta Grazian

ISBN 978-94-6483-055-2

An electronic version of this dissertation is available at
http://repository.tudelft.nl/.

To my mum,
who is the strongest woman I know.
To my dad,
who is always with me.

SUMMARY

Wireless charging has the potential to speed up the transition to electric vehicles (EVs) because it is intrinsically a user-friendly technology. Furthermore, it is essential when charging completely autonomous EVs, and it enables the charging of EVs in motion without using overhead cables. The most common technology used in EV wireless charging is inductive power transfer (IPT) with magnetic resonance coupling. This is based on the magnetic field exchange between coupled coils connected to compensation networks to minimize the circulating reactive power. IPT systems have two main variables influencing their operation: the coupling factor between the coils depending on their alignment, and the equivalent load based on the battery charging profile.

As explained in Chapter 1, the coils' alignment and load operating conditions might vary when considering different applications. Nevertheless, all IPT systems share the same challenges: ensuring a highly efficient power transfer, guaranteeing that the intentionally radiated electromagnetic field (EMF) is both safe for the living beings in the surroundings and lower than the recommended electromagnetic compatibility (EMC) limits as discussed in Appendix A and providing interoperability between IPT charging stations and EVs produced by different manufacturers. This thesis explores these matters, which content is divided into three main parts.

CONVENTIONAL INDUCTIVE POWER TRANSFER SYSTEMS

In IPT systems, the choice of the compensation network influences several factors, such as the selection of the high-frequency inverting and rectifying power stages, the power transfer behavior over the misalignment, the components' voltage and current stress, and the power transfer efficiency. Chapter 2 analyzes the most commonly used one-component and multi-component compensation networks to understand their features. Ultimately, guidelines are given to select a suitable IPT system for EV wireless charging. The series-series (S-S) and the double-sided LCC (DLCC) result in the most appropriate compensation networks because their parameters' tuning is independent of their operating conditions, they can be directly powered by a voltage source H-bridge inverter with soft-switching capability, and, additionally, they have a load independent output current that allows a direct connection of the output high-frequency rectifying stage to the EV battery. The S-S compensation can potentially reach the highest power transfer efficiency since it employs only one component. However, its power transfer characteristic is strongly dependent and inversely proportional to the coupled coils' mutual inductance, meaning that an adequate coils design is required for each specific application. The design process of IPT systems using the S-S compensation has been defined. Considering a 3.7 kW laboratory demonstrator, the DC-to-DC efficiency of 96.24% has been measured at about 3.3 kW and aligned coils. Conversely, with the DLCC compensation, the nominal output power delivered by the IPT system can be advantageously selected by tuning the compensation inductors. Moreover, the output power is directly

proportional to the coils' mutual inductance, which makes the DLCC intrinsically safe against high variations of misalignment. The implemented laboratory of an IPT system using the DLCC compensation has achieved a measured DC-to-DC efficiency of 95.23% at about 3.1 kW and aligned coils. Nevertheless, the analytical estimation of the H-bridge inverter's turn-off current essential to realize the soft-switching operation is not trivial when employing the DLCC compensation. The inverter current typically has a high harmonic distortion due to the input LC filter, meaning that the analysis based on the first harmonic approximation is inaccurate. An analytical model to estimate the inverter's current distortion has been proposed and experimentally validated in Appendix B, which also applies when the diode rectifier operates in discontinuous conduction mode.

VARIABLE COMPENSATION

Using a variable compensation introduces an additional control variable that would vary the circuit's resonant frequency. The advantages of using variable compensation networks are explored in Chapter 3. An efficiency enhancement strategy, called constant optimum load (COL), has been proposed and experimentally demonstrated. The main advantage of this solution is eliminating voltage control at the load side commonly used in the literature to maximize the power transfer efficiency through the optimum load matching. Alternatively, the proposed COL charging method employs variable series compensation capacitors to make the optimum load condition invariant of the coil's mutual inductance. Only the input power is regulated through the grid-connected power factor correction (PFC) rectifier, ensuring that the COL condition is met while the battery voltage increases during the charging cycle. The variable series compensation has been realized at both the primary and the secondary circuits as a switch-controlled capacitor (SCC), where two implementations called half-wave and full-wave modulations have been tested in a 3.7 kW laboratory demonstrator. The half-wave modulation results in overall higher efficiency than full-wave modulation, with a measured peak DC-to-DC efficiency of 96.30% for the input power of 3.2kW and at the maximum coils' alignment. Compared to the conventional S-S compensation with fixed capacitors, the efficiency gain is up to 0.68% at partial load. Additionally, the current harmonic distortion has been analyzed. The SCCs using the half-wave modulation introduce a higher total lumped distortion than the conventional S-S compensation result. However, in correspondence with the critical frequencies of the limit set by SAE J2954 on the radiated magnetic field, the amplitude of the single harmonic components is comparable to or lower than in the other implementations. The radiated EMF has been evaluated through finite element method (FEM) analysis, which resulted in compliance with the EMC and the human exposure limits. Furthermore, the radiated EMF has been measured in the surrounding of the laboratory demonstrator, validating the results from the FEM analysis relative to the human exposure limits.

VOLTAGE/CURRENT DOUBLER (V/I-D)

The nominal battery voltage of EVs is not necessarily the same, and mostly it could be either 400 V or 800 V. When considering public IPT charging stations, it is essential that wireless chargers can supply power efficiently to both battery classes guaranteeing interoperability. Generally, the most straightforward solution is employing an additional

onboard DC/DC converter to charge batteries with a voltage different from the nominal. However, the efficiency of the overall circuit would be impacted by the DC/DC converter's performance which, undoubtedly, adds cost and complexity on board the EV. Chapter 4 and Chapter 5 have proposed and demonstrated the functionality of the voltage/current doubler (V/I-D) converter, comprising two sets of series-compensated coupled coils, i.e., two primary and two secondary coils, connected to a dedicated H-bridge converter. The power transfer control is implemented only on the primary side. The secondary circuit comprises passive devices, resulting in a simple, cost-effective onboard circuit that does not require active control. The proposed V/I-D converter was experimentally verified with two different magnetic configurations. The first arrangement is proposed in Chapter 4, which employs two physically separated sets of rectangular coupled coils. At 7.2kW and with aligned coils, the DC-to-DC efficiency of 97.11% and 97.52% has been measured at 400V and 800V, respectively. As explained in Chapter 5, the second arrangement is more compact since it uses bipolar pads (BPPs) in which the two rectangular coils at each circuit side are deployed on the same ferrite layer. The unwanted cross-coupling in the BPPs has been analyzed with respect to the V/I-D converter's power transfer characteristics. At 7.2kW and with aligned BPPs, the DC-to-DC efficiency of 96.34% and 96.53% has been measured at 400V and 800V, respectively. The functionality of the V/I-D converter was also verified under different misalignment and loading conditions. The lower efficiency resulting from the BPP magnetic arrangement is mainly caused by the power losses due to the eddy currents in the BPPs' aluminum shield, which was not used for the rectangular coils. Finally, the interoperability of the proposed V/I-D converter has been experimentally proved when the primary BPP is coupled with the receiving standardized rectangular coil WPT2/Z2 from SAE J2954. This is important because it enlarges the usability of the proposed converter, ensuring interoperability with different coils' topologies.

SAMENVATTING

Draadloos opladen heeft de potentie om de overgang naar elektrische voertuigen (EV's) te versnellen, omdat het intrinsiek een gebruiksvriendelijke technologie is. Bovendien is het essentieel bij het opladen van volledig autonome EV's en maakt het opladen van EV's in beweging mogelijk zonder het gebruik van bovengrondse kabels. De meest gebruikte technologie bij het draadloos opladen van elektrische voertuigen is inductieve energieoverdracht (IPT) met magnetische resonantiekoppeling. Dit is gebaseerd op de magnetische velduitwisseling tussen gekoppelde spoelen die zijn aangesloten op compensatienetwerken om het circulerende reactieve vermogen te minimaliseren. IPT-systemen hebben in wezen twee variabelen die hun werking beïnvloeden: de koppelingsfactor tussen de spoelen, afhankelijk van hun uitlijning, en de equivalente belasting op basis van het laadprofiel van de batterij.

Zoals uitgelegd in Hoofdstuk 1, kunnen de uitlijning en belasting condities van de spoelen variëren bij het overwegen van verschillende toepassingen. Desalniettemin delen alle IPT-systemen dezelfde uitdagingen: zorgen voor een zeer efficiënte energieoverdracht, garanderen dat het opzettelijk uitgestraalde elektromagnetische veld (EMF) niet schadelijk is voor de levende wezens in de omgeving en dat het lager is dan de aanbevolen elektromagnetische compatibiliteit (EMC) limieten die zijn gedefinieerd in industriële voorschriften die worden besproken in Bijlage A, en die interoperabiliteit bieden tussen IPT-laadstations en EV's die door verschillende fabrikanten zijn geproduceerd. Dit proefschrift onderzoekt deze zaken, waarvan de inhoud is onderverdeeld in drie hoofddelen.

CONVENTIONELE INDUCTIEVE ENERGIEOVERDRACHT SYSTEMEN

In IPT-systemen beïnvloedt de keuze van het compensatienetwerk de selectie van de hoogfrequente inverterende en gelijkrichtende vermogensfasen, het gedrag van de vermogensoverdracht ten opzichte van de verkeerde uitlijning, de spannings- en stroombelasting van de componenten en de efficiëntie van de vermogensoverdracht. Hoofdstuk 2 analyseert de meest voorkomende enkel-component en multi-component compensatienetwerken om hun kenmerken te begrijpen en, uiteindelijk, worden richtlijnen gegeven om een geschikt IPT-systeem te selecteren voor draadloos opladen van elektrische voertuigen. De serie-serie (S-S) en het dubbelzijdige LCC (DLCC) compensatienetwerk worden gezien als de meest geschikte oplossingen omdat de afstemming van hun parameters onafhankelijk is van de werkingstoestand, ze kunnen rechtstreeks worden gevoed door een spanningsbron H-brugomvormer met soft-switching vermogen, en ze hebben een belastingonafhankelijke uitgangsstroom die een directe verbinding van de hoogfrequente gelijkrichting fase met de EV-batterij mogelijk maakt. De S-S-compensatie kan mogelijk de hoogste energieoverdracht efficiëntie bereiken, aangezien er slechts één component wordt gebruikt. De eigenschap van de vermogensoverdracht is echter sterk

afhankelijk van en omgekeerd evenredig met de wederzijdse inductantie van de gekoppelde spoelen, wat betekent dat voor elke specifieke toepassing een adequaat ontwerp van de spoelen vereist is. Het ontwerpproces van IPT-systemen die de S-S-compensatie gebruiken, is gedefinieerd met inachtneming van een 3.7 kW laboratorium prototype, waarbij een gemeten DC-naar-DC-efficiëntie van 96.24% op vol vermogen en uitgelijnde spoelen wordt bereikt. Omgekeerd kan met de DLCC-compensatie het door het IPT-systeem geleverde nominale uitgangsvermogen met voordeel worden geselecteerd door de compensatie-inductoren af te stemmen. Bovendien is het uitgangsvermogen recht evenredig met de wederzijdse inductantie van de spoelen, waardoor de DLCC intrinsiek veilig is tegen grote variaties in verkeerde uitlijning. Desalniettemin is de analytische schatting van de uitschakelstroom van de H-brugomvormer die essentieel is om de soft-switching-werking te realiseren, niet triviaal bij gebruik van de DLCC-compensatie. De stroom van de omvormer heeft doorgaans een hoge harmonische vervorming als gevolg van het ingangs-LC-filter, wat betekent dat de analyse op basis van de eerste harmonische benadering niet nauwkeurig is. Een analytisch model om de stroomvervorming van de omvormer te schatten is voorgesteld en experimenteel gevalideerd in Bijlage B, dat ook van toepassing is in het geval dat de diodegelijkrichter in discontinue geleidingsmodus werkt.

VARIABELE COMPENSATIE

Het gebruik van een variabele compensatie introduceert een extra regelvariabele die de resonantiefrequentie van het circuit zou variëren. De voordelen van het gebruik van variabele compensatienetwerken worden onderzocht in Hoofdstuk 3. Een strategie voor efficiëntieverbetering, genaamd constant optimum load (COL), is voorgesteld en experimenteel gedemonstreerd. Het belangrijkste voordeel van deze oplossing is de eliminatie van de in de literatuur gebruikelijke spanningsregeling aan de belastingszijde om de efficiëntie van de vermogensoverdracht te maximaliseren door optimale belastingafstemming. Als alternatief maakt de voorgestelde COL-oplaadmethode gebruik van variabele serie compensatie condensatoren om de optimale belasting toestand onveranderlijk te maken voor de wederzijdse inductantie van de spoel. Alleen het ingangsvermogen wordt geregeld via de netgekoppelde Power Factor Correction (PFC)-gelijkrichter, die ervoor zorgt dat aan de COL-voorwaarde wordt voldaan terwijl de accuspanning toeneemt tijdens de laadcyclus. De variabele seriecompensatie is gerealiseerd op zowel de primaire als de secundaire circuits als een schakelaargestuurde condensator (SCC), waar twee implementaties genaamd half-wave en full-wave modulaties zijn getest in een 3.7 kW laboratoriumdemonstratie. De half-wave modulatie resulteert in een algeheel hoger rendement dan full-wave modulatie, met 96.30% voor het ingangsvermogen van 3.2 kW en bij de maximale uitlijning van de spoelen. Vergeleken met de conventionele S-S-compensatie met vaste condensatoren is de efficiëntiewinst tot 0.68% bij deellast. Daarnaast is de huidige harmonische vervorming geanalyseerd. De SCC's die de half-wave modulatie gebruiken, introduceren een hogere totale samengevoegde vervorming dan het conventionele S-S-compensatieresultaat. Echter, in overeenstemming met de kritische frequenties van de limieten van SAE J2954, is de amplitude van de enkelvoudige harmonische componenten vergelijkbaar met of lager dan in de andere implementaties. Het uitgestraalde EMF is geëvalueerd door middel van de eindige-elementenmethode (FEM)-analyse, wat resulteerde in het voldoen aan de EMC en de menselijke blootstel-

lingslimieten. Bovendien is het uitgestraalde EMF gemeten in de omgeving van de laboratoriumdemonstrator die de resultaten van de FEM-analyse valideert ten opzichte van de menselijke blootstellingslimieten.

VOLTAGE/CURRENT DOUBLER (V/I-D) - SPANNING/STROOMVERDUBBELAAR

De nominale accuspanning van EV's is niet noodzakelijkerwijs hetzelfde, en kan meestal 400 V of 800 V zijn. Bij het overwegen van openbare IPT-laadstations is het van essentieel belang dat draadloze opladers efficiënt stroom kunnen leveren aan beide batterijklassen en interoperabiliteit garanderen. Over het algemeen is de eenvoudigste oplossing het gebruik van een extra ingebouwde DC/DC-omvormer om batterijen op te laden met een spanning die afwijkt van de nominale spanning. De efficiëntie van het totale circuit zou echter worden beïnvloed door de prestaties van de DC/DC-omvormer, wat ongetwijfeld de kosten en complexiteit aan boord van de EV verhoogt. Hoofdstuk 4 en Hoofdstuk 5 hebben de functionaliteit van de spanning/stroom verdubbelaar (V/I-D)-omzetter voorgesteld en gedemonstreerd, bestaande uit twee sets serie gecompenseerde gekoppelde spoelen, d.w.z. twee primaire en twee secundaire spoelen, verbonden met een speciale H-brug omvormer. De vermogensoverdrachtregeling is alleen aan de primaire zijde geïmplementeerd. Het secundaire circuit is samengesteld uit passieve componenten, wat resulteert in een eenvoudig en kosteneffectief circuit aan boord dat geen actieve besturing vereist. De voorgestelde V/I-D-omvormer werd experimenteel geverifieerd met twee verschillende magnetische configuraties. De eerste opstelling wordt voorgesteld in Hoofdstuk 4, waarbij gebruik wordt gemaakt van twee fysiek gescheiden stellen rechthoekig gekoppelde spoelen. Dit resulteert in een DC-naar-DC efficiëntie van 97.11% en 97.52% gemeten bij respectievelijk 400V en 800V. Zoals uitgelegd in Hoofdstuk 5, is de tweede opstelling compacter omdat deze gebruikmaakt van bipolaire pads (BPP's) waarin de twee rechthoekige spoelen aan elke circuitzijde op dezelfde ferriet laag zijn geplaatst. De ongewenste kruiskoppeling in de BPP's is geanalyseerd met betrekking tot de vermogensoverdrachtskarakteristieken van de V/I-D-converter. Bij 7.2 kW en met uitgelijnde BPP's is de DC-naar-DC-efficiëntie van respectievelijk 96.34% en 96.53% gemeten bij 400 V en 800 V. De functionaliteit van de V/I-D-converter werd ook gecontroleerd onder verschillende uitlijnings- en belasting omstandigheden. De lagere efficiëntie als gevolg van de magnetische opstelling van de BPP wordt voornamelijk veroorzaakt door de vermogensverliezen als gevolg van de wervelstromen in de aluminium afscherming van de BPP's, die niet werd gebruikt voor de rechthoekige spoelen. Ten slotte is de interoperabiliteit van de voorgestelde V/I-D-omzetter experimenteel bewezen wanneer de primaire BPP wordt gekoppeld aan een ontvangende gestandaardiseerde rechthoekige spoel van SAE J2954. Dit is belangrijk omdat het de bruikbaarheid van de voorgestelde omzetter vergroot, waardoor interoperabiliteit met verschillende spoel topologieën wordt gegarandeerd.

When wireless is fully applied
the earth will be converted into a huge brain,
capable of response in every one of its parts.

Nikola Tesla

CONTENTS

Acronyms **xvii**

List of symbols and convention **xix**

1 Introduction **1**
1.1 Outlook on wireless power transfer . . . 1
1.1.1 WPT technologies . . . 1
1.1.2 Brief history . . . 3
1.1.3 Applications . . . 5
1.2 Inductive power transfer with magnetic resonant coupling for EV wireless charging . . . 5
1.2.1 Power transfer efficiency . . . 7
1.2.2 EMC and EMF human exposure limits . . . 8
1.2.3 Interoperability . . . 8
1.3 Scope, objective, and research questions . . . 11
1.4 Methodology . . . 12
1.5 Outline of the thesis . . . 13
1.6 Research contributions . . . 15

I Conventional Inductive Power Transfer Systems **21**

2 Framework for the Design of IPT Systems **23**
2.1 Introduction . . . 24
2.1.1 High-frequency inverting and rectifying power stages . . . 25
2.1.2 Circuit modeling of the loosely coupled transformer . . . 27
2.1.3 Scope and contributions . . . 28
2.1.4 Outline . . . 28
2.2 One-component compensation networks . . . 28
2.2.1 Selection of the compensation capacitance . . . 29
2.2.2 Equivalent optimum load and bifurcation phenomenon . . . 31
2.2.3 Comparison of the one-component compensation networks . . . 34
2.3 Quality factor-based parameters selection for the one-component compensation networks . . . 36
2.3.1 Definition of the parametric guideline . . . 36
2.3.2 IPT system designs and analysis . . . 37
2.4 Design trade-offs between the coupled coils' inductance and the compensation capacitance in the S-S compensation network . . . 41
2.4.1 Analytical modeling of the S-S compensated circuit . . . 42
2.4.2 Selection of the target mutual inductance . . . 43
2.4.3 Selection of the coils' and compensation's parameters . . . 44

2.4.4 Example based on a WPT1 EV wireless charging system: analytical computation . . . 44
2.4.5 Example based on a WPT1 EV wireless charging system: coils design through the FEM analysis . . . 46
2.4.6 Laboratory prototype and experimental results . . . 49
2.5 Multi-component compensation networks . . . 53
2.5.1 LC compensation . . . 53
2.5.2 LCC compensation. . . . 55
2.5.3 Other multi-component compensations . . . 55
2.6 Hybrid compensation networks combining the S-S and the DLCC for a constant output power . . . 56
2.6.1 Concept . . . 57
2.6.2 Proposed implementation . . . 57
2.6.3 Circuit simulations. . . . 58
2.7 Conclusion . . . 60

II Variable Compensation **67**

3 Constant Optimum Load Charging Strategy through Variable Compensation **69**
3.1 Introduction . . . 70
3.1.1 Optimum load impedance matching. . . . 70
3.1.2 Variable compensation . . . 71
3.1.3 Scope and contributions . . . 72
3.1.4 Outline. . . . 72
3.2 Concept of the proposed COL charging strategy . . . 73
3.2.1 Analytical circuit modeling. . . . 73
3.2.2 Traditional optimum load impedance matching through voltage control . . . 75
3.2.3 Definition of the COL charging method . . . 75
3.2.4 Detailed COL charging process . . . 76
3.3 Implementation . . . 79
3.3.1 Mutual inductance measurement . . . 79
3.3.2 SCC as variable compensation capacitor. . . . 79
3.3.3 Design guideline for EV wireless charging systems . . . 82
3.3.4 Prototype of 3.7 kW EV wireless charging system. . . . 83
3.4 Experimental results . . . 87
3.4.1 Constant optimum load method with SCCs . . . 87
3.4.2 Comparison with the conventional S-S compensation . . . 92
3.5 Distortion of the measured coil currents . . . 94
3.5.1 Methodology. . . . 95
3.5.2 SCCs using the half-wave and the full-wave modulations . . . 96
3.5.3 Half-wave modulation SCC and the fixed S-S capacitors . . . 96
3.6 FEM simulation of the radiated magnetic field . . . 99
3.6.1 Comparison with the EMC limits . . . 99
3.6.2 Comparison with the human exposure limits . . . 100
3.7 Conclusion . . . 102

III Voltage/Current Doubler (V/I-D) 109

4 Voltage/Current Doubler Converter using Rectangular Coils 111
4.1 Introduction . . . 112
4.1.1 Scope and contributions . . . 112
4.1.2 Outline . . . 113
4.2 The V/I-D Converter . . . 113
4.2.1 Circuit analysis and operation . . . 114
4.2.2 Circuit parameters' selection . . . 117
4.3 Comparison with 1-to-1 coil IPT systems . . . 118
4.3.1 Circuit modeling of the 1-to-1 coil IPT system . . . 118
4.3.2 Power conversion stages . . . 118
4.3.3 Assumptions . . . 119
4.3.4 Analysis . . . 120
4.3.5 Cost and complexity considerations . . . 121
4.4 Experimental Implementation . . . 121
4.4.1 Laboratory prototype . . . 122
4.4.2 Analysis of the operating points . . . 122
4.4.3 V/I-D converter's performance at lower values of Δx . . . 125
4.5 Experimental Results . . . 126
4.5.1 Measurements at the coils' nominal alignment . . . 126
4.5.2 Measurements with coils' misalignment . . . 127
4.5.3 Power loss analysis . . . 130
4.6 Conclusion . . . 130

5 Advanced and Compact Voltage/Current Doubler Converter Using Bipolar Pads 133
5.1 Introduction . . . 134
5.1.1 Scope and contributions . . . 135
5.1.2 Outline . . . 136
5.2 Bipolar pads . . . 136
5.2.1 Overview: BPP as a magnetic coil arrangement . . . 136
5.2.2 Analysis: influence of BPPs' cross-coupling on the V/I-D converter's functionality . . . 136
5.2.3 Design: cross-coupling sensitivity analysis through FEM . . . 140
5.2.4 Implementation: coupled BPPs for the V/I-D converter . . . 143
5.3 Laboratory prototype . . . 145
5.3.1 Compensation capacitors' selection . . . 145
5.3.2 Analysis of the operating points . . . 145
5.4 Experimental results . . . 148
5.4.1 Measured efficiency and circuit waveforms . . . 148
5.4.2 Example of a CC-CV charging profile . . . 151

5.5 Interoperability of the primary BPP with the test station VA WP2/Z2 from SAE J2954 . . . 152
5.5.1 Circuit and analytical modeling . . . 152
5.5.2 Magnetic coupling and misalignment . . . 153
5.5.3 Operating conditions . . . 155
5.5.4 Experimental results . . . 157
5.6 Conclusion . . . 160

6 Conclusion **163**
6.1 Regarding the research questions . . . 163
6.2 Future work . . . 167

Appendix **169**

A Constraints and Requirements from Industrial Standards and Regulations on EV Wireless Charging **171**
A.1 Introduction . . . 171
A.2 IEC 61980 . . . 172
A.2.1 IEC 61980-1 . . . 172
A.2.2 IEC 61980-3 . . . 174
A.3 ISO 19363 . . . 175
A.4 SAE J2954 . . . 176
A.4.1 Power transfer . . . 176
A.4.2 Communication . . . 178
A.4.3 Safety and EMC . . . 179
A.4.4 EMF human exposure . . . 180
A.5 IEC PAS 63184 . . . 180
A.6 Comparison and discussion . . . 181
A.6.1 EMC . . . 181
A.6.2 Human and CIED exposure to radiated EMF . . . 181
A.6.3 EMC and EMF: quantitative and qualitative interpretation . . . 182
A.7 Conclusion . . . 183

B Modeling of the Current Distortion in the Double-sided LCC Compensation **185**
B.1 Introduction . . . 185
B.2 DLCC circuit modeling . . . 186
B.3 Prediction of the inverter current distortion . . . 190
B.4 Experimental verification . . . 193
B.5 Conclusions . . . 195

Acknowledgements **197**

List of Publications **201**

Curriculum Vitæ **205**

ACRONYMS

AIMD	Active implantable medical devices
BPP	Bipolar pad
CC, CV	Constant current, constant voltage
CIED	Cardiac implantable electronic devices
COL	Constant optimum load
CPT	Capacitive power transfer
CS	Current source
DDQP	Double-D Quadrature Pad
DDP	Double-D pad
DLCC	Double-sided LCC, i.e., LCC-LCC (compensation network)
EMC	Electromagnetic compatibility
EMF	Electromagnetic field
ESR	Equivalent series resistance
EV	Electric vehicle
FEM	Finite element method
FFT	Fast Fourier transform
f-w	full-wave (modulation of the SCC)
GA	Ground assembly
h-w	half-wave (modulation of the SCC)
I-D	Current doubler
IPT	Inductive power transfer
IPT-IC	Inductive power transfer with inductive coupling
IPT-MRC	Inductive power transfer with magnetic resonant coupling
KLV	Kirchhoff voltage law
LC, LCC	Inductor-capacitor, Inductor-capacitor-capacitor (compensation networks)
LCT	Loosely coupled transformer
PFC	Power factor correction
P-S, P-P	Parallel-series, parallel-parallel (compensation networks)
PAS	Publicly available specification
RF	Radio frequency

RMS	Root mean square
RP	Rectangular pad
RR	Reverse recovery
S-S, S-P	Series-series, series-parallel (compensation networks)
SAR	Specific absorption rate
SCC	Switch-controlled capacitor
SoC	State of charge
SPS	Solar-power satellite
SWIPT	Simultaneous wireless information and power transfer
THD	Total harmonic distortion
V/I-D	Voltage/current doubler
V-D	Voltage doubler
V2G	Vehicle to grid
VA	Vehicle assembly
VS	Voltage source
WPT	Wireless power transfer
WPT1...WPT5	Wireless power transfer power classes (see Appendix A)
Z1...Z3	Z-classes, i.e., ground clearance of the VA coil (see Appendix A)
ZPA	Zero phase angle
ZVS	Zero voltage switching

LIST OF SYMBOLS AND CONVENTION

a	Constant
B	Magnetic flux density
C_1, ..., C_4, C_{f1}, C_{f2}	Compensation capacitance
C_{ds}	MOSFET's drain-source capacitance
$C_{\text{f-w}}$	Equivalent capacitance from the SCC in f-w modulation
$C_{\text{h-w}}$	Equivalent capacitance from the SCC in h-w modulation
C_{s1}, C_{s2}	Compensation capacitance used in the SCC
C_{sp}, C_{sp1}, ..., C_{sp4}	Coil's spread
D	Largest dimension of an antenna
$D1$, ..., $D6$	Diodes of the high-frequency rectifiers
D_t	Measurement duration
d	Constant
d_w	External diameter of the Litz wire
df	FFT frequency resolution
E_{in}	Input energy
E_{sw}, E_{off}, E_{on}	Switching energy loss, i.e., E_{sw}=E_{off} + E_{on}
E_{rr}	Reverse recovery energy loss of the diode
f, f_0	Frequency of a signal, resonant frequency
f_n	FFT bandwidth
F_s	Sampling frequency
H	Magnetic field strength
h_{res}	Sampling period
I_1, ..., I_4, I_A, I_B	Current through the coupled coil
I_{AB}, I_{CD}	Input high-frequency current to the resonant circuit
I_{ab}, I_{cd}	Output high-frequency current from the resonant circuit
I_{batt}	Battery current
I_{OFF}	Turn-off current of the H-bridge inverter

$I_{OFF,min}$	Minimum theoretical I_{OFF} ensuring the ZVS turn-on operation
I_{out}	DC output current of the IPT system
k	Coupling factor
L_1, ..., L_4	Self-inductance of the coupled coil
L_{1D}, L_{2D}, L_D	Self-inductance of the coupled coil
L_A, L_B	Self-inductance of the coupled coil
L_{f1}, L_{f2}	Compensation inductance
L_t	Length of the signal
M	Mutual inductance between the coupled coils
M_{12}, M_{13}, M_{14}	Mutual inductance between the coupled coils
M_{23}, M_{24}, M_{34}	Mutual inductance between the coupled coils
M_D, M_{AB}	Mutual inductance between the coupled coils
M_{cross}	Mutual inductance related to the coils' cross-coupling
$M1$, ..., $M8$	MOSFETs of the high-frequency inverters
N, N_1, ..., N_4	Coil's number of turns
$P_{grid,max}$	Maximum input power that can be drawn from the utility grid
P_{in}	DC input power of the IPT system
P_{inv}	Power losses of the high-frequency inverter
P_{out}	DC output power of the IPT system
P_{rect}	Power losses of the high-frequency rectifier
Q_1, ..., Q_4, Q_D	Quality factor of the coupled coils
Q_1^*	Q_1 ensuring the optimum load and the bifurcation-free conditions
Q_{1c}, Q_{2c}	Quality factor of the resonant circuits
Q_{rr}	Reverse recovery charge of the diode
R_1, ..., R_4	ESR of the resonant circuit
R_{ac}	Equivalent high-frequency load resistance
R_L	Equivalent DC load resistance
$R_{ac,bif}$, $R_{L,bif}$	Boundary load resistance for a bifurcation-free operation
$R_{ac,opt}$, $R_{L,opt}$	Optimum load resistance for maximum efficiency
$S1$, $S2$, $S3$	MOSFETs of the SCCs
SW	Mechanical switch that connects the battery to the IPT system
s_m	Safety margin $s_m > 1$, such that $I_{OFF}=s_m \cdot I_{OFF,min}$
T	Period of a signal, i.e., $T=\frac{1}{f}$
t	Time
t_{dead}	Dead time of the high-frequency VS inverter

t_{on}	Conduction time of the SCC
V_{AB}, V_{CD}	Input high-frequency voltage to the resonant circuit
V_{ab}, V_{cd}	Output high-frequency voltage from the resonant circuit
V_{batt}	Battery voltage
$V_{ds,off}$	Blocking drain-source voltage of the MOSFET
V_{in}	DC input voltage to the IPT system
V_{out}	DC output voltage from the IPT system
x	Duty cycle of the SCC, i.e., x=$\frac{t_{on}}{T}$
x, y, z	Coordinate axes in the three-dimensional Cartesian system
x_a, y_a, z_a	Dimensions of the coil's aluminum shield
x_c, y_c	Winding length and width
x_f, y_f, z_f	Dimensions of the coil's equivalent ferrite layer
$x_{f,unit}$, $y_{f,unit}$	Dimensions of the single ferrite unit
x_l	Total length occupied by the coils in the BPP
$x_{overlap}$	Overlap between the BPP's coils
Z_{ag}	Air gap between the coupled coils
Z_{in}	Equivalent input impedance of the resonant circuit
Z_r	Equivalent reflected impedance in series to the primary coil
z_{f-c}	Distance between the winding and the ferrite layer
z_{f-a}	Distance between the ferrite layer and the aluminum shield
η_{ac}	Power transfer efficiency of the resonant circuit
$\eta_{\text{DC-to-DC}}$	Power transfer efficiency measured at the DC input and output
θ	Position angle, i.e., θ=$\omega \cdot t$
λ	Wavelength
μ_0, μ_r	Permeability of the vacuum, relative permeability
ϕ	Phase angle
ω, ω_0	Angular frequency of a signal, angular resonant frequency

The circuit analysis uses the phasor convention. Considering that $\boldsymbol{A}$ is a complex number representing a sinusoidal function with angular frequency ω=$2\pi f$, the following equivalent notations are used:

$$\boldsymbol{A} = A\angle\phi_A \quad \rightarrow \quad \text{polar form}$$
$$\boldsymbol{A} = \text{Re}[\boldsymbol{A}] + j\,\text{Im}[\boldsymbol{A}] \quad \rightarrow \quad \text{rectangular form}$$

where A is the amplitude (absolute value), and ϕ_A is the phase angle. Additionally, j is the imaginary unit, i.e., j^2=-1.

1

INTRODUCTION

1.1. OUTLOOK ON WIRELESS POWER TRANSFER

Wireless power transfer (WPT) consists of the exchange of electrical power with galvanic isolation between the transmitting and the receiving devices. Before discussing the wireless charging of batteries as a specific application of WPT, it is essential to explore different WPT technologies, their development in the last centuries, and their main industrial applications.

1.1.1. WPT TECHNOLOGIES

WPT takes place through the propagation of an electromagnetic field (EMF) or acoustic waves, of which the main technologies are listed in Figure 1.1. When considering electromagnetic waves, the WPT can occur in either the near-field or the far-field region depending on the distance between the transmitting and receiving antennas with respect to the EMF's wavelength. According to [1], D is defined as the largest dimension of the antenna and λ is the EMF's wavelength.

The WPT is realized in the far-field radiative region if the distance between the transmitting and the receiving antennas is larger than the Fraunhofer distance $2D^2/\lambda$ [1]. This condition is valid if D is large compared to λ. Consequently, the EMF propagation in the far-field region is achieved through waves with relatively high frequencies, e.g., higher than 10 MHz. In that region, the angular field distribution does not depend on the distance from the antenna, and this is why it is said that the EMF radiates. Additionally, in the far-field region, the absorption of the energy from a receiver does not affect the transmitter [2]. Far-field radiative WPT can operate in considerably long distances, e.g., in the order of 10 km, and the radiation can be omnidirectional or unidirectional [1]. However, at those relatively high frequencies, only low power can be transferred due to the stringent exposure limits imposed for the safety of humans and electrical devices. The overall power transfer efficiency is generally very low in the case of omnidirectional antennas. In contrast, unidirectional antennas require a complex tracking mechanism to achieve an interrupted line-of-sight [3]. Far-field WPT can propagate through different waves, such

1

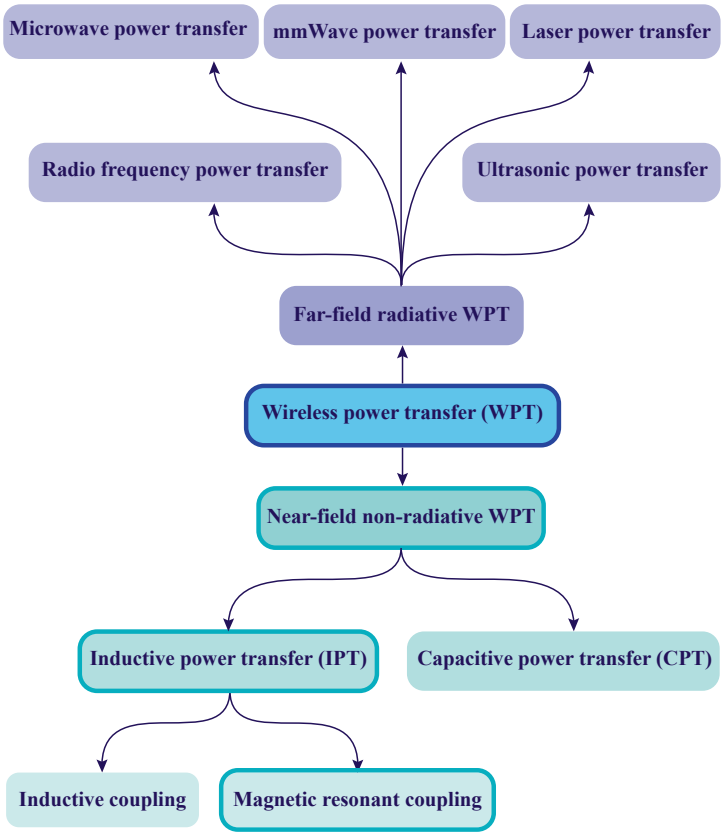

Figure 1.1: Summary of the WPT technologies depending on the electromagnetic field propagation.

as radio frequency (RF) waves, microwaves [4]–[6], laser beams [7], mmWave beams [6], and ultrasonic waves [8].

On the other hand, the near-field region is the immediate surrounding space around the transmitting antenna. When D is large compared to λ, the near-field region is divided into a reactive region and a radiative (Fresnel) region, whose boundary between them is defined at the distance $0.62\sqrt{D^3/\lambda}$ from the antenna surface [1]. Conversely, in the case of short antennas ($D < \lambda$) typical for EMF with frequencies below 10 MHz, the radiative near-field region might not exist, and the boundary between the near-field and the far-field regions is $\lambda/2\pi$ from the antenna surface [1]. All in all, the definitions of far-field and near-field regions are summarized in Figure 1.2, where Figure 1.2(a) is valid for antennas with $D > \lambda$ and Figure 1.2(b) is valid for antennas with $D < \lambda$.

In the near-field region, the angular field distribution is dependent on the distance, and it does not necessarily have a uniform pattern. This results in relatively short transmission distances, normally shorter than 10 m. Additionally, in the near-field region, the energy absorption from a receiver directly affects the transmitter and, consequently, this also takes the name of coupling-based WPT [2]. The near-field non-radiative WPT takes place either in the form of inductive power transfer (IPT) if it is based on the magnetic

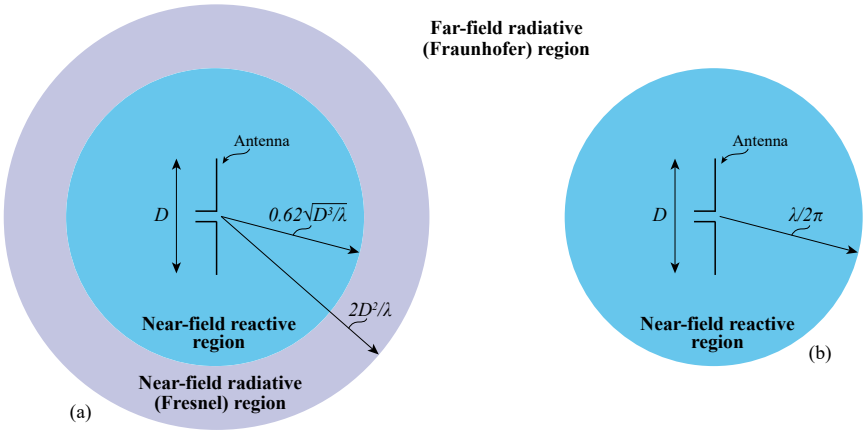

Figure 1.2: Definition of far-field and near-field regions of the EMF according to [1], valid for antennas such that: (a) $D > \lambda$, and (b) $D < \lambda$. Note that (b) is typical for applications with EMF frequencies below 10 MHz.

field exchange between coupled coils or as capacitive power transfer (CPT) if it is based on the electric field exchange between coupled metallic plates. IPT systems can use purely inductive coupling (IPT-IC) with the principle of magnetic induction. In this case, the separation between the coils is typically short, e.g., a few millimeters, to achieve a relatively strong coupling. IPT with inductive coupling requires typically a precise alignment which limits the flexibility in the receiving coil's position. Alternatively, IPT systems can use magnetic resonant coupling (IPT-MRC), which employs compensation networks connected to the coupled coils tuned to a specific resonant frequency. Operating the IPT system around that frequency minimizes the circulating reactive at low coupling factors (typically k <0.4), achieving considerably high power transfer efficiencies, which can be over 97% [9]. IPT with magnetic resonance allows more flexibility in the receiving coil's position, and the distance between the coupled coils can range from a few centimeters to several meters. Moreover, this technology is generally used to transfer high power levels up to the order of several hundreds of kW. Conversely, CPT can advantageously transfer power through metallic surfaces, it does not produce eddy currents, and it can achieve good misalignment tolerance. However, as explained in [10], CPT systems have a lower surface power density than IPT systems at relatively large air gaps. For this reason, CPT has been mostly used in applications with short distances between the coupled plates.

1.1.2. BRIEF HISTORY

The historical development of WPT has been summarized in the timeline shown in Figure 1.3. As acknowledged by [11]–[14], the first RF system was implemented by the physicist Heinrich Hertz with the aim of proving Maxwell's equation on electromagnetism. In 1887, Hertz proved electromagnetic wave propagation in free air by implementing the first radio system using a transmitting and a receiving end with a spark gap. However, he did not foresee any application for this system at that time.

The most famous pioneer of WPT is Nikola Tesla, which started being interested in the topic in the early 1890s. He was convinced that waves of electrical energy would propagate through the surface of the Earth by running alternating surges of currents

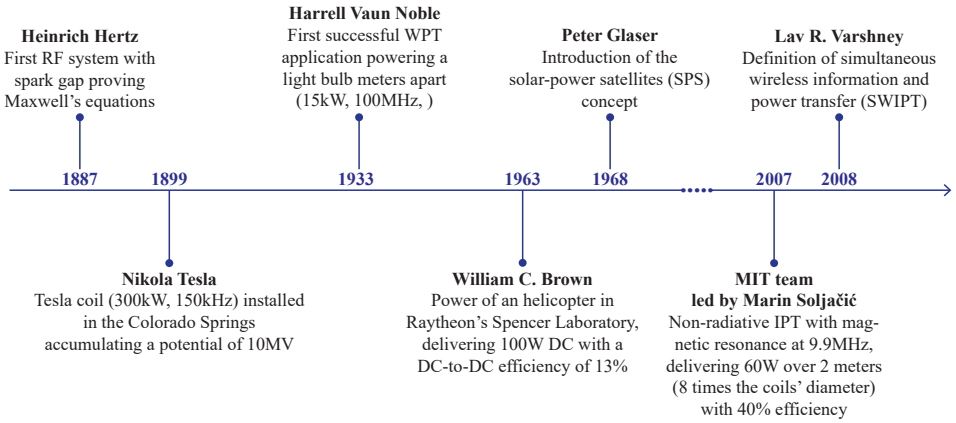

Figure 1.3: Summary of the historical developments on WPT.

through a mast. Then, it would be possible to realize a wireless power transmission by positioning receivers in optimum locations. For this purpose, in 1899, he ran experiments in the Colorado Springs laboratory using a large Tesla coil composed of a 61 m metallic mast with a 0.9 m ball mounted on top. Once the mast was electrified with 300 kW at 150 kHz, Tesla stated that a 10 MV RF potential was produced on the metallic sphere [4], [12]–[15]. His collaborators and the local residents witnessed this large discharge, but no measurements or conclusions resulted from this experiment. To continue his work on WPT, Tesla started the construction of the Wardenclyffe Tower Facility in 1901, which was supposed to be used for communication broadcasting and wireless power transmission. However, the project was never completed due to the lack of funding. Later in 1919, Tesla summarized his work on WPT in [11].

The next attempt at the realization of an efficient WPT took place in the early 1930s in the Westinghouse laboratory [12]–[14], where Harrell Vaun Noble demonstrated the RF power transfer at 100 MHz from a 15 kW transmitter to a light bulb 5 meters apart, without any rectification.

With the development of the available technologies, investigation on WPT based on microwaves was initiated in the 1950s. The first demonstration of a microwave beam powering a prototype helicopter was executed in 1963 by William C. Brown in Raytheon's Spencer Laboratory, delivering 100 W DC with a DC-to-DC efficiency of 13%. This seems to be the first demonstration of DC power delivery through microwaves. In 1964, a famous public demonstration of this technology was broadcasted by CBS news, where a helicopter was powered by a 2.45 GHz microwave beam generated by a 5 kW magnetron for 10 hours at the height of about 18 m [6], [12]–[14].

Further developments in microwave power transfer technology continued with the concept of the solar-power satellite (SPS) introduced by Peter Glaser in 1968 [16]. This consists in harvesting solar power through a satellite in the geostationary orbit and then transmitting the power to Earth through a microwave power beam. In [12], a detailed description of the initial SPS project can be found, which NASA decided to stop in 1980. Nevertheless, at the current date of publication of this thesis, there is still research done on SPS [5], [6], [14]. Additionally, [6] explains in detail the advancements in microwave

power transfer worldwide up to the current date.

In the early 2000s, two significant achievements were recorded by the Massachusetts Institute of Technology (MIT). In 2007, the team led by Marin Soljačić recorded the 45% power transfer efficiency from a near-field IPT system using magnetic resonance at 9.9 MHz delivering 60 W over 2 m distance between two air coils [17]. In the same year, Soljačić founded the company WiTricity as a spin-off from MIT. The second achievement from MIT date back to 2008 when Lav R. Varshney proposed the simultaneous wireless information and power transfer (SWIPT) [18].

Since the 2010s, the interest in WPT technologies has been mostly focused on their development in several industrial and consumer applications, including their standardization, with the goal of developing products ready for the market.

1.1.3. APPLICATIONS

The WPT technologies summarized in Figure 1.1 are used in commercial products when it is beneficial to eliminate the cable connection between the power transmitting device and the receiver end. Generally, WPT can be used to directly power devices or for charging their battery. Table 1.1 lists several applications that currently employ WPT.

Table 1.1: Example of applications that use WPT technologies.

Application	Far-field WPT	Near-field WPT	References
Road electric vehicles (EVs)	N/A	IPT-MRC, CPT	[10]
Autonomous underwater vehicles (AUVs)	N/A	IPT-MRC	[19]
Unmanned aerial vehicles (UAVs)	Microwaves	IPT-MRC	[12], [20]
Solar-power satellite (SPS)	Microwaves	N/A	[6], [16]
Implantable medical devices (IMDs)	Ultrasonic waves	IPT-IC, IPT-MRC, CPT	[8], [21]
Simultaneous wireless information and power transfer (SWIPT)	Microwaves	N/A	[13], [18], [22]
Electric toothbrush	N/A	IPT-IC	[23]
Consumer electronics devices	RF waves	IPT-IC, IPT-MRC	[24], [25]
Induction heating	N/A	IPT-MRC	[26], [27]

1.2. INDUCTIVE POWER TRANSFER WITH MAGNETIC RESONANT COUPLING FOR EV WIRELESS CHARGING

The Dutch government aims to reach zero-emission for all passenger vehicles by 2030 [28]. This means that the market for electric vehicles (EVs) is predicted to grow considerably in the coming years. According to [29], wireless charging increases the users' interest in EVs if this option is included. Therefore, wireless charging can play a key role in the driver's decision to buy an EV. This is mainly because wireless charging is an intrinsically user-friendly technology: it eliminates the inconvenience of handling charging cables, which might be bulky and not safe, especially in the presence of wet weather conditions. The wireless charging option becomes even more essential when considering completely autonomous EVs. Since these vehicles are driverless, they should be auto-

matically charged without people involved. Additionally, wireless charging enables the possibility of charging the EV in motion, called dynamic wireless charging. This could allow a more frequent recharge of the EV batteries, potentially reducing their size. Dynamic charging is widely used in public transportation via overhead cables, but it would be unfeasible in the case of private EVs. Furthermore, quasi-dynamic wireless charging represents another convenient use case for EVs that often move slowly in queues, such as taxi lanes in front of airports and stations or congested streets. It is not practical for drivers to charge their EVs with a plug-in cable since they might need to move up the line shortly after. In these examples, the need for wireless charging becomes evident.

Due to the growing industrial interest in this technology, standards and regulations have been released starting from 2015, such as SAE J2954, the IEC 61980 series, and ISO 19363 [30]. These standards define the main characteristics of EV wireless charging systems, such as the power classes, the possible relative positions between the charging station and the EV, the allowed operating frequency range, minimum communication features, and electromagnetic compatibility (EMC) limits. In short, the currently available standards regulate static wireless charging systems for light-duty EVs. SAE J2954 defines three power classes named WPT1, WPT2, and WPT3, limiting the maximum input power obtainable from the grid connection to 3.7kVA, 7.7kVA, and 11.1kVA, respectively. Additionally, the operating frequency of the IPT converter is limited between 79 kHz and 90 kHz. An updated and detailed overview of those standards can be found in Appendix A. Several companies have already commercialized EV wireless charging products and examples are WiTricity, IPT Group, Plugless Power, Momentum Dynamics, ElectReon, and WAVE. Additionally, the significant investment of Siemens in WiTricity announced in June 2022 clearly shows that the EV wireless charging market is predicted to grow considerably in the following years [31].

EV wireless charging is most commonly realized using IPT-MRC technology, which is explained in Section 1.1.1. The transmitting coil is placed on the ground (or embedded), and it is part of the ground assembly (GA) [32]. On the other hand, the receiving coil is mounted on the chassis of the EV, and it is part of the vehicle assembly (VA) [32]. Thereby, the coupled coils together with the compensation network constitute an isolated resonant converter. The coupled coils form a loosely coupled transformer since their distance is relatively large, typically equal or greater than 10 cm.

In this application, the converter essentially has two main variables influencing its operation. The first variable is the coupling factor k between the coils, which depends on their alignment as a function of the time [33]. For instance, in the case of static charging, the distance between the coils' magnetic centers is fixed during one charging cycle, while in the case of dynamic charging, it continuously changes. Conversely, quasi-dynamic charging can assume both characteristics during one charging cycle. The second variable is the equivalent load which changes continuously throughout the battery charging profile. For example, the Lithium-ion batteries' voltage rises during the constant current charging mode, while the current gradually decreases during the constant voltage charging mode. An IPT system for EV wireless charging must be able to operate in those different coils' alignment and load conditions.

The coils' alignment and load operating conditions might vary when considering different applications. Nevertheless, all IPT systems share the same challenges which are

essential to this research. The first challenge is ensuring a highly efficient power transfer. The second one is guaranteeing that the intentionally radiated EMF is not harmful to the living beings in the surroundings and that it is lower than the recommended EMC limits. Finally, another challenge is guaranteeing interoperability between IPT charging stations and EVs from different manufacturers.

1.2.1. POWER TRANSFER EFFICIENCY

In EV charging applications, the power transfer efficiency is defined as the ratio between the delivered DC output power to the EV battery and the input power drawn either from the utility AC grid or from a DC source. The true advantage of static EV wireless charging over cable charging must be supported by an efficient power transfer at different operating conditions. This would translate into a relatively low demand for input energy for each charging cycle, which is essential for realizing a sustainable and cost-effective EV charging solution.

The typical main power conversion stages used in two-stage high-power EV chargers are shown in Figure 1.4, where Figure 1.4(a) illustrates a conductive charger while Figure 1.4(b) shows a wireless charging implementation. Both technologies have a similar structure with galvanic isolation provided by a high-frequency transformer. The conductive charger employs a highly coupled transformer placed off-board the EV. On the other hand, in the wireless charging system, the primary winding is placed off-board while the secondary winding is placed on-board the EV, resulting in a loosely coupled transformer due to the large air gap. This relatively low coupling likely translates into a lower power density of the transformer with respect to the one used in conductive charging. This could result in the demand for longer transformer windings to achieve a minimum target of coupling factor, eventually leading to higher conduction losses. Moreover, the loosely coupled transformer results in a large leakage inductance which requires additional compensation networks. Most of the power losses in IPT systems are generally located in the resonant circuit, consisting of the coupled coils and their compensation

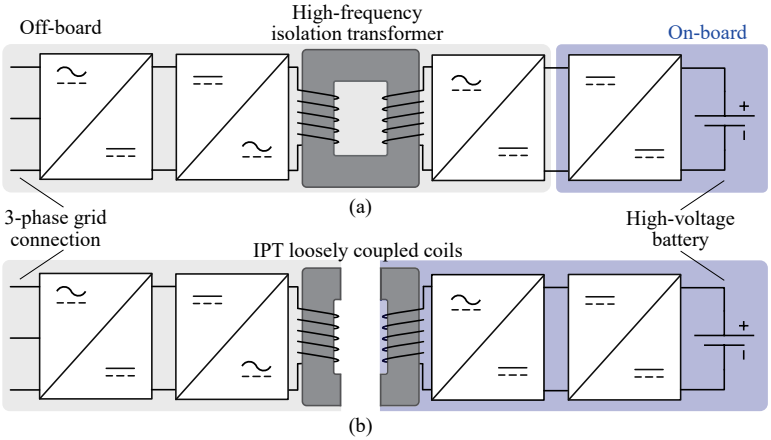

Figure 1.4: Typical structure of three-phase isolated high-power EV battery chargers using: (a) a cable connection, or (b) a wireless connection to the battery.

network, for which design and implementation must be carefully chosen.

The high power transfer efficiency of an EV wireless charging system must be accounted for when designing the system and during the charging operation. In the design stage, the optimized charging coils' structure has been widely investigated since they contribute to considerable power losses. In [34]–[38], multi-objective optimizations of the coils have been performed. The optimization of the cores' structures using artificial intelligence has been explored in [39]. Advancements in magnetic materials have been researched in [40]. To reduce the drop in magnetic coupling with the misalignment, multicoil configurations have been compared to the single coil ones in [37]. Additionally, the compensation network's selection and design would influence the power transfer performance. For instance, the compensation network can comprise a single capacitor connected in series or parallel with the coils. Conversely, the compensation network can be made of multiple components or even variable compensation components [33], [41]. For what concerns the power converters, wireless charging systems differ in the number of power conversion stages as summarized in [42], which depend on the implemented control strategy. Once the IPT system has been designed and implemented, the chosen operating scheme during the battery charging cycle will influence the power transfer efficiency. Therefore, the control strategy is ultimately important to achieve a highly efficient IPT system. Possible control strategies are discussed in [43] and [44].

1.2.2. EMC AND EMF HUMAN EXPOSURE LIMITS

EV wireless charging systems must comply with the EMC regulations to qualify as commercial products. In this technology, the most critical EMC aspect is the radiated disturbances from the intentional magnetic field realizing the WPT, which are regulated in the RF spectrum up to 30 MHz. Additionally, the fundamental component of the radiated EMF, which is within 79 kHz and 90 kHz, must be not harmful to the living beings in the accessible surrounding of the IPT system. The maximum exposure to magnetic fields is 27 μT for the general public, and 15 μT for cardiac implantable electronic devices (CIED) [32]. Moreover, SAE J2954 proposes shutdown ad detection methods that minimize the possible human exposure to high magnetic fields.

In the literature, shielding strategies have been proposed to reduce the magnetic field radiation around the IPT system. Examples are listed in [33] and [44], such as passive shielding (ferrite), passive conductive shielding (aluminum plates), active shielding, and reactive shielding. Another interesting approach is proposed in [45] based on spread spectrum techniques.

1.2.3. INTEROPERABILITY

The GAs and VAs must be compatible to allow the wireless charging process. Especially when considering public charging infrastructures, interoperability is fundamental to ensure that this technology can be used on a mass scale. The industrial standards and regulations provide minimum interoperability requirements for different EV wireless charging systems. However, no strategies have been defined for transferring power to EV batteries from different voltage classes or employing multicoil topologies for the magnetic pads' configuration.

BATTERY VOLTAGE INTEROPERABILITY

The nominal battery voltage of EVs is not necessarily the same. According to [46], the nominal voltage of EV batteries could mostly be either 400 V or 800 V, which is confirmed by Table 1.2. The first released EVs have a nominal battery voltage of around 400 V since more automotive-qualified components are available for that voltage class. However, some automotive original-equipment manufacturers are moving to 800 V architectures because the higher DC-link voltage results in two main advantages, being the substantial weight saving across the EV and the considerable reduction of the battery charging time [47]–[49]. Especially when considering applications such as public parking infrastructures, taxi pick-up locations in front of stations or airports, corporate fleets, car rental, or sharing facilities, it is essential that wireless chargers can supply power efficiently to both EV battery classes.

IPT systems can achieve high power transfer efficiency when operating at the nominal operating condition for a certain power level, i.e., at the chosen converter's voltage gain, defined as the ratio been the input and output voltage. Charging a battery with either double or half of the nominal voltage would dramatically worsen the system efficiency for the same output power [50]. Therefore, solutions must be found to guarantee battery interoperability.

Table 1.2: List of commercial EVs and their battery voltage. [50]

Year of launch	Manufacturer	Model	Battery voltage (latest model)	Source
2018	Audi	e-tron	396 V	[51], [52]
2020	FIAT	new 500e	364 V	[51]
2019	Mercedes-Benz	EQC	405 V	[51]
2021		EQA	420 V	
2022		EQB	420 V	
2013	Nissan	Leaf S	350 V	[51]
2010		Leaf SV Leaf SL	360 V	[51], [53]
2012	Tesla	Model S	400 V	[51], [54]
		Model X	350 V	[51]
2017		Model 3	360 V	
2010	Volkswagen	e-up!	374 V	[51]
214		e-Golf	323 V	[51], [55]
2019		ID.3	408 V	[51]
2019	Aston Martin	Rapide E	800 V	[51]
2021	Hyundai	IONIQ 5	800 V	[51], [56]
2021	KIA	EV6	697 V	[51]
2019	Porsche	Taycan	800 V	[51], [57]

COUPLED COILS INTEROPERABILITY

Furthermore, the coupled coils can have various configurations depending on the layout of the winding. For instance, SAE J2954 defines several examples of coils' design with a single winding which can be classified as either rectangular pads (RP) or double-D pads (DDPs). The winding of both topologies has a planar configuration placed on a ferrite layer, which is mounted on an aluminum plate for shielding and mechanical strength purposes. RPs consist of a planar rectangular-shaped winding as qualitatively shown in Figure 1.5(a), which are classified as nonpolarized pads [10]. Their radiated magnetic

field resembles the pattern generated in an E ferrite core inductor when the middle-leg winding conducts an alternating current. Other examples of nonpolarized pads are circular and squared pads with a field pattern similar to the RPs. On the other hand, DDPs consist of two planar rectangular-shaped windings connected in anti-series such that their current direction is opposite. A typical DDP is qualitatively shown in Figure 1.5(b), and due to their structure, DDPs are classified as polarized pads [10]. Their radiated magnetic field resembles the pattern generated in a U ferrite core inductor when its winding conducts an alternating current. As a result, nonpolarized pads are more sensitive to magnetic fields perpendicular (vertical) to their surface, while polarized pads are more sensitive to parallel (horizontal) ones. These different field patterns make it inconvenient to couple a polarized coil with a nonpolarized coil since their coupling factor would be poor. If their geometrical centers are aligned, their coupling factor would be close to zero. To mitigate this issue, SAE J2954 suggests alignment methods to enhance the coupling between polarized and nonpolarized pads, ensuring their magnetic centers are aligned.

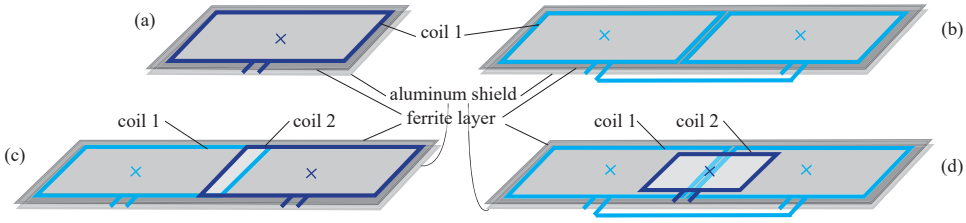

Figure 1.5: Typical structure of magnetic pads used in IPT systems. Single coil configurations: (a) rectangular pad, and (b) double-D pad. Multicoil configurations: (c) bipolar pad, and (d) double-D quadrature pad.

Conversely, multicoil pads could be used to achieve interoperability with RPs and DDPs since they can work selectively as a polarized or nonpolarized pad. In EV wireless charging applications, the most common multicoil pads are the bipolar pad (BPP) [58] and the double-D quadrature pad (DDQP) [59]. The BPP consists of two independent partially-overlapped rectangular coils as qualitatively shown in Figure 1.5(c). BPPs can work as a polarized or nonpolarized pad depending on the phase of the current flowing through each coil. On the other hand, the DDQP consists of a DDP with an RP overlapped in the center, as qualitatively shown in Figure 1.5(d). In this case, the DDP would be energized when coupled with another DDP, while the RP would be energized when coupled with another RP. Nevertheless, magnetic pads with multiple coils intrinsically have unwanted cross-coupling, which influences the power transfer and, eventually, the IPT system's performance.

1.3. SCOPE, OBJECTIVE, AND RESEARCH QUESTIONS

Scope:

This thesis focuses on the power conversion stages of IPT systems used for wireless charging of EVs, which block schematic is illustrated in Figure 1.6. Thereby, the GA includes the entire transmitting circuit located on the ground, while the VA consists of the receiving circuit, which is placed on the EV. The domain of this research is highlighted in Figure 1.6, which comprises the power conversion stages within the DC input voltage provided by a grid-connected boost-like power factor corrector (PFC) rectifier and the DC output voltage set by the EV battery. To limit the cost and the complexity of the circuit onboard the EV, it is assumed that no output DC/DC converter is employed, meaning that the battery is directly connected to the output of the IPT system.

This research considers static wireless charging applications, i.e., the coupling factor between the coils is fixed during the battery charging cycle. Moreover, the power levels adopted for the experimental verification are 3.7 kW and 7.7 kW. The following objective and research questions are defined in view of this domain.

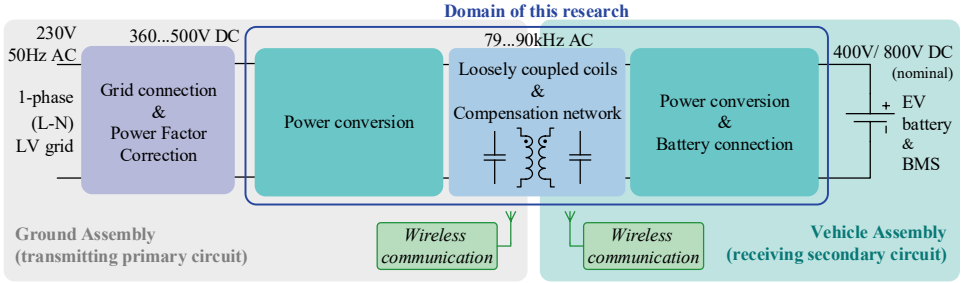

Figure 1.6: Domain of this research in the application of static EV wireless charging. The DC input voltage is the rectified voltage from the one-phase low-voltage grid, while the DC output voltage is given by the EV battery. The power levels considered for the experimental verification are 3.7 kW and 7.7 kW.

Objective:

Maximize the efficiency of inductive power transfer systems for charging electric vehicles at different coils' alignment and load conditions, ensuring that the system's operating frequency is always within the standardized range 79-90 kHz.

Research questions:

1. *Which are the most suitable compensation networks for EV wireless charging?*
   Chapter 2
   Considering the typically low coupling factor of the coupled coils, compensation networks must be used to minimize the IPT system's VA rating. Numerous compensation topologies can be adopted in IPT systems which can differ in the number of components, type of connection to the coupled coils, or tuning method. The main characteristics of the typical compensation networks used in IPT systems will be analyzed focusing on the application of EV wireless charging.

2. *Is it advantageous to employ variable compensation networks to mitigate the effects*

of misalignment on the IPT systems' performance? **Chapter 3**
The operating condition that results in the maximum power transfer efficiency is directly dependent on the coils' alignment. Normally, a DC/DC converter is connected to the battery to always match the optimum efficiency condition. It will be proved that employing a variable compensation can eliminate the need for output voltage control.

3. *How can EVs with different nominal battery voltage levels be charged efficiently at the same power class?* **Chapter 4, Chapter 5**
When considering public parking infrastructures, EV wireless chargers must efficiently deliver electric power EVs with both 400 V and 800 V nominal battery voltages. This can be normally achieved by regulating the output voltage through a DC/DC converter at the cost of higher onboard circuit complexity and lower overall efficiency. A universal wireless charging system named voltage/current doubler (V/I-D) will be proposed that maintains a high power transfer efficiency when charging EVs with both battery options at the same power level such that the power capability of the IPT charging station is always fully utilized.

4. *How does the cross-coupling of multicoil magnetic pads affect the performance of IPT systems?* **Chapter 4, Chapter 5**
The proposed V/I-D system uses two primary and two secondary magnetic pads. The option of employing multicoil pads will be evaluated considering bipolar pads in Figure 1.5(c). This choice for the magnetic arrangement leads to the presence of unwanted cross-coupling between the coils that affects the V/I-D functionality. Methods to compensate for the cross-coupling will be proposed regarding the BPP design, compensation components' selection, and the operating strategy which can be extended to other multicoil pads or IPT circuit topologies.

1.4. METHODOLOGY

The methodology used to answer the research question in Section 1.3 consists of the iterative process summarized in Figure 1.7. Each solution to a research question is first defined as a concept. The second step consists of developing the concept into an analytical model that can describe its characteristics. After that, the model is preliminarily validated through simulations. The final validation requires implementing the proposed solution so that experimental results can be collected.

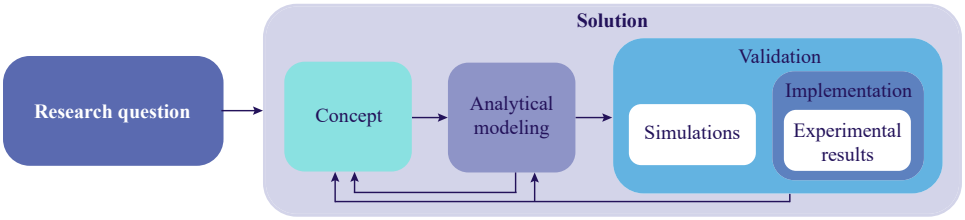

Figure 1.7: The research methodology used in this thesis concerning the research questions.

1.5. OUTLINE OF THE THESIS

This thesis is composed of six main chapters and two appendix chapters. Considering that the first chapter is the introduction while the last chapter is the conclusion, the research content is spread out over the four central chapters. Additionally, these four chapters are divided into three different parts depending on their topic. The structure of the thesis's outline is summarized in Figure 1.8.

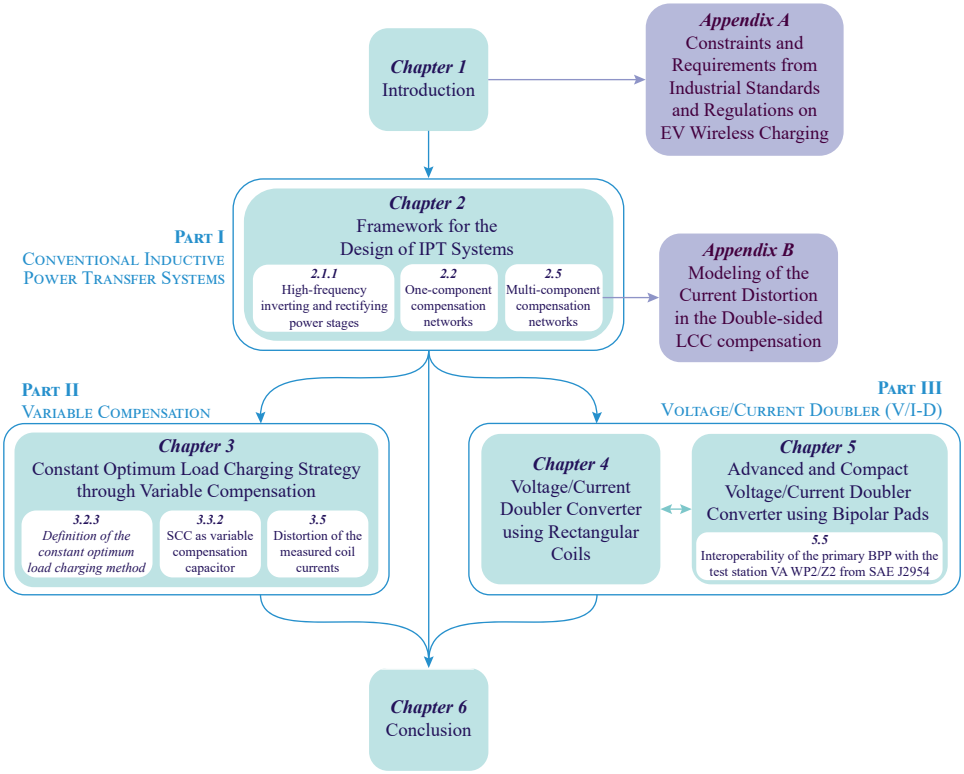

Figure 1.8: Outline of the thesis: definitions of the parts, the chapters, and their connections.

Chapter 1 is the introduction to this research on IPT systems for EV wireless charging. To ensure that this thesis's contributions would also have an industrial and commercial value, it is essential to be aware of the available standards and regulations on this technology. These constraints have been explored in Appendix A, which is an extension of Chapter 1.

Part I follows the introduction and discusses the conventional IPT systems as the state of the art of this application. This part consists of Chapter 2, which focuses on the modeling and the main features of the compensation networks, addressing how they influence the performance of IPT systems and the configuration of the high-frequency power conversion stages. Appendix B is an extension of Chapter 2 where the current distortion in the double-sided LCC compensation is analyzed and modeled in detail. After that, Part II and Part III propose original developments starting from the conventional

IPT systems discussed in Part I.

Part II explores the advantages of using a variable compensation. Thereby, Chapter 3 defines an efficiency enhancement charging method called constant optimum load that employs variable series compensation capacitors implemented as switch-controlled capacitors (SCCs). Moreover, the current distortion through the coils caused by the SCCs is analyzed and compared to the case of conventional fixed compensation capacitors.

Part III proposes a novel IPT system called V/I-D converter to achieve interoperability with EV batteries belonging to different voltage classes. Specifically, the V/I-D converter can efficiently charge EVs with the typically used 400 V and 800 V batteries at the same output power. The V/I-D converter uses two primary and two secondary coils. Chapter 4 investigates the concept of the V/I-D converter when the magnetic arrangement consists of two physically separated sets of rectangular coupled coils, resulting in a functionality close to the ideal intended one. In this implementation, the occupied space by the V/I-D converter might be considerably large, which might be critical, especially for small-size light-duty EVs. For that purpose, Chapter 5 explores a more advanced implementation of the V/I-D converter in which the magnetic configuration consists of multicoil pads, here being BPPs. This alternative implementation results in a compact magnetic configuration since the two coils at each circuit side are deployed on the same ferrite layer. Nevertheless, the proximity between the coils results in unwanted cross-coupling effects that influence the V/I-D converter performance. Chapter 5 analyzes this influence in detail, defining design and operating strategies that preserve the V/I-D converter's advantages and functionality. The interoperability between a GA consisting of a V/I-D converter with primary BPP and a VA composed of a secondary standardized coil has also been proved. This feature further enlarges the applicability of the proposed V/I-D converter.

Finally, Chapter 6 summarized the conclusions of this thesis by answering the research questions defined in Section 1.3.

1.6. RESEARCH CONTRIBUTIONS

This section lists the scientific publications relevant to this thesis.

Journal papers

- F. Grazian, T. B. Soeiro, P. Bauer, “Inductive Power Transfer based on Variable Compensation Capacitance to Achieve an EV Charging Profile with Constant Optimum Load”, in *IEEE Journal of Emerging and Selected Topics in Power Electronics*, 2022. **Chapter 3**

- F. Grazian, T. B. Soeiro, P. Bauer, “Voltage/Current Doubler Converter for an Efficient Wireless Charging of Electric Vehicles with 400V and 800V Battery Voltages”, in *IEEE Transaction on Industrial Electronics*, 2022. **Chapter 4**

- F. Grazian, T. B. Soeiro, P. Bauer, “Voltage/Current Doubler Converter for Electric Vehicle Wireless Charging Employing Bipolar Pads”, in *IEEE Journal of Emerging and Selected Topics in Power Electronics*, 2023. **Chapter 5**

- F. Grazian, G. Yu, G. Zhu, C. Riekerk, J.Dong, T. B. Soeiro, P. Bauer, “Modeling of the Inverter Current Distortion in the Double-sided LCC Compensation for Inductive Power Transfer Systems”, *submitted*. **Appendix B**

Conference papers

- F. Grazian, W. Shi, J. Dong, P. van Duijsen, T. B. Soeiro, P. Bauer, "Survey on Standards and Regulations for Wireless Charging of Electric Vehicles", *2019 AEIT International Conference of Electrical and Electronic Technologies for Automotive (AEIT AUTOMOTIVE)*, 2019, pp. 1-5. **Appendix A**

- F. Grazian, W. Shi, T. B. Soeiro, J. Dong, P. van Duijsen, P. Bauer, “Quality Factor Based Design Guideline for Optimized Inductive Power Transfer”, *2020 IEEE PELS Workshop on Emerging Technologies: Wireless Power Transfer (WoW)*, 2020, pp. 178-183. **Chapter 2**

- F. Grazian, T. B. Soeiro, P. Bauer, “Design Trade-Offs Between the Coupled Coils’ Inductance and the Series-Series Compensation Capacitance for EV Wireless Charging Systems”, *2022 International Symposium on Power Electronics, Electrical Drives, Automation and Motion (SPEEDAM)*, 2022, pp. 270-276. **Chapter 2**

- F. Grazian, T. B. Soeiro, P. Bauer, “Coils’ Current Distortion Due to Variable Series Compensation Capacitance in EV Wireless Charging for a Constant Optimum Load”, *2022 Wireless Power Week (WPW)*, 2022, pp. 54-59. **Chapter 3**

- F. Grazian, T. B. Soeiro, P. Bauer, “Interoperability of the Voltage/Current Doubler Converter Employing Bipolar Pads with the SAE J2954 VA WPT2/Z2 for EV Wireless Charging”, *2022 IEEE 20th International Power Electronics and Motion Control Conference (PEMC)*, 2022, pp. 346-352. **Chapter 5**

1

REFERENCES

[1] C. A. Balanis, *Antenna theory: analysis and design*. John Wiley & Sons, 2005.

[2] X. Lu, P. Wang, D. Niyato, D. I. Kim, and Z. Han, "Wireless charging technologies: Fundamentals, standards, and network applications", *IEEE Communications Surveys Tutorials*, vol. 18, no. 2, pp. 1413–1452, 2016. DOI: 10.1109/COMST.2015.2499783.

[3] M. T. Bevacqua, G. G. Bellizzi, and M. Merenda, "An efficient far-field wireless power transfer via field intensity shaping techniques", *Electronics*, vol. 10, no. 14, 2021, ISSN: 2079-9292. DOI: 10.3390/electronics10141609. [Online]. Available: https://www.mdpi.com/2079-9292/10/14/1609.

[4] J. Garnica, R. A. Chinga, and J. Lin, "Wireless power transmission: From far field to near field", *Proceedings of the IEEE*, vol. 101, no. 6, pp. 1321–1331, 2013. DOI: 10.1109/JPROC.2013.2251411.

[5] J. Huang, Y. Zhou, Z. Ning, and H. Gharavi, "Wireless power transfer and energy harvesting: Current status and future prospects", *IEEE Wireless Communications*, vol. 26, no. 4, pp. 163–169, 2019. DOI: 10.1109/MWC.2019.1800378.

[6] C. T. Rodenbeck, P. I. Jaffe, B. H. Strassner II, *et al.*, "Microwave and millimeter wave power beaming", *IEEE Journal of Microwaves*, vol. 1, no. 1, pp. 229–259, 2021. DOI: 10.1109/JMW.2020.3033992.

[7] K. Jin and W. Zhou, "Wireless laser power transmission: A review of recent progress", *IEEE Transactions on Power Electronics*, vol. 34, no. 4, pp. 3842–3859, 2019. DOI: 10.1109/TPEL.2018.2853156.

[8] S. Roy, A. N. M. W. Azad, S. Baidya, M. K. Alam, and F. Khan, "Powering solutions for biomedical sensors and implants inside the human body: A comprehensive review on energy harvesting units, energy storage, and wireless power transfer techniques", *IEEE Transactions on Power Electronics*, vol. 37, no. 10, pp. 12 237–12 263, 2022. DOI: 10.1109/TPEL.2022.3164890.

[9] W. Shi, J. Dong, T. B. Soeiro, *et al.*, "Design of a highly efficient 20-kw inductive power transfer system with improved misalignment performance", *IEEE Transactions on Transportation Electrification*, vol. 8, no. 2, pp. 2384–2399, 2022. DOI: 10.1109/TTE.2021.3133759.

[10] D. Vincent, P. S. Huynh, N. A. Azeez, L. Patnaik, and S. S. Williamson, "Evolution of hybrid inductive and capacitive ac links for wireless ev charging—a comparative overview", *IEEE Transactions on Transportation Electrification*, vol. 5, no. 4, pp. 1060–1077, 2019. DOI: 10.1109/TTE.2019.2923883.

[11] N. Tesla, "The true wireless", *The Electrical Experimenter*, 1919.

[12] W. Brown, "The history of power transmission by radio waves", *IEEE Transactions on Microwave Theory and Techniques*, vol. 32, no. 9, pp. 1230–1242, 1984. DOI: 10.1109/TMTT.1984.1132833.

[13] M. Xia and S. Aissa, "On the efficiency of far-field wireless power transfer", *IEEE Transactions on Signal Processing*, vol. 63, no. 11, pp. 2835–2847, 2015. DOI: 10.1109/TSP.2015.2417497.

[14] H. J. Visser, "A brief history of radiative wireless power transfer", in *2017 11th European Conference on Antennas and Propagation (EUCAP)*, 2017, pp. 327–330. DOI: 10.23919/EuCAP.2017.7928700.

[15] Z. Popovic, "Near- and far-field wireless power transfer", in *2017 13th International Conference on Advanced Technologies, Systems and Services in Telecommunications (TELSIKS)*, 2017, pp. 3–6. DOI: 10.1109/TELSKS.2017.8246215.

[16] P. E. Glaser, "Power from the sun: Its future", *Science*, vol. 162, no. 3856, pp. 857–861, 1968. DOI: 10.1126/science.162.3856.857.

[17] A. Kurs, A. Karalis, R. Moffatt, J. D. Joannopoulos, P. Fisher, and M. Soljačić, "Wireless power transfer via strongly coupled magnetic resonances", *Science*, vol. 317, no. 5834, pp. 83–86, 2007. DOI: 10.1126/science.1143254.

[18] L. R. Varshney, "Transporting information and energy simultaneously", in *2008 IEEE International Symposium on Information Theory*, 2008, pp. 1612–1616. DOI: 10.1109/ISIT.2008.4595260.

[19] C. R. Teeneti, T. T. Truscott, D. N. Beal, and Z. Pantic, "Review of wireless charging systems for autonomous underwater vehicles", *IEEE Journal of Oceanic Engineering*, vol. 46, no. 1, pp. 68–87, 2021. DOI: 10.1109/JOE.2019.2953015.

[20] J. M. Arteaga, S. Aldhaher, G. Kkelis, C. Kwan, D. C. Yates, and P. D. Mitcheson, "Dynamic capabilities of multi-mhz inductive power transfer systems demonstrated with batteryless drones", *IEEE Transactions on Power Electronics*, vol. 34, no. 6, pp. 5093–5104, 2019. DOI: 10.1109/TPEL.2018.2871188.

[21] A. N. M. S. Hossain, P. Mohseni, and H. M. Lavasani, "Design and optimization of capacitive links for wireless power transfer to biomedical implants", *IEEE Transactions on Biomedical Circuits and Systems*, pp. 1–14, 2022. DOI: 10.1109/TBCAS.2022.3213000.

[22] B. Clerckx, J. Kim, K. W. Choi, and D. I. Kim, "Foundations of wireless information and power transfer: Theory, prototypes, and experiments", *Proceedings of the IEEE*, vol. 110, no. 1, pp. 8–30, 2022. DOI: 10.1109/JPROC.2021.3132369.

[23] M. Stratmann and P. Trawinski, "Rechargeable toothbrushes with charging stations", US20030085687A1, 2003.

[24] *Wireless power consortium*, 2008. [Online]. Available: https://www.wirelesspowerconsortium.com/.

[25] *Airfuel alliance*, 2015. [Online]. Available: https://airfuel.org/.

[26] J. Acero, J. M. Burdio, L. A. Barragan, *et al.*, "Domestic induction appliances", *IEEE Industry Applications Magazine*, vol. 16, no. 2, pp. 39–47, 2010. DOI: 10.1109/MIAS.2009.935495.

[27] E. Plumed, I. Lope, J. Acero, and J. M. Burdío, "Induction heating of two magnetically independent loads with a single transmitter", *IEEE Transactions on Power Electronics*, vol. 37, no. 3, pp. 3391–3402, 2022. DOI: 10.1109/TPEL.2021.3117146.

[28] Netherlands Enterprise Agency (RVO), "Electric transport in the netherlands", 2022. [Online]. Available: https://english.rvo.nl/information/electric-transport.

[29] J. Andersson, M. Nilsson, and S. Pettersson, "Introducing wireless charging for drivers of electrical vehicles in sweden—effects on charging behaviour and attitudes", in *Advances in Human Aspects of Transportation*, Springer International Publishing, 2017, pp. 951–962, ISBN: 978-3-319-41682-3.

[30] F. Grazian, W. Shi, J. Dong, P. van Duijsen, T. B. Soeiro, and P. Bauer, "Survey on standards and regulations for wireless charging of electric vehicles", in *2019 AEIT International Conference of Electrical and Electronic Technologies for Automotive (AEIT AUTOMOTIVE)*, 2019, pp. 1–5. DOI: 10.23919/EETA.2019.8804573.

[31] Siemens Press, "Siemens invests in witricity to advance wireless charging for electric vehicles", 2022. [Online]. Available: https://press.siemens.com/global/en/pressrelease/siemens-invests-witricity-advance-wireless-charging-electric-vehicles.

[32] *J2954: Wireless power transfer for light-duty plug-in/ electric vehicles and alignment methodology*, Aug. 2022.

[33] H. Feng, R. Tavakoli, O. C. Onar, and Z. Pantic, "Advances in high-power wireless charging systems: Overview and design considerations", *IEEE Transactions on Transportation Electrification*, vol. 6, no. 3, pp. 886–919, 2020. DOI: 10.1109/TTE.2020.3012543.

[34] R. Bosshard, J. W. Kolar, J. Mühlethaler, I. Stevanović, B. Wunsch, and F. Canales, "Modeling and η-α-pareto optimization of inductive power transfer coils for electric vehicles", *IEEE Journal of Emerging and Selected Topics in Power Electronics*, vol. 3, no. 1, pp. 50–64, 2015. DOI: 10.1109/JESTPE.2014.2311302.

[35] R. Bosshard and J. W. Kolar, "Multi-objective optimization of 50 kw/85 khz ipt system for public transport", *IEEE Journal of Emerging and Selected Topics in Power Electronics*, vol. 4, no. 4, pp. 1370–1382, 2016. DOI: 10.1109/JESTPE.2016.2598755.

[36] M. Lu and K. D. T. Ngo, "A fast method to optimize efficiency and stray magnetic field for inductive-power-transfer coils using lumped-loops model", *IEEE Transactions on Power Electronics*, vol. 33, no. 4, pp. 3065–3075, 2018. DOI: 10.1109/TPEL.2017.2710141.

[37] S. Bandyopadhyay, P. Venugopal, J. Dong, and P. Bauer, "Comparison of magnetic couplers for ipt-based ev charging using multi-objective optimization", *IEEE Transactions on Vehicular Technology*, vol. 68, no. 6, pp. 5416–5429, 2019. DOI: 10.1109/TVT.2019.2909566.

[38] W. Shi, F. Grazian, S. Bandyopadhyay, J. Dong, T. B. Soeiro, and P. Bauer, "Analysis of dynamic charging performances of optimized inductive power transfer couplers", in *2021 IEEE 19th International Power Electronics and Motion Control Conference (PEMC)*, 2021, pp. 751–756. DOI: 10.1109/PEMC48073.2021.9432541.

[39] B.-G. Choi and Y.-S. Kim, "New structure design of ferrite cores for wireless electric vehicle charging by machine learning", *IEEE Transactions on Industrial Electronics*, vol. 68, no. 12, pp. 12 162–12 172, 2021. DOI: 10.1109/TIE.2020.3047041.

[40] M. Xiong, X. Wei, Y. Huang, Z. Luo, and H. Dai, "Research on novel flexible high-saturation nanocrystalline cores for wireless charging systems of electric vehicles", *IEEE Transactions on Industrial Electronics*, vol. 68, no. 9, pp. 8310–8320, 2021. DOI: 10.1109/TIE.2020.3016259.

[41] Z. Zhang, H. Pang, A. Georgiadis, and C. Cecati, "Wireless power transfer—an overview", *IEEE Transactions on Industrial Electronics*, vol. 66, pp. 1044–1058, 2019.

[42] Y. Jiang, L. Wang, J. Fang, R. Li, R. Han, and Y. Wang, "A high-efficiency zvs wireless power transfer system for electric vehicle charging withvariable angle phase shift control", *IEEE Journal of Emerging and Selected Topics in Power Electronics*, vol. 9, no. 2, pp. 2356–2372, 2021. DOI: 10.1109/JESTPE.2020.2984575.

[43] R. Bosshard, J. W. Kolar, and B. Wunsch, "Control method for inductive power transfer with high partial-load efficiency and resonance tracking", in *2014 International Power Electronics Conference (IPEC-Hiroshima 2014 - ECCE ASIA)*, 2014, pp. 2167–2174. DOI: 10.1109/IPEC.2014.6869889.

[44] A. Mahesh, B. Chokkalingam, and L. Mihet-Popa, "Inductive wireless power transfer charging for electric vehicles–a review", *IEEE Access*, vol. 9, pp. 137 667–137 713, 2021. DOI: 10.1109/ACCESS.2021.3116678.

[45] K. Inoue, K. Kusaka, and J.-I. Itoh, "Reduction in radiation noise level for inductive power transfer systems using spread spectrum techniques", *IEEE Transactions on Power Electronics*, vol. 33, no. 4, pp. 3076–3085, 2018. DOI: 10.1109/TPEL.2017.2710230.

[46] "Voltage casses for electric mobility", ZVEI - German Electrical and Electronic Manufacturers' Association Centre, Tech. Rep., 2013. [Online]. Available: https://www.zvei.org/fileadmin/user_upload/Presse_und_Medien/Publikationen/2014/april/Voltage_Classes_for_Electric_Mobility/Voltage_Classes_for_Electric_Mobility.pdf.

[47] C. Jung, "Power up with 800-v systems: The benefits of upgrading voltage power for battery-electric passenger vehicles", *IEEE Electrification Magazine*, vol. 5, no. 1, pp. 53–58, 2017. DOI: 10.1109/MELE.2016.2644560.

[48] I. Aghabali, J. Bauman, P. J. Kollmeyer, Y. Wang, B. Bilgin, and A. Emadi, "800-v electric vehicle powertrains: Review and analysis of benefits, challenges, and future trends", *IEEE Transactions on Transportation Electrification*, vol. 7, no. 3, pp. 927–948, 2021. DOI: 10.1109/TTE.2020.3044938.

[49] D.-W. Lee, B.-S. Lee, J.-H. Ahn, J.-Y. Kim, and J.-K. Kim, "New combined obc and ldc system for electric vehicles with 800 v battery", *IEEE Transactions on Industrial Electronics*, vol. 69, no. 10, 2022. DOI: 10.1109/TIE.2022.3148730.

[50] F. Grazian, T. B. Soeiro, and P. Bauer, "Voltage/current doubler converter for an efficient wireless charging of electric vehicles with 400 v and 800 v battery voltages", *IEEE Transactions on Industrial Electronics*, pp. 1–11, 2022. DOI: 10.1109/TIE.2022.3208582.

[51] *Evspecifications*, (Accessed on: 10/05/2022). [Online]. Available: www.evspecifications.com/.

[52] *Audi e-tron - battery and safety*, (Accessed on: 10/05/2022), Audi Technology Portal. [Online]. Available: www.audi-technology-portal.de/en/.

[53] *2018 leaf first responders' guide*, (Accessed on: 10/05/2022), 2018 NISSAN INTERNATIONAL S.A. [Online]. Available: www-europe.nissan-cdn.net/content/dam/Nissan/ireland/Brochures/First%5C%20Responders%5C%20Guide/2018%5C%20Leaf%5C%20First%5C%20Responders%5C%20Guide.pdf.

[54] *2014 model s emergency response guide*, (Accessed on: 10/05/2022), TESLA MOTORS, INC. [Online]. Available: www.tesla.com/sites/default/files/downloads/2014_Model_S_Emergency_Response_Guide_en.pdf.

[55] *International driving presentation of the new e-golf*, (Accessed on: 10/05/2022), Volkswagen. [Online]. Available: www.volkswagen-newsroom.com/en/.

[56] *Ioniq 5*, (Accessed on: 10/05/2022), Hyundai Motor UK Limited. [Online]. Available: www.hyundai.co.uk/new-cars/ioniq5.

[57] *Sophisticated thermal management, up to 800-volt system voltage*, (Accessed on: 10/05/2022), Dr. Ing. h.c. F. Porsche AG. [Online]. Available: media.porsche.com/mediakit/taycan/en/porsche-taycan/die-batterie.

[58] G. A. Covic, M. L. G. Kissin, D. Kacprzak, N. Clausen, and H. Hao, "A bipolar primary pad topology for ev stationary charging and highway power by inductive coupling", in *2011 IEEE Energy Conversion Congress and Exposition*, 2011, pp. 1832–1838. DOI: 10.1109/ECCE.2011.6064008.

[59] M. Budhia, J. T. Boys, G. A. Covic, and C.-Y. Huang, "Development of a single-sided flux magnetic coupler for electric vehicle ipt charging systems", *IEEE Transactions on Industrial Electronics*, vol. 60, no. 1, pp. 318–328, 2013. DOI: 10.1109/TIE.2011.2179274.

PART I
CONVENTIONAL INDUCTIVE POWER TRANSFER SYSTEMS

2

FRAMEWORK FOR THE DESIGN OF IPT SYSTEMS

Most EV wireless charging systems work through inductive power transfer (IPT) with magnetic resonance. These IPT systems consist of two coupled coils forming a loosely coupled transformer (LCT), e.g., the coupling factor k <0.5, due to their considerable distance. This translates into a considerable leakage inductance of the LCT, which must be compensated to minimize the IPT system's VA rating. For that purpose, passive components are normally connected to the LCT at both the primary and the secondary circuits, which take the name of compensation networks. As a result, IPT systems are essentially resonant converters with an LCT. Numerous compensation topologies can be adopted in IPT systems which can differ in the number of components, type of connection to the LCT, or tuning method. This chapter explains and analyzes the main characteristics of the typical compensation networks used in IPT systems focusing on the application of EV wireless charging. First, the one-component compensation networks are considered. Among them, the series-series (S-S) compensation is analyzed in detail, and a generalized designed method is proposed, which is supported by experimental results performed on a 3.7kW laboratory prototype. After that, the most common multi-component compensation networks are discussed, and their features are highlighted. Finally, the concept of the hybrid compensation network is proposed, which takes advantage of the one-component and multi-component compensation networks to achieve self-balancing of the output power against the coils' misalignment.

This chapter is based on:

- F. Grazian, W. Shi, T. B. Soeiro, J. Dong, P. van Duijsen, P. Bauer, "Quality Factor Based Design Guideline for Optimized Inductive Power Transfer", *2020 IEEE PELS Workshop on Emerging Technologies: Wireless Power Transfer (WoW)*, pp. 178-183.
- F. Grazian, T. B. Soeiro, P. Bauer, "Design Trade-Offs Between the Coupled Coils' Inductance and the Series-Series Compensation Capacitance for EV Wireless Charging Systems", *2022 International Symposium on Power Electronics, Electrical Drives, Automation and Motion (SPEEDAM)*, pp. 270-276.

2.1. INTRODUCTION

A typical inductive power transfer (IPT) system used for EV wireless charging is shown in Figure 2.1, where its power conversion stages are highlighted. For the SAE J2954 power classes WPT1 and WPT2, it is reasonable to consider that the IPT system is connected to one phase of the low-voltage AC grid, being 230 V 50 Hz in Europe. This voltage is then rectified through a power factor correction (PFC) rectifier. After that, a high-frequency inverter supplies an alternating voltage to the resonant circuit, which frequency is in the range of 79...90 kHz [1]. The received power at the secondary circuit is then rectified and supplied to the EV battery. Optional DC/DC converters can be employed at the DC-link of both the transmitting and the receiving side to achieve larger controllability of the DC voltage.

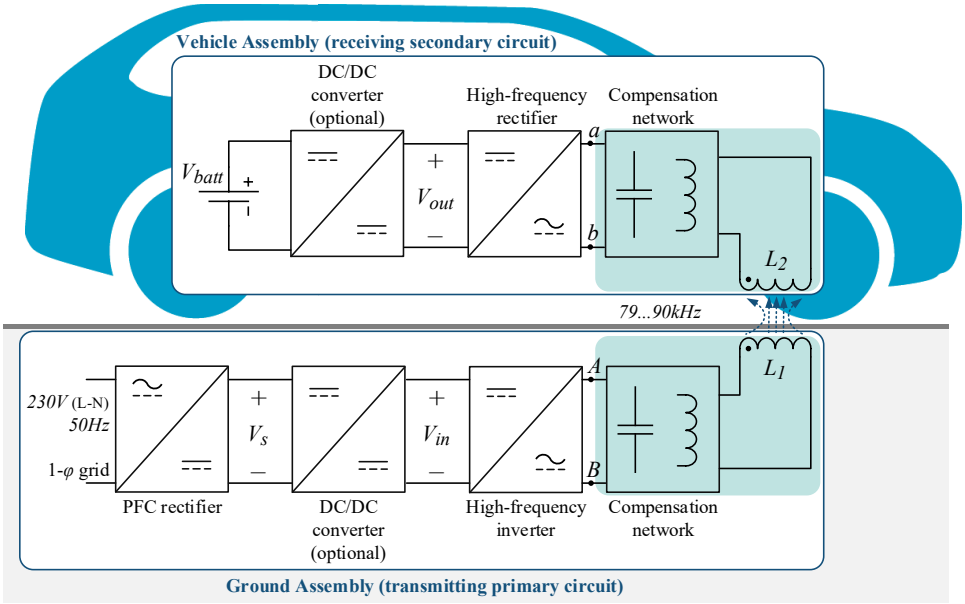

Figure 2.1: Typical power conversion stages of an IPT system used for EV wireless charging.

In IPT systems, the primary and the secondary coils are loosely coupled, i.e., their coupling factor k <0.5, because of their considerable physical separation. In other words, the coupled coils in IPT systems form a loosely coupled transformer (LCT). This means that a large leakage inductance characterizes the two circuits. Passive components are generally connected to the coils to limit reactive power circulating in the IPT system such that enough active power is delivered to the battery achieving high transfer efficiency. These passive components compensate for the inductive reactance of the coils, and for this reason, they are called compensation networks.

Compensation networks can be composed of only one component, in that case, a capacitor, or they might employ multiple components. The most used arrangements and their properties are discussed in the next sections of this chapter. Nevertheless, as explained in [2], the compensation networks must be designed to target the following

requirements.

- The primary compensation network must minimize the VA rating of the power supply. The secondary compensation network must maximize the power transfer capability to the load.
- Load-independent characteristic providing either a voltage-source or a current-source output.
- Soft-switching of the primary inverter through a slightly inductive input impedance.
- Bifurcation-free operation to guarantee control stability of the primary inverter, meaning that the resonant circuit has only one resonant frequency.
- Insensitivity to parameters change.
- Suitability for bidirectional power flow.

2.1.1. HIGH-FREQUENCY INVERTING AND RECTIFYING POWER STAGES

The choice of the compensation network highly influences the topology of the power conversion stages in Figure 2.1. For instance, each power conversion stage has either a voltage source or a current source behavior, and two consecutive power stages must have opposite behavior. For example, if the primary compensation network has a current source characteristic, it must be powered by a voltage source inverter and vice versa. Similar considerations can be made for the secondary compensation network connected to the rectifier. Considering that the inverter and rectifier consist of an H-bridge configuration where the inverter uses MOSFETs and the rectifier uses diodes, the possible voltage source and current source topologies are shown in Figure 2.2. Both full-wave rectifiers in Figure 2.2 can be directly connected to the EV battery, modeled as a voltage source, without a DC/DC converter. An alternative option could be employing active semiconductor devices in the voltage source full-wave rectifier to improve the converter's efficiency and implement synchronous rectification. This would allow a bidirectional power flow, enabling the vehicle-to-grid (V2G) power transfer option.

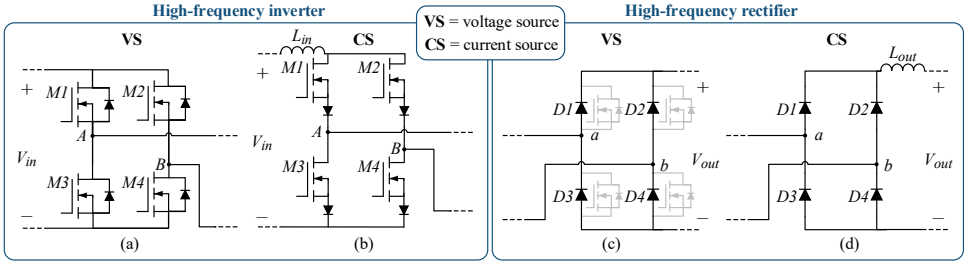

Figure 2.2: High-frequency inverting and rectifying power conversion stages. The H-bridge configuration is used, supposing that MOSFETs are employed for the inverter while diodes are used for the rectifier. Note that employing MOSFETs in the voltage source rectifier would implement synchronous rectification, improving the converter's efficiency and allowing bidirectional power transfer flow. (a) Voltage source inverter; (b) current source inverter; (c) voltage source rectifier; (d) current source rectifier.

The DC inductor in the current source configurations forces a continuous current flow through the semiconductor devices. This results in the hard-switching of the inverter and the reverse recovery of the rectifier. The MOSFETs of the current source inverter must be able to block the high resonant voltage across C_1 during their off-state.

Moreover, this topology is not intrinsically safe. In the case of an open circuit failure, the current source would be interrupted since it cannot flow through the body diodes, which would completely damage the circuit. Since the latter can cause problems for product certification, an alternative current path must be included for protection purposes which would increase the cost of the system. These consequences make the implementation of this topology inconvenient. On the other hand, the voltage source configurations process an approximately sinusoidal current resulting from the resonant circuit. In the voltage source inverter, the current can flow through the MOSFET's body diode, which enables the soft-switching operation. This operation is explained in detail in the next paragraph. For what concerns the voltage source rectifier, the diodes can naturally commutate when the output resonant current changes its polarity, preventing their reverse recovery. All in all, the compensation network topology directly influences the arrangement of the high-frequency inverting and rectifying power stages, and the ones with the soft-switching capability are preferable.

ZVS TURN-ON OF THE PRIMARY VOLTAGE SOURCE H-BRIDGE INVERTER

Assuming that the high-frequency inverting stage consists of the voltage source H-bridge inverter in Figure 2.1(a), a slight detuning from the resonance is desirable in any compensation network to achieve the zero voltage switching (ZVS) turn-on operation. This would limit the switching losses of the MOSFETs to the turn-off losses, which are typically low considering the high switching speed, especially of SiC MOSFETs. Moderate switching losses simplify the sizing of the H-bridge inverter's thermal management systems, and consequently, high power transfer efficiency can be achieved. Above all, it is fundamental to limit the semiconductor stress to safeguard the switches' reliability. The latter is particularly true for high-voltage Si-based MOSFETs, which suffer poor body-diode reverse recovery performance that can reduce the switch lifetime during hard-switching.

As explained in [3], the ZVS turn-on is realized when the output current from the H-bridge inverter i_{AB} lags the inverted voltage v_{AB} as illustrated in Figure 2.3. This means that the H-bridge inverter must operate in the inductive region of the resonant circuit. For that purpose, all MOSFETs must be switched off before the current crosses zero. During the dead time t_{dead}, the remaining current would flow through the anti-parallel diodes of the MOSFETs that were blocking the input voltage V_{in}. This turn-off current level has to be enough to discharge the drain-source capacitance C_{ds} of those MOSFETs before they are turned on and start conducting. Additionally, during t_{dead}, the C_{ds} of the MOSFETs that were just switched off is charged to block V_{in}.

The minimum turn-off current $I_{OFF,min}$ that ensures the ZVS turn-on can be calculated as shown in (2.1).

$$I_{OFF,min} \approx \frac{2 \cdot C_{ds} \cdot V_{in,max}}{t_{dead}} \tag{2.1}$$

In (2.1), it is assumed that the turn-off current I_{OFF} is constant. However, due to the resonant characteristic, I_{OFF} has likely a sinusoidal shape. This means that I_{OFF} should be larger than $I_{OFF,min}$ to guarantee the ZVS turn-on operation of the inverter. A safety margin $s_m > 1$ can be defined that must be calibrated during the commissioning phase depending on C_{ds} of the selected MOSFETs. At the same time, it is not preferable to set

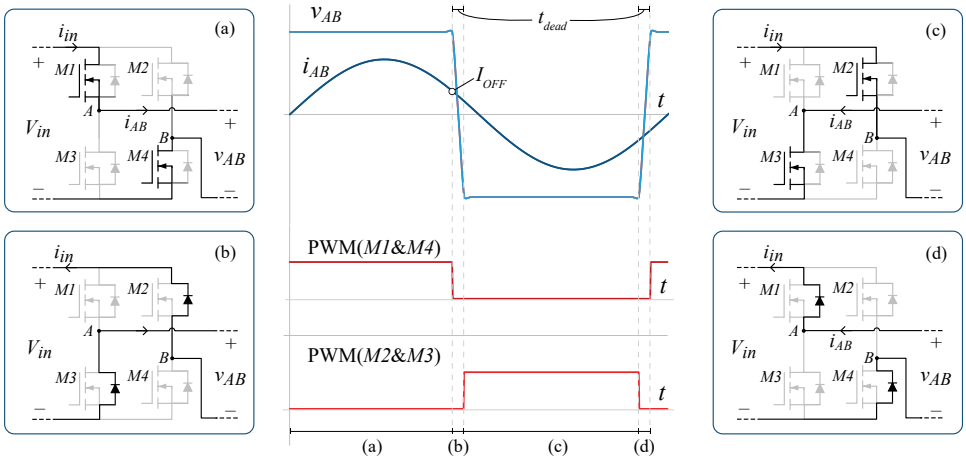

Figure 2.3: Inverted voltage v_{AB} and current i_{AB} that ensure the ZVS turn-on operation of the primary H-bridge inverter. (a) The MOSFETs $M1$ and $M4$ conduct the positive half-wave of i_{AB}. (b) $M1$ and $M4$ are turned off when the current is still positive, and, during the dead time, the current flows through the anti-parallel diodes of $M2$ and $M3$, which discharges their drain-source capacitance before they start conducting. At the same time, the drain-source capacitance of $M1$ and $M4$ is charged to block V_{in}. (c),(d) Operation of $M2$ and $M3$ that is equivalent to the previous half-period in (a),(b).

the operation too deep into the inductive region because this would increase the turn-off losses and eventually worsen the power transfer efficiency due to a higher circulating reactive current. Therefore, the turn-off current must be tuned to be equal or slightly larger than $s_m \cdot I_{OFF,min}$.

The selection of the compensation network's parameters directly influences the resonant frequency and, consequently, the inductive region of the resonant circuit. For this reason, this chapter considers the soft-switching capability in the analysis and design of the compensation networks.

2.1.2. CIRCUIT MODELING OF THE LOOSELY COUPLED TRANSFORMER

Unlike conventional resonant converters that employ highly coupled transformers, the IPT systems' reactance compensation is generally done considering the self-inductance of the coils rather than the leakage inductance. This is because the leakage inductance depends on the coupling k, which is not fixed in EV wireless charging. On the other hand, the self-inductances L_1 and L_2 only vary slightly at different alignments due to the changes in the LCT structure. For this reason, [4] explains that, while modeling the circuit of the LCT, it is preferable to use the mutual inductance M-model in Figure 2.4(a). This is derived from the classical transformer T-model shown in Figure 2.4(b) considering the particular case with the unity turns ratio. In the M-model, the influence of the coils' coupling is represented as a current-controlled voltage source. The coils' mutual inductance M is defined as

$$M = k\sqrt{L_1 L_2} \tag{2.2}$$

where typically k <0.5 in wireless charging applications and, L_1 and L_2 depict the self-inductance of the coils.

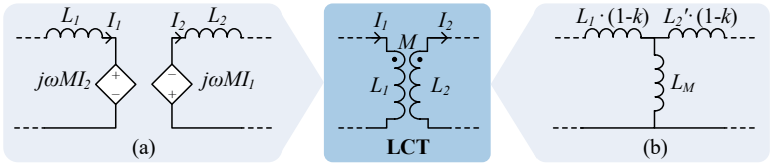

Figure 2.4: Equivalent circuit of the LCT through: (a) the M-model, (b) the classical T-model.

2.1.3. SCOPE AND CONTRIBUTIONS

This chapter investigates several compensation networks and assesses their feasibility for the application of EV wireless charging. The main contributions are:

- the modeling and the analysis of one-component and multi-component compensation networks, highlighting their main characteristics and proposing guidelines for their parameters' selection;
- explaining the detailed parameters' selection and the design procedure of the coupled coils with series-series compensation is explained, including experimental results performed on a 3.7 kW laboratory demonstrator;
- investigating the concept of the hybrid compensation networks, which combines the qualities of the one-component and multi-component compensation networks.

2.1.4. OUTLINE

The one-component compensation networks are analyzed in Section 2.2. For those compensation networks, a condition on the parameter selection is defined in Section 2.3 that ensures a bifurcation-free operation and optimum power transfer efficiency. An example of the design guideline is discussed in Section 2.4, when the trade-off between the coil's inductance and compensation capacitance is performed. After that, the main features and advantages of the multi-component compensation networks are explained in Section 2.5. Section 2.6 demonstrates the concept of hybrid compensation networks. Finally, Section 2.7 summarizes the features of the conventional compensation networks and how to choose and design the most suitable compensation network.

2.2. ONE-COMPONENT COMPENSATION NETWORKS

The simplest compensation network consists of one capacitor, which can be connected either in series or in parallel to the coil to compensate for their reactance. The possible combinations are shown in Figure 2.5 which are called series-series (S-S), series-parallel (S-P), parallel-series (P-S), and parallel-parallel (P-P) compensation networks.

In Figure 2.5, L_1 and L_2 are, respectively, the self-inductance of the primary and secondary coils, and R_1 and R_2 are their parasitic series resistance. C_1 and C_2 are the compensation capacitors, and, as a first approximation, it is assumed that their equivalent series resistance is negligible compared to R_1 and R_2. The coils' mutual inductance M is defined in (2.2). It must be noted that the variable relative position of the two coils makes k range from the maximum value at the perfect coils' alignment to 0 when they are completely apart from each other. In the equivalent circuits of Figure 2.5, the battery and the power handling are replaced by the equivalent first-harmonic load R_{ac} defined

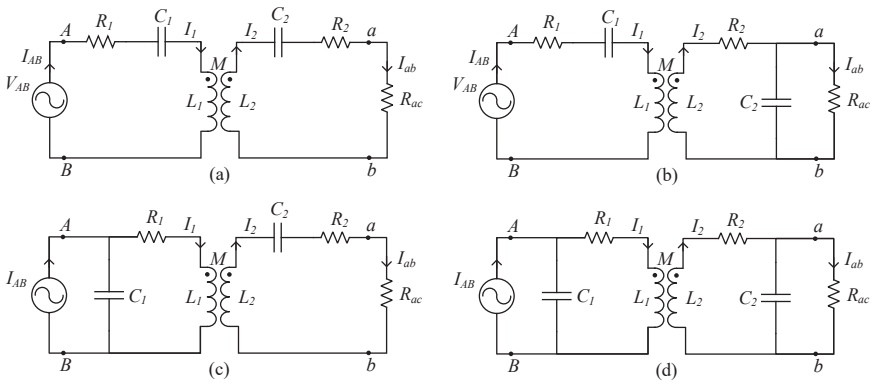

Figure 2.5: Equivalent circuit in the frequency domain of the one-component compensation networks: (a) series-series (S-S), (b) series-parallel (S-P), (c) parallel-series (P-S), and (d) parallel-parallel (P-P).

in (2.3) as explained by [5]. Thereby, $R_L = \frac{V_{out}}{I_{out}}$ represents the equivalent DC resistive load comprising the optional DC/DC converter and the EV battery in Figure 2.1.

$$R_{ac} = \frac{(\hat{V}_{ab})_1}{(\hat{I}_2)_1} \cong \begin{cases} \frac{8}{\pi^2} R_L = \frac{\frac{4}{\pi} V_{out}}{\frac{\pi}{2} I_{out}} & \text{if } C_2 \text{ is connected in series (current source output)} \\ \frac{\pi^2}{8} R_L = \frac{\frac{\pi}{2} V_{out}}{\frac{4}{\pi} I_{out}} & \text{if } C_2 \text{ is connected in parallel (voltage source output)} \end{cases} \tag{2.3}$$

The selection procedure of the compensation capacitance for the circuits in Figure 2.5 is well-known from the literature [2], [6]–[8]. However, for compensation networks different from the S-S, the works found in the literature do not give unanimous results. This happens because, in those cases, the computation is rather difficult, and, on top of that, compensation networks other than the S-S are not used often in high-power wireless charging. In this research, it is important to compute an exact mathematical model of all the compensation networks starting from the configurations in Figure 2.5 such that the analysis in the frequency domain can be executed.

2.2.1. SELECTION OF THE COMPENSATION CAPACITANCE

In the one-component compensation networks, the selection of the compensation normally starts with choosing the secondary capacitance C_2 such that it resonates with the secondary self-inductance L_2 at the resonant frequency $f_0 = \frac{\omega_0}{2\pi}$ as defined in (2.4).

$$C_2 = \frac{1}{\omega_0^2 L_2} \tag{2.4}$$

The primary compensation capacitance C_1 is chosen to compensate for the reactance of both L_1 and the one caused by the reflected impedance $\boldsymbol{Z_r}$ from the secondary to the primary circuit. This means that the chosen C_1 must lead to a purely resistive input impedance $\boldsymbol{Z_{in}} = \frac{\boldsymbol{V_{AB}}}{\boldsymbol{I_{AB}}}$ at $f = f_0$, i.e., the zero phase angle (ZPA) condition is achieved.

Therefore, C_1 must be selected such that the imaginary part of $\boldsymbol{Z_{in}}$ is zero at the chosen f_0. For the four possible compensation networks in Figure 2.5, the first step to find C_1 is computing $\boldsymbol{Z_{in}}$.

There are two equivalent methods to compute $\boldsymbol{Z_{in}}$. The first method uses the Kirchhoff voltage law listed in Table 2.1 for all the one-component compensation networks from which $\boldsymbol{V_{AB}}$ and $\boldsymbol{I_{AB}}$ can be found.

Table 2.1: Kirchhoff's equations for the one-component compensation networks in Figure 2.5.

S-S	$\boldsymbol{V_{AB}} = (R_1 + j\omega L_1 + \frac{1}{j\omega C_1})\boldsymbol{I_1} + j\omega M I_2 \quad \text{with} \quad \boldsymbol{I_{AB}} = \boldsymbol{I_1}$ $0 = (R_2 + R_{ac} + j\omega L_2 + \frac{1}{j\omega C_2})\boldsymbol{I_2} + j\omega M \boldsymbol{I_1}$
S-P	$\boldsymbol{I_2} = \boldsymbol{I_{C_2}} + \boldsymbol{I_{ab}} \quad \text{and} \quad \boldsymbol{I_{AB}} = \boldsymbol{I_1}$ $\frac{1}{j\omega C_2}\boldsymbol{I_{C_2}} = R_{ac}\boldsymbol{I_{ab}}$ $\boldsymbol{V_{AB}} = (R_1 + j\omega L_1 + \frac{1}{j\omega C_1})\boldsymbol{I_1} + j\omega M \boldsymbol{I_2}$ $0 = (R_2 + j\omega L_2)\boldsymbol{I_2} + \frac{1}{j\omega C_2}\boldsymbol{I_{C_2}} + j\omega M \boldsymbol{I_1}$
P-S	$\boldsymbol{I_{AB}} = \boldsymbol{I_1} + \boldsymbol{I_{C_1}}$ $\boldsymbol{V_{AB}} = \frac{1}{j\omega C_1}\boldsymbol{I_{C_1}}$ $0 = (R_1 + j\omega L_1)\boldsymbol{I_1} + j\omega M \boldsymbol{I_2} - \frac{1}{j\omega C_1}\boldsymbol{I_{C_1}}$ $0 = (R_2 + R_{ac} + j\omega L_2 + \frac{1}{j\omega C_2})\boldsymbol{I_2} + j\omega M \boldsymbol{I_1}$
P-P	$\boldsymbol{I_{AB}} = \boldsymbol{I_1} + \boldsymbol{I_{C_1}}, \boldsymbol{I_2} = \boldsymbol{I_{C_2}} + \boldsymbol{I_{ab}}$ $\boldsymbol{V_{AB}} = \frac{1}{j\omega C_1}\boldsymbol{I_{C_1}}$ $\frac{1}{j\omega C_2}\boldsymbol{I_{C_2}} = R_{ac}\boldsymbol{I_{ab}}$ $0 = (R_1 + j\omega L_1)\boldsymbol{I_1} + j\omega M \boldsymbol{I_2} - \frac{1}{j\omega C_1}\boldsymbol{I_{C_1}}$ $0 = (R_2 + j\omega L_2)\boldsymbol{I_2} + \frac{1}{j\omega C_2}\boldsymbol{I_{C_2}} + j\omega M \boldsymbol{I_1}$

On the other hand, the second method relies on the concept of the reflected impedance $\boldsymbol{Z_r}$. According to [6], $\boldsymbol{Z_r}$ is the equivalent impedance of the secondary circuit that is considered in series with the primary coil, as shown in Figure 2.6. As shown in Table 2.2, $\boldsymbol{Z_r}$ is dependent on the secondary impedance $\boldsymbol{Z_2}$.

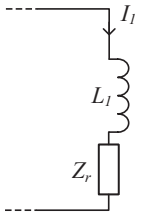

Figure 2.6: Schematic of the equivalent reflected impedance $\boldsymbol{Z_r}$ from the secondary to the primary circuit.

Then, depending on the type of compensation adopted at the primary circuit, $\boldsymbol{Z_{in}}$ can have two different expressions, which are shown in Table 2.2.

Table 2.2: Secondary impedance $\boldsymbol{Z_2}$, reflected impedance $\boldsymbol{Z_r}$ and input impedance $\boldsymbol{Z_{in}}$ of the one-component compensation networks in Figure 2.5.

	$\boldsymbol{Z_2}$	$\boldsymbol{Z_r}$		$\boldsymbol{Z_{in}}$
S-S and P-S	$R_2 + R_{ac} + j\omega L_2 + \dfrac{1}{j\omega C_2}$	$\dfrac{\omega^2 M^2}{\boldsymbol{Z_2}}$	S-S and S-P	$R_1 + j\omega L_1 + \dfrac{1}{j\omega C_1} + \boldsymbol{Z_r}$
S-P and P-P	$R_2 + j\omega L_2 + \dfrac{1}{j\omega C_2 + \dfrac{1}{R_{ac}}}$		P-S and P-P	$\dfrac{1}{j\omega C_1 + \dfrac{1}{R_1 + j\omega L_1 + \boldsymbol{Z_r}}}$

As mentioned before, C_1 is found to make $\boldsymbol{Z_{in}}$ purely resistive at the chosen resonant frequency f_0. In this research, it is chosen to derive definitions of C_1 that also consider R_1 and R_2 at least up to the first order. Table 2.3 shows the computed values of C_1 for all four one-component compensation networks.

2.2.2. EQUIVALENT OPTIMUM LOAD AND BIFURCATION PHENOMENON

Table 2.4 lists some key parameters of the one-component compensation networks, which are well-known from the literature [2], [6]. These are the reflected resistance R_r, the reflected reactance X_r, where $\boldsymbol{Z_r}$=R_r+jX_r, the quality factors of the primary and secondary resonant circuits Q_{1c} and Q_{2c}, the quality factors of the coils Q_1 and Q_2. The coils' quality factor Q_1 and Q_2 indicates how close the coils are to an ideal inductor. Additionally, it is interesting to notice that if the secondary coil is series compensated, the reflected reactance X_r to the primary circuit would be zero, meaning that C_1 would not have to compensate for that. Moreover, the reflected resistance R_r is used to compute the quality factor of the primary resonant circuit Q_{1c}. In [6], the calculation of Q_{1c} and Q_{2c} assumes that R_1=R_2=0 since they are negligible with respect to R_{ac}.

From the parameters in Table 2.4, two fundamental conditions of the one-component compensation networks can be found, which are the bifurcation-free criteria and the optimum load condition. These are summarized in Table 2.5 where it is possible to notice that both conditions put requirements on the equivalent resistive load R_{ac}.

The bifurcation phenomenon influences the ZVS turn-on of the H-bridge inverter. As explained in Section 2.1.1, a voltage source H-bridge inverter achieves the ZVS turn-on when the inverter's output current $\boldsymbol{I_{AB}}$ is inductive with respect to $\boldsymbol{V_{AB}}$. Generally, in resonant converters, this is realized by operating the H-bridge inverter at a

Table 2.3: Primary compensation capacitance C_1 for the one-component compensation networks including R_1 and R_2, where C_2 is defined in (2.4).

	C_1
S-S	$\frac{L_2 C_2}{L_1}$
S-P	$\frac{-\omega_0(C_2R_2 + R_{ac}L_2)^2 + (1/\omega_0)(R_{ac}+R_2-1)(1-R_2R_{ac})}{A\cdot\omega_0(C_2R_2+L_2R_{ac})+B\cdot(1-R_{ac}-R_2R_{ac})}$ where: $A = R_1R_{ac} - R_1 + \omega_0^2M^2R_{ac} - \omega_0^2L_1C_2R_2 - \omega_0^2L_1L_2R_{ac}$; $B = \omega_0^3M^2C_2 + \omega_0L_2R_{ac}R_1 + \omega_0L_1R_1 - \omega_0^3L_1L_2C_2 + \omega_0L_1R_{ac}R_2$
P-S	$\frac{L_1(R_2+R_{ac})^2}{\omega_0^2[L_1^2(R_2+R_{ac})^2 + 2M^2R_1(R_2+R_{ac}) + \omega_0^2M^4]}$
P-P	$\frac{-A\cdot(\omega_0L_2+\omega_0C_2R_2R_{ac}) - B\cdot R_2}{A\cdot(\omega_0^2M^2+\omega_0R_1R_2-\omega_0^3L_1L_2-\omega_0L_1C_2R_2R_{ac}) + B\cdot(-\omega_0^4M^2C_2R_2 - \omega_0^2(L_2R_1+C_2R_1R_2R_{ac}+L_1R_2))}$ where: $A = -R_1R_2\omega_0^2(L_1L_2 + L_1C_2R_2R_{ac} - M^2)$; $B = \omega_0(L_2R_1 + C_2R_1R_2R_{ac} + L_1R_2 + \omega_0^2M^2C_2R_{ac})$

Table 2.4: Reflected resistance R_r, reflected reactance X_r, quality factors Q_{1c} and Q_{2c} of the primary and secondary resonant circuit [6], and quality factors Q_1 and Q_2 of the coils.

C_2 connection	R_r	X_r	Q_{1c}	Q_{2c}	Q_1	Q_2
S	$\frac{\omega_0^2 M^2}{R_{ac}}$	0	$\frac{L_1 R_{ac}}{\omega_0 M^2}$	$\frac{\omega_0 L_2}{R_{ac}}$	$\frac{\omega_0 L_1}{R_1}$	$\frac{\omega_0 L_2}{R_2}$
P	$\frac{M^2 R_{ac}}{L_2^2}$	$-\frac{\omega_0 M^2}{L_2}$	$\frac{\omega_0 L_1 L_2^2}{M^2 R_{ac}}$	$\frac{R_{ac}}{\omega_0 L_2}$		

Table 2.5: Bifurcation-free criteria and optimum load condition for the one-component compensation networks in Figure 2.5. The quality factors Q_{1c}, Q_{2c}, Q_1 and Q_2 are defined in Table 2.4.

	Bifurcation-free criteria [6]		**Optimum load condition** [2]
S-S	$Q_{1c} > \frac{4Q_{2c}^3}{4Q_{2c}^2 - 1}$	$R_{ac} > R_{ac,bif} = \omega_0 L_2 \sqrt{2(1-\sqrt{1-k^2})}$	$R_{ac}{=}R_{ac,opt}{=}\sqrt{\frac{L_2}{C_2}}\frac{\sqrt{1+k^2Q_1Q_2}}{Q_2}$
P-S	$Q_{1c} > Q_{2c}$	$R_{ac} > R_{ac,bif} = \omega_0 M \sqrt{\frac{L_2}{L_1}}$	
S-P P-P	$Q_{1c} > Q_{2c} + \frac{1}{Q_{2c}}$	$R_{ac} < R_{ac,bif} = \sqrt{\frac{\omega_0^2 L_1 L_2^3}{M^2} - \omega_0^2 L_2^2}$	$R_{ac}{=}R_{ac,opt}{=}\sqrt{\frac{L_2}{C_2}}\frac{Q_2}{\sqrt{1+k^2Q_1Q_2}}$

switching frequency higher than the circuit's resonant frequency. However, this is valid if the phase angle $\phi(\boldsymbol{I_{AB}})$ is monotonic with respect to the frequency. Depending on both the loading condition and magnetic coupling between the primary and secondary coils, there might exist multiple frequencies that satisfy the ZPA condition ($\phi(\boldsymbol{I_{AB}})$=0), meaning that $\boldsymbol{I_{AB}}$ would not be monotonic. In the literature, this is called the bifurcation phenomenon or frequency splitting [7], [9]–[13]. In those cases, operating the H-bridge inverter above the resonant frequency leads to a capacitive-like behavior of

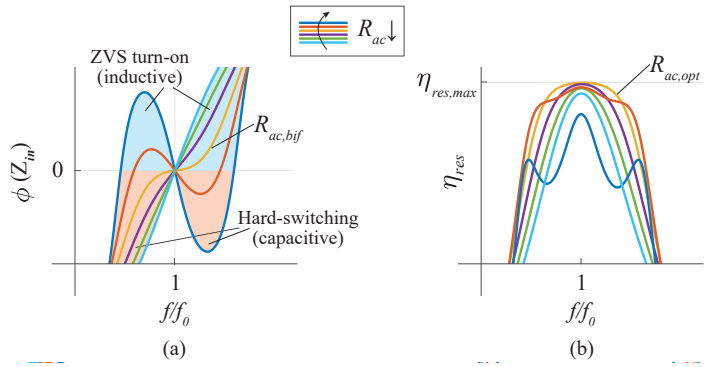

Figure 2.7: Typical analysis in the frequency domain based on the S-S compensation for different values of R_{ac}. (a) Phase angle of the input impedance $\phi(\boldsymbol{Z_{in}})$=$-\phi(\boldsymbol{I_{AB}})$. The bifurcation phenomenon is present when $\phi(\boldsymbol{Z_{in}})$ has multiple ZPAs, i.e., $\phi(\boldsymbol{Z_{in}})$=0 for multiple frequencies. (b) Efficiency of the resonant circuit η_{res} which is maximum when R_{ac}=$R_{ac,opt}$ at f=f_0.

$\boldsymbol{I_{AB}}$ causing the hard switched turn-on of the MOSFETs. Therefore, the operation must be bifurcation-free to guarantee soft-switching and stable controllability of the inverter. An example of the bifurcation phenomenon is shown through the frequency domain analysis of $\phi(\boldsymbol{Z_{in}})$=$-\phi(\boldsymbol{I_{AB}})$ in Figure 2.7(a) which considers the S-S compensation for different values of R_{ac}. It is preferable to design the resonant circuit such that the bifurcation does not occur for the entire operating range of R_{ac}. It can be noted from Table 2.5 that the bifurcation free-criteria is dependent on the mutual inductance M.

The optimum load condition states that the maximum power transfer efficiency of the resonant circuit η_{res} is achieved if the equivalent resistive load R_{ac} matches the optimum load $R_{ac,opt}$ at f=f_0. In [2] and [14], $R_{ac,opt}$ in Table 2.5 is the resulting equivalent resistive load that maximizes η_{res} in (2.5), where η_1 is the efficiency of the primary circuit while η_2 is the efficiency of the secondary circuit. An example of the resonant circuit efficiency computed for different values of R_{ac} in the frequency domain is shown in Figure 2.7(b), which considers the S-S compensation. Thereby, it is possible to notice that η_{res} is maximum at f=f_0 when R_{ac}= $R_{ac,opt}$.

$$\eta_{res} = \eta_1 \cdot \eta_2 = \frac{\mathrm{Re}(\boldsymbol{Z_r})}{\mathrm{Re}(\boldsymbol{Z_r}) + R_1} \cdot \frac{\mathrm{Re}(\boldsymbol{Z_2}) - R_2}{\mathrm{Re}(\boldsymbol{Z_2})} \tag{2.5}$$

2.2.3. COMPARISON OF THE ONE-COMPONENT COMPENSATION NETWORKS

The main properties of the one-component compensation networks in Figure 2.5 are listed in Table 2.6.

Table 2.6: Summary of the properties of the one-component compensation networks.

Properties	S-S	S-P	P-S	P-P
Inverter source type	VS	VS	CS	CS
Rectifier source type (direct battery connection)	VS	CS	CS	VS
Load-independent output	CC	CV	CC	CV
Possibility of inverter's ZVS turn-on	✓	✓	✗	✗
Soft-switching rectifier	✓	✗	✓	✗
Bifurcation influence	$R_{ac}\downarrow$	$R_{ac}\uparrow$	$R_{ac}\downarrow$	$R_{ac}\uparrow$
Coupling-independent P_{out}	✗	✗	✗	✗
C_1 dependence on k	✗	✓	✓	✓
C_1 dependence on R_{ac}	✗	✗	✓	✓
Real $\boldsymbol{Z_r}$ at f=f_0	✓	✗	✓	✗
Intrinsically suitable for bidirectional power flow	✓	✗	✗	✗
✓ = present ✗ = not present VS=voltage source, CS=current source, CV=constant voltage, CC=constant current				

The compensation networks with a series-connected primary capacitor, i.e., S-S and S-P, require a voltage source inverter which, as explained in Section 2.1.1, is preferable since it can achieve the ZVS turn-on operation. On the other hand, it is not possible to use a voltage source H-bridge inverter with the P-S and the P-P due to their primary compensation capacitor being directly connected in parallel to the output of the inverter.

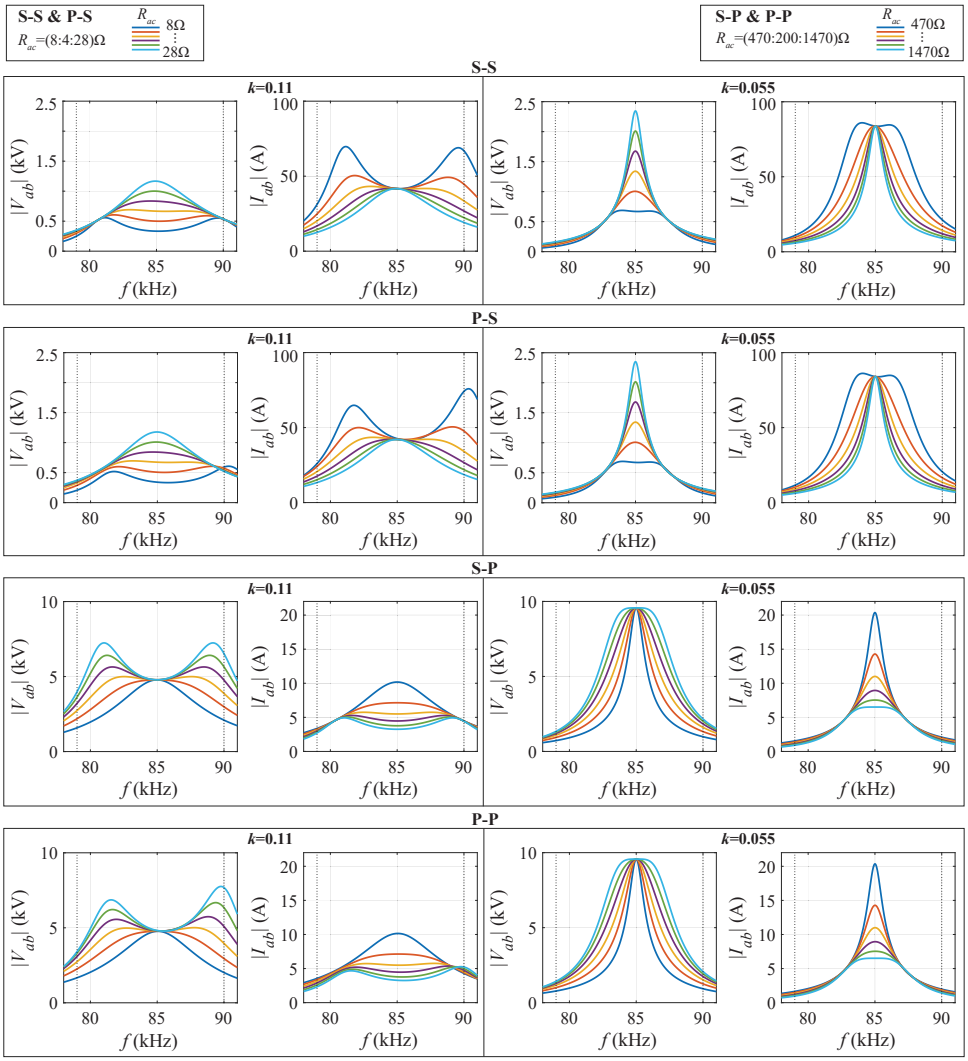

Figure 2.8: Analysis in the frequency domain of the output voltage $|V_{ab}|$ and current $|I_{ab}|$ of the one-component compensation networks for different values of R_{ac} and at two values of k. It is assumed that the input source is V_{in}=405 V for the S-S and the S-P compensations, and I_{in}=3.7 A for the P-S and the P-P compensations. The coils parameters are chosen based on [15], where L_1=206.53 µH, L_2=214.96 µH, k=[0.11 0.055]. Moreover, it is assumed that R_1=R_2=0 to assess the ideal behavior. Additionally, C_1 has been calculated based on Table 2.3, while C_2 follows from (2.4) where f_0=85 kHz.

As a consequence of the compensation capacitance tuning explained in Section 2.2.1, the one-component compensation networks have either a constant current (CC) or a constant voltage (CV) load-independent output in correspondence to the resonant frequency. For the investigated one-component compensation networks, this characteristic of the output has been assessed in the frequency domain analysis in Figure 2.8 for different values of the equivalent load R_{ac} and at two k conditions. All the compensation networks have been tuned such that f_0=85 kHz. The circuits with a series-connected

secondary capacitor have approximately a CC load-independent output in correspondence to the ZPA. This means that a voltage source rectifier can be employed. On the other hand, the compensation networks with a parallel-connected secondary capacitor have approximately a CV load-independent output in correspondence to the ZPA. The CC load-independent output can be achieved at a frequency higher than the resonance, but it would not result in the ZPA. However, [2] and [16] explain that the CC output characteristic could be achieved at the resonant frequency by adopting a different tuning of the compensation network. With a parallel-connected secondary compensation capacitor, a current source rectifier must be used to have a direct battery connection since the battery has a voltage source behavior. This option is not preferable since the rectifier would have reverse recovery losses during the switching transitions due to the continuous load current imposed by the output DC inductor L_{out} shown in Figure 2.2(d). Additionally, it must be pointed out that the CC or CV load-independent output of the one-component compensation network is dependent on the coupling factor k as shown in Figure 2.8. For instance, in the presence of misalignment, higher power is transferred if the input voltage or current supply is unvaried. This puts requirements on the control of the power flow and the circuit protections.

The S-S compensation is the only one in which both C_1 and C_2 are independent of the load R_{ac} and the coupling k. Moreover, it is also the only one that employs a voltage source inverter and a voltage source rectifier. These features make the S-S compensation intrinsically suitable for a bidirectional power flow when synchronous rectification is used. All in all, in the application of EV wireless charging, the S-S compensation is the most used among the one-component compensation networks.

2.3. QUALITY FACTOR-BASED PARAMETERS SELECTION FOR THE ONE-COMPONENT COMPENSATION NETWORKS

Depending on the parameters of the IPT system with a one-component compensation network in Figure 2.5, the condition that maximizes the power transfer efficiency and the one that ensures the ZVS turn-on of the inverter defined might be conflicting. For instance, in Table 2.5, the range of the bifurcation-free condition might not include the optimum load $R_{ac,opt}$. An example of this incompatibility is shown in [17] for an S-S compensation network, where a sub-optimum design needs to be chosen to prevent the bifurcation phenomenon. Therefore, this section defines a guideline for selecting coils' quality factors that simultaneously satisfy the optimum load and the bifurcation-free conditions defined in Table 2.5.

2.3.1. DEFINITION OF THE PARAMETRIC GUIDELINE

In the design process, it is possible to make sure that the condition for the optimum efficiency of the coils and the bifurcation-free operation are compatible at the same time. This can be done by relating the two conditions to each other. The analytical approach combining both conditions is shown in Table 2.7 for the one-component compensation networks. Once the secondary coil inductance L_2 and series resistance R_2, the operating frequency $\omega_0 = 2\pi f_0$, and the coupling factor k are designed, the primary coil's quality factor Q_1^* that satisfies both conditions can be computed for the four basic compensa-

Table 2.7: Parametric condition on the primary coil's quality factor Q_1 such that if Q_1=Q_1^* both the optimum load condition and the bifurcation-free criteria defined in Table 2.5 are satisfied at the same time.

	Design condition	Q_1^*
S-S	$R_{ac,opt} = aR_{ac,bif}$	$\frac{2a^2(1-\sqrt{1-k^2})\omega_0^2 L_2^2 - R_2^2}{k^2\omega_0 L_2 R_2}$
P-S	$R_{ac,opt} = aR_{ac,bif}$	$\frac{a^2k^2\omega_0^2 L_2^2 - R_2}{R_2 k^2 \omega_0 L_2}$
S-P P-P	$R_{ac,opt} = dR_{ac,bif}$	$\frac{k^2\omega_0 L_2^2 - d^2(1-k^2)R_2^2}{d^2(1-k^2)R_2 k^2 \omega_0^2 L_2}$
where $a > 1$ and $d < 1$		

tion networks. In Table 2.7, the condition on Q_1^* is not strict because it can be tuned by choosing the value of the coefficients a or d, where $a > 1$ and $d < 1$ must hold. The further a and d are from the unity, the more $R_{ac,opt}$ will differ from $R_{ac,bif}$. The conversion between the equivalent resistive load R_{ac} placed at the high-frequency side and the equivalent resistive load R_L placed at the DC output can be made through (2.3).

2.3.2. IPT SYSTEM DESIGNS AND ANALYSIS

To evaluate the parametric guideline in Table 2.7, examples of circuit parameters for 11 kW wireless battery charging systems have been computed for the four basic compensation networks at different values of the coefficients a and d. The results are summarized in Figure 2.9. It is assumed that:

- the coefficients a and d are selected as a = (1, 1.1, 1.3) and d = (0.7, 0.9, 1), within the range defined Table 2.7. This means that, for each compensation network, three designs are analyzed which have an optimum load $R_{L,opt}$ that can be equal, 10%, or 30% different from the bifurcation boundary load $R_{L,bif}$;
- the secondary coil in [18] is used as a reference, whose parameters are $L_2 = 214.96\,\mu H$ and $R_2 = 0.5\,\Omega$;
- the primary coil is designed such that Q_1=Q_1^*, k =0.11, R_1=$R_2 \cdot a$ for S-S and P-S, or R_1=R_2·(2-d) for S-P and P-P. It is assumed that a higher inductance corresponds to a higher series resistance because of an increase in the number of turns;
- the coupling factor k between the coils is fixed.

Figure 2.9(a) and Figure 2.9(c) show the resulting $R_{ac,opt}$ and $R_{ac,bif}$ at the different coefficients a and d. As expected from the design condition in Table 2.7, $R_{ac,opt}$ and $R_{ac,bif}$ are identical when a and d are equal to the unity. On the other hand, the further a and d are from the unity, the more $R_{ac,opt}$ differs from $R_{ac,bif}$. Additionally, given the above-mentioned assumptions, Figure 2.9(a) and Figure 2.9(c) show also the resulting coils' inductance L_1, L_2, and the coils' quality factors Q_1=Q_1^*, Q_2. When $R_{ac,opt} = R_{ac,bif}$, the inductance and quality factor of both coils are equivalent, which means that the primary and secondary coils are identical. The farthest a and d are from the unity, the larger the inductance of the primary coil is with respect to the secondary coil. However,

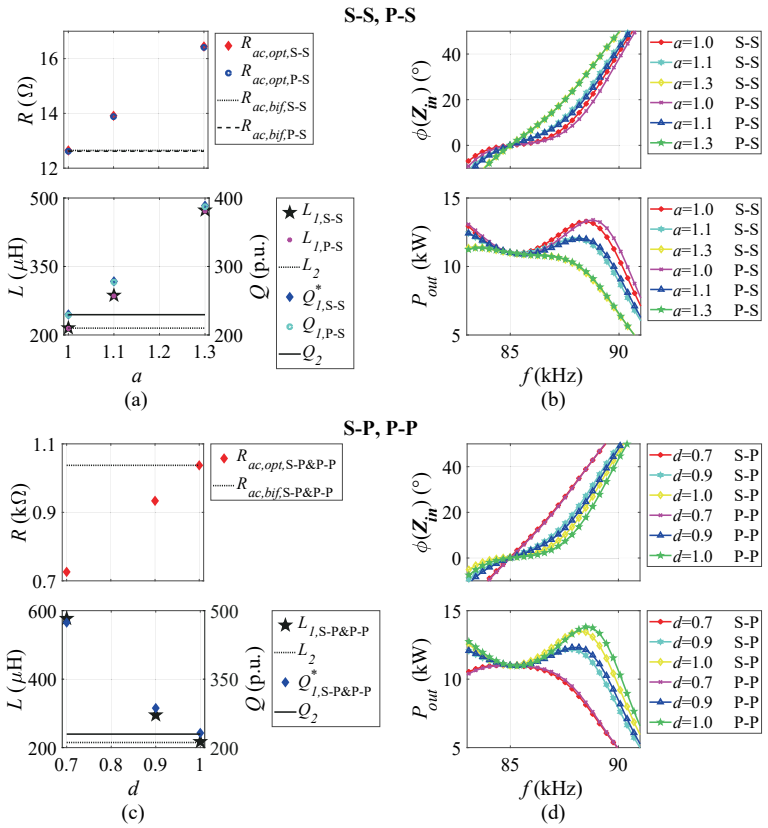

Figure 2.9: 11 kW wireless battery charging systems at different values of either the coefficient a for the S-secondary in (a),(b), or d for the P-secondary in (c),(d). (a),(c): optimum load, coils' inductance, and quality factor. (b),(d): phase angle of the input impedance and output power depending on the frequency.

the inductance is not the only parameter changing since the coils' quality factor also increases as a and d become more different than the unity. This means that L_1 is not only increased by adding more turns but also by modifying the coils' geometry and dimensions.

As explained in Section 2.3.1, the soft-switching of the inverter can be achieved by operating at a frequency higher than the system's resonant one, as long as the condition $a > 1$ or $d < 1$ is valid. However, within this condition, the values of a and d highly influence the phase angle of the input impedance $\phi(\boldsymbol{Z_{in}})$ seen by the inverter in the frequency domain. As a consequence, this affects the controllability of the inverter. Figure 2.9(b) and Figure 2.9(d) show that the further a and d are from the unity, the steeper $\phi(\boldsymbol{Z_{in}})$ becomes. This means that considerably higher inductive behavior can be achieved with small frequency variations. However, it is not preferable to have a sharp change in $\phi(\boldsymbol{Z_{in}})$ while changing the frequency because it is important to have smooth controllability of the reactive power circulating in the system. On the other hand, if the gradient of $\phi(\boldsymbol{Z_{in}})$ is relatively low, it might happen that the desired phase shift cannot be achieved within the allowed frequency range. For example, according to SAE J2954

[1], the allowed operating frequency range is 79...90 kHz. Therefore, if the nominal frequency is chosen as 85 kHz, the tuning range for the soft-switching has a bandwidth of only 5 kHz.

Besides the ZVS turn-on, another direct consequence of operating at a frequency slightly higher than the resonance is that the delivered output power P_{out} would vary from the design value. Figure 2.9(b) and Figure 2.9(d) show the characteristic of P_{out} depending on the operating frequency for different values of the coefficients a or d, where it is chosen that P_{out} = 11 kW at the resonant frequency of f_0=85 kHz. When a and d are close to the unity, P_{out} increases when operating at frequencies immediately higher than the resonance. This means that the DC input source (either V_{in} or I_{in}) must be lowered to set the value of P_{out} back to the nominal level. For example, this could be done by connecting a step-down converter at the input of the H-bridge inverter. However, above a certain frequency, P_{out} starts dropping, and the characteristic required from the DC input source would be the opposite. Therefore, if a and d are close to the unity, the converter connected at the input of the system might need both a step-up and step-down behavior. On the other hand, as the coefficients a and d become farther than the unity, P_{out} drops for the whole frequency range higher than the resonance. Consequently, the DC input source must only be stepped up to reach the nominal P_{out}. In this case, the operation would be inherently safer because the power would not be higher than the nominal. The controllability of the system becomes easier since it is only required in

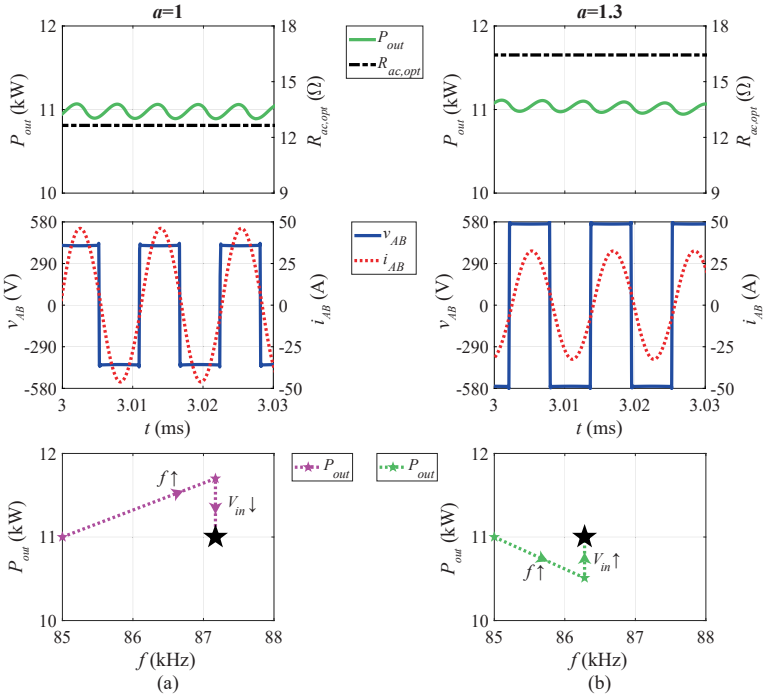

Figure 2.10: Simulated circuit waveforms of the 11 kW S-S compensation network resulting from Figure 2.9 where $f > f_0$ to achieve the ZVS turn-on of the inverter. The primary coil's quality factor Q_1^* is computed from Table 2.7 such that: (a) a=1, (b) a=1.3.

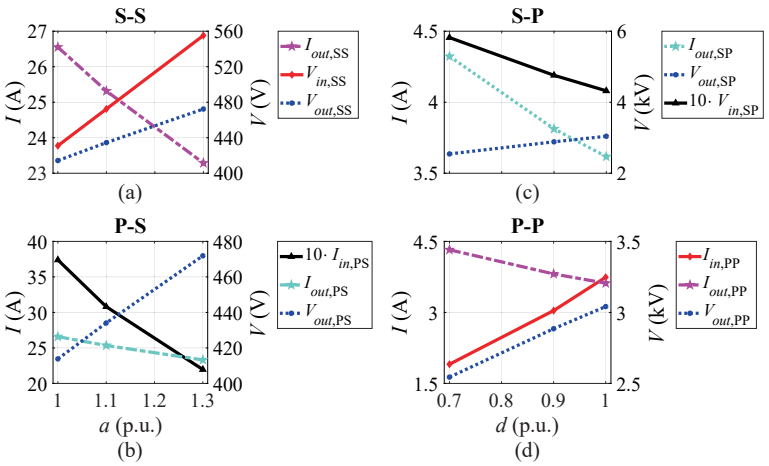

Figure 2.11: DC output V_{out}, I_{out} and DC input source (either V_{in} or I_{in}) at different values of either a or d considering P_{out} = 11 kW for: (a) the S-S, (b) the P-S, (c) the S-P, and (d) the P-P compensation networks.

one direction, and the DC input source range of the converter can be extended since only a step-up converter could be used rather than a step-up and step-down converter. However, as a and d become far from the unity, the effective bandwidth in which it is possible to deliver P_{out} reduces as it is shown in Figure 2.9(b) and Figure 2.9(d). A narrow bandwidth would become critical for the stability of the IPT, which is especially true in the presence of frequency detuning due to the parameters' tolerance. Therefore, selecting a value for a and d excessively different than unity is not preferable. From this example, it is clear that the choice of the coefficients a and d also affects the topology selection for the power electronics converter needed to ensure stable delivery of P_{out}.

The described characteristics of the IPT systems have been also verified through circuit simulations. Figure 2.10 shows the circuit waveforms of the 11 kW S-S compensation network designed with a=1 and a=1.3. Thereby, the H-bridge inverter operates at the ZVS turn-on with a positive switch current of 8 A, and the equivalent load R_{ac} is set at the computed optimum load $R_{ac,opt}$ in Figure 2.9(a). When the operating frequency is increased to achieve the ZVS turn-on, it is possible to observe that the P_{out} characteristic agrees with the one in Figure 2.9(b): P_{out} increases for a=1 and decreases for a=1.3. As a consequence, the input voltage V_{in} must be controlled to shift P_{out} back to 11 kW. In particular, in Figure 2.10(a), V_{in} has been lowered from 431 V to 417 V, while in Figure 2.10(c), it has been increased from 555.2 V to 567.2 V.

Additionally, it is interesting to notice from Figure 2.10 that the chosen value of a leads to different input and output voltages required to deliver the same output power at the optimum load condition. This means that the choice of a highly influences the power transfer characteristic. The main reason is that the two values of a result in different values of the mutual inductance M even though the coupling k is fixed. The effect of M on the DC input and output voltages of an IPT system with the S-S compensation is discussed more in detail in Section 2.4.2. The influence of a and b on the DC input and output quantities is analyzed for all the four compensation networks in Figure 2.11, considering P_{out} = 11 kW. Therefore, the value of a and d can be chosen such that V_{in}

is within the allowed voltage range from the grid connection and that V_{out} matches the nominal voltage of the battery.

2.4. DESIGN TRADE-OFFS BETWEEN THE COUPLED COILS' INDUCTANCE AND THE COMPENSATION CAPACITANCE IN THE S-S COMPENSATION NETWORK

In the case of static EV wireless charging, the S-S compensation is generally preferred since the resonant circuit has the minimum number of passive components, and the coils' misalignment generally happens in a limited range. The equivalent circuit of a typical IPT system using the S-S compensation is shown in Figure 2.12. The analytical modeling of the S-S compensation has been well-exploited in [2], [6], [7], [10], [11], [19]. However, while designing a certain wireless charging system, there are infinite combinations of coils' inductance and compensation capacitance values that resonate at a specific frequency. It is not always clear to engineers, designers, and researchers how to choose the values of these passive components. Nevertheless, it is fundamental to perform that selection process before designing and implementing the coupled coils and the compensation capacitors. The failure of this process could result in an EV wireless charging system with an unnecessary lower power transfer efficiency, poor utilization of the DC-link input voltage, or possibly the loss of the H-bride inverter's soft-switching.

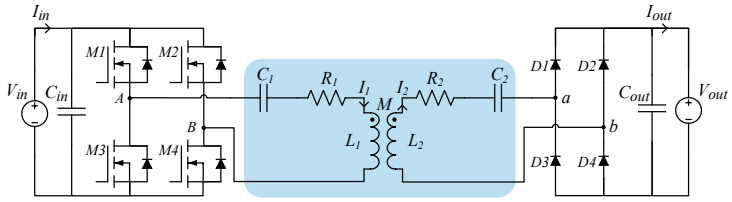

Figure 2.12: Equivalent circuit of an IPT system for wireless charging of EVs with the S-S compensation.

Specifically, the choice of the circuit parameters must result from the following considerations:

- the desired power transfer level must be met at the chosen operating frequency range, which, according to SAE J2954, it is 79...90 kHz for wireless charging of light-duty EVs;
- the DC input and output voltages must be within the allowed range defined by the power source, the load, and the implemented converter circuit components. The use of additional non-isolated DC/DC converters cascaded to the basic resonant converter allows the extension of the input or output voltage range to fulfill the application's power transfer requirements. However, the voltage range of these converters is also limited, and it is preferable to use as few conversion stages as possible to guarantee low power losses and avoid additional manufacturing costs;
- the current flowing through the switches must be kept low, and soft-switching must be ensured to limit the power losses in the converters' switches;
- the resonant circuit's voltage and current stress must be reasonable to reduce component cost, limit losses, and simplify the manufacturing process.

The most favorable ratio between coils' inductance and compensation capacitance must satisfy all these requirements.

2.4.1. ANALYTICAL MODELING OF THE S-S COMPENSATED CIRCUIT

As previously stated in Table 2.1, the behavior in the frequency domain of the S-S compensation network is described by (2.6). Thereby, L_1 is the primary coil's self-inductance, and L_2 is the coil's secondary self-inductance of which the magnetic coupling k depends on the coils' mutual inductance M as shown in (2.7). Moreover, C_1 and C_2 are the S-S compensation network's capacitances, and R_1 and R_2 are the lumped series resistances modeling the losses of the primary and the secondary circuits' components. The primary and secondary circuits' impedance $\boldsymbol{Z_1}$, $\boldsymbol{Z_2}$ are defined in (2.8). According to [5], the input voltage $\boldsymbol{V_{AB}}$ and the equivalent resistive load R_{ac} are defined in (2.9). Note that the voltage and current phasors are expressed in terms of their amplitude.

$$\begin{cases} \boldsymbol{V_{AB}} = \boldsymbol{Z_1 I_1} + j\omega M \boldsymbol{I_2} \\ 0 = (\boldsymbol{Z_2} + R_{ac})\boldsymbol{I_2} + j\omega M \boldsymbol{I_1} \end{cases} \tag{2.6}$$

$$M = k\sqrt{L_1 L_2} \tag{2.7}$$

$$\boldsymbol{Z_i} = R_i + j\omega X_i, \quad X_i = \omega L_i - \frac{1}{\omega C_i} : \quad i = 1...2 \tag{2.8}$$

$$\boldsymbol{V_{AB}} = V_{AB}\underline{/0°} = \frac{4}{\pi} V_{in}, \quad R_{ac} = \frac{8}{\pi^2} R_L = \frac{8}{\pi^2} \frac{V_{out}^2}{P_{out}} \tag{2.9}$$

Additionally, for a given processed power, the resonant circuit's efficiency $\eta_{\text{AB-to-ab}}$ is defined in (2.10).

$$\eta_{\text{AB-to-ab}} = \frac{R_{ac} |\boldsymbol{I_2}|^2}{V_{AB} |\operatorname{Re}[\boldsymbol{I_1}]|} \tag{2.10}$$

The total DC-to-DC efficiency $\eta_{\text{DC-to-DC}}$ also considers the power losses of the inverting and rectifying stages, of which parameters can be extrapolated from the devices' datasheet. Assuming that the H-bridge inverter operates in ZVS turn-on, its power losses are

$$P_{inv} = 4 \cdot R_{ds,on} \cdot \left[\left(\frac{|\boldsymbol{I_1}|}{2} \right)^2 \right] + \sum_{i=1}^{4} E_{off_{(Mi)}} \cdot f_0 \tag{2.11}$$

where $R_{ds,on}$ is the on-resistance of the MOSFETs and E_{off} is their turn-off energy loss. Since C_2 is chosen such that $X_2 \approx 0$, the rectifier's power losses are mainly due to the conduction:

$$P_{rect} = 4 \cdot \left[V_F \left(\frac{|\boldsymbol{I_2}|}{\pi} \right) + r \left(\frac{|\boldsymbol{I_2}|}{2} \right)^2 \right] \tag{2.12}$$

In (2.12), V_F is the forward voltage drop of the bipolar technology, while r models the linear increment of the voltage drop across the diode as a function of the flowing current.

Finally, $\eta_{\text{DC-to-DC}}$ can be computed as

$$\eta_{\text{DC-to-DC}} = \eta_{\text{AB-to-ab}} \cdot \frac{P_{out}}{P_{out} + P_{inv} + P_{rec}} \tag{2.13}$$

2.4.2. SELECTION OF THE TARGET MUTUAL INDUCTANCE

In the design of an IPT system, generally, the chosen battery charging application defines the desired power level P_{out}, the nominal battery voltage V_{out} and its charging range, the available range of input voltage V_{in} from the power source, and the allowed resonant frequency range f_0=$\frac{\omega_0}{2\pi}$. After the identification of these inputs, it is possible to compute the approximate required M which results in (2.14). The latter has been calculated from (2.6)-(2.9), assuming: X_1=X_2=R_1=R_2=0.

$$M = \frac{8}{\pi^2}\frac{V_{in}V_{out}}{\omega_0 P_{out}} \tag{2.14}$$

When considering the application of EVs, SAE J2954 [20] regulates three power classes, namely WPT1, WPT2, and WPT3, which correspond to a maximum input power from the AC-grid of (3.3, 7.7, 11.1)kVA, respectively. The guidelines for 22kVA (WPT4 power class) are still under consideration [1]. Moreover, SAE J2954 defines the operating frequency range for the H-bridge inverter in Figure 2.12, being 79...90 kHz.

From (2.14), it is intuitive that, for the same V_{in}, V_{out} and ω_0, each power level requires a different value of M. An example of that is shown in Figure 2.13. Thereby, the power classes WPT1 and WPT2 have a single-phase (1-ϕ) connection to the European low-voltage 50 Hz grid, while a 3-ϕ grid connection is considered for WPT3 and WPT4. This choice is due to the fact that households in Europe have limited access to grid connections with more than 16 A for each 230 V phase.

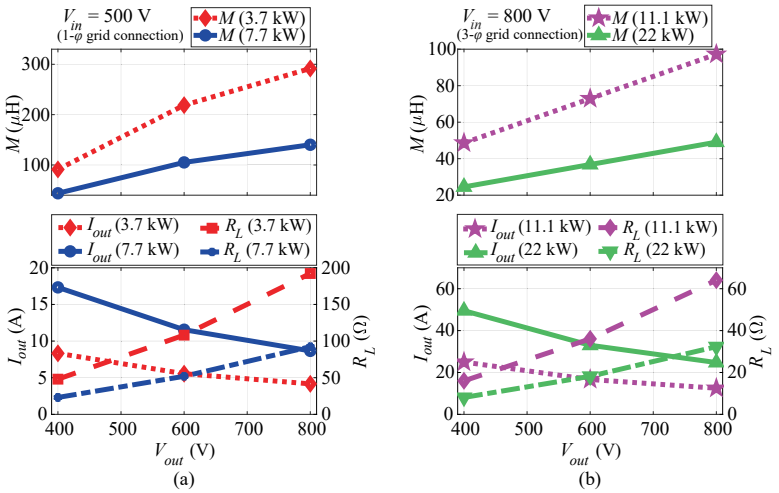

Figure 2.13: Required mutual inductance M, DC output current I_{out}, and equivalent resistive load R_L depending on the nominal battery voltage V_{out} for the power levels P_{in} of: (a) 3.7 kW (WPT1), 7.7 kW (WPT2), and (b) 11.1 kW (WPT3), 22 kW (WPT4), where P_{out}=0.9·P_{in} and f_0 = 85 kHz.

Figure 2.13 shows that the constraints imposed on a specific EV wireless charging application result in a required M that might differ considerably from other applications with different battery voltages or power classes. For instance, considering all the uses cases in Figure 2.13, the required M can be in the range 20...300 µH. If the coils' implementation does not result in the target M, the use of additional non-isolated DC/DC

converters cascaded to the basic resonant converter allows the extension of the input or output voltage range to fulfill (2.14). However, this is not preferable to limit the power losses and avoid extra manufacturing costs.

2.4.3. SELECTION OF THE COILS' AND COMPENSATION'S PARAMETERS

After the identification of the target M, it is now important to choose the combination of inductance and capacitance that leads to a high-efficiency operation. The selection of the coils' parameters L_1, R_1, L_2, R_2 and k is performed through (2.15). This ensures that the IPT circuit's operating frequency is within the allowed range from the standard. Moreover, it guarantees that the equivalent resistive load R_L=$\frac{V_{out}}{I_{out}}$ coincides with the optimum load $R_{L,opt}$ achieving the load impedance matching described in [15], [21], [22]. Additionally, the bifurcation phenomenon is avoided by imposing the condition defined in Table 2.7 on the primary and secondary coils' quality factor Q_1, Q_2. The optimum load condition and the bifurcation phenomenon have been previously discussed in Section 2.2.2.

A relationship between the coupled coils' parameters can be computed from (2.15) which depends on Q_1, Q_2, and k. This dependence is going to be discussed in the example of Section 2.4.4. A specific solution of the coupled coils' parameters would result from their physical characteristics which are a consequence of their geometry and structure. This point is addressed in Section 2.4.5.

$$\begin{cases} f_{sw} = f_0 = 79...90\,\text{kHz} \\ k\sqrt{L_1 L_2} = \dfrac{8}{\pi^2}\dfrac{V_{in}V_{out}}{\omega_0 P_{out}} \quad \text{from (2.7) and (2.14)} \\ R_L = R_{L,opt} = \dfrac{\pi^2}{8}\omega_0 M\sqrt{\dfrac{R_2}{R_1}} \\ Q_1 = \dfrac{2a^2Q_2^2(1-\sqrt{(1-k^2)})-1}{k^2Q_2} \quad \text{where:} \\ \quad a>1, \quad Q_1 = \dfrac{\omega_0 L_1}{R_1}, \quad Q_2 = \dfrac{\omega_0 L_2}{R_2} \end{cases} \tag{2.15}$$

Finally, C_1 and C_2 can be calculated from (2.8) by imposing $X_1 > 0$ and X_2=0. This choice translates into an inductive primary current necessary to achieve the ZVS turn-on of the H-bridge inverter explained in Section 2.1.1.

2.4.4. EXAMPLE BASED ON A WPT1 EV WIRELESS CHARGING SYSTEM: ANALYTICAL COMPUTATION

From (2.14), when considering $P_{out,max}$=3.4 kW, V_{in}=490 V, V_{out}=400 V, and f_0=79 kHz, the target M is estimated to be 94.14 µH. At this point, the optimized combination of inductance and capacitance needs to be selected.

Figure 2.14 shows the resulting circuit parameters depending on the values of k, Q_1, and Q_2, which, in turn, result from the coils' dimensions and geometry.

Figure 2.14(a) shows that the inductance and the capacitance are independent of Q_1 and Q_2. For instance, to achieve the same M, the required L_1 and L_2 increase as k drops. Therefore, for the same value of k, both Q_1 and Q_2 derive from the coils' resistance.

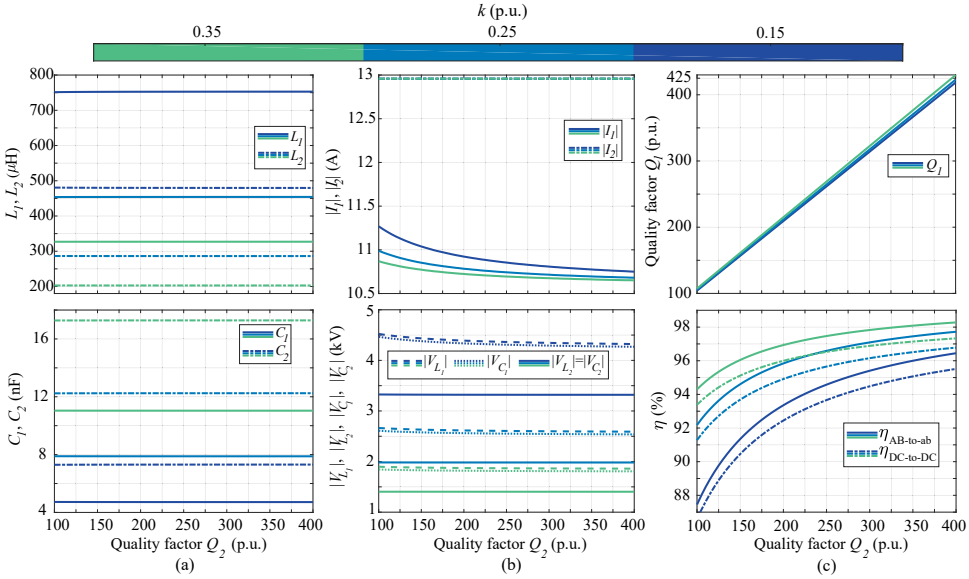

Figure 2.14: Parameters of the WPT1 EV wireless charging system resulting for different coupling k and secondary coil's quality factor Q_2 (M=94.14μH). (a) Coils' self-inductance L_1 and L_2, and compensation capacitance C_1 and C_2. (b) Peak current and peak voltage in both primary and secondary resonant circuits. (c) Primary coil's quality factor Q_1 from (2.15) with a=1.02, the resonant circuit's efficiency $\eta_{\text{AB-to-ab}}$ and the overall efficiency $\eta_{\text{DC-to-DC}}$ of the IPT system computed from (2.10) and (2.13).

According to Figure 2.14(b), the secondary circuit's current stress $|I_2|$ is invariant of the coils' parameters since V_{out} and P_{out} have been fixed while keeping flexibility on V_{in}. For this reason, the current stress on the primary circuit $|I_1|$ can differ among these designs up to 5.5%. Generally, $|I_1|$ is lower for higher values of k and Q_2. As a consequence of the current stress and the inductance and capacitance values in Figure 2.14(a), the voltage stress at both primary and secondary circuits can drop up to 60% as k increases. The resulting voltage stress highly influences the design of the passive components. When considering the main coils, enough distance needs to be allocated between each neighboring turn and the coil's terminals to ensure isolation. This distance depends on the total voltage stress. On the other hand, assuming that a single unit capacitor is used to form the total compensation capacitance, the voltage stress on the compensation capacitors influences the required number of series connections between the single units based on their voltage rating. A larger number of series connections translate into more necessary parallel connections to reach the same capacitance value. Consequently, this affects the number of used components, the total size of the printed circuit board (PCB), and above all the system's total cost. In general, higher voltage stress requires larger distances between the elements, increasing the occupied space by the IPT system.

By using (2.15), Figure 2.14(c) shows that in all designs, the bifurcation phenomenon is avoided if $Q_1 > Q_2$. Moreover, the power transfer efficiency improves with higher k and Q_2 values because of the lower current stress and the reduced coils' resistance. It can be noticed that, to reach a certain DC-to-DC efficiency $\eta_{\text{DC-to-DC}}$ when k is low, there is the

Table 2.8: Dimensions (mm) valid for both coils referring to Figure 2.15.

x_a, y_a, z_a	x_f, $x_{f,unit}$, y_f, $y_{f,unit}$, z_f	x_c, y_c	$z_{f\text{-}c}$	$z_{f\text{-}a}$	d_w
570, 370, 2	559, 43, 364, 28, 4.1	545, 350	2	4	2.5
Ferrite units: E planar core 3C95; Litz wire: 600 strands x 0.071mm					

need to design coils with higher quality factor than in the case with higher k. For example, to achieve $\eta_{\text{DC-to-DC}}$=95.8%, Q_2=395 is required at k=0.15, while Q_2=235 is required at k=0.25, and Q_2=165 is required at k=0.35. Higher Q_2 values can be obtained by changing the coil's structure or employing a Litz wire with a larger diameter, i.e., reducing the current density of the coil. These considerations are discussed further in Section 2.4.5.

2.4.5. EXAMPLE BASED ON A WPT1 EV WIRELESS CHARGING SYSTEM: COILS DESIGN THROUGH THE FEM ANALYSIS

In Section 2.4.4, different options have been explored for the choice of the IPT system parameters, which are summarized in Figure 2.14. These are dependent on k and Q_2, which are consequences of the coils' geometry and structure.

In EV applications, the available space for the coils' placement is limited, which restraints their maximum area. In this analysis, the main coils' dimensions were given as listed in Table 2.8 referring to Figure 2.15. The dimensions of the aluminum shield, the ferrite layer, the outer sides of the winding, and the Litz wire's diameter are fixed, and they are identical for both coils. However, there is still room to choose their coil's spread C_{sp} defined in Figure 2.15, their number of turns N and the distance between them in the z-direction, being $Z_{ag} \geq 100\,\text{mm}$. It must be noted that the following method also applies if there are more degrees of freedom in the coils' structure or geometry. Additionally, this approach could also be included in a coils' design based on multi-objective optimization such as [15], [21] and[23]. In those cases, the spectrum of possible solutions would be wider.

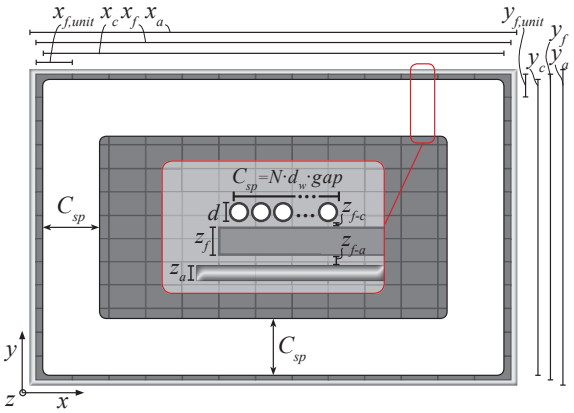

Figure 2.15: Coils' geometry which dimensions are specified in Table 2.8.

The values of C_{sp1}, C_{sp2}, N_1, N_2 and Z_{ag} are selected by performing a FEM analysis on different possible designs of the coupled coils while making sure that the conditions in (2.15) are satisfied. According to Section 2.4.4, the coupled coils must result in

M=94.14 µH at f_0=79 kHz for the aligned condition. Moreover, the optimum load condition in (2.15) must satisfy $R_{L,opt}$=R_L=47.06 Ω which translate into $\frac{R_2}{R_1}$=0.666. To avoid the bifurcation phenomenon, $Q_1 > Q_2$ must hold.

FEM ANALYSIS OF SINGLE (UNCOUPLED) COILS

To understand the influence of C_{sp} and N on the coil's inductance L and resistance R, a sensitivity analysis has been performed by sweeping those parameters. The rectangular coil in Figure 2.15 has been considered and fixed dimensions are specified in Table 2.8. In this first stage, the coil is placed in the free air, and it is not coupled to another coil to ensure that a specific magnetic coupling does not influence the results.

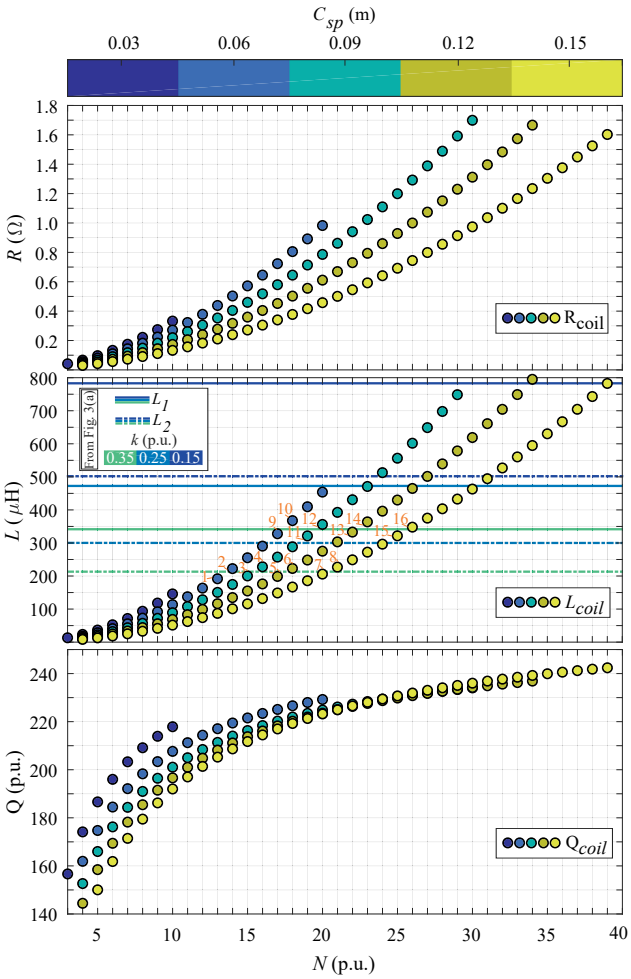

Figure 2.16: Parameters of single (uncoupled) coils that have different coil's spread C_{sp} and number of turns N, resulting from the FEM analysis. The coils' geometry is defined in Table 2.8 and Figure 2.15.

Figure 2.16 shows the resulting coil's resistance R_{coil}, inductance L_{coil}, and quality factor Q_{coil} for different C_{sp} and N. These have been found from the FEM analysis per-

Table 2.9: Parameters of the coupled coils from the FEM analysis. The primary and secondary coils' designs derive from Figure 2.16.

Coupled coils from Figure 2.16					
Secondary	Primary	k	$\frac{R_2}{R_1}$	Q_1, Q_2 (p.u.)	Z_{ag} (mm)
2	12	0.324	0.613	220, 219	105.5
	13	0.333	0.650	219, 220	105.0
	16	0.32	0.627	222, 220	106.5
3	11	0.357	0.643	220, 213	105.5
	15	0.356	0.639	222, 214	109.4
4	10	0.316	0.662	227, 215	108.0
	12	0.320	0.655	222, 217	114.0
	14	0.317	0.638	223, 217	120.0
5	15	0.357	0.643	224, 214	114.5
6	13	0.335	0.687	223, 217	119.5
	16	0.327	0.664	227, 218	122.8
7	11	0.352	0.666	221, 216	110.5
	15	0.352	0.659	224, 218	117.6
8	9	0.332	0.744	225, 216	104.8
	13	0.332	0.693	223, 220	121.5
	16	0.325	0.672	228, 221	125.0

formed through COMSOL Multiphysics. The same outer diameter d_w=2.5 mm of the Litz wire has been considered for all designs since the coil's current density will not change drastically for the same value of M as shown in Figure 2.14(b). Additionally, for each value of C_{sp}, the maximum allowable N is found such that $gap \geq 1.2$, where gap is dimensionless as defined in Figure 2.15. This ensures a minimum distance between adjacent turns that guarantees electrical isolation and limits the proximity effect.

According to Figure 2.16, it is worth mentioning that a higher value of Q_{coil} can be achieved by reducing C_{sp} for the same N as long as $N \leq 25$. On the other hand, a larger C_{sp} can accommodate more number of turns N and, consequently, higher values of self-inductance can be achieved.

In Figure 2.16, the target coils' self-inductance values L_1 and L_2 found in Figure 2.14(a) are compared to L_{coil} resulting from the FEM analysis of different designs. It is possible to notice that C_{sp}=0.03 m results in L_{coil} lower than the target values for $k \leq 0.35$. Therefore, that coil's spread is discarded.

The analysis of single coils in Figure 2.16 is valuable since it gives a first indication of the parameters to be expected from a certain coil's design. Nevertheless, it is essential to also assess the final configuration with the coupled coils, in which their parameters might differ due to the magnetic coupling.

FEM ANALYSIS OF COUPLED COILS

According to Figure 2.14(c), greater values of k at the aligned position lead to higher power transfer efficiency for the same coils' quality factor. Therefore, this analysis first considers the coils' designs in which L_1 and L_2 correspond to the target values at k=0.35. In Figure 2.16, these are labeled with orange numbers. In particular, the coupled coils' configurations that satisfy $\frac{R_2}{R_1}=(1\pm0.04)\cdot0.666$ are chosen since most likely to meet the

target of $\frac{R_2}{R_1}$=0.666. The distance Z_{ag} between the coils is chosen such that M=94.14 µH. A combination of coupled coils is considered acceptable only if the target M is met while $Z_{ag} \geq 100$ mm.

The combinations of coupled primary and secondary coils are assessed through FEM analysis, and their resulting parameters are summarized in Table 2.9. The chosen configuration is the one that has 11 as the primary coil and 7 as the secondary coil because it has the highest k while meeting the requirements on $\frac{R_2}{R_1}$ and Z_{ag}.

The implementation of the chosen coupled coils is shown in Figure 2.17(a)-(d). In Table 2.10, the coils' parameters measured at 79 kHz through an LCR meter are compared to the ones resulting from the FEM analysis.

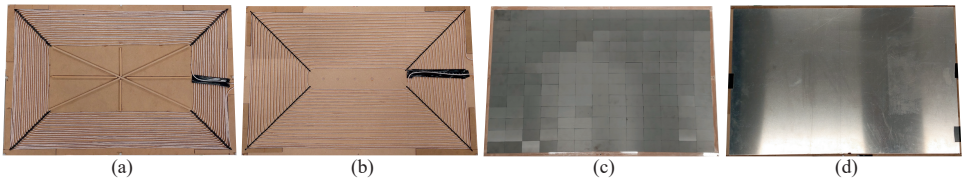

(a) (b) (c) (d)

Figure 2.17: The coils' implementation for the 3.7 kW EV wireless charging prototype: (a) winding of the primary coil, (b) Winding of the secondary coil, (c) ferrite layer and (d) aluminum shield defined in Figure 2.15 which is identical for both coils.

Table 2.10: Parameters of the chosen coupled coils design from the FEM analysis compared to the values resulting from the laboratory implementation in Figure 2.17.

	C_{sp}(m), N(p.u.)	Z_{ag}=111 mm		L(µH)	R(Ω)	Q(p.u.)	M(µH)
L_1	0.09, 19		**FEM**	332.3	0.744	221.6	93.75
L_2	0.15, 20			215.8	0.494	216.6	
Coils in Figure 2.16/Table 2.9: primary=11, secondary=7			**lab**	338.0	0.650	258.1	93.90
				223.7	0.440	252.4	

2.4.6. LABORATORY PROTOTYPE AND EXPERIMENTAL RESULTS

The overall wireless charging system is shown in Figure 2.18 whose parameters are listed in Table 2.11. One bidirectional DC power supply has been used as the power source, while a second one has been employed in the current-sinking mode to emulate the EV battery. When considering the lump resistance of the coils, the compensation capacitors, and the semiconductor devices, the equivalent optimum load results in $R_{L,opt}$=48.78 Ω which is acceptable since it translates into a nominal P_{out}=3.28 kW ≤ $P_{out,max}$=3.4 kW. Two coils' alignments are considered of which mutual inductance is M=M_{max} and M=M_{min}.

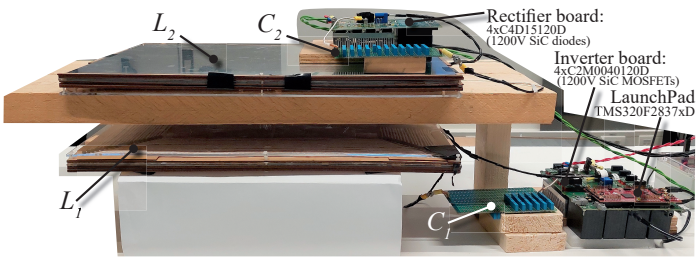

Figure 2.18: Laboratory prototype of the implemented WPT1 EV wireless charging system.

Table 2.11: Circuit parameters and components used in the proposed 3.7 kW EV wireless charging system in Figure 2.18.

Circuit parameters					**Component**	**Function**	**Units**	**Manufacturer**	**Name**
f (Hz)	79110		**Primary**	**Secondary**	MOSFETs*	Inverter	4	CREE/Wolfspeed	C2M0040120D
$P_{\text{grid,max}}$ (kW)	3.7	L_1, L_2	338.0	224.7	Diodes**	Rectifier	4		C4D15120D
V_{in}(V)	[360 500]	C_1, C_2 (nF)	13.45	18.53	6.8 nF	C_1	8x4	EPCOS	B32671L
V_{batt}(V)	[280 400]	R_{L_1}, R_{L_2} (Ω)	0.65	0.44	500 V_{RMS}	C_2	11x4		
$R_{L,opt}$ (Ω)	48.78	M (μH)	[61.72 93.90]		**Misalignment** [(x,y,z) mm]		$M_{\max} \rightarrow (0, 0, Z_{ag})$		
Z_{ag} (mm)	111		[$M_{\min}$ $M_{\max}$]				$M_{\min} \rightarrow [(90, 0, Z_{ag})]$		
*[$R_{ds,on}$=50 mΩ, E_{off}=15μJ]; **[V_F=0.8 V, r=75 mΩ]									
Measuring and supplying equipment	Oscilloscope: YOKOGAWA DLM4058 2.5GS/s 500MHz Power analyzer: YOKOGAWA WT500 Bidirectional DC power supplies: DELTA ELEKTRONIKA SM500-CP-90 (input), SM1500-CP-30 (output)								

At M=M_{max}, the DC-to-DC efficiency $\eta_{\text{DC-to-DC}}$ has been measured at different output voltage and current values to characterize the overall IPT system. These values are shown in Figure 2.19. Thereby, I_{out} has been regulated by controlling V_{in} through the input DC power supply. This could be performed through a boost-like PFC converter for the operating points with $I_{out} \geq 6$A since the required V_{in} is in the range 360...500V. Lower I_{out} could be set by phase shifting the H-bridge inverter in Figure 2.12 to reduce the fundamental component of V_{AB}. According to Figure 2.19, the highest $\eta_{\text{DC-to-DC}}$ can be achieved throughout the entire V_{out} range by operating at the optimum load condition, i.e., when R_L=$R_{L,opt}$.

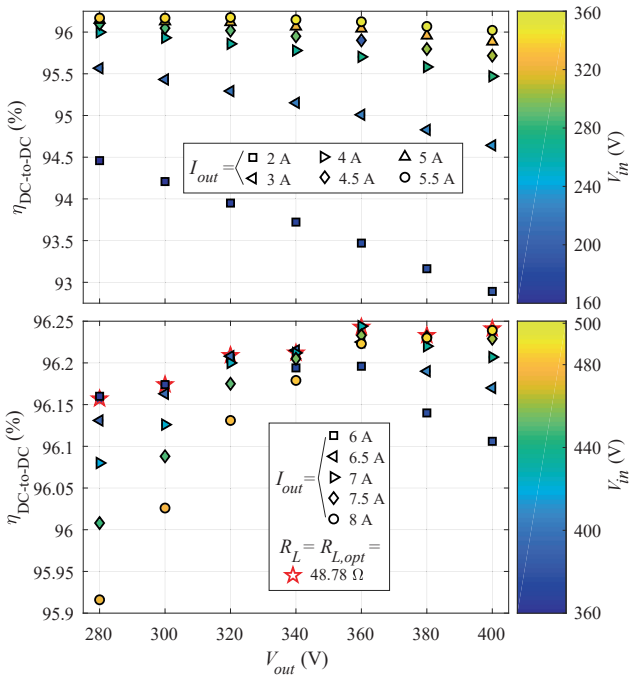

Figure 2.19: Measured $\eta_{\text{DC-to-DC}}$ at different load conditions while M=M_{max}. The output current I_{out} has been regulated by controlling V_{in}.

In Figure 2.20, the measured $\eta_{\text{DC-to-DC}}$ at both M=M_{max} and M=M_{min} are plotted for the CC charging profile where I_{out}=8.2A. Only the CC charging mode is considered because it takes place for most of the charging process in EV applications with the WPT1 power class. Additionally, the measured waveforms at the nominal battery voltage are shown in Figure 2.21 for both coils' alignments. It must be noted that the ZVS turn-on of the H-bridge inverter is always maintained with the chosen compensation capacitance.

According to Figure 2.20, it is possible to follow the CC charging profile for the entire battery voltage range by regulating V_{in} through the PFC stage at both coils' alignments. The misalignment range can be further extended by phase-shifting the H-bridge inverter in Figure 2.12. When the coils' misalignment occurs, the efficiency drops up to 2.2% at the nominal battery voltage. This efficiency drop has three main causes. First, according to (2.14), a lower V_{in} is required to achieve the same output power. Conse-

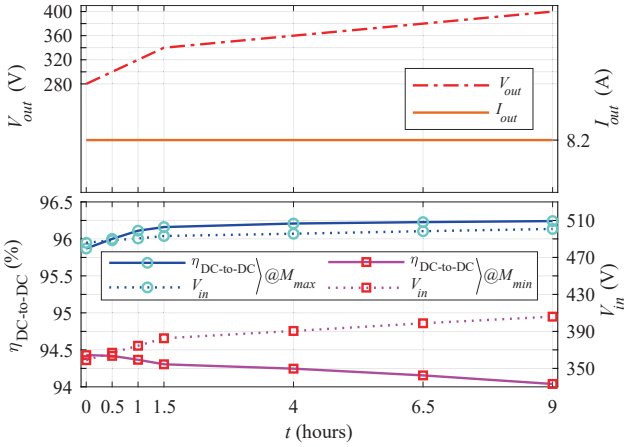

Figure 2.20: Measured $\eta_{\text{DC-to-DC}}$ and supplied V_{in} at both M=M_{max} and M=M_{min} for the CC mode of a typical EV battery charging cycle. The total energy received by the battery would be about 26.5 kWh.

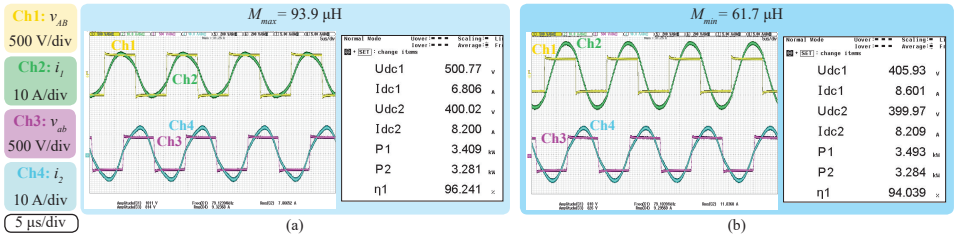

Figure 2.21: Measured circuit waveforms and DC-to-DC efficiency at: (a) M=M_{max}, and (b) M=M_{min}.

quently, as shown in Figure 2.21(b), there is a higher current circulating at the primary circuit, which increases the conduction losses. Second, as described in (2.15), the optimum load $R_{L,opt}$ is directly proportional to M. This means that $R_{L,opt}$ differs for the two coils' alignments: $R_{L,opt}$=48.78 Ω for M=M_{max}, and $R_{L,opt}$=32.98 Ω M=M_{min}. However, independently of M, the equivalent resistive load R_L varies in the range 34.14...48.78 Ω during the CC charging mode. This means that, at M=M_{min}, R_L never matches $R_{L,opt}$. Due to this characteristic of $R_{L,opt}$, the highest efficiency is reached at the minimum battery voltage when M=M_{min}. Finally, Figure 2.21 shows that the primary current is more inductive M=M_{min} than in the aligned case which worsens the turn-off losses. The reason for this becomes clear by analyzing the expression of the input impedance Z_{in} in (2.16), which has been derived from (2.6) assuming that X_1 >0 and X_2=0 at $\omega = \omega_0$. Considering the variations of X_1 negligible, it can be noticed from (2.16) that R_{in}, i.e., the real part of $\boldsymbol{Z_{in}}$, is directly dependent on M^2. This means that, as M decreases due to the coils' misalignment, R_{in} would also decrease leading to a more inductive $\boldsymbol{Z_{in}}$.

$$\boldsymbol{Z_{in}} = \frac{\boldsymbol{V_{AB}}}{\boldsymbol{I_1}} = \underbrace{R_1 + \frac{(\omega_0 M)^2}{R_2 + R_{ac}}}_{R_{in}} + j\underbrace{\left(\omega_0 L_1 - \frac{1}{\omega_0 C_1}\right)}_{X_{in}=X_1} \tag{2.16}$$

2.5. MULTI-COMPONENT COMPENSATION NETWORKS

The one-component compensation networks discussed from Section 2.2 to Section 2.4 are the simplest resonant circuit used in IPT systems for battery charging applications. Since the least number of components are employed, the one-component compensation networks can potentially achieve the highest peak power transfer efficiency. However, their parameters strictly depend on the LCT configuration, which limits the design freedom. Compensation networks with multiple components provide more design flexibility and power transfer profiles which can be advantageous, especially in extreme misalignment conditions. This section discusses the most common multi-component compensation networks and their main characteristics.

2.5.1. LC COMPENSATION

The most immediate multi-component compensation network is the LC configuration, a development of the one-component parallel compensation. As explained in Section 2.2.3, the primary parallel compensation requires a current source inverting stage. Similarly, the secondary parallel compensation must be connected to a current source rectifying stage to be directly interfaced with a battery. As shown in Figure 2.2, those current source topologies consist of a bulky DC inductor, and the soft-switching operation cannot be achieved since the semiconductor devices are processing a continuous current.

With the parallel compensation, it is possible to employ the voltage source inverting and rectifying power stages shown in Figure 2.2 by shifting the inductor from the DC-link to the high-frequency resonant circuit as shown in Figure 2.22. This strategy converts the one-component parallel compensation into a multi-component compensation called LC compensation, forming the well-known LCL topology. This configuration can realize the soft-switching operation, and it requires an inductor smaller than the DC inductor used in the current source H-bridge inverter.

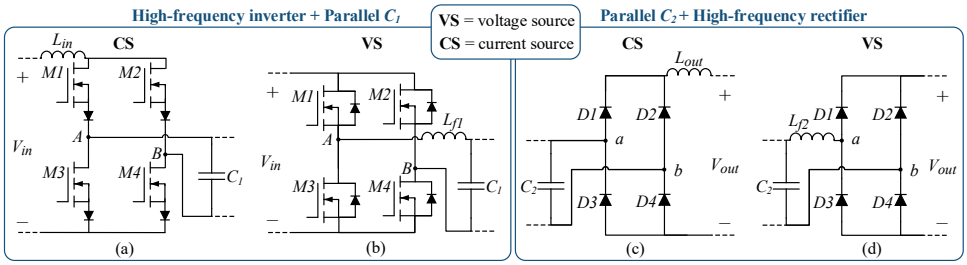

Figure 2.22: High-frequency inverting and rectifying power conversion stages discussed in Section 2.1.1 suitable for a parallel compensation. (a) Current source inverter (primary P compensation); (b) voltage source inverter (primary LC compensation); (c) current source rectifier (secondary P compensation); (d) voltage source rectifier L_{f2} (secondary LC compensation).

Several methods can be used to tune the LC compensation. In [24] and [25], the power transfer resulting from the LC compensation adopted at the primary circuit has been investigated for different values of the compensation inductance L_{f1}. The value of L_{f1}, the load and coupling conditions influence the inverter's current, which might be heavily distorted due to the multiple resonant frequencies of the circuit.

Another strategy consists of splitting the parallel compensation capacitor into two

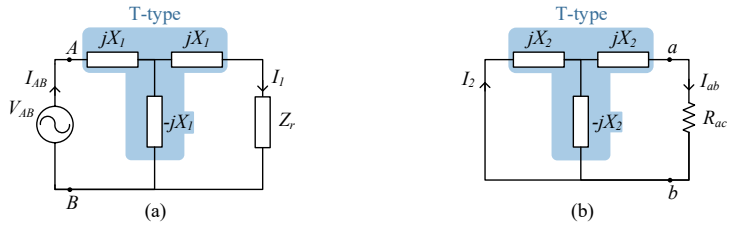

Figure 2.23: T-type compensation network for IPT systems at: (a) the primary circuit; (b) the secondary circuit.

parallel capacitors. One capacitor is tuned according to the loosely coupled transformer (LCT), while the other is adjusted based on the compensation inductor. This approach is especially advantageous when the primary and the secondary compensation networks differ from each other. Moreover, this approach gives more flexibility since the LC parameters are not strictly dependent on the LCT, and they can be customized to achieve a certain power level, power transfer efficiency, and density. Examples of this method are given in [26] and [4].

On the other hand, the LC compensation network can be tuned as the T-type resonant circuit explained in [27], which circuit schematic is shown in Figure 2.23. Figure 2.23(b) shows the equivalent circuit of a secondary LC compensation network where the right-hand and the left-hand sides consist, for simplicity, of the pure reactance jX_2 while the down-side is composed of the purely capacitive reactance $-jX_2$. According to the method explained in Section 2.2.1, the equivalent $\boldsymbol{Z_2}$ can be computed as shown in (2.17). Considering that $\boldsymbol{Z_2}$ is purely resistive in the T-type compensation, the reflected impedance $\boldsymbol{Z_r}$ defined in Table 2.2 would also be resistive.

$$\boldsymbol{Z_2} = jX_2 + [(-jX_2)//(jX_2 + R_{ac})] = \frac{X_2^2}{R_{ac}} \tag{2.17}$$

If the primary circuit consists of an LC compensation network, its schematic would be the one illustrated in Figure 2.23(a). In that case, the input impedance $\boldsymbol{Z_{in}}$ is

$$\boldsymbol{Z_{in}} = jX_1 + [(-jX_1)//(jX_1 + \boldsymbol{Z_r})] = \frac{X_1^2}{\boldsymbol{Z_r}} = \frac{X_1^2 \boldsymbol{Z_2}}{\omega^2 M^2} \tag{2.18}$$

According to (2.18), $\boldsymbol{Z_{in}}$ is purely resistive if $\boldsymbol{Z_2}$ is resistive which, from (2.17), is the case of the secondary T-type LC compensation. This characteristic eases the tuning of the T-type compensation network, which parameters result in

$$X_i = \omega_0 L_i = \omega_0 L_{fi} = \frac{1}{\omega_0 L C_i} \quad \rightarrow \quad L_i = L_{fi}, \quad C_i = \frac{1}{\omega_0^2 L_i} = \frac{1}{\omega_0^2 L_{fi}} \; : \; i = [1, 2] \tag{2.19}$$

The configuration of the T-type compensation has been used in [28]–[30]. The main advantages of the double-sided LC (DLC) compensation are the adoption of the voltage source inverter shown in Figure 2.22(b), resulting in the ZVS turn-on capability and the load-independent current source output. Moreover, the output current is directly proportional to the coupled coils' mutual inductance M, which is not the case in the one-component compensation network as shown in Figure 2.8. This makes the DLC circuit

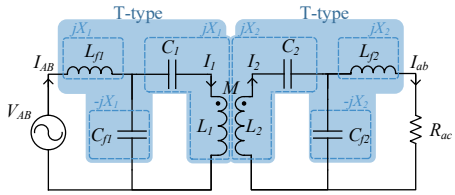

Figure 2.24: Double-sided LCC compensation defined from the T-type compensation network in Figure 2.23.

inherently safe against misalignment. However, this also means that the nominal output power might not be delivered in the presence of misalignment. One limitation of the DLC is that, according to (2.19), the parameters of the DLC are still strictly dependent on the LCT, similar to the one-component compensation networks. This means that there is no flexibility in the parameters' selection of the DLC. Moreover, the size of the compensation inductor might be relatively large since its inductance must be equal to the coupled coil's inductance.

2.5.2. LCC COMPENSATION

The LCC compensation network is a T-type resonant circuit in which, compared to the LC compensation, an extra capacitor is connected in series to the coupled coil [8]. The circuit schematic of the double-sided LCC (DLCC) compensation is shown in Figure 2.24. The DLCC tuning is defined in (2.20). The DLCC compensation has two main advantages compared to the DLC discussed in Section 2.5.1. First, the needed compensation inductance is lower than the coils' inductance which translates into a smaller inductor size. Potentially, this reduces the inductor's cost, weight, and space. Moreover, by selecting the value of the compensation inductances, the nominal output power can be chosen without modifying the LCT.

$$X_i = \omega_0 L_i - \frac{1}{\omega_0 C_i} = \omega_0 L_{fi} = \frac{1}{\omega_0 C_{fi}} \rightarrow C_{fi} = \frac{1}{\omega_0^2 L_{fi}}, \quad C_i = \frac{1}{\omega_0^2 (L_i - L_{fi})} : i = [1,2] \tag{2.20}$$

Similarly to the DLC, the DLCC has a load-independent output current directly proportional to the coils' mutual inductance M. This makes the DLCC compensation network inherently safe against misalignment, and for this reason, the DLCC is generally adopted in dynamic EV wireless charging applications. A detailed analysis of the DLCC can be found in Appendix B, where the distortion of i_{AB} is analyzed resulting from the multiple resonance frequencies present in the multi-component compensation networks.

The LCC compensation has also been used in the configuration of LCC-S and S-LCC, in which the output has a load-independent voltage source behavior.

2.5.3. OTHER MULTI-COMPONENT COMPENSATIONS

Besides the LC and the LCC compensations, other multi-component compensation networks have been proposed in the literature to solve the limitations of the one-component compensations. Some examples are summarized in the following paragraphs.

In [16] and [31], the S-SP compensation is proposed, which has a load-independent output voltage less sensitive than the one of the S-P compensation to the LCT parameters variation, including k. The tuning method adopted for the S-SP compensation is based on the T-model of the LCT shown in Figure 2.4(b): the series capacitors compensate

for the leakage inductances while the parallel secondary capacitor compensates for the mutual inductance. As a result, this approach can result in severe current distortion at both the primary and the secondary circuits, which is analyzed in detail to predict the actual behavior of the S-SP.

In [32], the SP-S compensation has been used such that the power transferred is less dependent on the misalignment. Different behaviors can be achieved by defining a tuning ratio between the primary compensation capacitors. The drawback of this compensation is that it requires an input power supply with a current source characteristic.

2.6. HYBRID COMPENSATION NETWORKS COMBINING THE S-S AND THE DLCC FOR A CONSTANT OUTPUT POWER

In EV wireless charging systems, the delivered output power is highly dependent on the mutual inductance between the two main coils. Since the relative position between the coils is not fixed, the power flow must be controlled to ensure a constant output power level at the different coupling conditions. This becomes especially challenging in dynamic wireless charging applications because the control must be prompt enough to react to the fast rate of change of the mutual inductance.

This section evaluates a strategy that takes advantage of the characteristics of the S-S and the DLCC compensations to realize the self-balancing of the output power over the misalignment. This is possible since both compensations have a load-independent output current which, in the S-S compensation, is inversely proportional to M while in the DLCC, the output current is directly proportional to M. It is interesting to verify if these opposite trends can be used to stabilize the power flow over the misalignment without requiring active control of the power converters or communication systems.

A similar approach has been investigated in [33]–[37]. These circuits were first defined by [33] with the name of hybrid compensation networks. Multicoil pads are used in these hybrid compensations since two compensation networks are employed. Specifically, [33] and [34] use a parallel connection between the S-S and the DLCC. This configuration can become critical at a certain level of misalignment since the current in the S-S compensation increases exponentially with the misalignment. To solve that issue, [35] proposed a series-connected hybrid compensation limiting the current rise of the S-S over the misalignment passively. Moreover, [36] summarized the characteristics of the hybrid topologies while giving an example of the hybrid topology consisting of the LCC-S and the S-LCC compensations, which have a load-independent output voltage characteristic. On the other hand, [37] proposed a double-sided CLLLC topology. Alternatively, [38] and [39] propose a dual-frequency hybrid compensation in which, oppositely to the previous examples, only one set of coupled coils with one compensation network is used. This IPT system is designed to result in two different equivalent circuits at two distinct operating frequencies: the fundamental frequency and the third-order harmonic frequency. At the fundamental frequency, the equivalent circuit resembles the S-S compensation. At the third-order harmonic frequency, the equivalent circuit in [38] resembles the LC-LC compensation, while the one in [39] resembles the LCC-S compensation. However, this method is hardly applicable to EV wireless charging, given the narrow operating frequency allowed by SAE J2954.

2.6.1. CONCEPT

From (2.14), it can be found that the output power P_{out} delivered to the battery by an IPT system using the S-S compensation network is inversely proportional to the mutual inductance between the two coils M:

$$P_{out} = \frac{8}{\pi^2} \frac{V_{in} V_{out}}{\omega_0 M} \tag{2.21}$$

This means that, for the same values of V_{in} and V_{out}, P_{out} increases when the coils become more misaligned.

On the other hand, based on [8], the delivered P_{out} to the battery by an IPT system using the DLCC compensation network is directly proportional to M:

$$P_{out} = \frac{8}{\pi^2} \frac{M V_{in} V_{out}}{\omega_0 L_{f1} L_{f2}} \tag{2.22}$$

According to (2.21) and (2.22), P_{out} transferred from the S-S and the DLCC compensations has an opposite dependence of M. From this consideration, it could be possible to balance the received P_{out} against the coils' misalignment by combining the two compensation networks in the same IPT system.

2.6.2. PROPOSED IMPLEMENTATION

A possible configuration is shown in the circuit schematic of Figure 2.25.

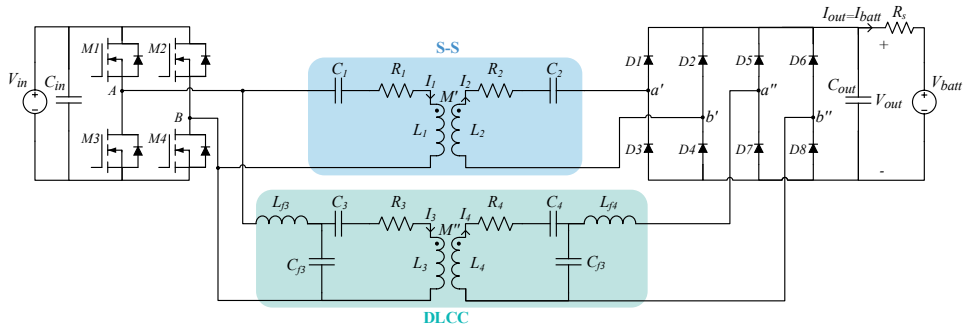

Figure 2.25: Circuit schematic of the proposed EV wireless charging system combining the S-S and the DLCC compensation networks to realize self-balancing of the output power over the misalignment.

The same inverter powers the two compensation networks. For instance, their input terminals are connected in parallel. On the other hand, the output terminals of the two compensation networks are not connected in parallel because their output currents have opposite phase angles and would cancel out each other. Therefore, one dedicated rectifying stage is needed for each compensation network. Then, their DC outputs are connected in parallel to add up the two currents. The resulting terminals are connected to the battery load modeled as a voltage source.

According to Figure 2.25, the proposed circuit consists of four coils, of which two are placed at the primary circuit and the other two at the secondary circuit. Figure 2.26 shows two possible magnetic arrangements. Figure 2.26(a) illustrates two coupled bipolar pads (BPPs), each of them consisting of two partially overlapped rectangular coils.

This coils' configuration for the hybrid compensation network has been used in [33]. Figure 2.26(b) shows two coupled DDQ pads, each of them consisting of a DD coil overlapped in the center with a rectangular, also called quadrature (Q) coil. This configuration has been used in [34], [36], [37]. In Figure 2.26, the coils within each pad are overlapped to ensure they are mutually decoupled. Furthermore, [35] uses two coupled DD pads.

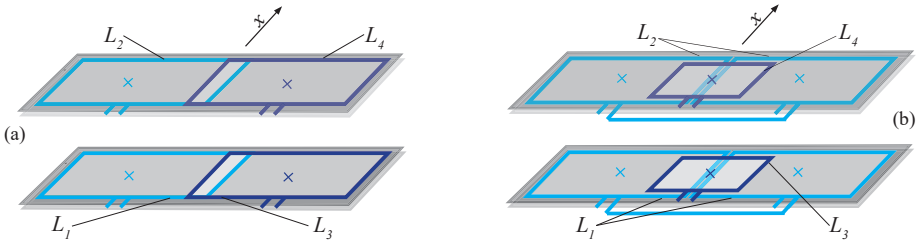

Figure 2.26: Possible coils' arrangements for the proposed circuit in Figure 2.25. (a) Coupled bipolar pads; (b) coupled DDQ pads, based on Figure 1.5.

2.6.3. CIRCUIT SIMULATIONS

As a preliminary proof of concept, circuit simulations of the schematic in Figure 2.25 have been executed. This analysis assumes that there is no cross-coupling between opposite coils. Additionally, the simulations corresponding to the two values of M have been performed separately to evaluate the two steady-state operating conditions.

In the simulations, the parameters of the coils have been chosen based on the 22 kW rectangular coils of [40], which parameters are summarized in Table 2.12. The target P_{out} to the battery load is 22 kW, and the IPT system has been tuned such that each of the two compensation networks contributes to delivering a part of P_{out}. Specifically, at k=k_{max}, the S-S compensation network delivers about 9 kW, and the double-sided LCC delivers 13 kW. The DC voltages V_{in}, V_{out} have been selected such that the S-S compensation operates at the optimum load condition for k=k_{max}.

Table 2.12: Circuit parameters used to simulate the IPT system in Figure 2.25.

f_{sw}	k_{max}	$C_{in,out}$	$L_{1,3}$	$L_{2,4}$	C_1	C_2	L_{f3}	L_{f4}
85 kHz	0.182	250 µF	344.8 µH	212.8 µH	10.2 nF	16.5 nF	39.3 µH	41.4 µH
V_{in}	V_{out}	R_S	$R_{1,3}$	$R_{2,4}$	C_3	C_4	C_{f3}	C_{f4}
538 V	566 V	1 Ω	0.17 Ω	0.23 Ω	11.5 nF	20.5 nF	0.5 nF	0.5 nF

The circuit in Figure 2.25 has been simulated at the maximum coupling condition k=k_{max}=0.182 and at k=$\frac{k_{max}}{2}$=0.091, which operating waveforms are shown in Figure 2.27(a) and Figure 2.27(b), respectively. In the two operating points, the switching frequency f_{sw}, V_{in}, and V_{out} are kept fixed at the values specified in Table 2.12. It is possible to notice that the output power stays nearly constant when k is decreased. This response can be optimized further by re-tuning the circuit parameters. According to the current waveforms I_{L2} and I_{Lf4}, the double-sided LCC would carry most of the power at k=k_{max} as expected from the initial design. On the other hand, when the coils are misaligned, the current output from the double-sided LCC drops, and the S-S compensation will

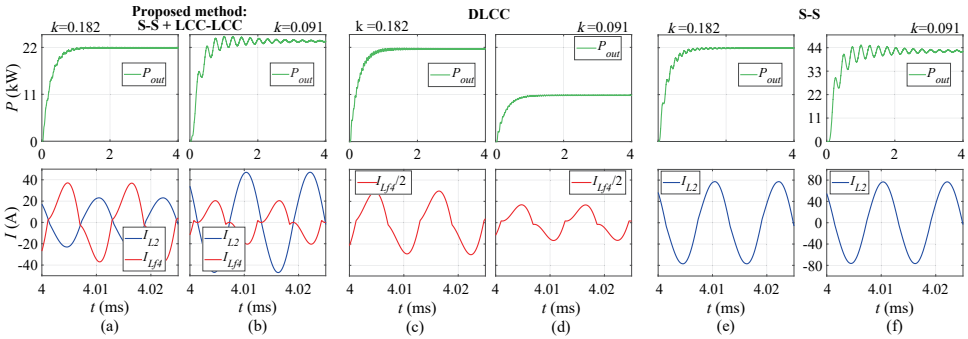

Figure 2.27: Circuit simulations using the parameters in Table 2.12. (a)-(b) Waveforms from the proposed circuit in Figure 2.25, simulated at: (a) k=0.182, (b) k=0.091. (c)-(d) Waveforms from the DLCC compensation, simulated at: (c) k=0.182, (d) k=0.091. (e)-(f) Waveforms from the S-S compensation, simulated at: (e) k=0.182, (f) k=0.091. Each system keeps the same f_{sw}, V_{in} and V_{out} over the changes in k.

process most of the power. This is the expected behavior from (2.21) and (2.22). These simulations prove that the proposed circuit can achieve the self-balancing of P_{out} over different coupling conditions.

It is interesting to compare these results with those that would be achieved by operating just a single set of coupled coils L_1 and L_2, compensated by either the DLCC or the S-S network. In both cases, the system would be tuned to deliver 22 kW to the battery load at k=k_{max}. The simulations of the DLCC use the same V_{in} and V_{out} as in Table 2.12. On the other hand, for the S-S compensation network, V_{in}=841 V and V_{out}=860 V have been selected such that the operation at k=k_{max} and P_{out}=22 kW matches the optimum load condition. For k=k_{max} and k=$\frac{k_{max}}{2}$, the operating waveforms of the DLCC compensation are shown in Figure 2.27(c)-(d), while the ones of the S-S compensation are shown in Figure 2.27(e)-(f). As expected from (2.21) and (2.22), it is possible to notice that, in the presence of coil's misalignment and with no changes in V_{in} or f_{sw}, P_{out} increases dramatically when the S-S compensation is used which might not be safe for the IPT system. This could be mitigated by controlling either V_{in} or f_{sw}. However, the size of the DC input capacitor might be too large to ensure that V_{in} varies fast enough for some dynamic EV charging systems. Besides, it might be possible to lower P_{out} by increasing f_{sw} such that more reactive power is circulating in the circuit. Nevertheless, this strategy has limited potential due to the narrow operating frequency band allowed for EV wireless charging (79-90 kHz). On the other hand, the system is inherently safe with the DLCC compensation since P_{out} drops with the coils' misalignment. However, in this case, the demand of P_{out} cannot be met, leading to longer charging times.

Finally, the features of the proposed circuit in Figure 2.25 for the self-balancing of the output power in EV wireless charging systems are summarized in Table 2.13.

Table 2.13: Advantages and disadvantages of the proposed system in Figure 2.25.

Advantages	Disadvantages
Self-balancing of P_{out} over changes of k	Need of two rectifying stages
Simplification of the control strategy	Need for multicoil pads
No need for communication	Need for two compensation networks
Double sided-LCC do not require the full-power rating	Cross-coupling at some coils' alignments

2.7. CONCLUSION

Compensation networks are fundamental parts of an IPT system. Together with the loosely coupled transformer (LCT), these form a resonant circuit with a specific power transfer behavior over the misalignment, components' voltage and current stress, and power transfer efficiency. Additionally, the chosen compensation network influences the selection of the high-frequency inverting and rectifying power stages. Therefore, it is essential to model and analyze the most common compensation networks to understand their features and, ultimately, to design a suitable IPT system for a specific application.

Section 2.1 explains the differences between the voltage source and the current source high-frequency inverting and rectifying converters. The voltage source topologies are preferable since they have soft-switching capability and they can allow a bidirectional power transfer. Additionally, it has been found that in IPT systems, it is more suitable to model the LCT with the mutual inductance M-model in Figure 2.4(a), meaning that the compensation networks are tuned based on the self-inductances of the LCT. In the M-model, the influence of the coils' coupling is represented as a current-controlled voltage source.

The compensation networks employing only one component, being a capacitor, have been analyzed in Section 2.2. As shown in Figure 2.8, the output of the one-component compensation networks has either a load-independent voltage or current output, which is inversely dependent on the magnetic coupling. A design guideline on the coil's quality factor has been proposed in Section 2.3 that ensures that the optimum load condition and the bifurcation-free operation are achieved at the target output power. Among the one-component compensation networks, the series-series (S-S) compensation is the most suitable for EV wireless charging since the tuning of the compensation capacitors is dependent on neither the load nor the magnetic coupling. Moreover, the S-S compensation requires a voltage source H-bridge inverter, which means that the ZVS turn-on can be achieved. The S-S compensation also allows the direct connection to a battery load since it has a load-independent output current, which is particularly important in EV wireless charging. Even though the S-S is commonly used in the literature, the choice of the IPT system's parameters is not obvious. Given a resonant frequency, infinite combinations of inductance and capacitance resonate at that frequency. Section 2.4 proposes a generalized method to choose the parameters of an IPT system with S-S compensation. The first parameter to be selected is the target mutual inductance of the LCT, which can be computed from the given conditions, such as the DC input and output voltage, the nominal output power, and the resonant frequency. For selecting the resonant circuit parameters, the design condition defined in Section 2.3 is used while ensuring that the optimum load condition coincides with the equivalent resistive load. However, the specific values depend on the LCT's physical configuration: the planar coils' area, structure, and distance between them. Based on those, the coils' quality and the coupling factors can be found, resulting in the values of the self-inductance and the series compensation.

Multiple passive components can be used in the compensation networks. The most common arrangements of the multi-component compensation networks are discussed in Section 2.5. For example, the LC compensation is a development of the one-component parallel compensation, in which the inductor has been shifted from the DC link to the resonant circuit. This compensation results in the well-known LCL resonant circuit.

The main benefit is the possibility of adopting a voltage source power conversion stage, which is not the case with parallel compensation. In the case of the double-sided LC (DLC) compensation, the output current is load-independent and directly proportional to the mutual inductance. This means that the DLC compensation is safe with respect to the misalignment, which is not the case with the S-S compensation. However, the tuning of the LC compensation based on the T-type circuit in Figure 2.23 still depends on the parameters of the LCT, where the compensation inductor has to be equal to the self-inductance of the coupled coil. To overcome these issues, the double-sided LCC (DLCC) compensation is commonly employed in which an extra capacitor is connected in series with the coupled coils. The parameters' tuning of the DLCC is still based on the T-type circuit in Figure 2.23. Similarly to the DLC, the DLCC compensation has a load-independent output current which is directly proportional to the mutual inductance. However, in the case of the DLCC, the compensation inductance is smaller than the LCT's self-inductance, and the amount of the nominal transferred output power depends on the values of the compensation inductors, which means that it is not limited by the LCT.

All in all, the S-S and the DLCC are the most common compensation networks used in EV wireless charging applications. Both compensations can be directly powered by a voltage source H-bridge inverter with soft-switching capability, and they have a load-independent output current. Since the S-S compensation employs the least number of components, it can potentially reach the highest power transfer efficiency. However, its output current is inversely dependent on the coils' mutual inductance, which might be unsafe for the IPT system, especially in applications in which the mutual inductance changes in a large range, e.g., in dynamic EV wireless charging. Moreover, its power transfer characteristic is directly dependent on the LCT based on the relationship described by (2.14). This means that, given the input constraints of the IPT system, it might not be possible to deliver the target output power. This is likely the case when the LCT has not been appositely designed, resulting in a nominal mutual inductance far from the target computed in (2.14). Even though the DLCC compensation can theoretically reach lower power transfer efficiencies, its power transfer capability is not limited by the LCT, and the nominal output power delivered by the IPT system can be advantageously selected by tuning the compensation inductances. Moreover, the load-independent output current in the DLCC compensation is directly dependent on the coils' mutual inductance resulting in an intrinsically safe IPT system over the misalignment. For this reason, it is convenient to employ the DLCC compensation in applications where the coils' mutual inductance varies in a large range, simplifying the circuit protections.

Finally, the concept of hybrid compensation networks has been preliminary investigated and proved through circuit simulations in Section 2.6. These employ both the S-S and DLCC compensations taking advantage of the fact that their load-independent output current has opposite dependence with respect to the coils' mutual inductance. Therefore, the hybrid compensation networks constitute IPT systems with a self-balancing output power over the coils' misalignment.

REFERENCES

[1] *J2954 (r) wireless power transfer for light-duty plug-in/ electric vehicles and alignment methodology*, Oct. 2020.

[2] W. Zhang and C. C. Mi, "Compensation topologies of high-power wireless power transfer systems", *IEEE Transactions on Vehicular Technology*, vol. 65, no. 6, pp. 4768–4778, 2016.

[3] F. Grazian, P. van Duijsen, T. B. Soeiro, and P. Bauer, "Advantages and tuning of zero voltage switching in a wireless power transfer system", in *2019 IEEE PELS Workshop on Emerging Technologies: Wireless Power Transfer (WoW)*, 2019, pp. 367–372.

[4] Y. Wang, Y. Yao, X. Liu, D. Xu, and L. Cai, "An lc/s compensation topology and coil design technique for wireless power transfer", *IEEE Transactions on Power Electronics*, vol. 33, pp. 2007–2025, 2018.

[5] R. L. Steigerwald, "A comparison of half-bridge resonant converter topologies", *IEEE Trans. Power Electron.*, vol. 3, no. 2, 1988.

[6] C.-S. Wang, G. Covic, and O. Stielau, "General stability criterions for zero phase angle controlled loosely coupled inductive power transfer systems", in *27th Annual Conference of the IEEE Industrial Electronics Society (IECON)*, 2001.

[7] S. Chopra and P. Bauer, "Analysis and design considerations for a contactless power transfer system", in *IEEE 33rd International Telecommunications Energy Conference (INTELEC)*, 2011.

[8] S. Li, W. Li, J. Deng, T. D. Nguyen, and C. C. Mi, "A double-sided lcc compensation network and its tuning method for wireless power transfer", *IEEE Transactions on Vehicular Technology*, vol. 64, pp. 2261–2273, 2015.

[9] O. H. Stielau and G. A. Covic, "Design of loosely coupled inductive power transfer systems", in *PowerCon 2000. 2000 International Conference on Power System Technology. Proceedings (Cat. No.00EX409)*, vol. 1, 2000, 85–90 vol.1.

[10] C.-S. Wang, G. Covic, and O. Stielau, "Power transfer capability and bifurcation phenomena of loosely coupled inductive power transfer systems", *IEEE Transactions on Industrial Electronics*, vol. 51, pp. 148–157, 2004.

[11] C.-S. Wang, O. H. Stielau, and G. A. Covic, "Design considerations for a contactless electric vehicle battery charger", *IEEE Transactions on Industrial Electronics*, vol. 52, no. 5, pp. 1308–1314, 2005.

[12] M. Iordache, L. Mandache, D. Niculae, and L. Iordache, "On exact circuit analysis of frequency splitting and bifurcation phenomena in wireless power transfer systems", in *2015 International Symposium on Signals, Circuits and Systems (ISSCS)*, 2015, pp. 1–4.

[13] S. Liu, Y. Shen, Y. Wu, J. Lin, and M. Hu, "Study on frequency tracking for wireless power transfer system using magnetic resonant coupling", in *2018 13th IEEE Conference on Industrial Electronics and Applications (ICIEA)*, 2018, pp. 2569–2572.

[14] W. Zhang, S.-C. Wong, C. K. Tse, and Q. Chen, "Analysis and comparison of secondary series- and parallel-compensated inductive power transfer systems operating for optimal efficiency and load-independent voltage-transfer ratio", *IEEE Transactions on Power Electronics*, vol. 29, pp. 2979–2990, 2014.

[15] S. Bandyopadhyay, P. Venugopal, J. Dong, and P. Bauer, "Comparison of magnetic couplers for ipt-based ev charging using multi-objective optimization", *IEEE Transactions on Vehicular Technology*, vol. 68, no. 6, pp. 5416–5429, 2019. DOI: 10.1109/TVT.2019.2909566.

[16] J. Hou, Q. Chen, X. Ren, X. Ruan, S.-C. Wong, and C. K. Tse, "Precise characteristics analysis of series/series-parallel compensated contactless resonant converter", *IEEE Journal of Emerging and Selected Topics in Power Electronics*, vol. 3, pp. 101–110, 2015.

[17] R. Bosshard, J. W. Kolar, and B. Wunsch, "Control method for inductive power transfer with high partial-load efficiency and resonance tracking", in *2014 International Power Electronics Conference (IPEC-Hiroshima 2014 - ECCE ASIA)*, 2014, pp. 2167–2174. DOI: 10.1109/IPEC.2014.6869889.

[18] W. Shi, J. Dong, S. Bandyopadhyay, F. Grazian, T. B. Soeiro, and P. Bauer, "Comparative study of foreign object and misalignment in inductive power transfer systems", in *45th Annual Conference of the IEEE Industrial Electronics Society (IECON)*, 2019.

[19] F. Grazian, W. Shi, T. B. Soeiro, J. Dong, P. van Duijsen, and P. Bauer, "Quality factor based design guideline for optimized inductive power transfer", in *2020 IEEE PELS Workshop on Emerging Technologies: Wireless Power Transfer (WoW)*, 2020, pp. 178–183. DOI: 10.1109/WoW47795.2020.9291261.

[20] F. Grazian, W. Shi, J. Dong, P. van Duijsen, T. B. Soeiro, and P. Bauer, "Survey on standards and regulations for wireless charging of electric vehicles", in *AEIT International Conference of Electrical and Electronic Technologies for Automotive (AEIT AUTOMOTIVE)*, 2019.

[21] R. Bosshard, J. W. Kolar, J. M. and Ivica Stevanovic, B. Wunsch, and F. Canales, "Modeling and η-α-pareto optimization of inductive power transfer coils for electric vehicles", *IEEE Journal of Emerging and Selected Topics in Power Electronics*, vol. 3, pp. 50–64, 2015.

[22] F. Grazian, W. Shi, T. B. Soeiro, J. Dong, and P. Bauer, "Electric vehicle charging based on inductive power transfer employing variable compensation capacitance for optimum load matching", in *IECON 2020 The 46th Annual Conference of the IEEE Industrial Electronics Society*, 2020, pp. 5262–5267. DOI: 10.1109/IECON43393.2020.9254920.

[23] W. Shi, F. Grazian, J. Dong, T. B. Soeiro, and P. Bauer, "Analysis of magnetic field emissions in inductive power transfer ev chargers following reference designs in sae j2954/2019", in *2020 IEEE International Symposium on Circuits and Systems (ISCAS)*, 2020, pp. 1–5.

[24] C.-S. Wang, G. A. Covic, and O. H. Stielau, "Investigating an lcl load resonant inverter for inductive power transfer applications", *IEEE Transactions on Power Electronics*, vol. 19, pp. 995–1002, 2004.

[25] Y. Su, C. Tang, S. Wu, and Y. Sun, "Research of lcl resonant inverter in wireless power transfer system", in *International Conference on Power System Technology*, 2006.

[26] J. Zhou, F. Wu, R. Zhang, and X. Dai, "Design and analysis of the lcl resonant convertor in inductive power transfer system", in *International Power Electronics and Application Conference and Exposition*, 2014.

[27] Q. Zhu, L. Wang, Y. Guo, C. Liao, and F. Li, "Applying lcc compensation network to dynamic wireless ev charging system", *IEEE Transactions on Industrial Electronics*, vol. 63, no. 10, pp. 6557–6567, 2016. DOI: 10.1109/TIE.2016.2529561.

[28] N. Keeling, G. A. Covic, F. Hao, L. George, and J. T. Boys, "Variable tuning in lcl compensated contactless power transfer pickups", in *2009 IEEE Energy Conversion Congress and Exposition*, 2009, pp. 1826–1832. DOI: 10.1109/ECCE.2009.5316169.

[29] N. A. Keeling, G. A. Covic, and J. T. Boys, "A unity-power-factor ipt pickup for high-power applications", *IEEE Transactions on Industrial Electronics*, vol. 57, pp. 744–751, 2010.

[30] H. H. Wu, A. Gilchrist, K. D. Sealy, and D. Bronson, "A high efficiency 5 kw inductive charger for evs using dual side control", *IEEE Transactions on Industrial Informatics*, vol. 8, pp. 585–595, 2012.

[31] J. Hou, Q. Chen, S.-C. Wong, C. K. Tse, and X. Ruan, "Analysis and control of series/series-parallel compensated resonant converter for contactless power transfer", *IEEE Journal of Emerging and Selected Topics in Power Electronics*, vol. 3, no. 1, pp. 124–136, 2015. DOI: 10.1109/JESTPE.2014.2336811.

[32] J. L. Villa, J. Sallan, J. F. S. Osorio, and A. Llombart, "High-misalignment tolerant compensation topology for icpt systems", *IEEE Transactions on Industrial Electronics*, vol. 59, pp. 945–951, 2012.

[33] L. Zhao, D. J. Thrimawithana, and U. K. Madawala, "Hybrid bidirectional wireless ev charging system tolerant to pad misalignment", *IEEE Transactions on Industrial Electronics*, vol. 64, no. 9, pp. 7079–7086, 2017. DOI: 10.1109/TIE.2017.2686301.

[34] L. Zhao, S. Ruddell, D. J. Thrimawithana, U. K. Madawala, and P. A. Hu, "A hybrid wireless charging system with ddq pads for dynamic charging of evs", in *2017 IEEE PELS Workshop on Emerging Technologies: Wireless Power Transfer (WoW)*, 2017, pp. 1–6. DOI: 10.1109/WoW.2017.7959397.

[35] L. Zhao, D. J. Thrimawithana, U. K. Madawala, A. P. Hu, and C. C. Mi, "A misalignment-tolerant series-hybrid wireless ev charging system with integrated magnetics", *IEEE Transactions on Power Electronics*, vol. 34, no. 2, pp. 1276–1285, 2019. DOI: 10.1109/TPEL.2018.2828841.

[36] X. Qu, Y. Yao, D. Wang, S. Wong, and C. K. Tse, "A family of hybrid ipt topologies with near load-independent output and high tolerance to pad misalignment", *IEEE Transactions on Power Electronics*, vol. 35, no. 7, pp. 6867–6877, 2020. DOI: 10.1109/TPEL.2019.2955299.

[37] B. Yang, Y. Chen, W. Ruan, H. Liu, Y. Ren, and R. Mai, "Current stress optimization for double-sided clllc topology-based ipt system with constant output current tolerating pad misalignments", *IEEE Transactions on Industry Applications*, vol. 58, no. 1, pp. 1032–1043, 2022. DOI: 10.1109/TIA.2021.3125281.

[38] Z. Liu, Q. Zhu, M. Su, and P. A. Hu, "A wireless selective frequency hybrid compensation network with constant power profile against pad misalignment", in *2020 IEEE PELS Workshop on Emerging Technologies: Wireless Power Transfer (WoW)*, 2020.

[39] Z. Liu, M. Su, Q. Zhu, L. Zhao, and A. P. Hu, "A dual frequency tuning method for improved coupling tolerance of wireless power transfer system", *IEEE Transactions on Power Electronics*, vol. 36, no. 7, pp. 7360–7365, 2021. DOI: 10.1109/TPEL.2020.3043784.

[40] W. Shi, J. Dong, T. B. Soeiro, *et al.*, "Design of a highly efficient 20-kw inductive power transfer system with improved misalignment performance", *IEEE Transactions on Transportation Electrification*, vol. 8, no. 2, pp. 2384–2399, 2022. DOI: 10.1109/TTE.2021.3133759.

PART II
VARIABLE COMPENSATION

3

CONSTANT OPTIMUM LOAD CHARGING STRATEGY THROUGH VARIABLE COMPENSATION

Wireless charging must be highly efficient throughout the entire battery charging profile to compete in the electric vehicle (EV) industry. Thus, optimum load matching is commonly used: it operates at the equivalent load that maximizes the efficiency, which depends on the coil's alignment. In this chapter, the optimum load condition is made independent of the coils' position by changing the system's resonant frequency through switch-control capacitors (SCCs). This eliminates the need for load-side voltage control. The output current follows the battery voltage rise during the battery charging cycle always to match the optimum load, which can be achieved by regulating the input voltage via the power factor correction converter. This method is called here constant optimum load (COL). Two SCC topologies have been implemented in a 3.7kW hardware demonstrator. The one implementing the half-wave modulation achieves higher efficiency than the one employing full-wave modulation, with 96.30% at 3.2kW and aligned coils. When misalignment occurs, the half-wave modulation technique results in higher efficiency than the conventional-fixed compensation, where the efficiency is lower by up to 0.68% at partial load. Moreover, the SCCs' impact on the measured coils' current distortion has been analyzed up to 30MHz by computing the fast Fourier transform (FFT) compared to the distortion resulting from

---

This chapter is based on:

- F. Grazian, T. B. Soeiro, P. Bauer, "Inductive Power Transfer based on Variable Compensation Capacitance to Achieve an EV Charging Profile with Constant Optimum Load", in *IEEE Journal of Emerging and Selected Topics in Power Electronics*, vol. 11, no. 1, pp. 1230-1244, Feb. 2023.
- F. Grazian, T. B. Soeiro, P. Bauer, "Coils' Current Distortion Due to Variable Series Compensation Capacitance in EV Wireless Charging for a Constant Optimum Load", *2022 Wireless Power Week (WPW)*, pp. 54-59.

the conventional series-series compensation with fixed capacitance. The SCCs using the half-wave modulation result in the highest total-lumped distortion. However, the individual amplitudes corresponding to the critical frequencies of the radiated magnetic field's limit from SAE J2954 are comparable to or lower than those resulting from the other implementations. Finally, the radiated magnetic field resulting from each strategy has been evaluated using the finite element method. All results are well within the SAE J2954 recommended limits at 10 m. Moreover, a minimum distance of 25 cm from the outer sides of the coupled coils ensures safe exposure to both the general public and implanted medical devices according to the ICNIRP reference levels. Based on these results, the proposed COL method is proved suitable for 3.7kW EV-static wireless charging achieving one of the highest peak efficiencies listed in today's literature for the same power class.

3.1. INTRODUCTION

3.1.1. OPTIMUM LOAD IMPEDANCE MATCHING

During the charging process, it is fundamental to maximize the power transfer efficiency while the control strategy follows the conventional EV battery charging profile consisting of the constant current (CC) and the constant voltage (CV) modes. As explained in Section 2.2.2, the maximum efficiency can be achieved by operating at the optimum load condition. This means that the equivalent resistive load R_{ac} must satisfy R_{ac}=$R_{ac,opt}$, where $R_{ac,opt}$ is the equivalent optimum load. According to Table 2.5, the value of $R_{ac,opt}$ is directly proportional to the coils' coupling factor k. This means that, when the coils' position varies, the condition $R_{ac,opt}$ would also change. Furthermore, during the CC and CV battery charging modes, the equivalent resistive load R_{ac} varies continuously, meaning that the condition R_{ac}=$R_{ac,opt}$ would be met only in one operating point.

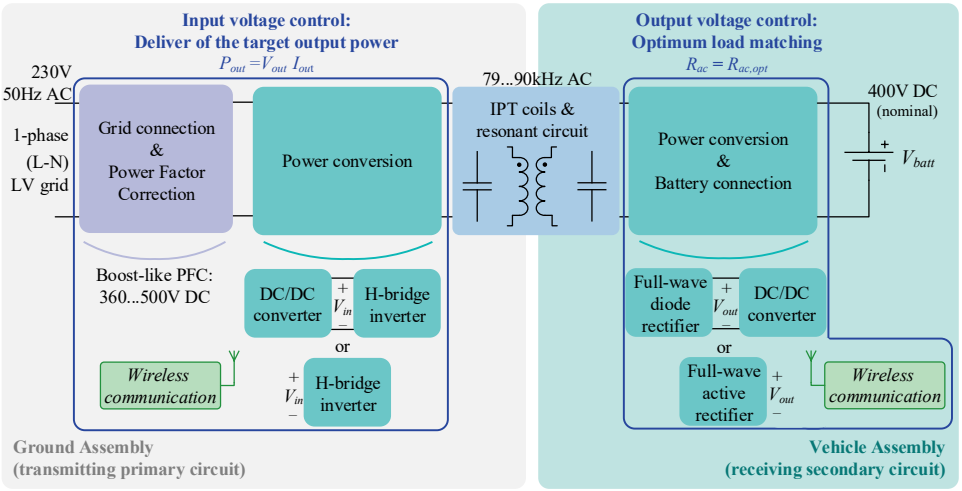

Figure 3.1: Measured peak DC-to-DC efficiency $\eta_{\text{DC-to-DC}}$ of this work compared to the available literature with the same J2954-based EV charger power class (WPT1=3.7 kVA maximum input [1]).

The optimum load impedance matching defined in [2] and [3] has been widely adopted to control the power flow [4]–[12]. This strategy sets the operation at the equivalent optimum load while delivering the target output power set by the battery charging profile. This control strategy of the power flow is achieved by regulating both the input and the output voltages of the IPT system. The voltage regulation might have different implementations, as qualitatively shown in Figure 3.1. The condition R_{ac}=$R_{ac,opt}$=$\frac{8}{\pi^2}\frac{V_{out}}{I_{out}}$ must be valid for a certain amount of process power P_{out}=$V_{out}\cdot I_{out}$. When considering IPT systems using the S-S compensation, the output voltage control gives controllability on V_{out}. In contrast, the input voltage control is used to regulate I_{out} since $I_{out} \propto V_{in}$ (see (3.7)). In this way, the conditions on R_{ac} and P_{out} can be met simultaneously.

The output voltage control in [5], [7]–[9] is implemented through a post-regulating DC/DC converter. For what concerns the input voltage control, [4] and [9] use a boost-type power factor correction (PFC) rectifier while [5] and [8] use an additional DC/DC converter. Undoubtedly, those auxiliary power converter stages introduce extra losses that would worsen the system's overall efficiency in some operating ranges. Since the battery voltage increases during one charging cycle, the voltage regulation at both the input and output must always be active. Consequently, the losses introduced by these converters are not negligible when accounting for the entire charging process. On the other hand, [6] performs the optimum load matching through the phase-shift modulation of both the high-frequency H-bridge inverter and rectifier. However, the switching losses become considerable in some operating conditions. To achieve the zero voltage switching (ZVS) in the whole operating range, [11] uses the asymmetrical phase-shift modulation for both H-bridge converters. Moreover, the circulating reactive power is minimized by utilizing switch-controlled capacitors (SCCs) as compensation. A flat efficiency is achieved for a wide output power range, but the resulting efficiency is not shown when the coil misalignment occurs. Additionally, [12] uses a semi-active rectifier to match the optimum load as the load varies. At the same time, the amount of reactive power is controlled by employing an SCC as secondary compensation. Thereby, the input voltage is not controlled since minor variations of the coupling factor are considered.

3.1.2. VARIABLE COMPENSATION

The SCC was first introduced by [13] to regulate resonant converters instead of varying the switching frequency. Setting the duty cycle of the SCC's switch makes it possible to change the capacitance in a continuous range. Considering the elevated switching frequencies of IPT systems, the switches of the SCCs consist of semiconductor devices.

Besides in [11] and [12], SCCs have been used in other IPT systems. For instance, they have been utilized to match the resonant frequency with the selected constant operating frequency as the self-inductance of the coils changes in the presence of misalignment [14]–[18]. Additionally, SCCs have been employed as part of IPT systems with high-order compensation networks (such as LCC-LCC and LCC-S) to control the output power [19]–[21]. However, all these works consider relatively low power levels (≤ 500 W). Therefore, the SCC applicability to IPT systems with power levels typical of EV charging has not been proven yet. This might be critical, especially due to the high voltage stress that characterizes the compensation capacitors, translating into the high required blocking voltage from the SCC semiconductors. The requirement for relatively high blocking volt-

age semiconductors is critical for two reasons. First, the typical static losses are larger than in the lower voltage classes [22], and possibly the supply chain is limited for higher blocking voltages, e.g., > 1200 V.

Another possible implementation that can vary the IPT system's compensation continuously employs saturable reactors [23]–[26]. An auxiliary winding is wound around the core, which carries a DC current that can partially saturate the core. This changes the relative permeability of the magnetic material and, consequently, the equivalent compensation inductance. However, the sensitivity of the core's magnetic permeability complicates this implementation.

The compensation capacitance can also be changed in steps, assuming only specific discrete values. For example, in [27]–[29], the capacitance value is varied between two values with AC switches that can assume either the on-state or the off-state to achieve the CC and CV charging modes. Additionally, [30] uses an M × N capacitor matrix to achieve energy encryption when charging multiple EVs. The capacitor matrix consists of relays, and the resonant state can be matched when the operating frequency is adjusted.

3.1.3. SCOPE AND CONTRIBUTIONS

This chapter explains and proves experimentally an efficiency enhancement strategy for EV wireless charging, which consists of making the optimum load invariant of the coils' alignments as preliminary explained in [31]. Hereby, this method is named constant optimum load (COL) charging, which substitutes the conventional CC mode. As shown in the circuit schematic of Figure 3.2(c), the COL charging strategy relies on the input voltage control and employs a series-connected SCC to compensate both the primary and secondary coils.

The main contributions are:

- proof that the proposed COL charging method can be achieved through SCCs and the PFC rectifier for a range of magnetic coupling and battery voltage which is typical or static EV wireless charging while respecting the standardized operating frequency range 79-90 kHz;
- detailed analytical modeling, implementation, and comparison in terms of efficiency of two different SCCs for EV wireless charging, where one implements the full-wave modulation and the other uses the half-wave modulation;
- benchmark of the proposed COL charging with SCCs against the conventional constant current (CC) mode with fixed compensation capacitors where the primary coil current distortion is also analyzed;
- analysis of the coils' current distortion resulting from adopting SCCs with the full-wave modulation and the half-wave modulation, which has been compared to the one resulting from fixed series-connected compensation capacitors.

3.1.4. OUTLINE

The analytical modeling and the overall process of the proposed COL method are explained in Section 3.2, while the implementation is discussed in Section 3.3, resulting in the design of a 3.7 kW laboratory prototype. The experimental results are illustrated and discussed in Section 3.4. Section 3.5 analyzes the measured current distortion resulting from using SCCs. The radiated magnetic field is preliminary evaluated in Section 3.6

through the FEM analysis. Finally, the main conclusions on the proposed COL charging method related to its performance are drawn in Section 3.7.

3.2. CONCEPT OF THE PROPOSED COL CHARGING STRATEGY

This section discusses the analytical modeling of the circuit in Figure 3.2, and it explains the proposed COL charging method compared with the conventional optimum load matching through voltage control.

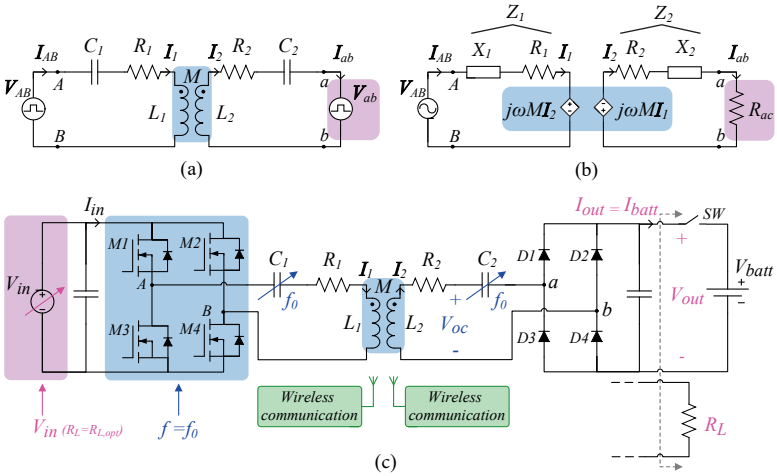

Figure 3.2: Equivalent circuits of the S-S compensation network. Simplified high-frequency circuits based on: (a) the realistic IPT system; (b) the equivalent circuit where M is modeled as a current-controlled voltage source and the load is depicted as the equivalent first-harmonic resistance R_{ac}. (c) Implementation of the proposed constant optimum load (COL) charging method, which concept is shown in Figure 3.5.

3.2.1. ANALYTICAL CIRCUIT MODELING

The equivalent circuit of an EV wireless charging system that uses the S-S compensation network is shown in Figure 3.2. Thereby, L_1 is the primary coil self-inductance, and L_2 is the coil secondary self-inductance of which the magnetic coupling $k=\frac{M}{\sqrt{L_1 L_2}}$ depends on the coils' mutual inductance M. Moreover, C_1 and C_2 are the S-S network's compensation capacitances, and R_1 and R_2 are the lumped series resistances modeling the losses of the primary and the secondary circuits' components. The currents flowing through the primary and secondary circuits are $\boldsymbol{I_{AB}}=\boldsymbol{I_1}$ and $\boldsymbol{I_{ab}}=\boldsymbol{I_2}$, respectively. To match a more realistic configuration of an IPT system, Figure 3.2(a) represents both the input supply $\boldsymbol{V}_{AB}$ and the output load $\boldsymbol{V}_{ab}$ as square-wave voltage sources. On the other hand, Figure 3.2(b) shows a further simplified equivalent circuit based on the M-model explained in Section 2.1.2. This is useful to verify the circuit's performance in a single static operating point in which all voltages and currents are assumed to be sinusoidal waveforms with the fundamental frequency of $\boldsymbol{V}_{AB}$. In this case, the influence of M is represented as current-controlled voltage sources, and the load is depicted as the equivalent resistance R_{ac}. It must be pointed out that M and R_{ac} are likely to vary in IPT systems because the coils' position is not fixed, and the voltage of lithium-ion batteries changes during the charging process as the battery's state-of-charge (SoC) varies.

For a given operation, the voltages and currents of the circuit in Figure 3.2(b) can be found from the Kirchhoff voltage law in (3.1) where $\boldsymbol{V_{AB}}$ is taken as reference such that, according to the phasor convention, $\boldsymbol{V_{AB}}=\hat{V}_{AB}\angle 0°$. According to [32], $\hat{V}_{AB}$ and R_{ac} are defined in (3.2) and (3.3) based on the fundamental component of $\boldsymbol{V_{AB}}$, $\boldsymbol{V_{ab}}$ and $\boldsymbol{I_2}$. Furthermore, the primary and secondary impedances $\boldsymbol{Z_1}$ and $\boldsymbol{Z_2}$ are defined in (3.4).

$$\begin{cases} \boldsymbol{V_{AB}} = \boldsymbol{Z_1 I_1} + j\omega M \boldsymbol{I_2} \\ 0 = (\boldsymbol{Z_2} + R_{ac})\boldsymbol{I_2} + j\omega M \boldsymbol{I_1} \end{cases} \tag{3.1}$$

$$\hat{V}_{AB} = \frac{4}{\pi} V_{in} \tag{3.2}$$

$$R_{ac} = \frac{\boldsymbol{V_{ab}}}{\boldsymbol{I_2}} \approx \frac{8}{\pi^2} R_L \tag{3.3}$$

$$\begin{aligned} \boldsymbol{Z_1} &= R_1 + j\omega X_1, \quad X_1 = \omega L_1 - \frac{1}{\omega C_1} \\ \boldsymbol{Z_2} &= R_2 + j\omega X_2, \quad X_2 = \omega L_2 - \frac{1}{\omega C_2} \end{aligned} \tag{3.4}$$

One of the main challenges in IPT systems used in charging applications is to achieve a highly efficient power transfer at different coupling and load conditions. The power transfer efficiency η_{ac} can be computed from (3.1) resulting in (3.5). The latter is maximized when R_{ac} is equal to the optimum load $R_{ac,opt}$ in (3.6).

$$\eta_{ac} = \frac{R_{ac}|\boldsymbol{I_{ab}}|^2}{V_{AB}\,\mathrm{Re}[\boldsymbol{I_{AB}}]} = \frac{R_{ac}(\omega M)^2}{\mathrm{Re}\left[\dfrac{|(R_{ac}+Z_2)Z_1+(\omega M)^2|^2}{Z_2+R_{ac}}\right]\left((R_{ac}+Z_2)Z_1+(\omega M)^2\right)} \tag{3.5}$$

$$R_{ac,opt} = \underbrace{R_2\sqrt{\frac{(\omega_0 M)^2}{R_2 R_1}+1}}_{\frac{d}{dR_{ac}}(\eta_{ac})\,|_{\omega=\omega_0}=0} \approx \underbrace{\omega_0 M\sqrt{\frac{R_2}{R_1}}}_{\frac{d}{dR_{ac}}\left(\frac{R_1 I_1^2+R_2 I_2^2}{R_{ac} I_{ab}^2}\right)|_{\omega=\omega_0}=0} \tag{3.6}$$

Moreover, if $(\omega_0 M)^2 \gg R_2 R_1$ is valid, $R_{ac,opt}$ corresponds to the equivalent load that minimizes the sum of the primary and secondary circuits' conduction losses with respect to the output power defined in [4]. When R_1 and R_2 are the lump equivalent series resistances modeling the losses of the whole circuit (semiconductors, compensation capacitor, and coil), $R_{ac,opt}$ maximizes the efficiency of the entire system. The respective $R_{L,opt}$ is found by substituting (3.6) into (3.3).

According to (3.6), $R_{ac,opt}$ is directly proportional to the coils' mutual inductance M. This means that, when the coils' position varies, the condition $R_{ac,opt}$ would also change. Furthermore, during the CC and CV battery charging modes, the equivalent resistive load R_{ac} varies continuously, meaning that the condition R_{ac}=$R_{ac,opt}$ would be met only in one operating point. These concerns can be noticed in the battery charging profile shown in Figure 3.3(a), which is based on one measured charging cycle of a Nissan Leaf's battery [33]. Therefore, a control strategy must be adopted to match the optimum load at different coupling and load conditions.

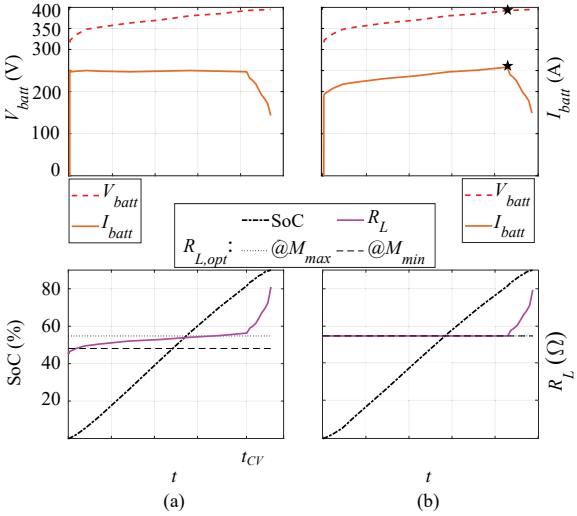

Figure 3.3: Battery charging profile that uses: (a) the traditional CC method; (b) the proposed COL method. This example is based on one measured charging cycle of a Nissan Leaf's battery [33]. Top plots: battery voltage V_{batt} and current I_{batt}. Bottom plots: the battery state of charge or SoC, the equivalent load resistance R_L and the optimum load $R_{L,opt}$ at both the minimum M_{min} and maximum M_{max} mutual inductance values.

3.2.2. TRADITIONAL OPTIMUM LOAD IMPEDANCE MATCHING THROUGH VOLTAGE CONTROL

As explained in Section 3.1.1, the traditional optimum load matching strategy is based on controlling both the input and output voltages. Figure 3.4 shows examples of V_{in} and V_{out} ranges required to achieve optimum load matching during the CC charging mode in Figure 3.3(a) for different M values. The power classes defined by SAE J2954 have been chosen where the specified power level is the maximum allowed from the AC grid connection. Among these, 22 kW is currently under consideration [1]. The power classes in Figure 3.4(a) uses the one-phase (1-ϕ) connection to the European low-voltage 50 Hz grid, while a 3-ϕ grid connection is considered for the power classes in Figure 3.4(b). This choice is due of the fact that households in Europe have limited access to grid connections with more than 16 A for each 230 V phase. This analysis assumes that $\boldsymbol{Z_1}$=$\boldsymbol{Z_2}$=0 when operating at ω=ω_0, and M is computed from (3.7).

$$I_{out} \approx \frac{2}{\pi}\hat{I}_{ab} \approx \frac{8}{\pi^2}\frac{V_{in}}{\omega_0 M} \tag{3.7}$$

Figure 3.4 shows that, in all power classes, the input and output voltages must be continuously controlled to achieve the optimum load matching at different M while following the CC charging mode.

3.2.3. DEFINITION OF THE COL CHARGING METHOD

Instead of varying R_L to always match the M-dependent $R_{L,opt}$, the proposed COL method consists of keeping the value of $R_{L,opt}$ constant over different M by varying the system's resonant frequency f_0=$\frac{\omega_0}{2\pi}$ as qualitatively shown in Figure 3.5. This strategy defines the constant optimum load operation. According to (3.6), this is possible since $R_{ac,opt}$ is di-

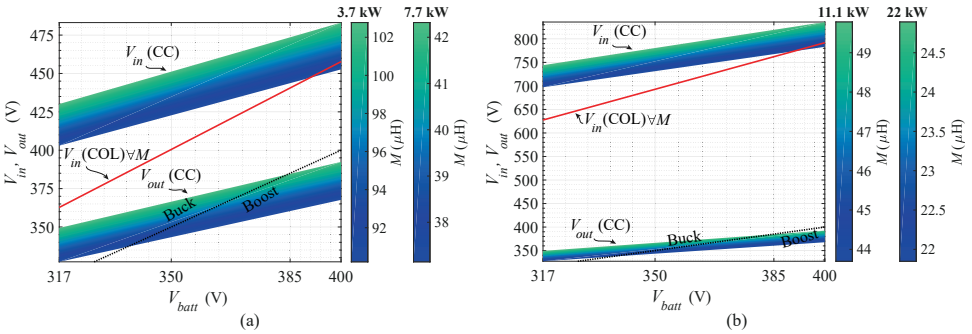

Figure 3.4: Required DC voltages V_{in} and V_{out} from the CC charging and the proposed COL charging methods depending on M for a complete charging cycle of a 400 V EV battery. Example for the power levels of: (a) 3.7 kW (I_{batt}=7 A, t_{CV}=8.1 h) and 7.7 kW (I_{batt}=17 A, t_{CV}=3.4 h); (b) 11.1 kW (I_{batt}=25 A, t_{CV}=2.3 h) and 22 kW (I_{batt}=50 A, t_{CV}=1.2 h). The values of I_{batt} and t_{CV} are defined based on the charging profile in Figure 3.3(a).

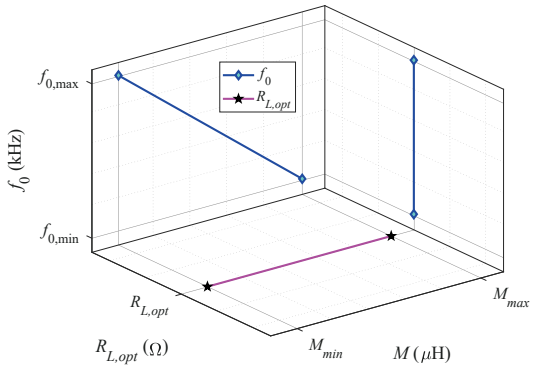

Figure 3.5: Qualitative representation of the proposed COL method over different coils' alignments: the resonant frequency f_0 is varied to keep the optimum load $R_{L,opt}$ fixed over different coils' mutual inductance M. The frequency range from $f_{0,min}$ to $f_{0,max}$ must be within the standardized range 79-90 kHz established for the switching frequency of the IPT inverter bridge.

rectly proportional to both M and ω_0. Figure 3.3(b) shows the proposed battery charging profile. For most of the charging cycle and for the whole range of M=[M_{min} M_{max}], R_L is equal to $R_{L,opt}$ which ensures maximum power transfer efficiency. The proposed COL charging only requires input voltage control, as shown in Figure 3.4. The main advantage is that there is no need for voltage control at the secondary circuit to satisfy R_L=$R_{L,opt}$. This can eliminate one power conversion stage, consequently allowing power loss reduction. It must be noted that standards for static EV wireless charging applications [1] and [34] constrain the range of the H-bridge inverter operating frequency between 79 kHz and 90 kHz limiting the M range covered by the COL implementation as considered in Figure 3.4. However, the following sections will show that the proposed COL concept can be well exploited in the frequency range established by these standards within the charging cycle and misalignment range typical of commercial EVs.

3.2.4. DETAILED COL CHARGING PROCESS

The circuit of the proposed COL method is shown in Figure 3.2(c). The process is summarized in the flowchart of Figure 3.6.

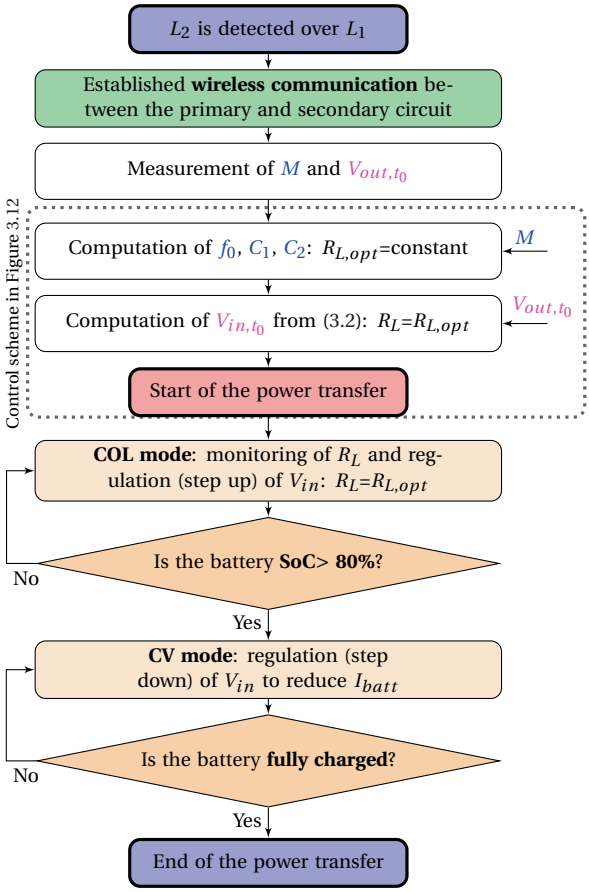

Figure 3.6: Flowchart of the charging process proposed in Section 3.2.4.

BEFORE THE START OF THE POWER TRANSFER

The process starts with the measurement of the coils' mutual inductance M explained in Section 3.3.1. Based on the value of M, the system's resonant frequency f_0=$\omega_0/2\pi$ that keeps $R_{L,opt}$ constant to the value at perfect alignment can be calculated from (3.3) and (3.6). Then, the resulting f_0 can be set by employing one variable compensation capacitor at both the primary and secondary circuits.

In (3.4), the value of C_2 must be selected such that i_2 is slightly capacitive with respect to v_{ab} at f=f_0 to reduce losses due to the reverse recovery (RR) of the rectifier's diodes. At the same time, the reactive power circulating in the secondary circuit must be minimized. This can be achieved by selecting

$$X_2 = R_{ac} \cdot \tan\left[\sin^{-1}\left(\frac{I_{RR}}{\hat{I}_2}\right)\right] \tag{3.8}$$

On the other hand, C_1 must be tuned at f=f_0 such that the inverted current i_1 would lag the inverted voltage v_{AB}, which makes the primary inverter achieving zero voltage

switching (ZVS) turn-on. As explained in Section 2.1.1, to minimize the reactive power in the primary circuit, the inverter's turn-off current I_{OFF} must be slightly larger than the minimum value given in (3.9) that ensures ZVS turn-on of the opposite leg by completely discharging the MOSFETs' drain-source capacitance C_{ds} during the dead time t_{dead}. In (3.9), it is assumed that the turn-off current I_{OFF} is constant. However, due to the resonant characteristic of the S-S compensation, I_{OFF} likely has a sinusoidal shape. This means that I_{OFF} should be larger than $I_{OFF,min}$. A safety margin $s_m > 1$ can be taken into account depending on the selected MOSFETs, such that I_{OFF}=$s_m \cdot I_{OFF,min}$.

$$I_{OFF,min} \approx \frac{2 \cdot C_{ds} \cdot V_{in,max}}{t_{dead}} \tag{3.9}$$

Therefore,

$$X_1 = R_{in} \cdot \tan\left[\sin^{-1}\left(\frac{I_{OFF}}{\hat{I}_1}\right)\right] \tag{3.10}$$

where R_{in} is the real part of the input impedance $\boldsymbol{Z_{in}}$ in (3.11) which is seen from the source V_{AB} at f=f_0. In (3.11), X_2 has been neglected since it is assumed that $R_{ac} \gg X_2$. The step-by-step computation of (3.10) is explained in [35].

$$\boldsymbol{Z_{in}} = \underbrace{R_1 + \frac{(\omega_0 M)^2}{R_2 + R_{ac}}}_{R_{in}} + j\underbrace{\left(\omega_0 L_1 - \frac{1}{\omega_0 C_1}\right)}_{X_{in}=X_1} \tag{3.11}$$

The resulting C_1 and C_2 can be found from (3.12). After that, the inverter's operating frequency is set at $f \approx f_0$.

$$C_1 = \frac{1}{(\omega_0 L_1 - X_1)\omega_0}, \quad C_2 = \frac{1}{(\omega_0 L_2 - X_2)\omega_0} \tag{3.12}$$

In static wireless charging applications, M stays the same during one charging cycle. Therefore, the measurement of M and the selection of f_0, C_1, C_2 must be performed only once before starting of a new power transfer.

The initial battery voltage V_{out,t_0} is measured and communicated to the primary circuit. The input voltage V_{in,t_0} is regulated according to (3.7) such that the output current I_{out} would generate R_L=$R_{L,opt}$=$\frac{V_{out,t_0}}{I_{out}}$. The control of V_{in} is executed through a boost-type PFC rectifier which can be implemented as explained in [36] and [37]. At this point, the power transfer is started.

DURING THE POWER TRANSFER

The value of R_L is continuously monitored such that V_{in} can be adjusted to keep R_L=$R_{L,opt}$ while V_{out} increases. R_L can be computed by measuring the DC output components for the voltage and current, V_{out} and I_{out}. This is easier to implement than directly monitoring R_{ac} deriving from the high-frequency output variables. Assuming that the diodes are in continuous conduction mode and that the operating frequency is close to the resonant frequency of the secondary circuit, R_{ac} can be derived from (3.3). The proposed COL strategy results in the battery charging profile shown in Figure 3.3(b).

For the considered Nissan Leaf battery [33], the SoC reaches 80% of the full charge, and the standard CV charging phase starts. In particular, I_{batt} is gradually reduced by

lowering V_{in} through the PFC. This last CV charging phase would eventually not operate at the maximum efficiency, but this is acceptable since this time interval only contributes to the last 10% increase of the battery SoC and, according to Figure 3.3, it has a much shorter duration and lower power processing than the COL mode.

3.3. IMPLEMENTATION

The functionality of the wireless charging scheme proposed in Section 3.2 must be proved experimentally. Hereby, the implementation of such a system is explained.

3.3.1. MUTUAL INDUCTANCE MEASUREMENT

Once the secondary coil has been detected by the primary circuit, the coil's mutual inductance M can be estimated as shown in (3.13). This is valid by assuming that the battery is disconnected from the rest of the circuit, which is possible through the mechanical switch SW in Figure 3.2(c).

$$M = \frac{V_{oc}}{\omega_0 I_1} \tag{3.13}$$

Since the system operates at $f=f_0$ by varying the value of C_1, there is no need for measuring the phase angle of V_{oc} and I_1.

3.3.2. SCC AS VARIABLE COMPENSATION CAPACITOR

The variable compensation capacitors of both the primary and the secondary circuits in Figure 3.2(c) are implemented as the SCCs illustrated in Figure 3.7. The SCC was first introduced by [13] to regulate resonant converters instead of varying the switching frequency. According to [13], the SCC has two possible implementations depending on the control strategy chosen for the semiconductor switches which, for the chosen application, are SiC MOSFETs. When the SCC is switched on and off twice during one switching cycle, the control takes the name of full-wave modulation. The typical operating waveform and the switch arrangement are shown in Figure 3.7(a). On the other hand, Figure 3.7(b) shows another possible control strategy called half-wave modulation, where the SCC is switched on and off only once during one switching cycle. Hereby, the series-connected SCC has been selected to limit the maximum voltage stress on the MOSFETs, which is going to be discussed in Section 3.3.4. Both modulations have the control signal synchronized with the current $i_{C_{s1}}$ flowing through the SCC series capacitor C_{s1}. Once the MOSFETs are turned off, that current would start flowing through C_{s2}. At that moment, the voltage across C_{s2} starts rising to reach the maximum when the current equals zero. After that, the current through C_{s2} would assume the opposite sign causing the decrease of $v_{C_{s2}}$. Once $v_{C_{s2}}$ approaches zero, the MOSFETs are turned on again. This operation guarantees the ZVS of the SCCs.

Intuitively, the highest equivalent series capacitance is achieved when the semiconductor switches are always conducting, while the capacitance would be minimum if they are always blocking. Therefore, the equivalent capacitance $C_{s2,eq}$ depends on the on-time t_{on} of the switches, which can be found from (3.14) by computing the fundamental component's amplitude of the voltage $v_{C_{s2}}$. This results in (3.15) for the full-wave modulation and in (3.16) for the half-wave modulation, where x is the duty cycle $x=\frac{t_{on}}{T}=[0...\frac{1}{2}]$.

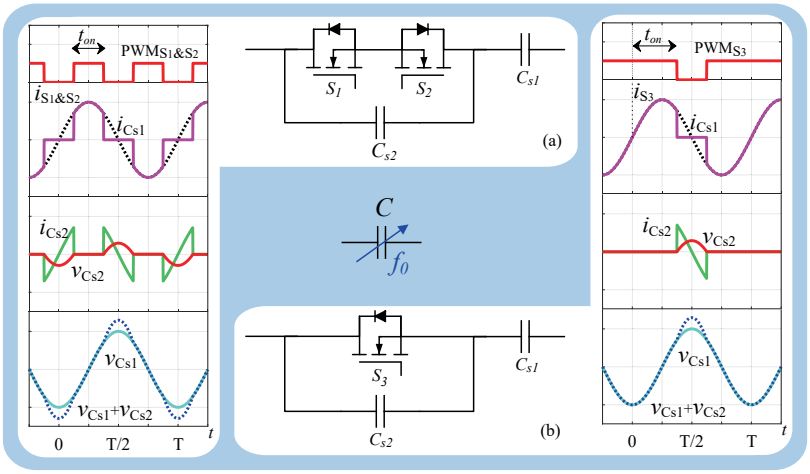

Figure 3.7: Implementation of variable compensation capacitors as SCC with: (a) full-wave and (b) half-wave modulation, where the equivalent capacitance results in (3.15) and in (3.16), respectively.

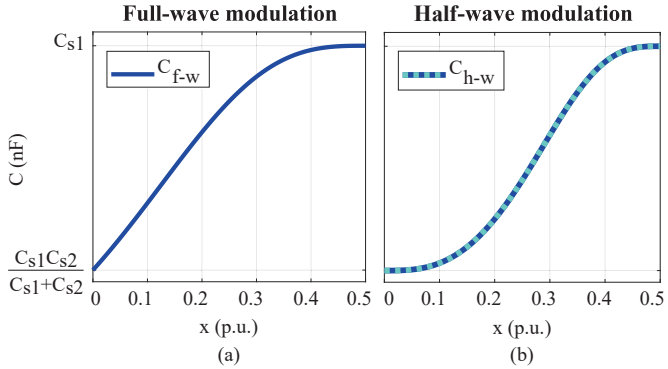

Figure 3.8: Compensation capacitance $C_{\text{f-w}}$ and $C_{\text{h-w}}$ depending on x=$\frac{t_{on}}{T}$ where the SCC uses: (a) full-wave and (b) half-wave modulation.

The capacitance variation of both $C_{\text{f-w}}$ and $C_{\text{h-w}}$ is shown in Figure 3.8 as a function of x. In Section 3.4, the performance of both implementations is evaluated and compared with respect to the proposed COL battery charging method.

$$\left(\hat{V}_{Cs2}\right)_1 = \frac{2}{T}\int_0^T v_{Cs2}(t)\cdot\cos\left(\frac{2\pi}{T}t\right)dt = -\frac{\hat{I}_{Cs1}}{\omega}\frac{1}{C_{s2,eq}} \tag{3.14}$$

$$C_{\text{f-w}} = \frac{1}{\frac{1}{C_{s1}}+\frac{1}{C_{s2,eq}}} = \frac{1}{\frac{1}{C_{s1}}+\frac{1}{C_{s2}}\left(\frac{\pi-2\pi\text{x}-\sin 2\pi\text{x}}{\pi}\right)} \tag{3.15}$$

$$C_{\text{h-w}} = \frac{1}{\frac{1}{C_{s1}}+\frac{1}{C_{s2,eq}}} = \frac{1}{\frac{1}{C_{s1}}+\frac{1}{C_{s2}}\left(\frac{2\pi-4\pi\text{x}+\sin 4\pi\text{x}}{2\pi}\right)} \tag{3.16}$$

Besides the capacitance variation with respect to the duty cycle x, it is interesting to model the losses of the SCC. The switching losses of the SCC can be considered negligible

if the ZVS operation is achieved. The conduction losses directly depend on x since it defines the current conduction path within the SCC. The equivalent resistance of the SCC is described by (3.17) and (3.18) for the full-wave and the half-wave modulation, respectively. Thereby, $\mathrm{ESR}_{C_{s1}}$ and $\mathrm{ESR}_{C_{s2}}$ are the equivalent series resistance of the SCC capacitors, while $R_{ds,on}$ symbolizes the MOSFETs' equivalent on-resistance. Moreover, the coefficients A and B are defined in (3.19) and (3.20), respectively. If $\mathrm{ESR}_{C_{s2}}$ is similar to $R_{ds,on}$, the equivalent resistance of the SCC would be approximately constant over x. Otherwise, the SCC resistance would vary with a similar trend to Figure 3.8.

$$R_{\text{f-w}} = A\left(2\text{x} + \frac{\sin\pi(1-2\text{x})}{\pi}\right) + \mathrm{ESR}_{C_{s2}} + \mathrm{ESR}_{C_{s1}} \tag{3.17}$$

$$R_{\text{h-w}} = B\left(2\text{x} - \frac{\sin 4\pi\text{x}}{2\pi}\right) + \mathrm{ESR}_{C_{s2}} + \mathrm{ESR}_{C_{s1}} \tag{3.18}$$

$$A = R_{ds,on(S_1)} + R_{ds,on(S_2)} - \mathrm{ESR}_{C_{s2}} \tag{3.19}$$

$$B = R_{ds,on(S_3)} - \mathrm{ESR}_{C_{s2}} \tag{3.20}$$

STEP BY STEP COMPUTATION OF (3.17) AND (3.18)

The conduction losses of the two SCC implementations shown in Figure 3.7 are given by the RMS current that flows in each parallel branch of the SCC which depends on the SCC duty cycle x=$\frac{t_{on}}{T}$=[0...0.5]. During one switching period T, the current of the SCC series capacitor $i_{C_{s1}}$ flows through the semiconductor branch of the SCC for the interval 2xT, while it flows through C_{s2} for (1-2x)T. The resulting RMS current of each SCC parallel branch is shown in (3.21) and (3.22) for the full-wave and the half-wave modulations, respectively. As expected, these expressions are functions of $\hat{I}_{C_{s1}}$ and x.

$$\text{f-w}: \begin{cases} I_{C_{s2}} = \hat{I}_{C_{s1}}\sqrt{(\frac{1}{2}-x) - \dfrac{\sin(\pi(1-2\text{x}))}{2\pi}} \\ I_{S_1\&S_2} = \hat{I}_{C_{s1}}\sqrt{x + \dfrac{\sin(\pi(1-2\text{x}))}{2\pi}} \end{cases} \tag{3.21}$$

$$\text{h-w}: \begin{cases} I_{C_{s2}} = \hat{I}_{C_{s1}}\sqrt{(\frac{1}{2}-x) + \dfrac{\sin(4\pi\text{x})}{4\pi}} \\ I_{S_3} = \hat{I}_{C_{s1}}\sqrt{x - \dfrac{\sin(4\pi\text{x})}{4\pi}} \end{cases} \tag{3.22}$$

After that, the conduction loss of the SCC can be calculated as shown in (3.23) and (3.24). From those, the equivalent resistance of the SCC can be computed by isolating $I_{C_{s1}}$ which $R_{\text{f-w}}$ results in (3.17) and $R_{\text{h-w}}$ in (3.18).

$$\begin{aligned} P_{SCC(\text{f-w})} &= \mathrm{ESR}_{C_{s2}} I_{C_{s2}}^2 + (R_{ds,on(S_1)} + R_{ds,on(S_2)}) I_{S_1\&S_2}^2 \\ &= R_{\text{f-w}} I_{C_{s1}}^2 \end{aligned} \tag{3.23}$$

$$\begin{aligned} P_{SCC(\text{h-w})} &= \mathrm{ESR}_{C_{s2}} I_{C_{s2}}^2 + R_{ds,on(S_3)} I_{S_3}^2 \\ &= R_{\text{h-w}} I_{C_{s1}}^2 \end{aligned} \tag{3.24}$$

3.3.3. DESIGN GUIDELINE FOR EV WIRELESS CHARGING SYSTEMS

The design requirements for an EV wireless charging system that operates with the proposed COL method are:

- the range of V_{batt} during one complete charging cycle;
- the maximum $P_{\text{grid,max}}$ that can be drawn from the grid;
- the range of V_{in} available from the PFC;
- the maximum voltage stress $\hat{V}_{C_{s2}}$ allowed by the SCC semiconductor switches.

The battery voltage V_{batt} varies while its SoC increases: V_{batt} ranges from a minimum $V_{batt,\text{min}}$ to a maximum $V_{batt,\text{max}}$. These values are intrinsic to each EV battery.

Assuming that the input reactive power is negligible, the maximum input active power $P_{\text{grid,max}}$ depends on the selected SAE J2954 power class, here being 3.7 kW (WPT1).

When considering the input to be connected to one phase of the European 50 Hz grid, the phase-to-neutral voltage is 230 V RMS with a tolerance of ±10%. Thus, the available range of V_{in} from a boost-like single-phase PFC is > 358 V.

At this point, given the range of V_{batt}, $P_{\text{grid,max}}$, V_{in}, and a preliminary-conservative efficiency η^* assumption, e.g. 92%, measured between the 50 Hz AC connection and the EV battery, the maximum deliverable output current $I_{out,\text{max}}$ can be calculated through (3.25). The latter considers that V_{out}=V_{batt} as shown in Figure 3.2(c). During one battery charging cycle, I_{out}=$I_{out,\text{max}}$ corresponds to the maximum power point of the COL profile, which has been marked with five-pointed stars in Figure 3.3(b).

$$I_{out,\text{max}} = \frac{P_{\text{grid,max}} \cdot \eta^*}{V_{out,\text{max}}} \tag{3.25}$$

The primary and secondary circuits are designed to satisfy all conditions in (3.26).

From the first condition in (3.26), the ratio $\frac{R_1}{R_2}$ is calculated such that V_{in} and V_{out} are within the given ranges. After that, the span of M from which it is possible to keep $R_{L,opt}$ constant is computed by solving the second condition of (3.26), where $I_{out,\text{max}}$ is given in (3.25). For instance, M_{max} is found for ω_0=$\omega_{0,min}$=$2\pi \cdot 79$ kHz, while M_{min} is found for ω_0=$\omega_{0,max}$=$2\pi \cdot 90$ kHz. This target range of M can result from any arrangement of coupled coils. However, the value of L_1, L_2, and k in the third condition must be selected such that the peak voltage stress on the SCC's MOSFET is within the rating of the selected semiconductor switch. This is discussed more in detail in Section 3.3.4.

$$\begin{cases} (3.7) = \dfrac{V_{out,max}}{R_{L,opt}} \rightarrow \sqrt{\dfrac{R_1}{R_2}} = \dfrac{V_{in,max}}{V_{out,max}} \\ R_{L,opt} = \dfrac{V_{out,\text{max}}}{I_{out,\text{max}}} \rightarrow M = \dfrac{8}{\pi^2}\dfrac{1}{\omega_0}\dfrac{V_{out,\text{max}}}{I_{out,\text{max}}}\sqrt{\dfrac{R_1}{R_2}} \quad \text{where:} \\ \qquad\qquad\qquad\qquad\qquad\qquad \omega_0 = 2\pi[79...90]\text{kHz} \\ Q_1 = \dfrac{\omega_0 L_1}{R_1},\ Q_2 = \dfrac{\omega_0 L_2}{R_2} \rightarrow \dfrac{L_1}{L_2} = \dfrac{Q_1}{Q_2}\left(\dfrac{V_{in,max}}{V_{out,max}}\right)^2 \\ kL_1L_2 = M \rightarrow (3.14) : \hat{V}_{C_{s2,1}}, \hat{V}_{C_{s2,2}} < V_{ds,\text{off}(S_1/S_2)} \end{cases} \tag{3.26}$$

3.3.4. PROTOTYPE OF 3.7 KW EV WIRELESS CHARGING SYSTEM

The guideline of Section 3.3.3 has resulted in the circuit parameters and components summarized in Table 3.1. The laboratory prototype is shown in Figure 3.9.

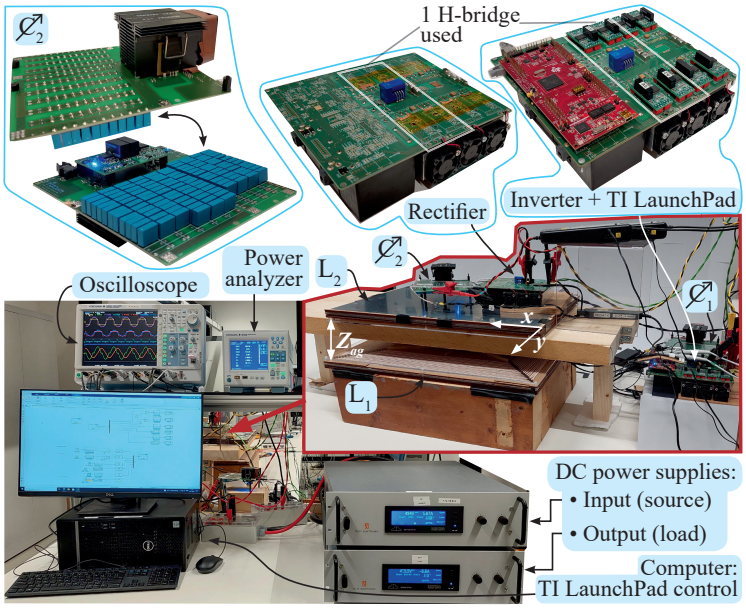

Figure 3.9: Prototype of the 3.7 kW EV wireless charging system.

VARIABLE COMPENSATION CAPACITORS C_1, C_2

To achieve the COL operation at different coil's alignments, f_0 of the IPT system must be varied as shown in Figure 3.5. The value of the passive components must be chosen such that the voltage stress over the SCC's MOSFETs is within its rated value including a safe margin to account for dynamic operating conditions.

Figure 3.10 shows examples of the voltage stress and the values of L_1, L_2, C_{s1} and C_{s2} depending on k for different power levels. The design guidelines in (3.26) have been used assuming that Q_1=Q_2. The peak voltage on C_{s2} has been computed through (3.27) and (3.28) for the two modulations where the primary and secondary currents are calculated through (3.29). Since 1700 V SiC MOSFETs are used in the SCCs, the conservative maximum voltage stress of 1 kV is selected in Figure 3.10 for the steady-state operation to ensure enough safety margin also when transients occur.

$$\hat{V}_{C_{s2},\,\text{f-w}} = \int_{\text{x}\frac{T}{2}+\frac{T}{4}}^{\frac{T}{2}} \frac{\hat{I}_{C_{s1}}}{C_{s2}} \sin\omega t dt = \frac{\hat{I}_{C_{s1}}}{\omega C_{s2}} \left[1+\cos\pi(\frac{1}{2}+\text{x})\right] \tag{3.27}$$

$$\hat{V}_{C_{s2},\,\text{h-w}} = \int_{\text{x}T}^{\frac{T}{2}} \frac{\hat{I}_{C_{s1}}}{C_{s2}} \sin\omega t dt = \frac{\hat{I}_{C_{s1}}}{\omega C_{s2}} (1+\cos 2\pi\text{x}) \tag{3.28}$$

$$\hat{I}_1 \approx \left|\frac{4}{\pi} I_{out} \frac{R_{L,opt}}{\omega_{0,max} M_{min}}\right|, \quad \hat{I}_2 \approx \frac{\pi}{2} I_{out} \tag{3.29}$$

Table 3.1: Circuit parameters and components used in the proposed 3.7 kW EV wireless charging system in Figure 3.9.

Circuit parameters					**Component**	**Function**	**Units**	**Manufacturer**	**Name**
f (kHz)	[79 90]		**Primary**	**Secondary**	1200V SiC MOSFET	Inverter	4	Wolfspeed	C2M0040120D
$P_{\text{grid,max}}$ (kW)	3.7	C_{s1_1}, C_{s1_2} (nF)	13.50	18.57	1200V SiC diode	Rectifier	4		C4D15120D
η^* (%)	92	C_{s2_1}, C_{s2_2} (nF)	28.03	52.08	1700V SiC MOSFET	SCC **	1/2x2		C2M0045170P
V_{in} (V)	[358 510]	L_1, L_2 (μH)	336.90	224.15	6.8nF 500V_{RMS}	C_{s1_1}	11x4	EPCOS	B32671L
V_{batt} (V)	[317 410]	R_{L_1}, R_{L_2} (Ω)	0.75	0.5		C_{s2_1}	6x3		
$R_{L,opt}$ (Ω)	54.8	M (μH)	[102.6 95.4 90.1]			C_{s1_2}	16x4		
Z_{ag} (mm)	105		[M_{max} M_{mid} M_{min}]			C_{s2_2}	11x3		
Misalignment [(x,y,z) mm]		$M_{\text{max}} \rightarrow (0, 0, Z_{ag})$				C_1^{***}	9x4		
		$M_{\text{mid}} \rightarrow [(67, 0, Z_{ag})$ or $(0, 37, Z_{ag})]$				C_2^{***}	11x4		
		$M_{\text{min}} \rightarrow [(82, 0, Z_{ag})$ or $(0, 45, Z_{ag})]$			** h-w/f-w, *** fixed S-S: C_1/C_2=(15.14/18.55)(nF)				
Measuring and supplying equipment		Oscilloscope: YOKOGAWA DLM4058 2.5GS/s 500MHz Power analyzer: YOKOGAWA WT500 Bidirectional DC power supplies: DELTA ELEKTRONIKA SM1500-CP-30 (input), SM500-CP-90 (output)							

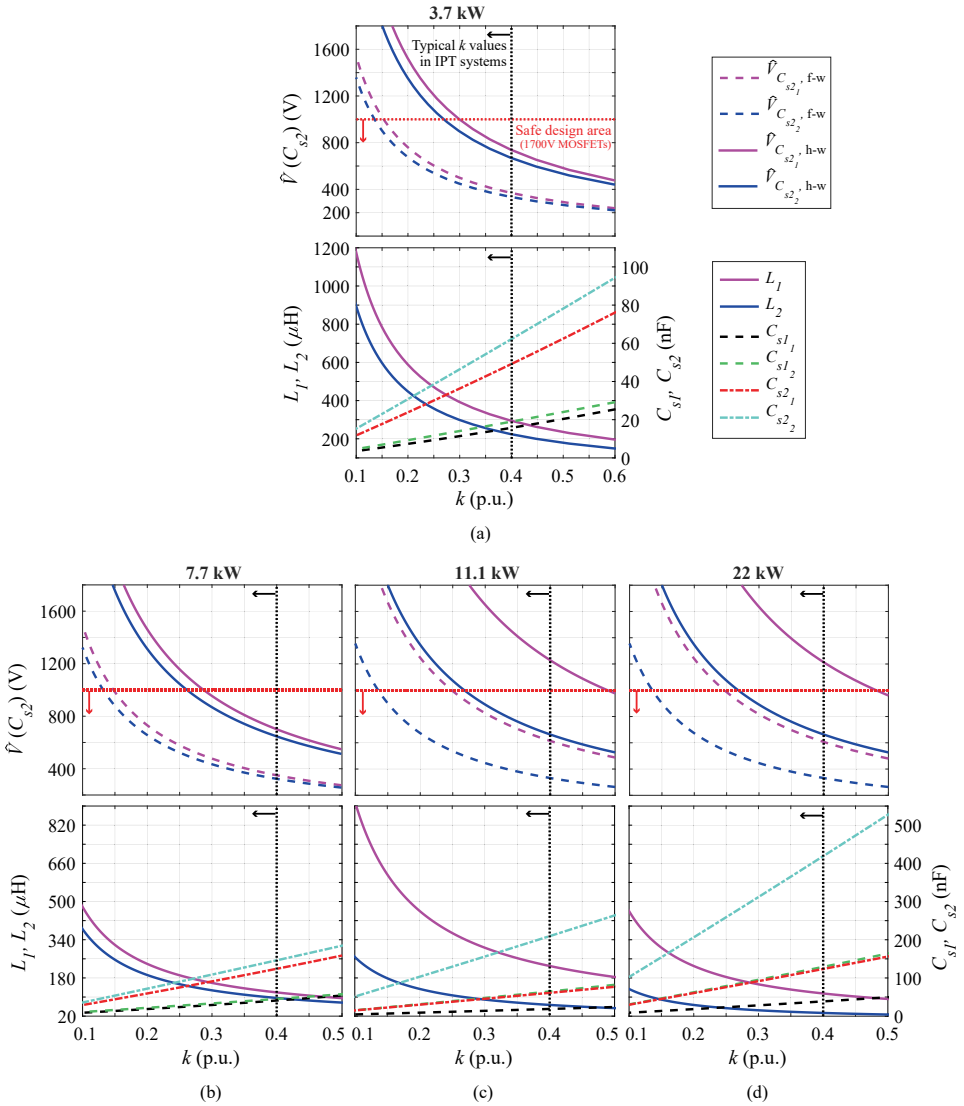

Figure 3.10: Voltage stress across the SCC's MOSFETs, values of L_1, L_2, C_{s1} and C_{s2} depending on k at different power levels: (a) 3.7 kW (I_{batt}=7.48 A, M_{min}=90.1 µH); (b) 7.7 kW (I_{batt}=17 A, M_{min}=37.6 µH); (c) 11.1 kW (I_{batt}=25 A, M_{min}=43.6 µH); and (d) 22 kW (I_{batt}=50 A, M_{min}=21.8 µH).

The values of C_{s1} and C_{s2} have been chosen such that the f_0 variation in the range 79...90 kHz is achievable given L_1 and L_2, and considering that x is fully utilized. For instance, if L is the coils' inductance, the minimum, and maximum needed capacitance can be found from (3.12) as

$$C_{min} = \frac{1}{(\omega_{0,max} L - X) \cdot \omega_{0,max}}$$
$$C_{max} = \frac{1}{(\omega_{0,min} L - X) \cdot \omega_{0,min}} \tag{3.30}$$

Then, C_{s1} and C_{s2} are computed as

$$C_{s1} = C_{max}, \quad C_{s2} = \frac{C_{max} \cdot C_{min}}{C_{max} - C_{min}} \tag{3.31}$$

Based on the resulting voltage stress in Figure 3.10, it is possible to employ SCCs with both modulations for the power levels of 3.7 kW and 7.7 kW. On the other hand, that might not be the case for the two highest power levels. Generally, the full-wave modulation comprehends a wider range of coils' arrangements that would ensure an SCC's voltage stress within the safe area. In particular, if the coupled coils have relatively high k, e.g., $k \approx 0.4$, it might be possible to employ 1200 V SiC MOSFETs for SCCs using the full-wave modulation. The advantages of this choice are discussed in Section 3.4.1.

According to the implemented 3.7 kW prototype shown in Figure 3.9, the resulting variations of C_1 and C_2 are illustrated in Figure 3.11(a) and Figure 3.11(b) by using SCCs with full-wave modulation and half-wave modulation, respectively. Thereby, C_1 and C_2 follow the trend described by (3.15) and (3.16) which depends on SCC's duty cycle x=$\frac{t_{on}}{T}$=[0...0.5]. The validity of these analytical expressions has been proved by measuring the circuit's resonant frequency at different values of x. To prevent the coils' mutual inductance from altering this calculation, the measurements have been executed considering the primary and the secondary circuits separately. Assuming that L_1 and L_2 are known, one can compute the equivalent compensation capacitance from (3.4) by imposing X_1=X_2=0.

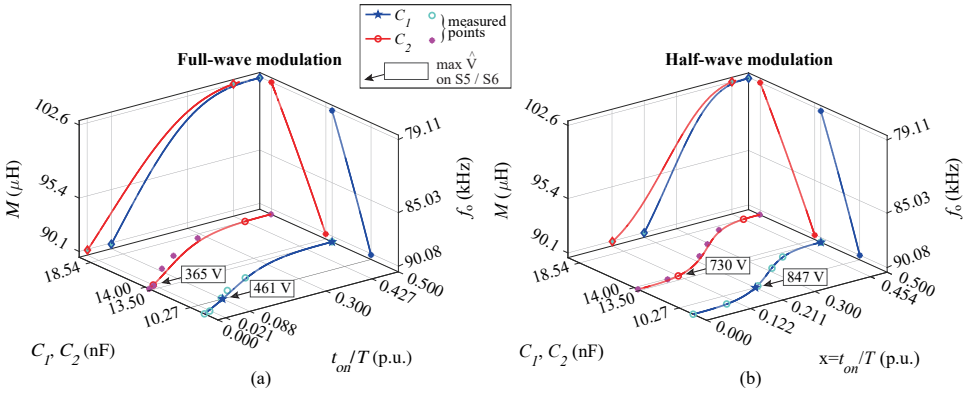

Figure 3.11: Values of C_1 and C_2 by using the SCCs with (a) full-wave and (b) half-wave modulation. Note that the standardized operating frequency range 79-90 kHz established by IPT-based EV charging is satisfied in the current system design.

CONTROL SCHEME FOR V_{in} AND $f_0(C_1,C_2)$

The detailed control scheme is summarized in Figure 3.12. There are two sets of parameters to be regulated in the proposed system. One is the duty cycle of the PFC rectifier D_{PFC} that sets the target V_{in}. The other is the duty cycle of both SCCs, namely x_1 and x_2, establishing the IPT system's resonant frequency f_0. In the prototype of Figure 3.9, the input voltage V_{in} is regulated by a DC power supply which resembles the voltage range that the PFC rectifier could provide. This is reasonable since the PFC rectifier is a necessary power conversion stage for any EV wireless charging system, given that they are

commonly connected to the AC grid. Additionally, the battery behavior is emulated by a bidirectional DC power supply.

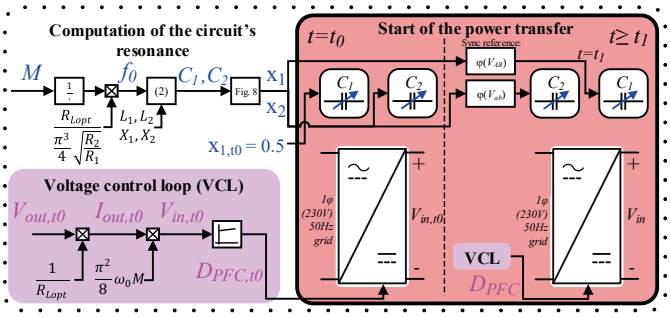

Figure 3.12: Detailed control scheme referring to the charging process in Figure 3.6. In the prototype of Figure 3.9, the operation of the PFC rectifier is modeled by the input DC power supply.

Before the start of the power transfer, the values of x_1, x_2, and $D_{PFC,t0}$ are computed based on the measurements of M, $V_{out,t0}$ and the reference R_{Lopt}.

When the power transfer starts at the instant t=t_0, the operating frequency of the inverter is set to the target f_0 and the input voltage would be $V_{in,t0}$. However, at that instant of time, the duty cycle of the primary SCC assumes the initial value $x_{1,t0}$=0.5 while $x_{2,t0}$=x_2. This results in the operation being in the inductive region of the resonant circuit since C_1 assumes its highest value, which translates into a safe operation for the H-bridge inverter. At the instant t=t_1, x_1 is set for the primary SCC, which control signal is synchronized to the output voltage from the H-bridge inverter V_{AB}. On the other hand, the control signal of the secondary SCC is synchronized with respect to the rectifying H-bridge's input voltage V_{ab}. Assuming that, from (3.8)-(3.11), the phase delay of both the primary and the secondary currents is known, a phase shift can be set to x_1 and x_2 making sure that they are synchronized with the resonant currents, resulting in the ZVS of the SCCs. Measurements based on this proposed start-up scheme can be found in Section 3.4.1.

For the rest of the charging process ($t > t_1$), the same SCC control signals apply. Therefore, the SCC signals must be adjusted only at the beginning of the charging process. On the other hand, D_{PFC} starts from the initial value $D_{PFC,t0}$ and it is continuously modified by the voltage control loop to achieve the COL charging mode in Figure 3.3(b).

3.4. EXPERIMENTAL RESULTS

The proposed COL charging strategy has been experimentally validated for both the SCC implementations based on the laboratory prototype in Figure 3.9. After that, the performance resulting from the SCC half-wave modulation has been compared to the one using conventional S-S compensation with fixed capacitors.

3.4.1. CONSTANT OPTIMUM LOAD METHOD WITH SCCS

MEASURED CIRCUIT WAVEFORMS

Figure 3.13(a)-(b) show the measured waveforms of the proposed COL method at different values of M defined in Table 3.1. Two sets of measurements have been executed to

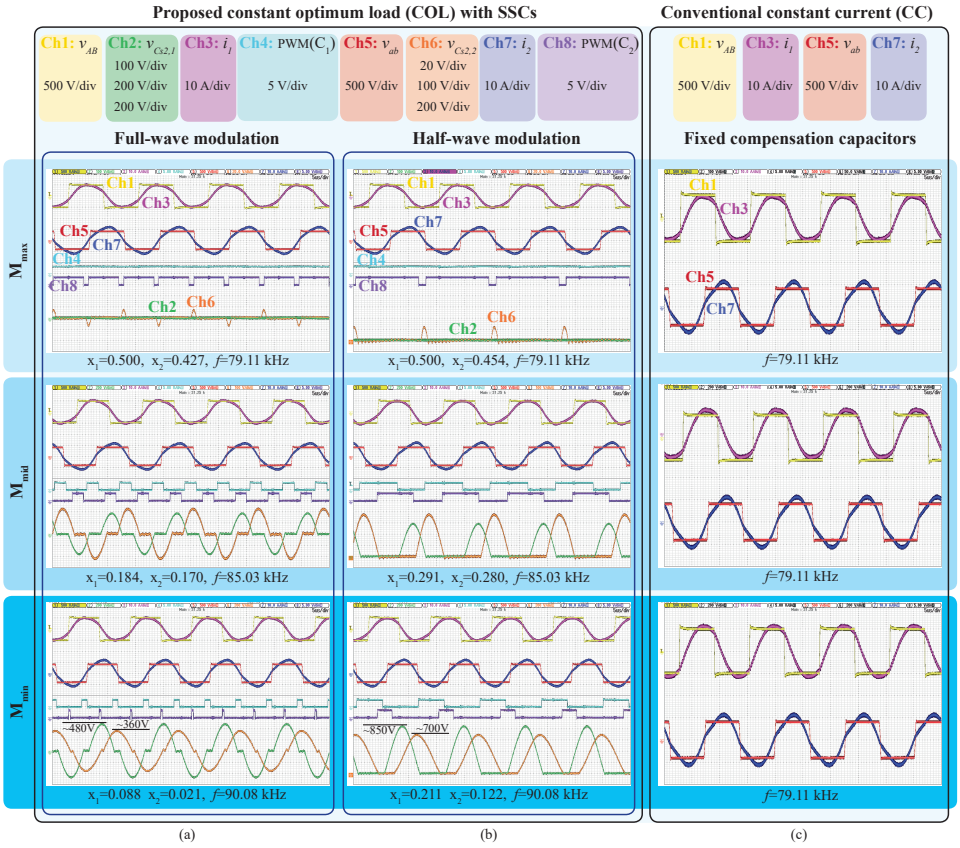

Figure 3.13: Waveforms measured at full power and at different coils' alignments: (a)-(b) result from the proposed COL by using the SCCs with the full-wave and half-wave modulations, respectively; (c) results from the conventional S-S compensation with fixed capacitors.

compare the performance of the two possible SCC implementations illustrated in Figure 3.7. For instance, the measurements in Figure 3.13(a) have been performed while employing SCCs with full-wave modulation. On the other hand, the measurements in Figure 3.13(b) use SCCs with half-wave modulation. As expected, the resonant circuit's input and output waveforms from the two implementations are equivalent for the same operating conditions. The main difference between the two implementations is the voltage $v_{C_{s2}}$ due to the different modulation strategies. As a result, the voltage stress on the MOSFETs of the SCCs with half-wave modulation is about twice the voltage stress of each MOSFET employed in the full-wave modulation. The measured peaks of $\hat{V}_{C_{s2,1}}$ and $\hat{V}_{C_{s2,2}}$ agree with the expected values from the analytical model shown in Figure 3.11.

The worst-case start-up transient following the control strategy illustrated in Figure 3.12 has been measured at V_{batt}=410V as shown in Figure 3.14 and Figure 3.15 for the full-wave and the half-wave modulations, respectively. This operation occurs if the charging cycle starts at full power when the battery's (SoC≈80%). All these measurements have been executed at M=M_{min} since it leads to the highest voltage stress on the

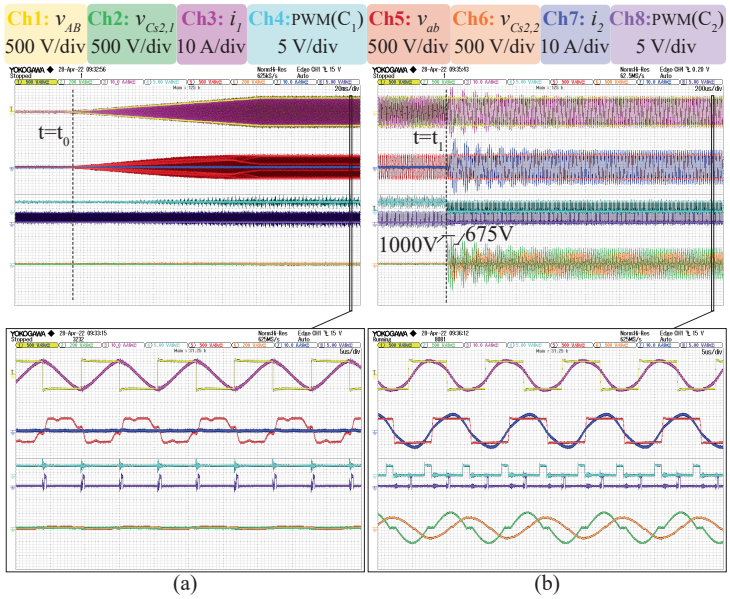

Figure 3.14: Start of the power transfer with SCCs using the full-wave modulation at M=M_{min} and V_{batt}=410V, referring to Figure 3.12. (a) At t=t_0, $V_{in,t0}$ is applied while $x_{1,t0}$=0.5 and x_2=0.021. (b) At t=t_1, x_1=0.088 is applied. The channels are displayed in the same sequence as Figure 3.13.

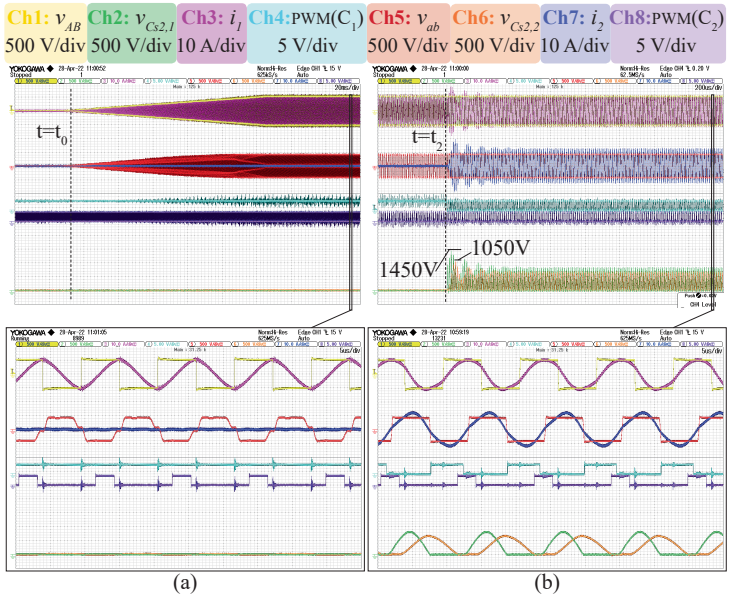

Figure 3.15: Start of the power transfer with SCCs using the half-wave modulation at M=M_{min} and V_{batt}=410V referring to Figure 3.12. (a) At t=t_0, $V_{in,t0}$ is applied while $x_{1,t0}$=0.5 and x_2=0.122. (b) At t=t_1, x_1=0.211 is applied. The channels are displayed in the same sequence as Figure 3.13.

SCCs' MOSFETs. It is possible to notice that the ZVS turn-on of the H-bridge is maintained during the whole transient since i_1 is always inductive. The SCC MOSFETs' peak

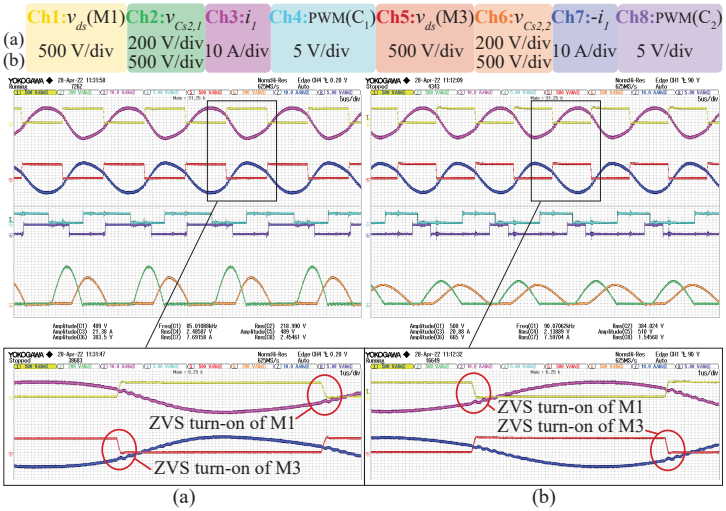

Figure 3.16: Measured drain-source voltage v_{ds} of the MOSFETs $M1$ and $M3$ in Figure 3.2 when operating the SCCs with the half-wave modulation at full power for: (a) M=M_{mid}, and (b) M=M_{min}. The channels are displayed in the same sequence as Figure 3.13.

voltage stress is well below 1700 V. The worst measured voltage stress is $\hat{V}_{C_{s2},1}$=1000 V using the full-wave modulation, and $\hat{V}_{C_{s2},1}$=1450 V for the half-wave modulation.

According to Figure 3.13, the SCCs introduce some distortion in the currents. This is particularly clear when employing the half-wave modulation where the positive and the negative currents' half-waves are not symmetrical. This is due to the asymmetrical nature of the half-wave modulation that foresees the switching only in correspondence with one zero crossing during one switching period. Nevertheless, the ZVS turn-on operation can be observed by analyzing the H-bridge inverter output voltage in Figure 3.13, which has a smooth $\frac{dv}{dt}$ transition, i.e., without abrupt variations. The asymmetry in the primary current would cause the H-bridge inverter's turn-off point to vary slightly in the two switching transitions. This is shown in Figure 3.16 where the drain-source voltage v_{ds} of both MOSFETs $M1$ and $M3$ is measured at M=M_{mid} and M=M_{min}. The ZVS turn-on is achieved since the $\frac{dv}{dt}$ is smooth, and the primary current lags that transition.

POWER TRANSFER EFFICIENCY

The DC-to-DC efficiency $\eta_{\text{DC-to-DC}}$ of these two implementations are illustrated in Figure 3.17 in relation to a charging profile similar to the one in Figure 3.3(b). The implementation of SCCs with half-wave modulation leads to higher efficiency mainly because it employs two fewer SiC MOSFETs than the full-wave modulation, resulting in lower conduction losses. The switching losses are also lower since the SCC is switched on and off only once every switching cycle, while these transitions occur twice in the full-wave modulation. For instance, the measured $\eta_{\text{DC-to-DC}}$ at the maximum P_{in} (around 3.2 kW) is 96.30% for M=M_{max}, and 96.07% for M=M_{min} when using the half-wave modulation. For the same operating points, the measured $\eta_{\text{DC-to-DC}}$ are 96.18% and 95.76% in the case of the full-wave modulation. However, the latter has a margin still for improvement.

According to the start-up transient in Figure 3.14, the peak voltage stress on the SCC's MOSFETs is 1000 V when using the full-wave modulation. This means that 1200 V SiC

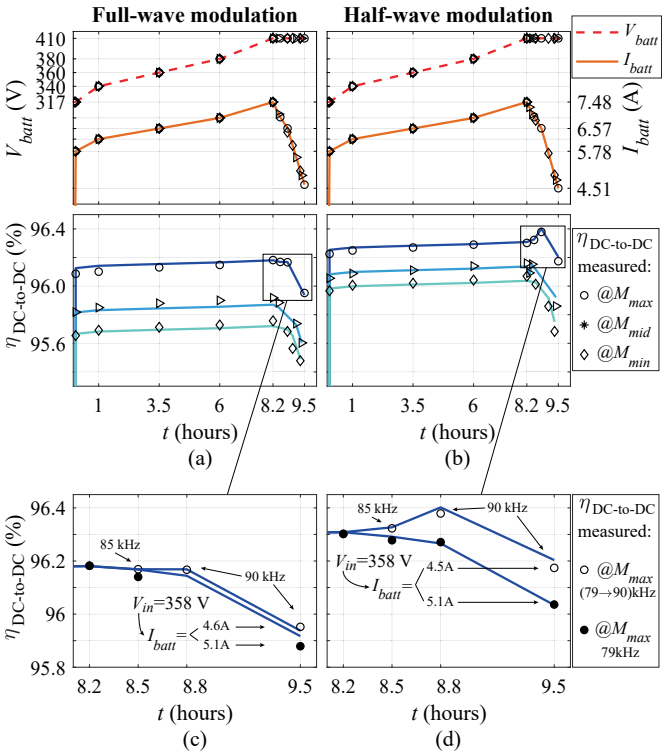

Figure 3.17: Measured DC-to-DC efficiency $\eta_{\text{DC-to-DC}}$ at different M of the proposed COL charging method that uses SCCs as compensation implemented with (a) full-wave and (b) half-wave modulation. (c)-(d) Possibility of improving $\eta_{\text{DC-to-DC}}$ and reaching lower I_{batt} at partial load by varying f_0 and setting f=f_0. The continuous lines are the expected results from the analytical model.

Table 3.2: Wolfspeed SiC MOSFETs characteristics and computed $\eta_{\text{DC-to-DC}}$ when employing them for SCCs with full-wave modulation.

SiC MOSFET	V_{ds} (V)	$R_{ds,on}$ (mΩ)	Cost (€)*	$\eta_{\text{DC-to-DC}}$ (%)**
C2M0045170P	1700	45	75.85	96.18
C3M0032120K	1200	32	24.39	96.32
C3M0021120K	1200	21	28.43	96.41
C3M0016120K	1200	16	66.92	96.45

*Source: Digi-key Electronics (accessed: 03/05/2022). Unit price (100+)

**Computed at full power, i.e., V_{batt}=410V and M=M_{max}

MOSFETs could be employed in that case. The main advantages of these devices are their larger market availability and lower $R_{ds,on}$ for the same current rating due to their thinner epitaxial layer. Table 3.2 shows that, at full power when M=M_{max}, the SCC using the full-wave modulation employing 1200V SiC MOSFETs could outperform the efficiency measured with the half-wave modulation for a lower total semiconductor's cost ($\approx -25\%$). On the other hand, according to the peak voltage stress in Figure 3.15, it is not possible with the current design to choose MOSFETs with lower voltage rating in the case of SCCs with the half-wave modulation.

As explained in Section 3.2.4, the CV charging profile can be achieved by controlling the input voltage through the PFC. The CV mode is characterized by a charging current lower than the nominal, i.e., R_L>$R_{L,opt}$. By considering the definition of $R_{L,opt}$ in (3.6), the system's natural frequency f_0 can be varied through the SCCs such that $R_{L,opt}$ is closer to R_L at partial loads. This can potentially increase the efficiency at partial load. Moreover, according to I_{out} in (3.2), the increase of f_0 would also allow the CV mode to reach lower currents for the same V_{in}. The effect of this partial-load strategy is shown in Figure 3.17(c)-(d) for M=M_{max}, where both the resonant and operating frequency are increased from 79 kHz to 90 kHz. Thereby, $\eta_{\text{DC-to-DC}}$ improvement is up to 0.13% for the half-wave modulation and up to 0.07% for the full-wave modulation. On top of this, about 10% lower output current can be achieved for the same input voltage.

3.4.2. COMPARISON WITH THE CONVENTIONAL S-S COMPENSATION

To investigate further the advantages of the proposed COL method, it is important to compare its performance with the conventional CC changing mode implemented with an S-S compensation with fixed capacitance. The parameters of the latter are listed in Table 3.1. C_1 has been chosen such that the inverter achieves the ZVS turn-on at 79 kHz in any operating condition, and the output power can be controlled through the full voltage range available from the PFC stage. Figure 3.13(c) shows the operating waveforms at full power and different coils' alignments.

The measured DC-to-DC efficiency $\eta_{\text{DC-to-DC}}$, the set input voltage V_{in} and power P_{in}, the equivalent resistive load R_L and the optimum load $R_{L,opt}$ of these two different implementations are illustrated in Figure 3.18 in relation to a charging profile similar to the one of the Nissan Leaf's battery in Figure 3.3.

The implementation of SCCs with half-wave modulation leads to 0.13% lower $\eta_{\text{DC-to-DC}}$ at M=M_{max} than the conventional S-S compensation throughout the COL charging profile mainly because of conduction losses due to the SCC extra series capacitor in parallel with the SiC MOSFET. This can be noticed in the losses breakdown of Figure 3.19. On the other hand, in the presence of coils' misalignment, the half-wave modulation leads to higher $\eta_{\text{DC-to-DC}}$ since the condition R_L=$R_{L,opt}$ is kept constant. According to Figure 3.18, this drop in $\eta_{\text{DC-to-DC}}$ when using fixed capacitors occurs at partial load and lower magnetic coupling. This happens because, in that cases, the condition R_L=$R_{L,opt}$ is poorly matched, which results in an imbalanced distribution of the power losses between the primary and the secondary circuits shown in Figure 3.19. Additionally, from the power losses' distribution in Figure 3.19(a), it is clear that the amount of circulating reactive current with the proposed method is approximately constant at different coils' alignments which limits the turn-off losses of the H-bridge inverter. These features are not found in the conventional S-S compensation resulting in higher losses in the primary circuit as shown in Figure 3.19(b). As depicted in the plot of P_{in}, higher $\eta_{\text{DC-to-DC}}$ results in lower required input energy E_{in}=$P_{in}\cdot t$ by up to ΔE_{in}=440 Wh which translated into lower charging cost even though the charging duration is slightly higher due to the variable I_{batt} characteristic of the proposed COL method.

The measurements of V_{in} show that it is possible to follow the battery charging profile in both implementations by only regulating the power through the PFC stage. It is also interesting to notice that the S-S compensation with fixed capacitors could reach

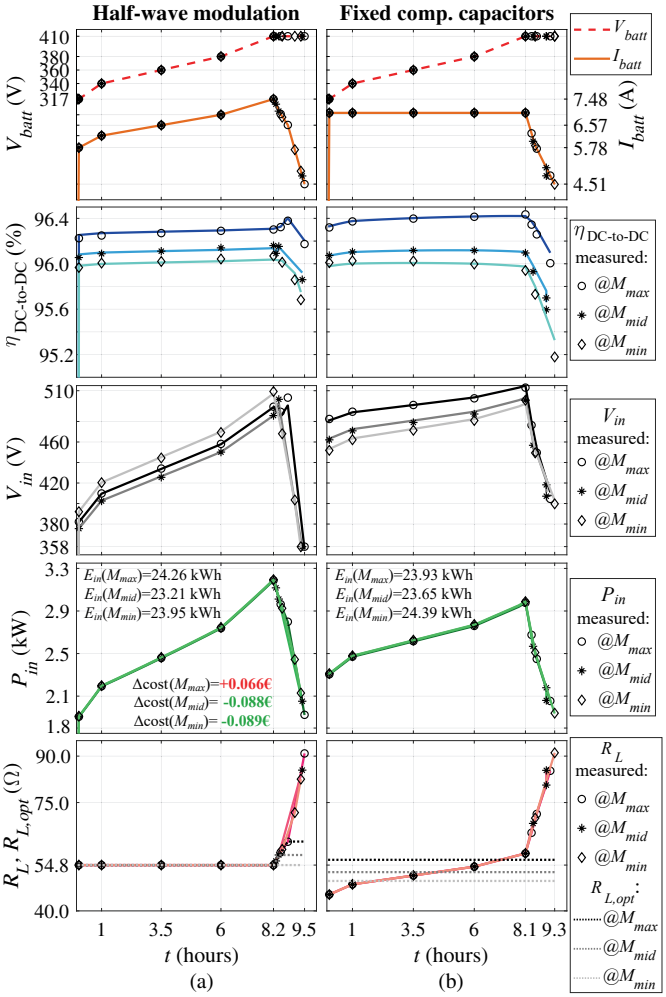

Figure 3.18: Measured DC-to-DC efficiency $\eta_{\text{DC-to-DC}}$, input voltage V_{in}, input power P_{in}, equivalent resistive load R_L and optimum load $R_{L,opt}$ achieved from: (a) the proposed COL method implemented with SCCs using half-wave modulation; (b) the traditional CC method employing fixed capacitors. The continuous lines are the expected results from the analytical model.

lower I_{batt} values in the CV mode since V_{in} still has a margin to be lowered to 358V. However, only the values of I_{batt} comparable to the ones achieved with the half-wave modulation have been reported in Figure 3.18 for being able to compare the two CV modes fairly.

For the selected power level of 3.7kW and with reference to Figure 3.20, it is worth mentioning that in this work, the designed IPT system reached a measured peak efficiency of 96.30% which is remarkably high with respect to the available literature [6], [38]–[48]. In Figure 3.20, the losses of the necessary PFC rectifier are not included since they would be present in all the IPT systems. Additionally, the overall efficiency could be considerably improved if SiC MOSFETs were used in the rectification stage instead of diodes. For example, by using the same SiC MOSFETs as the inverter, the measured full-

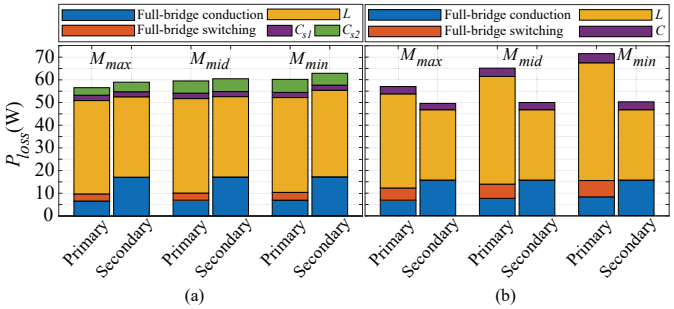

Figure 3.19: Breakdown of the power losses at full power resulting from: (a) the proposed COL method with SCCs using half-wave modulation; (b) the traditional CC method employing fixed compensation capacitors. The coils' and capacitors' losses also include losses due to cables and connections.

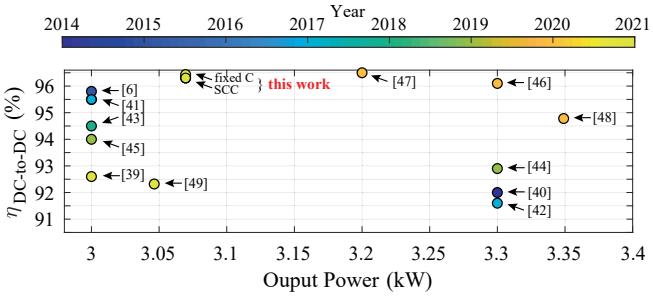

Figure 3.20: Measured peak DC-to-DC efficiency $\eta_{\text{DC-to-DC}}$ of this work compared to the available literature with the same J2954-based EV charger power class (WPT1=3.7 kVA maximum input [1]).

power efficiency of 96.30% could improve to 96.77% when employing SCCs with half-wave modulation at M=M_{max}. Similarly, at M=M_{min}, the full-power efficiency could jump to 96.5% from the measured 96.07%. In this case, the proposed method would be even more efficient than the available literature in Figure 3.20.

3.5. DISTORTION OF THE MEASURED COIL CURRENTS

Intuitively, the SCCs connected in series with the coupled coils would introduce some distortion in the coils' current. According to Figure 3.13, the full-wave modulation introduces symmetrical distortions, while the half-wave modulation introduces asymmetrical distortions due to their nature. Higher frequency current harmonics potentially can radiate a magnetic field which must be within the recommended limit from SAE J2954 in Figure 3.21 defined for wireless charging of light-duty EVs (for more details see Appendix A). During the preliminary research stage, it is reasonable to conduct a qualitative and comparative analysis on the coils' current distortion rather than considering the radiated magnetic field. This investigation cannot guarantee compliance with the recommended limits, but it can preliminarily assess the impact of the proposed method on the currents' higher-order harmonics. All in all, this section qualitatively analyzes and compares the FFT of the measured coils' current that results from the SCC half-wave and full-wave modulations and the conventional S-S compensation. After that, the FEM analysis of the radiated magnetic field is performed in Section 3.6.

3.5.1. METHODOLOGY

CURRENT MEASUREMENT CONDITIONS

When measuring the circuit waveforms at the operating points shown in Figure 3.13, another set of measurements of I_1 and I_2 has been performed with 50 MHz N2782B Keysight current probes such that the signals are acquired with the maximum vertical resolution. The horizontal scale of 2 ms/div is chosen that makes the measurement duration D_t=20 ms. A whole number of periods of the measured signals has been considered for computing the currents' FFT. These scope settings resulted in a length of the signal L_t=12.5·10^6. Therefore, for each measured signal, the sampling period and the sampling frequency are h_{res}=$\frac{D_t}{L_t}$=1.6 ns and F_s=$\frac{1}{h_{res}}$=625 MHz, respectively. According to the Nyquist-Shannon sampling theorem, the FFT bandwidth f_n=$\frac{F_s}{2}$=312.5 MHz is large enough for the upper frequency limit (30 MHz) in Figure 3.21. Additionally, the FFT frequency resolution is df=$\frac{F_s}{L_t}$=50 Hz which is reasonably small compared to the current's fundamental frequency (~ 85 kHz).

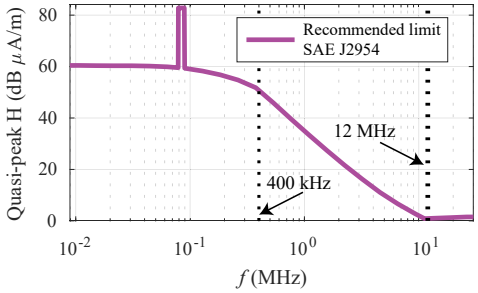

Figure 3.21: Recommended limit from SAE J2954 on the quasi-peak radiated magnetic field H measured at 10 m distance [1].

CHOSEN OPERATING CONDITION

For each implementation, the total harmonic distortion (THD) of both I_1 and I_2 has been computed, which is listed in Table 3.3 for all the considered coils' alignments. However, discussing the amplitude of individual harmonics rather than the THD is more significant since those determine the compliance to the limits in Figure 3.21. It is worth mentioning that this limit drops exponentially from 400 kHz to 12 MHz where the minimum value is reached, and it is roughly maintained constant until 30 MHz. The peak amplitude of the harmonic components has been considered since it coincides with the quasi-peak value in continuous wave signals. Nevertheless, the quasi-peak is always equal to or lower than the relative peak and, for this reason, the peak normally gives an extra safety margin.

Table 3.3: THD of the measured I_1 and I_2 at the rated output power for different coils' alignment conditions.

	THD(I_1) (%)			THD(I_2) (%)		
	M_{min}	M_{mid}	M_{max}	M_{min}	M_{mid}	M_{max}
SCC: f-w	6.84	7.83	7.28	7.11	8.38	8.14
SCC: h-w	7.89	10.57	7.37	7.36	10.98	8.16
const C	6.16	6.65	7.69	8.16	8.51	9.04

In the following analysis, the middle-point of coil's alignment M=M_{mid} is considered since it leads to the highest distortion due to the SCCs switching at relatively high currents as shown in Figure 3.13. Only I_1 is discussed in detail since, according to Figure 3.22, larger distortions have been found at the primary circuit due to the band-pass filter characteristic of the resonant network as explained in [49]. Figure 3.23 shows the FTT I_1 resulting from the SCC half-wave and full-wave modulations measured at M=M_{mid}. The FFT of the respective I_2 is shown in Figure 3.24. On the other hand, Figure 3.25 shows the FTT of I_1 resulting from the SCC half-wave modulation and the compensation with fixed capacitors both measured at M=M_{mid}. The FFT of the respective I_2 is shown in Figure 3.26.

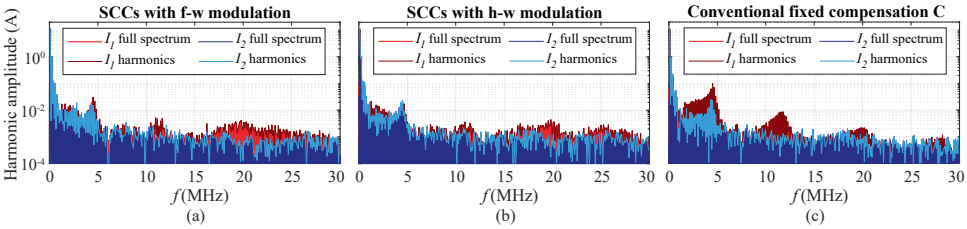

Figure 3.22: FFT of I_1 and I_2 at the maximum power point for M=M_{mid} when using: (a) SCCs with full-wave (f-w) modulation, (b) SCCs with half-wave (h-w) modulation, and (c) fixed S-S compensation (const C). The FTT is plotted for the entire frequency spectrum and also for only the harmonic components.

3.5.2. SCCs USING THE HALF-WAVE AND THE FULL-WAVE MODULATIONS

From the lower-frequencies zoom of Figure 3.23, the half-wave modulation has more significant even-order harmonic components than the full-wave modulation due to its asymmetrical nature. This can be seen especially in the 2$^{\text{nd}}$-order harmonic highlighted by (1). This 2$^{\text{nd}}$-order harmonic might not be particularly worrying because it would not be likely the only one compromising the compliance since its amplitude is similar to the 3$^{\text{rd}}$-harmonic from the full-wave modulation. Similarly, the half-wave modulation's 7$^{\text{th}}$-order harmonic (595 kHz) pointed out from (2) is about 2.8 times higher than the full-wave modulation's 53$^{\text{th}}$-order harmonic (4.5 MHz) marked by (3). Nevertheless, according to Figure 3.21, the limit at 595 kHz is about 25 times lager than the one at 4.5 MHz.

Considering the zoom on the highest frequencies of Figure 3.23, it is clear from (4) that the full-wave modulation has the most compromising harmonic amplitude in the range of 12-30 MHz.

From this analysis, it can be concluded that the half-wave modulation leads to more total-lumped distortion in I_1, which is confirmed by the THD. However, since the harmonic components have comparable amplitude, it cannot be stated that one specific modulation strategy would compromise the recommended limits more than the other. Similar considerations are also valid for the harmonic distortion of the respective measured I_2 shown in Figure 3.24.

3.5.3. HALF-WAVE MODULATION SCC AND THE FIXED S-S CAPACITORS

In the lower-frequencies zoom of Figure 3.25, it is possible to notice that the half-wave modulation has larger even-order harmonic components due to its asymmetrical nature.

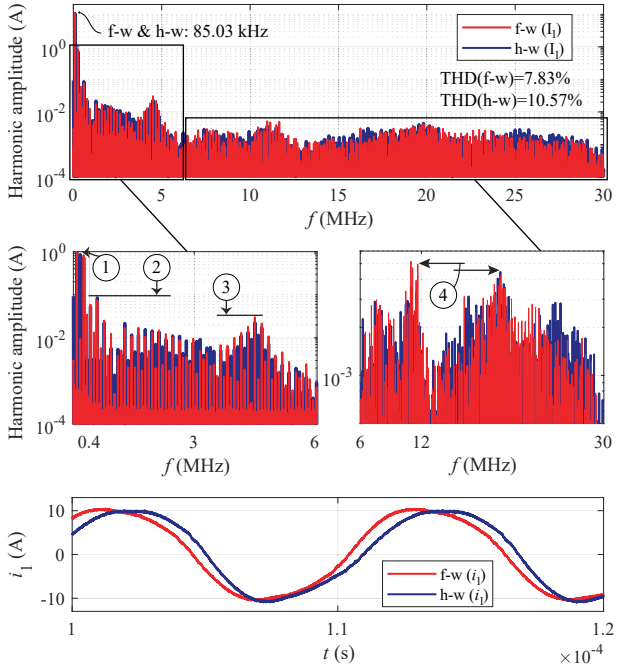

Figure 3.23: FFT of I_1 at full power for M=M_{mid} when using SCCs with both modulations.

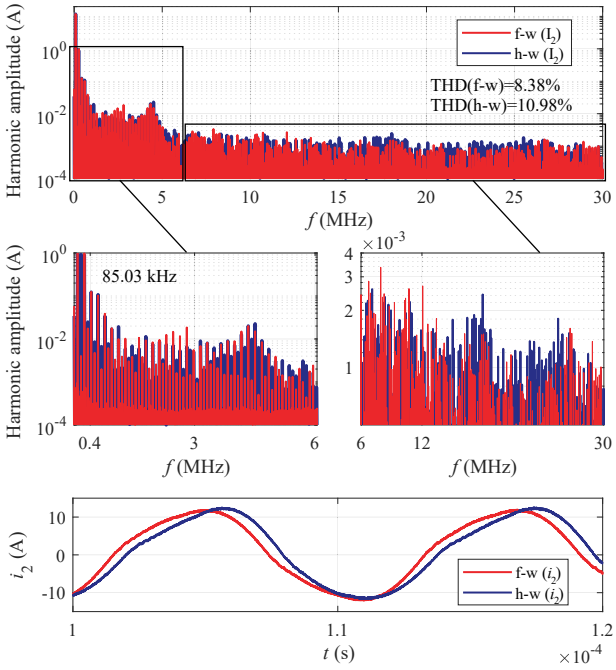

Figure 3.24: FFT of I_2 at full power for M=M_{mid} when using SCCs with both modulations.

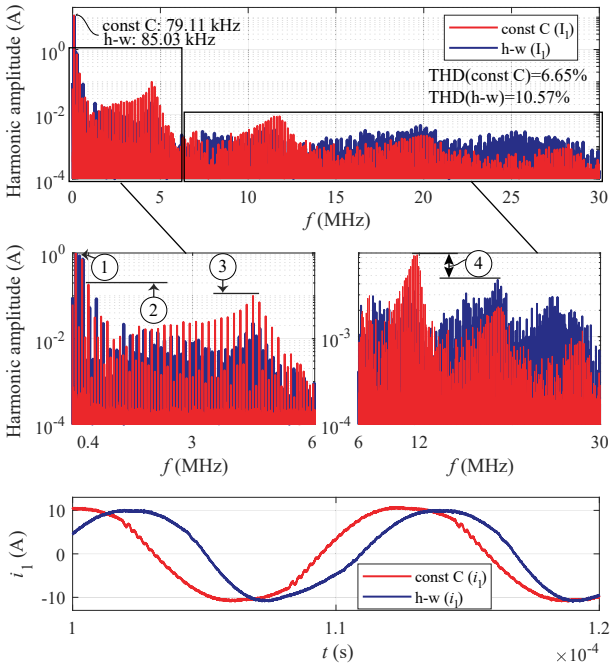

Figure 3.25: FFT of I_1 at full power for M=M_{mid} when using the fixed S-S compensation (const C), and the SSC half-wave (h-w) modulation.

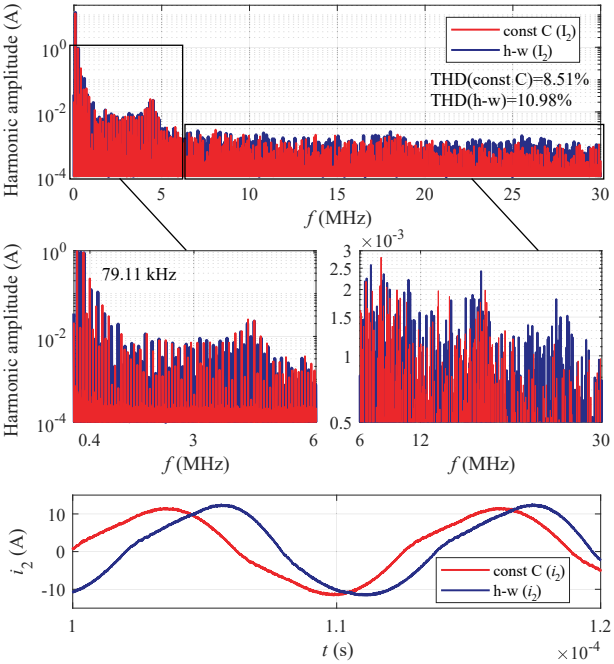

Figure 3.26: FFT of I_2 at full power for M=M_{mid} when using the fixed S-S compensation (const C), and the SSC half-wave (h-w) modulation.

However, similarly to the previous analysis, the 2nd-order harmonic highlighted from (1) might not be particularly worrying. After this, it is interesting to notice that the largest amplitudes in the interval from 400 kHz to 12 MHz are generated by the compensation with fixed capacitors, marked by (2) and (3).

Considering the zoom on the highest frequencies of Figure 3.25, it is clear at (4) that the fixed capacitors lead to compromising harmonic amplitudes also in the range 12-30 MHz. This high-frequency ringing visible in the measured signal is due to the parasitic capacitance of the coil. This ringing might be less attenuated when using fixed capacitors because the resistance of the resonant circuit is lower than in the implementations with SCCs. This reduces the conduction losses, but it worsens the dumping of high-frequency oscillations.

The half-wave modulation leads to higher total-lumped distortion in I_1. However, considering that the compensation with fixed capacitors leads to larger amplitudes of the harmonic components at the most stringent limits, it can be deduced that if the latter complies with the recommended limits, the implementation with SCCs using half-wave modulation also would. Similar considerations are also valid for the harmonic distortion of the respective measured I_2 shown in Figure 3.26.

3.6. FEM SIMULATION OF THE RADIATED MAGNETIC FIELD

After analyzing the current distortion, it is interesting to evaluate whether the radiated magnetic field generated by these currents is below the EMC limits in Figure 3.21. For that purpose, the coils in Figure 3.9 have been modeled in Comsol Multiphysics for the alignment condition corresponding to M_{mid} where the assigned I_1 and I_2 have harmonic components equal to the measured ones in amplitude and phase. According to Figure 3.22, it is reasonable to consider only the higher-order harmonic components instead of the full spectrum since the peaks occur in correspondence with those. The radiated magnetic field has been evaluated through the FEM analysis for each configuration in Figure 3.22. To ensure high accuracy of the solutions at 10 m, the infinite element domain is applied to the external layer of the air domain shown in Figure 3.27 [50]. All evaluation points are shown in Figure 3.28 of which height is $z=\frac{Z_{ag}}{2}$. This analysis is conservative since the receiver coil lacks a large aluminum shield resembling the EV chassis.

3.6.1. COMPARISON WITH THE EMC LIMITS

Figure 3.29 shows the comparison between the radiated magnetic field and the recommended limits from SAE J2954 in the four 10 m-distant points illustrated in Figure 3.28. The resulting B_{peak} has been converted by using (3.32).

$$\overbrace{H_{peak}}^{(dB_{\mu A/m})} = 20 \cdot \log_{10}\left[\frac{\overbrace{B_{peak}}^{(T)}}{\mu_0} \cdot 10^6\right] \tag{3.32}$$

The radiated field is well below the limits as expected since the considered power level of 3.7 kW is the lowest regulated by SAE J2954. A radiated B_{peak} up to 43 times larger than the maximum resulting one of 50 dB would still satisfy the limit in the nomi-

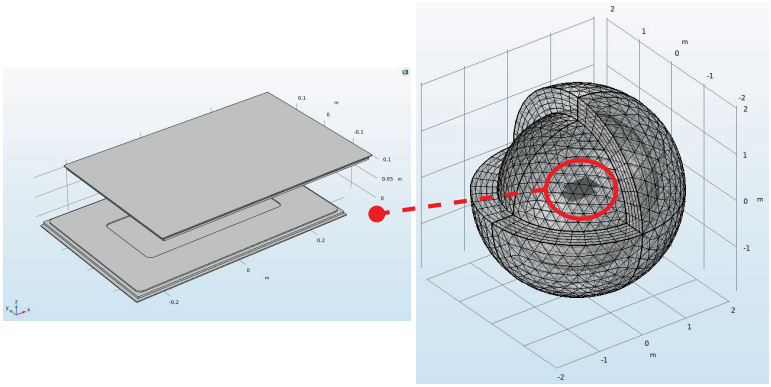

Figure 3.27: Model of the coupled coils to evaluate the radiated magnetic field.

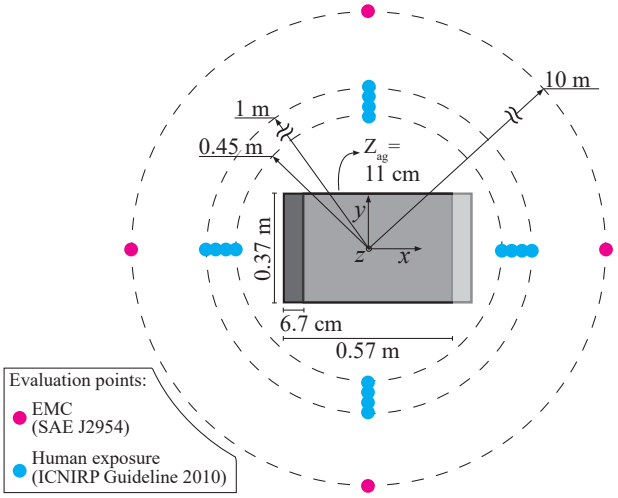

Figure 3.28: Locations of the evaluated radiated magnetic field for the lateral misalignment of the receiver coil in the x direction corresponding to M_{mid}.

nal operating frequency range 79-90 kHz. Thereby, SAE J2954 also suggests reducing the limit by 15 dB if sensitive equipment is present within 10 m. In that case, the radiated B_{peak} can be up to 7 times larger.

3.6.2. COMPARISON WITH THE HUMAN EXPOSURE LIMITS

Besides compliance with the EMC limits, the magnetic field radiated by the coupled coils must be safe for the living beings surrounding the EV wireless charging system. The ICNIRP Guideline 2010 defines reference levels for the general public exposure being B_{RMS}=27 µT, while the limit B_{RMS}=15 µT holds for implanted medical devices (IMDs) and pacemakers [51]. These limits are valid for all the areas around the IPT system accessible to people.

Figure 3.30 shows the evaluated radiated magnetic field in the four directions specified in Figure 3.28. It can be deduced that, in this case, a minimum distance of 25 cm

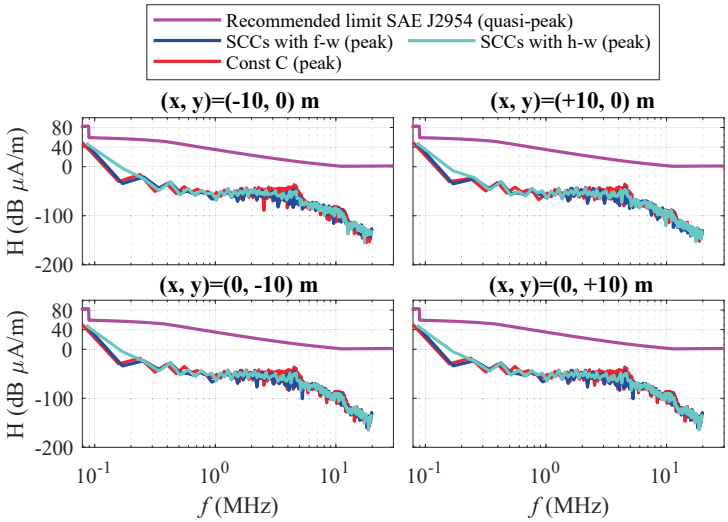

Figure 3.29: Computed radiated magnetic field at 10 m.

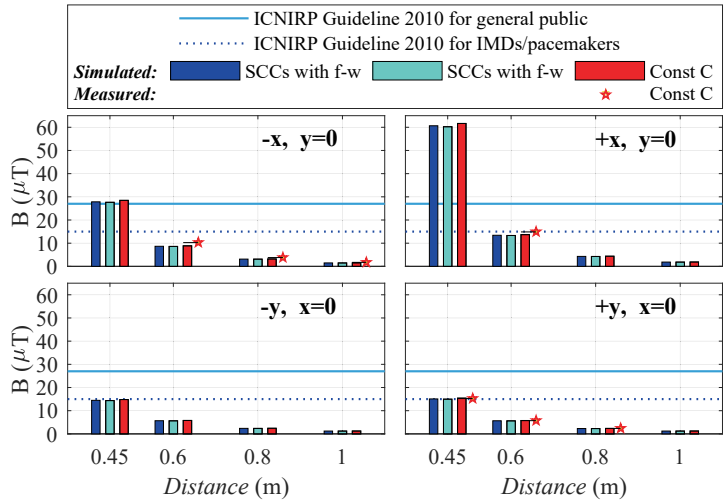

Figure 3.30: Computed and measured radiated magnetic field within 1 m (RMS values).

from the outer sides of the coupled coils guarantees a radiated $B_{RMS} \leq 15\mu T$. The EV chassis can easily provide this safety distance when considering the wireless charging system mounted on the EV. The simulated magnetic field has been verified experimentally with the exposure level tester Narda ELT-400 in the measurement setup shown in Figure 3.31. The circuit using the fixed S-S compensation has been considered, and the magnetic field has been measured at distances that were physically accessible in the surroundings of the prototype. According to Figure 3.31, the measured magnetic field is in agreement with the simulated values, which confirms the developed FEM model and the previous analysis.

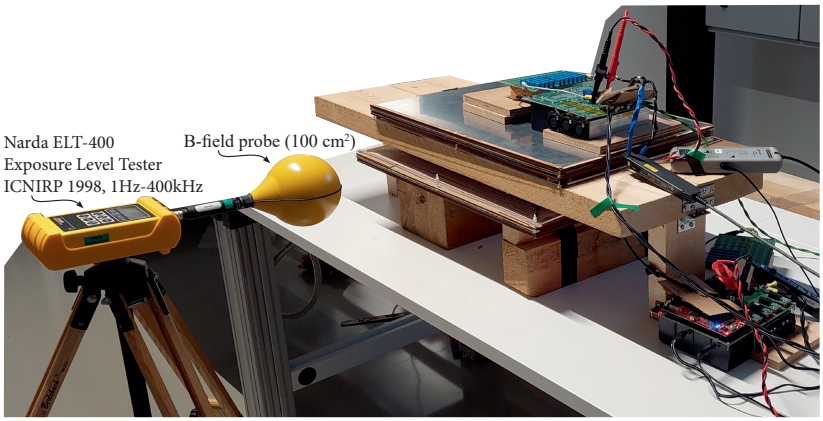

Figure 3.31: Test setup used to perform the radiated magnetic field measurements recorded in Figure 3.30.

3.7. CONCLUSION

Optimum load matching is widely used in EV wireless charging systems, where the equivalent output load is always set to equal the so-called optimum load. The latter maximizes the power transfer efficiency, and its value depends on the coils' alignment. In contrast, this chapter proposes to make the optimum load condition invariant of the coil's magnetic coupling by changing the natural resonant frequency of the system. This method is defined here as constant optimum load, and its concept is explained in detail in Section 3.2. The advantage of this solution is eliminating voltage control at the load side. Only the input power is regulated through the PFC, ensuring that the COL condition is met while the battery voltage increases during the charging cycle. The system's resonant frequency is varied, employing SCCs as series compensation. In particular, two SCC implementations, namely the full-wave modulation and the half-wave modulation, have been implemented in a 3.7kW prototype described in Section 3.3, and their performances have been compared and benchmarked against the conventional S-S compensation with fixed capacitors in Section 3.4. The half-wave modulation results in overall higher efficiency than full-wave modulation, with 96.30% for the input power of 3.2kW and at the maximum coils' alignment. For the same power and minimum alignment, the efficiency drops only by 0.27%. The minimum measured efficiency is 95.68% at partial load and minimum coupling, proving that the proposed method leads to relatively high efficiency in the entire operating range. On the other hand, at 3.2kW and the maximum magnetic coupling, the full-wave modulation results in 96.18%, and the efficiency drops by 0.42% at the minimum alignment. When misalignment occurs, the SCC half-wave modulation is more efficient than the conventional S-S compensation with fixed capacitors. The efficiency gain is up to 0.68% at partial load. Considering the high power transfer efficiency measured for a coil's misalignment range and throughout a charging cycle typical of a 3.7kW static EV wireless charger, this research has proved the suitability of the proposed COL charging method for that application.

Additionally, the current distortion introduced using SCCs and conventional capacitors as series compensation has been analyzed in Section 3.5. This is important to preliminary assess the radiated magnetic field in the higher frequency domain. The SCCs

are employed to change the circuit's resonant frequency such that the optimum load condition is kept constant over different coils' alignments. The coils' current has been measured in a 3.7kW EV wireless charging system for three implementations: SCCs with half-wave modulation, SCCs with full-wave modulation, and conventional fixed capacitance. By computing the current's FFT up to 30MHz, the SCCs using the half-wave modulation introduce the highest total lumped distortion because of their asymmetrical nature. However, in correspondence with the critical frequencies of the limits set by SAE J2954, the amplitude of the single harmonic components are comparable to or lower than in the other implementations. Finally, the radiated magnetic field from each configuration has been evaluated through FEM analysis in Section 3.6. The results at a 10 m distance are all far below the EMC limits from SAE J2954 up to 30 MHz. When considering the human exposure limits set by ICNIRP, a minimum distance of 25 cm from the outer sides of the coupled coils ensures a safe magnetic field level for both the general public and implanted medical devices, which have been validated experimentally.

REFERENCES

[1] *J2954 (r) wireless power transfer for light-duty plug-in/ electric vehicles and alignment methodology*, Oct. 2020.

[2] R. Bosshard, J. W. Kolar, J. Mühlethaler, I. Stevanović, B. Wunsch, and F. Canales, "Modeling and η-α-pareto optimization of inductive power transfer coils for electric vehicles", *IEEE Journal of Emerging and Selected Topics in Power Electronics*, vol. 3, no. 1, pp. 50–64, 2015. DOI: 10.1109/JESTPE.2014.2311302.

[3] R. Bosshard, J. W. Kolar, and B. Wunsch, "Control method for inductive power transfer with high partial-load efficiency and resonance tracking", in *2014 International Power Electronics Conference (IPEC-Hiroshima 2014 - ECCE ASIA)*, 2014, pp. 2167–2174. DOI: 10.1109/IPEC.2014.6869889.

[4] S. Bandyopadhyay, P. Venugopal, J. Dong, and P. Bauer, "Comparison of magnetic couplers for ipt-based ev charging using multi-objective optimization", *IEEE Transactions on Vehicular Technology*, vol. 68, no. 6, pp. 5416–5429, 2019. DOI: 10.1109/TVT.2019.2909566.

[5] H. Li, J. Li, K. Wang, W. Chen, and X. Yang, "A maximum efficiency point tracking control scheme for wireless power transfer systems using magnetic resonant coupling", *IEEE Transactions on Power Electronics*, vol. 30, no. 7, pp. 3998–4008, 2015. DOI: 10.1109/TPEL.2014.2349534.

[6] T. Diekhans and R. W. De Doncker, "A dual-side controlled inductive power transfer system optimized for large coupling factor variations and partial load", *IEEE Transactions on Power Electronics*, vol. 30, no. 11, pp. 6320–6328, 2015. DOI: 10.1109/TPEL.2015.2393912.

[7] W. X. Zhong and S. Y. R. Hui, "Maximum energy efficiency tracking for wireless power transfer systems", *IEEE Transactions on Power Electronics*, vol. 30, no. 7, pp. 4025–4034, 2015. DOI: 10.1109/TPEL.2014.2351496.

[8] T.-D. Yeo, D. Kwon, S.-T. Khang, and J.-W. Yu, "Design of maximum efficiency tracking control scheme for closed-loop wireless power charging system employing series resonant tank", *IEEE Transactions on Power Electronics*, vol. 32, no. 1, pp. 471–478, 2017. DOI: 10.1109/TPEL.2016.2523121.

[9] R. Bosshard and J. W. Kolar, "All-sic 9.5 kw/dm^3 on-board power electronics for 50 kw/85 khz automotive ipt system", *IEEE Journal of Emerging and Selected Topics in Power Electronics*, vol. 5, no. 1, pp. 419–431, 2017. DOI: 10.1109/JESTPE.2016.2624285.

[10] R. Mai, Y. Liu, Y. Li, P. Yue, G. Cao, and Z. He, "An active-rectifier-based maximum efficiency tracking method using an additional measurement coil for wireless power transfer", *IEEE Transactions on Power Electronics*, vol. 33, no. 1, pp. 716–728, 2018. DOI: 10.1109/TPEL.2017.2665040.

[11] J. Zhang, J. Zhao, Y. Zhang, and F. Deng, "A wireless power transfer system with dual switch-controlled capacitors for efficiency optimization", *IEEE Transactions on Power Electronics*, vol. 35, no. 6, pp. 6091–6101, 2020.

[12] Z. Huang, C.-S. Lam, P.-I. Mak, R. P. d. S. Martins, S.-C. Wong, and C. K. Tse, "A single-stage inductive-power-transfer converter for constant-power and maximum-efficiency battery charging", *IEEE Transactions on Power Electronics*, vol. 35, no. 9, pp. 8973–8984, 2020. DOI: 10.1109/TPEL.2020.2969685.

[13] Wen-Jian Gu and K. Harada, "A new method to regulate resonant converters", *IEEE Transactions on Power Electronics*, vol. 3, no. 4, pp. 430–439, 1988.

[14] J. Osawa, T. Isobe, and H. Tadano, "Efficiency improvement of high frequency inverter for wireless power transfer system using a series reactive power compensator", in *2017 IEEE 12th International Conference on Power Electronics and Drive Systems (PEDS)*, 2017, pp. 992–998. DOI: 10.1109/PEDS.2017.8289240.

[15] D. Kim and D. Ahn, "Self-tuning lcc inverter using pwm-controlled switched capacitor for inductive wireless power transfer", *IEEE Transactions on Industrial Electronics*, vol. 66, no. 5, pp. 3983–3992, 2019.

[16] J. Zhao, J. Zhang, Y. Zhang, Z. Din, and J. Juri, "A reactive compensation method using switch controlled capacitor for wireless power transfer", in *2019 IEEE Energy Conversion Congress and Exposition (ECCE)*, 2019, pp. 2112–2117. DOI: 10.1109/ECCE.2019.8912183.

[17] W. Li, G. Wei, C. Cui, X. Zhang, and Q. Zhang, "A double-side self-tuning lcc/s system using a variable switched capacitor based on parameter recognition", *IEEE Transactions on Industrial Electronics*, vol. 68, no. 4, pp. 3069–3078, 2021.

[18] R. Matsumoto and H. Fujimoto, "Wireless ev charging system using pwm-controlled variable capacitor for maximum power transfer under severe coil misalignment", in *2022 International Power Electronics Conference (IPEC-Himeji 2022- ECCE Asia)*, 2022, pp. 1476–1480. DOI: 10.23919/IPEC-Himeji2022-ECCE53331.2022.9806942.

[19] J. Wang, Z. Chang, B. Zhang, X. Yang, and H. Tang, "Analysis of icpt system with lcc resonant topology based on the switch-controlled capacitor", in *2020 IEEE Wireless Power Transfer Conference (WPTC)*, 2020, pp. 178–182. DOI: 10.1109/WPTC48563.2020.9295600.

[20] S. Lu, T. Lämmle, and N. Parspour, "Analysis and design of a t-compensation network with switch-controlled capacitor for wireless power transfer system", in *2021 IEEE PELS Workshop on Emerging Technologies: Wireless Power Transfer (WoW)*, 2021, pp. 1–6. DOI: 10.1109/WoW51332.2021.9462860.

[21] X. Wang, J. Xu, M. Leng, H. Ma, and S. He, "A hybrid control strategy of lcc-s compensated wpt system for wide output voltage and zvs range with minimized reactive current", *IEEE Transactions on Industrial Electronics*, vol. 68, no. 9, pp. 7908–7920, 2021. DOI: 10.1109/TIE.2020.3013788.

[22] M. Schweizer and T. B. Soeiro, "Heatsink-less quasi 3-level flying capacitor inverter based on low voltage smd mosfets", in *2017 19th European Conference on Power Electronics and Applications (EPE'17 ECCE Europe)*, 2017, P1–P.10. DOI: 10.23919/EPE17ECCEEurope.2017.8098916.

[23] N. Keeling, G. A. Covic, F. Hao, L. George, and J. T. Boys, "Variable tuning in lcl compensated contactless power transfer pickups", in *2009 IEEE Energy Conversion Congress and Exposition*, 2009, pp. 1826–1832. DOI: 10.1109/ECCE.2009.5316169.

[24] M. Zaheer, N. Patel, and A. P. Hu, "Parallel tuned contactless power pickup using saturable core reactor", in *2010 IEEE International Conference on Sustainable Energy Technologies (ICSET)*, 2010, pp. 1–6. DOI: 10.1109/ICSET.2010.5684407.

[25] S. Aldhaher, P. C.-K. Luk, and J. F. Whidborne, "Electronic tuning of misaligned coils in wireless power transfer systems", *IEEE Transactions on Power Electronics*, vol. 29, no. 11, pp. 5975–5982, 2014. DOI: 10.1109/TPEL.2014.2297993.

[26] A. Dayerizadeh, H. Feng, and S. M. Lukic, "Dynamic wireless charging: Reflexive field containment using saturable inductors", *IEEE Transactions on Industry Applications*, vol. 56, no. 2, pp. 1784–1792, 2020. DOI: 10.1109/TIA.2020.2964215.

[27] X. Qu, H. Han, S.-C. Wong, C. K. Tse, and W. Chen, "Hybrid ipt topologies with constant current or constant voltage output for battery charging applications", *IEEE Transactions on Power Electronics*, vol. 30, no. 11, pp. 6329–6337, 2015. DOI: 10.1109/TPEL.2015.2396471.

[28] R. Mai, Y. Chen, Y. Li, Y. Zhang, G. Cao, and Z. He, "Inductive power transfer for massive electric bicycles charging based on hybrid topology switching with a single inverter", *IEEE Transactions on Power Electronics*, vol. 32, no. 8, pp. 5897–5906, 2017. DOI: 10.1109/TPEL.2017.2654360.

[29] Y. Chen, M. Li, B. Yang, *et al.*, "Variable-parameter t-circuit-based ipt system charging battery with constant current or constant voltage output", *IEEE Transactions on Power Electronics*, vol. 35, no. 2, pp. 1672–1684, 2020. DOI: 10.1109/TPEL.2019.2920948.

[30] Z. Zhang, W. Ai, Z. Liang, and J. Wang, "Topology-reconfigurable capacitor matrix for encrypted dynamic wireless charging of electric vehicles", *IEEE Transactions on Vehicular Technology*, vol. 67, no. 10, pp. 9284–9293, 2018. DOI: 10.1109/TVT.2018.2859779.

[31] F. Grazian, W. Shi, T. B. Soeiro, J. Dong, and P. Bauer, "Electric vehicle charging based on inductive power transfer employing variable compensation capacitance for optimum load matching", in *IECON 2020 The 46th Annual Conference of the IEEE Industrial Electronics Society*, 2020, pp. 5262–5267.

[32] R. L. Steigerwald, "A comparison of half-bridge resonant converter topologies", *IEEE Trans. Power Electron.*, vol. 3, no. 2, 1988.

[33] T. B. Soeiro and P. Bauer, "Fast dc-type electric vehicle charger based on a quasi-direct boost - buck rectifier", in *2019 AEIT International Conference of Electrical and Electronic Technologies for Automotive (AEIT AUTOMOTIVE)*, 2019, pp. 1–6. DOI: 10.23919/EETA.2019.8804493.

[34] *Iec 61980-1:2020 electric vehicle wireless power transfer (wpt) systems - part 1: General requirements*, Nov. 2020.

[35] F. Grazian, T. B. Soeiro, and P. Bauer, "Inductive power transfer based on variable compensation capacitance to achieve an ev charging profile with constant optimum load", *IEEE Journal of Emerging and Selected Topics in Power Electronics*, pp. 1–1, 2022. DOI: 10.1109/JESTPE.2022.3188060.

[36] J. W. Kolar, J. Biela, and J. Minibock, "Exploring the pareto front of multi-objective single-phase pfc rectifier design optimization - 99.2% efficiency vs. 7kw/din^3 power density", in *2009 IEEE 6th International Power Electronics and Motion Control Conference*, 2009, pp. 1–21. DOI: 10.1109/IPEMC.2009.5289336.

[37] M. S. Ortmann, T. B. Soeiro, and M. L. Heldwein, "High switches utilization single-phase pwm boost-type pfc rectifier topologies multiplying the switching frequency", *IEEE Transactions on Power Electronics*, vol. 29, no. 11, pp. 5749–5760, 2014. DOI: 10.1109/TPEL.2014.2301814.

[38] L. Zhao, D. J. Thrimawithana, U. K. Madawala, and A. P. Hu, "A push-pull parallel resonant converter-based bidirectional ipt system", *IEEE Transactions on Power Electronics*, vol. 35, no. 3, pp. 2659–2667, 2020. DOI: 10.1109/TPEL.2019.2930283.

[39] X. Zhang, Y. Zhang, Z. Zhang, and M. Li, "Mode conversion and structure optimization of quadrature coils for electric vehicles wireless power transfer", *IEEE Transactions on Energy Conversion*, vol. 35, no. 2, pp. 575–590, 2020. DOI: 10.1109/TEC.2020.2972584.

[40] C. Xiao, B. Cao, and C. Liao, "A fast construction method of resonance compensation network for electric vehicle wireless charging system", *IEEE Transactions on Instrumentation and Measurement*, vol. 70, pp. 1–9, 2021. DOI: 10.1109/TIM.2021.3055783.

[41] B.-G. Choi and Y.-S. Kim, "New structure design of ferrite cores for wireless electric vehicle charging by machine learning", *IEEE Transactions on Industrial Electronics*, vol. 68, no. 12, pp. 12 162–12 172, 2021. DOI: 10.1109/TIE.2020.3047041.

[42] Q. Zhu, L. Wang, and C. Liao, "Compensate capacitor optimization for kilowatt-level magnetically resonant wireless charging system", *IEEE Transactions on Industrial Electronics*, vol. 61, no. 12, pp. 6758–6768, 2014. DOI: 10.1109/TIE.2014.2321349.

[43] T. Kan, T.-D. Nguyen, J. C. White, R. K. Malhan, and C. C. Mi, "A new integration method for an electric vehicle wireless charging system using lcc compensation topology: Analysis and design", *IEEE Transactions on Power Electronics*, vol. 32, no. 2, pp. 1638–1650, 2017. DOI: 10.1109/TPEL.2016.2552060.

[44] L. Zhao, D. J. Thrimawithana, and U. K. Madawala, "Hybrid bidirectional wireless ev charging system tolerant to pad misalignment", *IEEE Transactions on Industrial Electronics*, vol. 64, no. 9, pp. 7079–7086, 2017. DOI: 10.1109/TIE.2017.2686301.

[45] K. Inoue, K. Kusaka, and J.-I. Itoh, "Reduction in radiation noise level for inductive power transfer systems using spread spectrum techniques", *IEEE Transactions on Power Electronics*, vol. 33, no. 4, pp. 3076–3085, 2018. DOI: 10.1109/TPEL.2017.2710230.

[46] J. Lu, G. Zhu, D. Lin, S.-C. Wong, and J. Jiang, "Load-independent voltage and current transfer characteristics of high-order resonant network in ipt system", *IEEE Journal of Emerging and Selected Topics in Power Electronics*, vol. 7, no. 1, pp. 422–436, 2019. DOI: 10.1109/JESTPE.2018.2823782.

[47] L. Zhao, D. J. Thrimawithana, U. K. Madawala, A. P. Hu, and C. C. Mi, "A misalignment-tolerant series-hybrid wireless ev charging system with integrated magnetics", *IEEE Transactions on Power Electronics*, vol. 34, no. 2, pp. 1276–1285, 2019. DOI: 10.1109/TPEL.2018.2828841.

[48] Z. Zhang, F. Zhu, D. Xu, P. T. Krein, and H. Ma, "An integrated inductive power transfer system design with a variable inductor for misalignment tolerance and battery charging applications", *IEEE Transactions on Power Electronics*, vol. 35, no. 11, pp. 11 544–11 556, 2020. DOI: 10.1109/TPEL.2020.2987906.

[49] H. Zeng, S. Yang, and F. Z. Peng, "Design consideration and comparison of wireless power transfer via harmonic current for phev and ev wireless charging", *IEEE Transactions on Power Electronics*, vol. 32, no. 8, 2017. DOI: 10.1109/TPEL.2016.2616111.

[50] W. Shi, F. Grazian, J. Dong, T. B. Soeiro, and P. Bauer, "Analysis of magnetic field emissions in inductive power transfer ev chargers following reference designs in sae j2954/2019", in *2020 IEEE International Symposium on Circuits and Systems (ISCAS)*, 2020, pp. 1–5.

[51] *Icnirp guidelines for limiting exposure to time-varying electric and magnetic fields (1hz - 100 khz)*, Health Physics 99(6):818-836, International Commission on Non-Ionizing Radiation Protection, 2010.

PART III
VOLTAGE/CURRENT DOUBLER (V/I-D)

4

VOLTAGE/CURRENT DOUBLER CONVERTER USING RECTANGULAR COILS

The lithium-ion battery of an electric vehicle (EV) is typically rated at 400V or 800V. When considering public parking infrastructures, EV wireless chargers must efficiently deliver electric power to both battery options. This can be normally achieved by regulating the output voltage through a DC/DC converter at the cost of higher onboard circuit complexity and lower overall efficiency. This work proposes a wireless charging system that maintains a high power transfer efficiency when charging EVs with either 400V or 800V nominal battery voltage at the same power level. The voltage levels of 400V and 800V are considered since they are becoming a norm in low-end and high-end EVs, respectively. The control scheme is implemented at the power source side, and only passive semiconductor devices are employed on board the EV. The presented system, called voltage/current doubler (V/I-D), comprises two sets of series-compensated coupled coils, each connected to a dedicated H-bridge converter. The equivalent circuit has been analyzed while explaining the parameters' selection. The analytical power transfer efficiency has been compared to that of the conventional 1-to-1 coil system at 7.2kW. For the same power level, the DC-to-DC efficiency of 97.11% and 97.52% have been measured at 400V and 800V voltage outputs, respectively. Finally, the V/I-D converter's functionality has been proved experimentally at both even and uneven misalignment of the two sets of coupled coils and for battery voltages ranging from 75% to 106% of the nominal value.

This chapter is based on:

- F. Grazian, T. B. Soeiro, P. Bauer, "Voltage/Current Doubler Converter for an Efficient Wireless Charging of Electric Vehicles with 400V and 800V Battery Voltages", in *IEEE Transactions on Industrial Electronics*, vol. 70, no. 8, pp. 7891-7903, Aug. 2023.

4.1. INTRODUCTION

With the advent of more EV models crowding the streets, it is noticeable that their nominal battery voltage is not necessarily the same, which is clear from Table 1.2.

IPT systems of EV wireless charging can achieve high power transfer efficiency when operating at the nominal operating condition for a certain power level, i.e., at the chosen converter's voltage gain, defined as the ratio been the input and output voltage. Highly efficient systems have been demonstrated in [1]–[3]. Charging a battery with either double or half of the nominal voltage would dramatically worsen the system efficiency for the same output power. This can be explained because, in those conditions, the equivalent operating resistive load would differ four times from the equivalent optimum load defined in [4] and [5]. At the current date, no research has been found in the available literature on EV wireless charging systems that can efficiently provide both 400 V and 800 V batteries with the same power.

The efficiency degradation that occurs when the battery voltage differs from the nominal could be mitigated in several ways. One solution could be charging 400 V and 800 V batteries at different power levels to match the optimum load condition. This would deliver 1/4 of the nominal power to 400 V batteries. However, when considering the wireless charging of light-duty EVs, SAE J2954 defines three power classes for wireless chargers. These power classes limit the maximum input power obtainable from the grid connection to 3.7kVA, 7.7kVA, and 11.1kVA. Charging 400 V batteries with lower power than 800 V batteries means that the power capability of a wireless charging transmitter belonging to a specific SAE J2954 power class would not be fully utilized. Consequently, this would extend considerably the charging times, which might already be quite long at these power levels. Therefore, it is preferable to fully utilize the power available from the grid connection when charging both 400 V and 800 V batteries. Alternatively, a DC/DC converter can be employed between the IPT system's output and the EV battery. In this way, the IPT system would still operate at the nominal voltage gain while the DC/DC converter sets the required voltage ratio and power exchange. In other words, the equivalent operating load would still match the optimum load condition. Consequently, the worsening of the power transfer efficiency of the IPT system would only depend on the performance of the DC/DC converter. Nevertheless, using a DC/DC converter would increase the complexity of the circuit and the control onboard the EV.

4.1.1. SCOPE AND CONTRIBUTIONS

This chapter proposes an IPT system that can charge both 400 V and 800 V EV battery classes at the same output power while maintaining high power transfer efficiency. This is a universal solution for both EV battery classes, which makes its installation practical and it eases its later reconfiguration. Moreover, it guarantees that the available power from the grid connection is fully utilized.

The main contributions are:

- definition of the novel voltage/current double (V/I-D) converter illustrated in Figure 4.1 as an IPT system that charges both 400 V and 800 V EV battery classes at the same output power while maintaining high power transfer efficiency;
- analytical modeling and comparison with the conventional 1-to-1 coil IPT system employing a 99% efficient DC/DC converter;

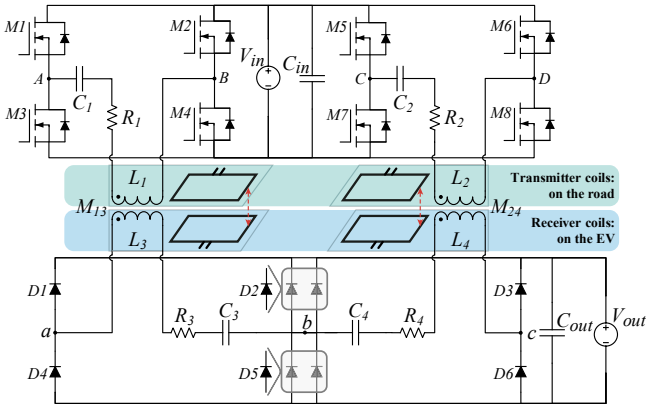

Figure 4.1: Circuit of the V/I-D converter for battery charging applications through IPT. Herein, $D2$ and $D5$ can be advantageously assembled with two parallel diodes of the same technology used in $D1$, $D3$, $D4$, and $D6$. In this case, the current rating of the converter's circuit components is similar for a given charging power independently of the operation.

- implementation of the V/I-D converter with two sets of coupled coils, including the analysis of the power transfer depending on their cross-coupling;
- experimental validation of the V/I-D converter at different coil's misalignment profiles and load variations.

4.1.2. OUTLINE

The analytical modeling, equivalent circuit, and operation of the V/I-D converter are discussed in Section 4.2. In Section 4.3, the comparison with the standard 1-to-1 coil IPT system is performed. The laboratory demonstrator of the V/I-D converter and the expected operating points are discussed in Section 4.4. The proposed concept is proved experimentally in Section 4.5 at the power level of 7.7 kW with aligned and misaligned coils. Finally, the main conclusions are given in Section 4.6.

4.2. THE V/I-D CONVERTER

The proposed V/I-D converter in Figure 4.1 delivers the same output power to 400 V and 800 V batteries depending on the modulation of the two H-bridge inverters. A similar strategy has been used in [6] and [7] to achieve a wide output voltage regulation. For that purpose, [6] proposes a phase-shifted multiple H-bridge DC/DC power supply (non-resonant). In contrast, [7] uses an interleaved LLC resonant converter with variable frequency and phase-shift control. However, these topologies fundamentally differ from the proposed V/I-D converter because they use highly coupled transformers. Thereby, the output voltage is regulated by continuously controlling the phase-shift angle between the two H-bridge inverters in the range 0°...180°. This cannot be applied directly to IPT systems for battery charging since the battery gives the output voltage. Moreover, controlling that phase-shift angle in the entire range is not suitable for IPT systems since it would lead to an unbalance of the two input impedances, resulting in the hard-switching of one of the H-bridge inverters while the other would be operating deeply in the inductive region. Thus, the proposed V/I-D converter in Figure 4.1 is an original concept for IPT systems for battery charging.

4.2.1. CIRCUIT ANALYSIS AND OPERATION

The proposed V/I-D converter in Figure 4.1 consists of two H-bridge inverters, two sets of coupled coils with their series-series (S-S) compensation, and two full-wave diode rectifiers. The control is only implemented at the power source circuit resulting in an onboard circuit with only passive devices.

When the half-bridge legs with mid-point A and C have the modulation shown in Figure 4.2(a), the current through the secondary coils has the same direction and, consequently, L_3 and L_4 result in a series connection. In the rectification stage, only D1 and D6 conduct during the positive half-wave of V_{ac}, while D3 and D4 conduct in the negative one. The two secondary coils conduct the same nominal current as shown in Figure 4.2(a). This modulation is called voltage doubler mode since it is suitable for the rated power charging of 800 V batteries.

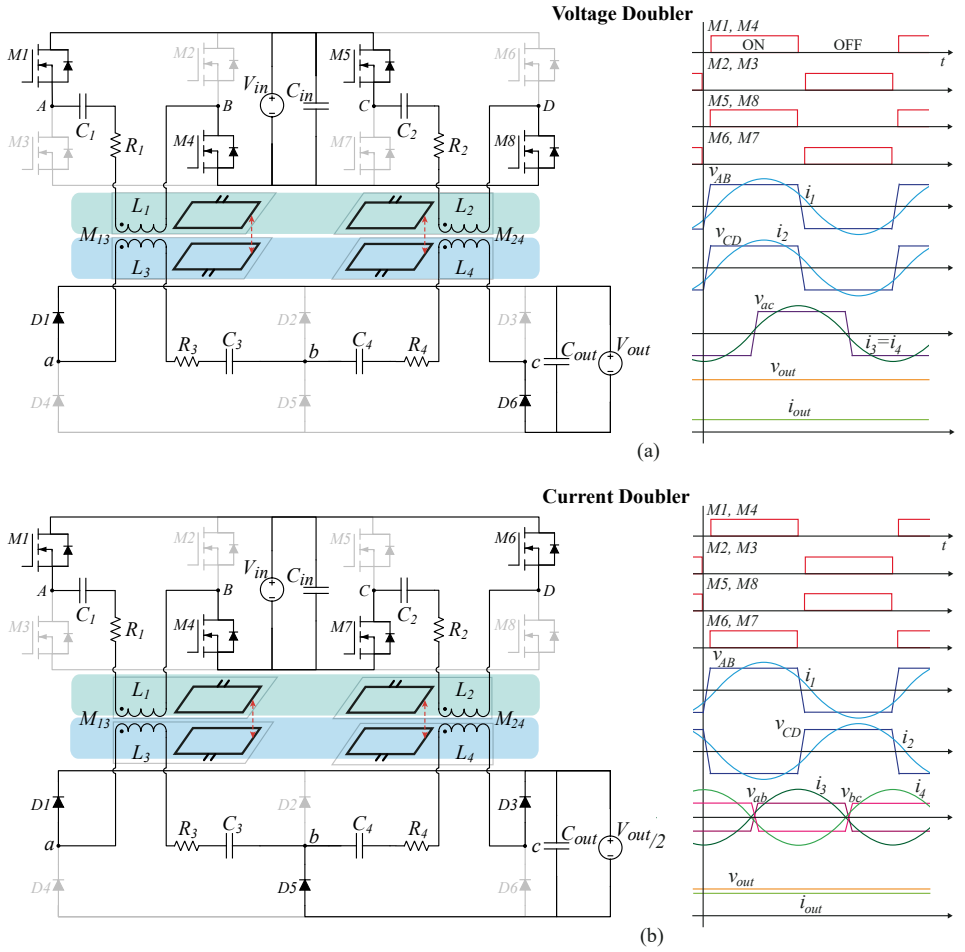

Figure 4.2: Semiconductor devices conducting during the positive half wave of V_{AB} and typical waveforms when the V/I-D converter operates as: (a) voltage doubler and (b) current doubler, which equivalent circuits are shown in Figure 4.3(a), and Figure 4.3(b), respectively.

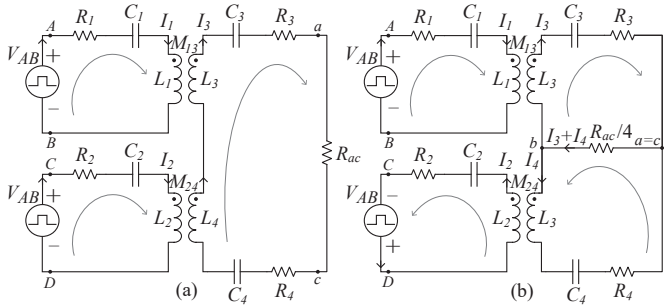

Figure 4.3: Equivalent circuit in the frequency domain of Figure 4.1 when operating as: (a) voltage doubler, and (b) current doubler.

Contrarily, when the half-bridge legs with mid-point A and D have the modulation shown in Figure 4.2(b), the current through the secondary coils has opposite direction and, consequently, L_3 and L_4 result in an equivalent parallel connection. In this case, D1, D3, and D5 conduct during the positive half-wave of V_{ab} while D2, D4, and D6 conduct during the negative one. Figure 4.2 shows that the secondary coils conduct the same nominal current as in the previous modulation, but their parallel connection results in double the load current. This modulation is called current doubler mode since it is suitable for the rated power charging of 400 V batteries.

The equivalent circuit in the frequency domain of the voltage doubler mode is shown in Figure 4.3(a), while the current doubler mode is shown in Figure 4.3(b). The circuit in Figure 4.3(a) is described by the Kirchhoff voltage law in (4.1) while the one in Figure 4.3(b) is described by (4.2). Thereby, the EV battery is replaced by the equivalent first-harmonic load R_{ac} in (4.3) defined in [8] and [9].

Thereby, the impedance $\boldsymbol{Z_i}$ of each resonant circuit is defined in (4.4), and the mutual inductances M_{ih} are expressed in (4.5) which depend on the coupling factor k_{ih}. Figure 4.1, Figure 4.2, and Figure 4.3 highlight only M_{13} and M_{24} since they are the main mutual inductances functional to the operation of the V/I-D converter. On the other hand, M_{12} and M_{34} are due to the cross-coupling present between the two coils placed at each side of the two transformers, while M_{14} and M_{23} are due to the diagonal cross-coupling between the two transformers. $\boldsymbol{V_{AB}}$ is taken as reference according to the phasor convention, and it is defined in (4.6) through the first-harmonic approximation.

$$\begin{bmatrix} \boldsymbol{V_{AB}} \\ \boldsymbol{V_{CD}} \\ 0 \\ 0 \end{bmatrix} = \begin{bmatrix} \boldsymbol{Z_1} & j\omega M_{12} & j\omega(M_{13}+M_{14}) & 0 \\ j\omega M_{12} & \boldsymbol{Z_2} & j\omega(M_{23}+M_{24}) & 0 \\ j\omega(M_{13}+M_{14}) & j\omega(M_{23}+M_{24}) & (\boldsymbol{Z_3}+\boldsymbol{Z_4}+R_{ac}+2j\omega M_{34}) & 0 \\ 0 & 0 & 1 & -1 \end{bmatrix} \begin{bmatrix} \boldsymbol{I_1} \\ \boldsymbol{I_2} \\ \boldsymbol{I_3} \\ \boldsymbol{I_4} \end{bmatrix} \tag{4.1}$$

$$\begin{bmatrix} \boldsymbol{V_{AB}} \\ \boldsymbol{V_{CD}} \\ 0 \\ 0 \end{bmatrix} = \begin{bmatrix} \boldsymbol{Z_1} & -j\omega M_{12} & j\omega M_{13} & -j\omega M_{14} \\ -j\omega M_{12} & \boldsymbol{Z_2} & -j\omega M_{23} & j\omega M_{24} \\ j\omega M_{13} & -j\omega M_{23} & (\boldsymbol{Z_3}+\frac{R_{ac}}{4}) & (-j\omega M_{34}+\frac{R_{ac}}{4}) \\ -j\omega M_{14} & j\omega M_{24} & (-j\omega M_{34}+\frac{R_{ac}}{4}) & (\boldsymbol{Z_4}+\frac{R_{ac}}{4}) \end{bmatrix} \begin{bmatrix} \boldsymbol{I_1} \\ \boldsymbol{I_2} \\ \boldsymbol{I_3} \\ \boldsymbol{I_4} \end{bmatrix} \tag{4.2}$$

$$R_{ac} = \frac{8}{\pi^2} R_L = \frac{8}{\pi^2} \frac{V_{out,\max}^2}{P_{out}} \tag{4.3}$$

$$\boldsymbol{Z_i} = R_i + j\omega X_i, \quad X_i = \omega L_i - \frac{1}{\omega C_i}: \quad i = 1...4 \tag{4.4}$$

$$M_{ih} = M_{hi} = k_{ih}\sqrt{L_i L_h}: \quad i,h = 1...4 \wedge i \neq h \tag{4.5}$$

$$\boldsymbol{V_{AB}} = V_{AB}\underline{/0°} = \frac{4}{\pi} V_{in}, \quad V_{AB} = V_{CD} \tag{4.6}$$

Additionally, for a given processed power, the V/I-D resonant circuit's efficiency η_{res} is defined in (4.7).

$$\eta_{res} = \begin{cases} \dfrac{R_{ac}|\boldsymbol{I_3}|^2}{V_{AB}(|\mathrm{Re}[\boldsymbol{I_1}]| + |\mathrm{Re}[\boldsymbol{I_2}]|)} & \text{if voltage doubler (from(4.1))} \\ \dfrac{\frac{R_{ac}}{4}(|\boldsymbol{I_3}| + |\boldsymbol{I_4}|)^2}{V_{AB}(|\mathrm{Re}[\boldsymbol{I_1}]| + |\mathrm{Re}[\boldsymbol{I_2}]|)} & \text{if current doubler (from(4.2))} \end{cases} \tag{4.7}$$

The total DC-to-DC efficiency $\eta_{\text{DC-to-DC}}$ also considers the power losses of the inverting and rectifying stages of which parameters can be extrapolated from the devices' datasheet.

The power losses of the H-bridge inverters are

$$P_{inv} = 4 \cdot R_{ds,on} \cdot \left[\left(\frac{\hat{I}_1}{2} \right)^2 + \left(\frac{\hat{I}_2}{2} \right)^2 \right] + E_{sw} \cdot f_0 \tag{4.8}$$

where $R_{ds,on}$ is the on-resistance of the MOSFETs and E_{sw} is the total switching energy loss defined in (4.9). Thereby, E_{off} is the turn-off energy loss, E_{on} is the turn-on energy loss, and Q_{rr} is the reverse recovery charge of the body diode.

$$E_{sw} = \sum_{i=1}^{8} E_{off_{(Mi)}} + \sum_{i=1}^{8} E_{on_{(Mi)}} + \sum_{i=1}^{8} Q_{rr_{(Mi)}} V_{ds,off} \tag{4.9}$$

Since C_3 and C_4 are chosen such that $X_3 \approx X_4 \approx 0$, the rectifier's power losses are mainly due to the conduction:

$$P_{rect} = \begin{cases} 4 \cdot \left[V_F \left(\dfrac{\hat{I}_3}{\pi} \right) + r \left(\dfrac{\hat{I}_3}{2} \right)^2 \right] & \text{if V-Doubler} \\ 4 \cdot \left[V_F \left(\dfrac{\hat{I}_3 + \hat{I}_4}{\pi} \right) + r \left(\dfrac{\hat{I}_3 + \hat{I}_4}{2} \right)^2 \right] & \text{if I-Doubler} \end{cases} \tag{4.10}$$

In (4.10), it is assumed that the diodes $D2$ and $D5$ are assembled with two parallel diodes of the same technology used in $D1$, $D3$, $D4$, and $D6$. Therein, V_F is the constant voltage drop of the bipolar technology, while r models the linear increment of the voltage drop across the diode as a function of the flowing current.

Finally, $\eta_{\text{DC-to-DC}}$ can be computed as

$$\eta_{\text{DC-to-DC}} = \eta_{res} \cdot \frac{P_{out}}{P_{out} + P_{inv} + P_{rec}} \tag{4.11}$$

4.2.2. CIRCUIT PARAMETERS' SELECTION

The parameters of the V/I-D converter must be chosen to ensure high power transfer efficiency. For simplicity, the parameters' selection criteria consider the symmetry in (4.12) between the primary and the secondary circuits. Additionally, Section 4.5 will prove the V/I-D converter' functionality even in the case that this ideal symmetry is not met.

$$\begin{aligned} &L_1 = L_2 = L_{1D}; \quad L_3 = L_4 = L_{2D}; \\ &R_1 = R_2 = R_{1D}; \quad R_3 = R_4 = R_{2D}; \\ &M_D = M_{13} = M_{24}; \quad k_D = k_{13} = k_{24} \end{aligned} \tag{4.12}$$

In (4.12), L_{1D} and R_{1D} are the self-inductance and the resistance of the primary coils, L_{2D} and R_{2D} are the self-inductance and the resistance of the secondary coils, M_D is the value of both main functional mutual inductances, and k_D is their relative coupling factor. Moreover, it is assumed that the coils' cross-coupling is negligible.

The choice of L_{1D} and L_{2D} follows from (4.14)-(4.16). The first condition in (4.14) ensures that the conduction losses in the primary and the secondary circuits are balanced. To achieve that, the ratio between the coils' resistances R_{1D} and R_{2D} must be dependent on the ratio between the maximum DC input voltage $V_{in,max}$ available and the minimum battery voltage $V_{out,min}$ which has been derived from (4.13). The second condition in (4.15) has been found by assuming that the coils' quality factor Q_{1D}, Q_{2D} differs from the constant a, which depends on the coils' geometry and structure. Finally, the target value of mutual inductance M_D can be found from (4.16), which is well-known from the S-S compensation. M_D depends on $V_{in,max}$, the maximum battery voltage $V_{out,max}$, the target output power P_{out}, and the resonant angular frequency ω_0=2πf_0. Finally, the values of L_{1D} and L_{2D} resulting from (4.14)-(4.16) are shown in (4.17).

$$\begin{aligned} &\hat{I}_{1D} = \frac{\pi}{2} I_{in}, \quad \hat{I}_{2D} = \frac{\pi}{2} I_{out} \\ &P_{in} \approx P_{out} \quad \rightarrow \quad \frac{I_{in}}{I_{out}} = \frac{V_{out,min}}{V_{in,max}} = \frac{I_{1D}}{I_{2D}} \end{aligned} \tag{4.13}$$

$$\begin{cases} R_{1D} I_{1D}^2 = R_{2D} I_{2D}^2 \quad \rightarrow \quad \dfrac{R_{1D}}{R_{2D}} = \dfrac{I_{2D}^2}{I_{1D}^2} = \dfrac{V_{in,max}^2}{V_{out,min}^2} & (4.14) \\ Q_{1D} = a \cdot Q_{2D} \quad \rightarrow \quad \dfrac{\omega_0 L_{1D}}{R_{1D}} = \dfrac{a \cdot \omega_0 L_{2D}}{R_{2D}} & (4.15) \\ M_D = \dfrac{8}{\pi^2} \dfrac{V_{in,max} V_{out,max}}{\omega_0 P_{out}} = k_D \sqrt{L_{1D} L_{2D}} & (4.16) \end{cases}$$

$$L_{1D} = \frac{M_D}{k_D} \frac{I_{2D}}{I_{1D}} \sqrt{a}, \quad L_{2D} = \frac{M_D}{k_D} \frac{I_{1D}}{I_{2D}} \frac{1}{\sqrt{a}} \tag{4.17}$$

The compensation capacitance values are selected by imposing X_i=0 in (4.4) for the secondary coils, i.e., if i=[3, 4]. On the other hand, the condition X_i >0 holds for the primary coils, i.e., if i=[1, 2], to ensure slightly inductive primary currents achieving the zero voltage switching (ZVS) turn-on of all MOSFETs in Figure 4.1 [10]–[12].

4.3. COMPARISON WITH 1-TO-1 COIL IPT SYSTEMS

To evaluate the advantages of the proposed V/I-D system, its efficiency is compared analytically to the one resulting from a conventional 1-to-1 coil IPT system with S-S compensation in Figure 4.4. A generalized comparison is performed such that engineers and researchers can evaluate the performance of the proposed system based on their specific application.

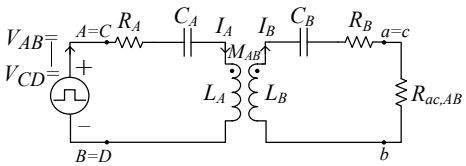

Figure 4.4: Equivalent circuit of the conventional 1-to-1 coil IPT system in the frequency domain. Note that the same semiconductor devices are used as in the V/I-D converter in Figure 4.1.

4.3.1. CIRCUIT MODELING OF THE 1-TO-1 COIL IPT SYSTEM

The circuit in the frequency domain of the 1-to-1 coil IPT system in Figure 4.4 is described by the Kirchhoff voltage law in (4.18). Thereby, the impedances $\boldsymbol{Z_i}$ of the two resonant circuits are defined in (4.19), and the mutual inductance M_{AB} is expressed in (4.20) where k_{AB} is the relative coupling factor. $\boldsymbol{V_{AB}}$ is identical to (4.6). The first-harmonic load $R_{ac,AB}$ depends on the nominal battery voltage as defined in (4.21) for the same output power. This 1-to-1 coil system employs half of the passive components than the V/I-D converter. The same amount of MOSFETs and diodes of the V/I-D converter is used to have equal semiconductor costs for the high-frequency inverting and rectifying power conversion stages.

$$\begin{cases} \boldsymbol{V_{AB}} = \boldsymbol{Z_A I_A} + j\omega M_{AB} \boldsymbol{I_B} \\ 0 = (\boldsymbol{Z_B} + R_{ac,AB}) \boldsymbol{I_B} + j\omega M_{AB} \boldsymbol{I_A} \end{cases} \tag{4.18}$$

$$\boldsymbol{Z_i} = R_i + j\omega X_i, \quad X_i = \omega L_i - \frac{1}{\omega C_i} : \quad i = [A, B] \tag{4.19}$$

$$M_{AB} = k_{AB} \sqrt{L_A L_B} \tag{4.20}$$

$$R_{ac,AB} = \begin{cases} R_{ac} & \text{if tuned for 800 V batteries} \\ R_{ac}/4 & \text{if tuned for 400 V batteries} \end{cases} \tag{4.21}$$

4.3.2. POWER CONVERSION STAGES

The power conversion stages employed by the V/I-D converter and the 1-to-1 coil IPT systems are shown in Figure 4.5, starting from the grid connection to the EV battery. Both solutions rely on the regulation of the input voltage since, as explained in [13], the S-S compensation has a current-source output directly proportional to $\boldsymbol{V_{AB}}$. By connecting to the 1-ϕ European 230 V RMS-rated grid line-to-neutral voltage through a boost-like power factor correction (PFC) rectifier as shown in Figure 4.5, V_{in} can be safely regulated in the range of 360...500 V. Lower values of the $\boldsymbol{V_{AB}}$ fundamental can be achieved by phase shifting the H-bridge inverters.

The V/I-D converter employs only the input voltage control and has a direct connection to the EV battery. On the other hand, the 1-to-1 coil system is provided with a 99%

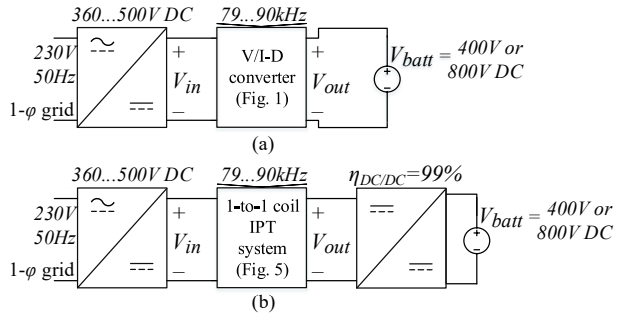

Figure 4.5: Power conversion stages of: (a) the V/I-D converter, (b) the conventional 1-to-1 coil IPT system.

efficient DC/DC converter, as shown in Figure 4.5(b), which would conduct only in the case that the current EV battery voltage differs from the nominal to match the optimum load condition.

4.3.3. ASSUMPTIONS

The comparison between the proposed V/I-D converter and the 1-to-1 coil system has been performed considering the input parameters and semiconductor devices listed in Table 4.1. Both systems are designed for the nominal operation such that V_{in} is in the range of 500 V.

Table 4.1: Input parameters and semiconductor devices used in the comparison of Section 4.3.

Input parameters	P_{out}	7.2 kW	**Semiconductors***	$M1...M8$	C2M0040120D
	V_{out}	400 V, 800 V		$R_{ds,on}$	50 mΩ
	V_{in}	360...500 V (1ϕ)		E_{off}	1 µJ
	f_0	85 kHz		D1...D8	C4D15120D
	k_D	0.15, 0.25, 0.35		V_F	0.8 V
	Q_D	100...400		r	75 mΩ
	M_D	82.63 µH from (4.16)		*datasheet values @125 °C	

For the 1-to-1 coil system, two designs have been considered: one with 400 V as nominal battery voltage, and the other with 800 V. In both cases, when the battery voltage differs from the nominal value, the 1-to-1 coil system can supply the same output power through a DC/DC converter, as shown in Figure 4.5(b). Moreover, the option of not using the DC/DC converter is also explored for the 400 V 1-to-1 coil system. In this case, only the input voltage is regulated to deliver the same output power to 800 V batteries.

Table 4.2: Circuit parameters of the conventional 1-to-1 coil IPT system relatively to the V/I-D system' ones.

	M_{AB}	I_A	L_A	R_A	Q_A
400 V	$M_D/2$	$2 \cdot I_{1D}$	$L_{1D}/2$	$R_{1D}/2$	Q_{1D}
800 V	M_D	$2 \cdot I_{1D}$	$L_{1D}/2$	$R_{1D}/2$	
	k_{AB}	I_B	L_B	R_B	Q_B
400 V	k_D	$2 \cdot I_{2D}$	$L_{2D}/2$	$R_{2D}/2$	Q_{2D}
800 V		I_{2D}	$2 \cdot L_{2D}$	$2 \cdot R_{1D}$	

The 1-to-1 circuit parameters in Table 4.2 have been chosen in terms of the V/I-D's ones assuming that:

- at the nominal operating conditions, the lumped conduction power losses are equal in the resonant circuits of the 1-to-1 coil system and the V/I-D system;
- the coefficient a in (4.15) is considered such that a=1, resulting in the primary and secondary coils having the same quality factor: Q_{1D}=Q_{2D}=Q_D.

4.3.4. ANALYSIS

The computed efficiency comparison is shown in Figure 4.6 in terms of Q_D and k_D. Figure 4.6(a) shows the efficiency comparison of the resonant circuits, while Figure 4.6(b) and Figure 4.6(c) show the overall DC-to-DC efficiency including the losses of the semi-

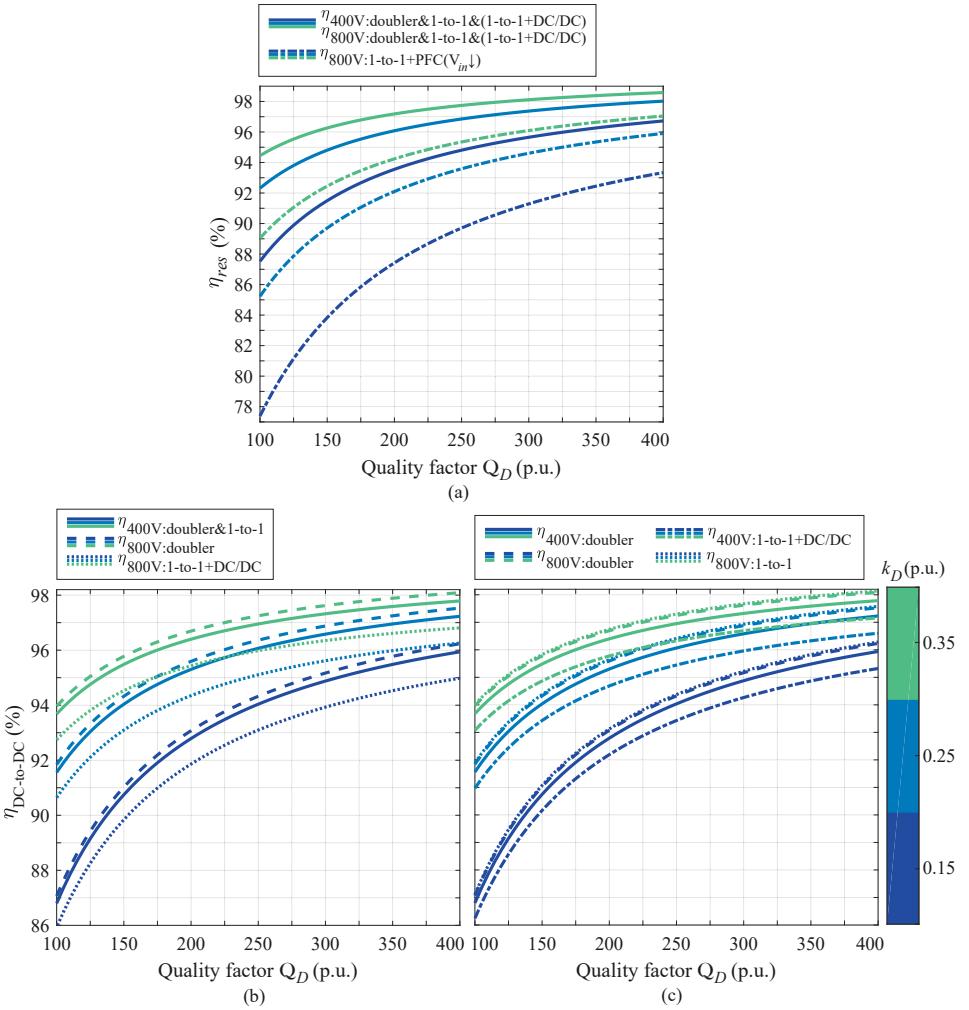

Figure 4.6: Analytical power transfer efficiency of the proposed V/I-D converter and the 1-to-1 coil IPT system at different coils' magnetic coupling k_D and quality factor Q_D=Q_{1D}=Q_{2D} defined in (4.12). Plot of: (a) resonant circuit efficiency; (b),(c) DC-to-DC efficiency (the power losses consider both the semiconductor devices and resonant circuits), where 1-to-1 coil IPT system is designed for a nominal battery voltage of: (b) 400 V, (c) 800 V.

conductor devices whose main parameters are listed in Table 4.1. Thereby, several values of Q_D and k_D are considered for the same M_D in Table 4.1. This makes the analysis generic and applicable to all typical IPT systems designed at this power level.

Figure 4.6(a) shows that, in the two systems, the losses of the resonant circuits stay the same at both 400 V and 800 V if the 1-to-1 coil system uses a DC/DC converter to match the optimum load condition. On the other hand, if the 400 V 1-to-1 coil system delivers the same power to 800 V batteries by stepping down the input voltage without a DC/DC converter, the power transfer efficiency of the resonant circuit would considerably decrease by up to 10%. This is caused by R_L being four times larger than the nominal optimum condition leading to a higher primary current. Given this large efficiency drop, this solution is discarded in the following comparisons.

Contrarily than in Figure 4.6(a), Figure 4.6(b) and Figure 4.6(c) show that there is a difference between the computed efficiencies at 400 V and 800 V. In the case of solely considering the V/I-D converter, the current doubler mode (400 V battery) has more losses since the number of diodes conducting is twice that of the voltage doubler mode (800 V battery). This has been shown in Figure 4.2(b). When considering the 1-to-1 coil system, the designs with 800 V as nominal V_{out} are more efficient than the ones at 400 V since the current flowing through the rectifying diodes is halved for the same power.

When comparing the two different systems, the proposed V/I-D system is up to 1% more efficient. For instance, at the same k_D, the two systems would have the same efficiency if the 1-to-1 coil system is equipped with coils having a larger quality factor. This might put more requirements on the coils' design. For example, when k_D=0.35 in Figure 4.6(c), an efficiency of 97% can be reached by the V/I-D converter operating in the current doubler mode (400 V battery) if Q_D=250. The same efficiency can be achieved by the 1-to-1 coil system when operating with a 400 V battery if the coils have Q_D=350. This difference is even more considerable in Figure 4.6(b).

4.3.5. COST AND COMPLEXITY CONSIDERATIONS

The V/I-D converter has the great advantage of employing only passive semiconductor devices at the secondary circuit, simplifying the circuit and control on board the EV.

Regarding the cost, it is reasonable to assume that the two systems use the same high-frequency inverting and rectifying power conversion stages since each H-bridge of the V/I-D converter is sized for half the power of the 1-to-1 coil system. When considering the coupled coils, from Table 4.2, it can be deduced that the 1-to-1 coil system requires using a Litz wire with more strands in the windings while the core magnetic saturation must also be fulfilled. Thus, the transformer will be naturally sized according to the processed power. Therefore, the size of the components in the two systems would be equivalent if they are fully utilized. Nevertheless, the possible total higher cost of implementing two sets of coupled coils in the V/I-D converter would be undoubtedly overcome by the price of a highly efficient DC/DC converter that must operate in an extensive range, i.e., between 400 V and 800 V.

4.4. EXPERIMENTAL IMPLEMENTATION

The proposed V/I-D converter has been implemented as a laboratory demonstrator suitable for the 7.7 kW power class.

4.4.1. LABORATORY PROTOTYPE

The two sets of coupled coils have been designed as shown in Figure 4.7. The parameters' selection follows the approach explained in Section 4.2.2, and they are summarized in Table 4.3. The coils have a different number of turns to prove that the V/I-D converter can also operate in the case that the ideal condition in (4.12) is not met. The resulting M_{13} and M_{24} are similar, and they are in the same range of the target M_D in Table 4.1. Since the distance Δx between the two sets is much larger than the coils' dimensions, their cross-coupling mutual inductances M_{12}, M_{34}, M_{14}, M_{23} are negligible.

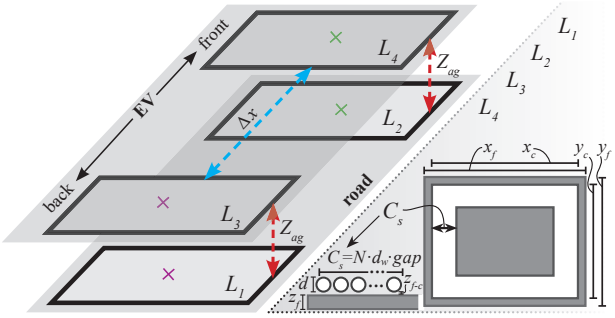

Figure 4.7: Coils arrangement of the proposed V/I-D system for EV wireless charging which circuit schematic is shown in Figure 4.1.

Figure 4.8 shows the 7.7 kW prototype, including the compensation capacitors and the power converters. The Delta Elektronika bidirectional power supplies SM500-CP-90 and SM1500-CP-30 are used as input and output voltage sources. The input power supply operates in the voltage range that resembles the boost-like PFC converter, which could be implemented as explained in [14] and [15], while the output power supply emulates the EV battery voltage. It is assumed that V_{in} is set according to the load, which information is given by the wireless communication required from the IPT system for several features such as guided positioning, pairing, and safety.

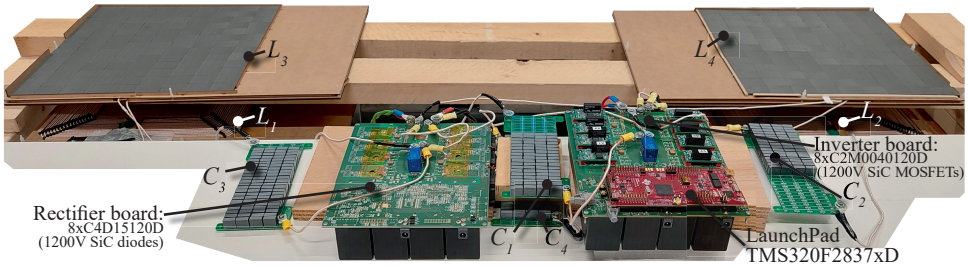

Figure 4.8: Developed 7.7 kW V/I-D converter for EV wireless charging.

4.4.2. ANALYSIS OF THE OPERATING POINTS

Before validating the functionality of the V/I-D converter experimentally, it is essential to assess the operating points resulting from different misalignment conditions between the coupled coils. In particular, given the sets of coupled coils in Figure 4.8, two misalignment profiles have been identified: the lateral misalignment in either the x- or the y-direction shown in Figure 4.9(a), and the tilted misalignment shown in Figure 4.9(b).

Table 4.3: Measured circuit parameters and coils' dimensions.

	N	L (µH)	R (mΩ)	M (µH)	Coils' dimensions (mm) with respect to Figure 4.7		
L_1	17	246.9	420	M_{13}	x_f, y_f, z_f	C_s	$z_{f\text{-}c}$
L_2	18	276.1	440	80.2	387, 364, 4.1	65	4
L_3	15	185.3	360	M_{24}	x_c, y_c, d_w	Z_{ag}	Δx
L_4	14	161.7	340	78.5	355, 350, 2.4	100	1000
E planar core: 3C95, PLT43/28/4.1					Litz wire: 600 x 0.071mm		
(C_1, C_2, C_3, C_4) = (14.92, 13.27, 19.05, 21.62)nF →4x(18,16,23,25)*							
*(series x parallel): KEMET R76TF13305050J 3.3 nF (ESR=0.22 Ω)							

Considering that the coils are roughly squared shaped, the two directions of lateral misalignment would have a similar impact on the power transfer, and, in that case, M_{13} and M_{24} would vary proportionally. On the other hand, a tilted misalignment would cause an imbalance between M_{13} and M_{24}. The effect of these two misalignment profiles is investigated in Figure 4.10 resulting from the analytical model of Section 4.2.1. The performance of the V/I-D converter is assessed in both the voltage doubler (800 V batteries) and the current doubler (400 V batteries) modes for an output power of 7.2 kW. The switching frequency of 86.5 kHz is chosen since it is confined within the range of 79...90 kHz established by SAE J2954 [16] and it ensures the ZVS turn-on of the H-bridge inverters at the nominal alignment with low circulating reactive currents. The performance is assessed in terms of the absolute value and the phase angle of the primary currents $\boldsymbol{I_1}$ and $\boldsymbol{I_2}$, the absolute value of the secondary currents $\boldsymbol{I_3}$ and $\boldsymbol{I_4}$, the $\eta_{\text{DC-to-DC}}$, and the required V_{in}.

Figure 4.10(a) addresses the effect of the lateral misalignment on the power transfer. For that purpose, M_{13} and M_{24} are proportionally reduced up to 50% of their nominal value in Table 4.3. It is possible to notice that the $\eta_{\text{DC-to-DC}}$ drops with the misalignment. This is due to the lower V_{in} required to deliver the same output power, translating into higher primary currents, which worsen the conduction losses. The ZVS turn-on of the H-bridge inverters is preserved. However, the primary currents become more inductive with the lateral misalignment leading to larger circulating reactive currents and higher turn-off losses. The input voltage can be regulated through the PFC rectifier up to 68% of the nominal mutual inductance.

On the other hand, Figure 4.10(b) and Figure 4.10(c) investigate the effect of the tilted misalignment on the power transfer. Thereby, only one mutual inductance is gradually reduced while keeping the other constant to its nominal value. In the voltage doubler operation, this misalignment profile would eventually cause the hard-switching of the H-bridge inverter supplying the coils with higher coupling while the other H-bridge in-

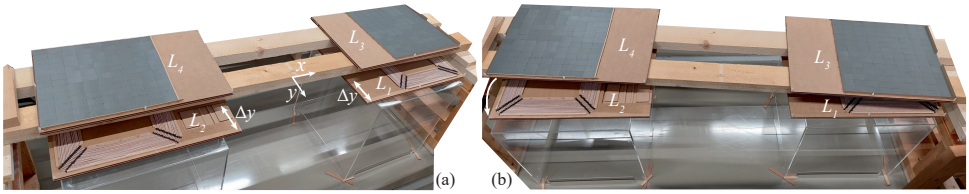

Figure 4.9: Coils' position in the presence of: (a) lateral misalignment, (b) tilted misalignment.

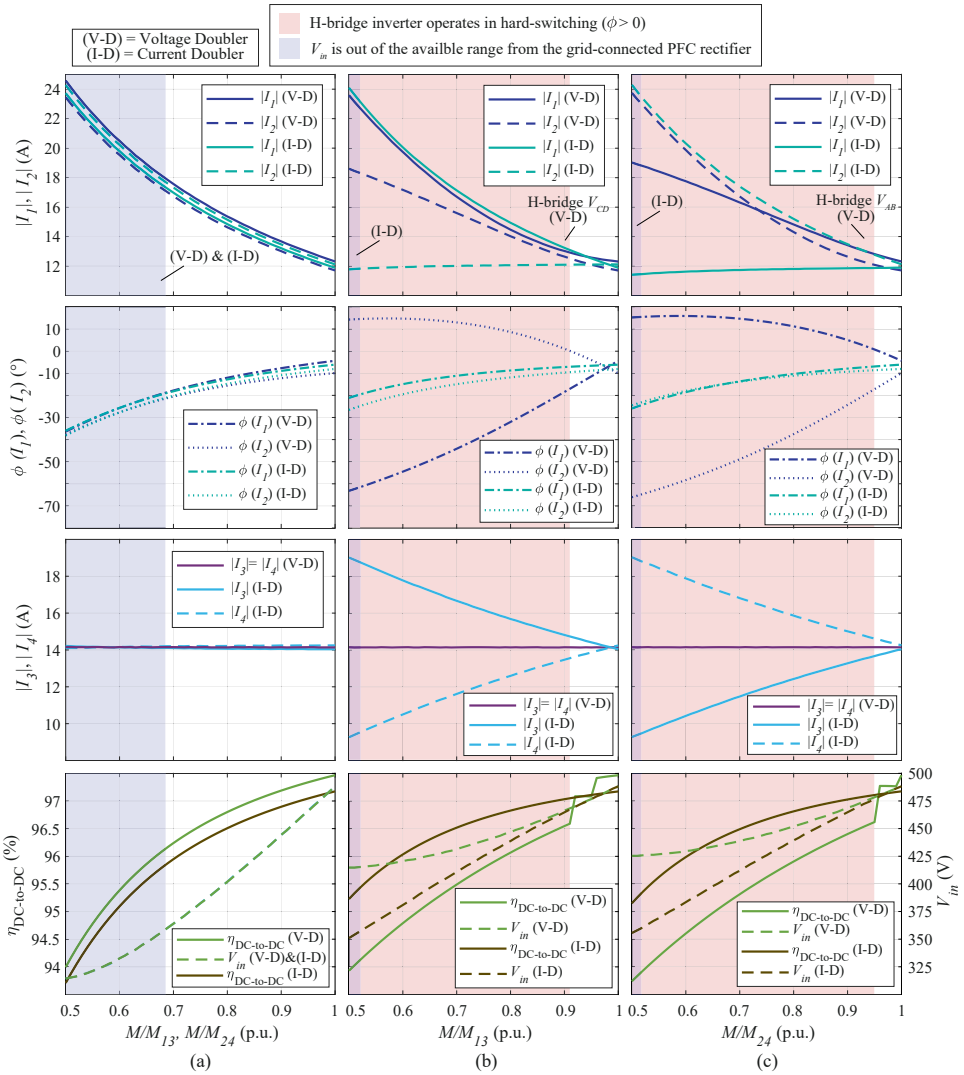

Figure 4.10: Operating points of the V/I-D converter in terms of the absolute value and phase angle of $\boldsymbol{I_1}$ and $\boldsymbol{I_2}$, the absolute value of $\boldsymbol{I_3}$ and $\boldsymbol{I_4}$, the $\eta_{\text{DC-to-DC}}$, and the required V_{in} depending on the normalized main mutual inductances with respect to the nominal M_{13} and M_{24} in Table 4.3. (a) Both M_{13} and M_{24} are varied proportionally (lateral misalignment); (b) only M_{13} is varied (tilted misalignment); (c) only M_{24} is varied (tilted misalignment). The results are computed from the analytical model supposing that the output power of 7.2 kW is delivered at a switching frequency of 86.5 kHz. The red-shaded areas denote the operating regions in which the hard-switching of the H-bridge inverter occurs. The blue-shaded areas indicate whether the required V_{in} is out of the available range from the grid-connected PFC rectifier.

verter would operate in a highly inductive region of the resonant circuit. This operation is due to the unbalanced reflected impedance at the primary circuits while the secondary circuits conduct the same amount of current. This means that the MOSFETs of the inverting stages must be equipped with a suitable thermal management system to with-

stand the additional power losses introduced by the hard-switching operating points. This behavior is not present in the current doubler operation due to the equivalent parallel connection of the secondary circuits, which allows their currents to be unequal. Nevertheless, the current doubler mode has a considerable current unbalance between the two resonant circuits. Additionally, the tilted misalignment requires an input voltage that can be mainly supplied PFC rectifier.

In Figure 4.10, the resulting $\eta_{\text{DC-to-DC}}$ is mostly over 94%. Note that the sharp decreases in $\eta_{\text{DC-to-DC}}$ correspond to transitions into hard-switching operating areas.

4.4.3. V/I-D CONVERTER'S PERFORMANCE AT LOWER VALUES OF Δx

In the laboratory demonstrator illustrated in Figure 4.8, the two sets of coupled coils are placed considerably far from each other to minimize the undesired cross-coupling. However, in reality, a shorter distance would ease the installation of the proposed V/I-D converter on EVs. For that purpose, it is interesting to assess the minimum distance Δx that would still lead to a negligible cross-coupling.

Figure 4.11 shows the values of the self-inductance and the mutual inductance of all four coils depending on Δx resulting from measurement and simulated through the finite element method (FEM) in COMSOL Multiphysics. The self-inductances, M_{13}, and M_{24} stay approximately constant over Δx. Conversely, the mutual inductances related to the cross-coupling become larger as Δx approaches zero. It must be noted that those instances have negative values due to the direction of the concatenated magnetic field.

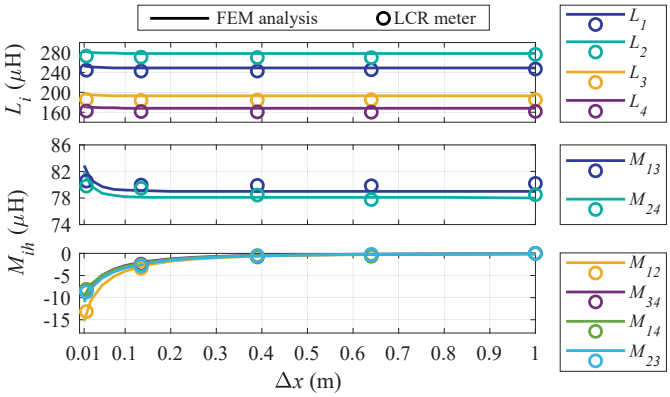

Figure 4.11: Values of the self-inductance and the mutual inductance of the four rectangular coils depending on the Δx in Figure 4.7.

To determine the minimum value of Δx that makes the cross-coupling tolerable, the performance of the V/I-D converter has been assessed for the whole range of Δx. This analysis has been performed through the analytical model for an output power of 7.2 kW, 86.5 kHz switching frequency and aligned coils. The results are summarized in Figure 4.12. The operating points marked with the light blue-shaded areas, i.e., for Δx>0.25 m, would result in a performance similar to the one at Δx=1 m used in Figure 4.8. Nevertheless, it is preferable to conservatively select Δx=0.35 m as the minimum distance to guarantee that the cross-coupling would be negligible also when the receiver coils have a lateral misalignment of 10 cm.

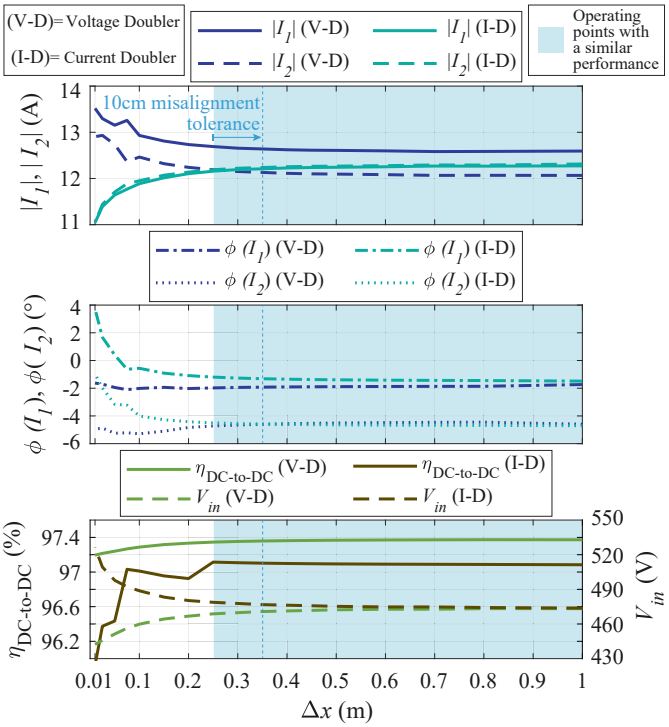

Figure 4.12: Analysis of the V/I-D converter in terms of the absolute value and phase angle of $\boldsymbol{I_1}$ and $\boldsymbol{I_2}$, the $\eta_{\text{DC-to-DC}}$, and the required V_{in} depending on distance Δx in Figure 4.7. The results are computed from the analytical model supposing that the output power of 7.2 kW is delivered at a switching frequency of 86.5 kHz. The light blue-shaded areas denote the operating regions with similar performance.

4.5. EXPERIMENTAL RESULTS

The laboratory prototype in Figure 4.8 has been tested to prove the functionality of the V/I-D converter.

4.5.1. MEASUREMENTS AT THE COILS' NOMINAL ALIGNMENT

The circuit waveforms and the DC input and output measurements for the V/I-D system operating at rated power are shown in Figure 4.13(a) for the current doubler mode, while Figure 4.13(b) shows the voltage doubler mode. The operation of the H-bridge inverters follows the same logic illustrated in Figure 4.2 and Figure 4.2. The operating frequency of 86.5 kHz selected in Section 4.4.2 leads to the ZVS turn-on of all MOSFETs. The DC-to-DC efficiency of 97.11% and 97.52% have been measured at 7.2 kW for an output voltage of 400 V and 800 V, respectively. As expected, the efficiency is slightly lower in the current doubler mode because the number of diodes conducting is twice that in the voltage doubler mode.

In reality, V_{out} increases during the constant current (CC) mode of the battery charging cycle. Measurements have been performed for (0.75...1.06)·V_{out} while maintaining I_{out} constant. These measurements are summarized in Figure 4.14. This also proves that the V/I-D scheme works even if V_{out} is not exactly 400 V or 800 V as shown in Table 1.2.

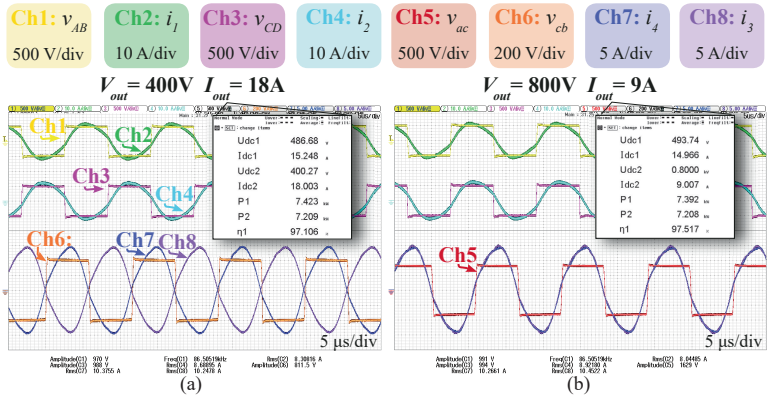

Figure 4.13: Measured circuit waveforms and DC-to-DC efficiency with aligned coils when operating at 86.5 kHz and rated power for both nominal V_{out}: (a) current doubler, (b) voltage doubler.

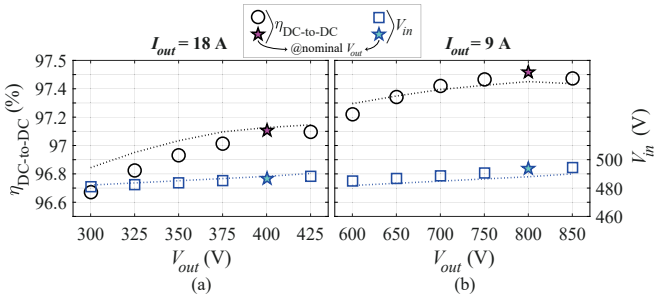

Figure 4.14: Measured DC-to-DC efficiency $\eta_{\text{DC-to-DC}}$ and input voltage V_{in} from the prototype in Figure 4.8 with aligned coils as: (a) current doubler, (b) voltage doubler. The dotted lines result from the analytical model.

During the constant voltage (CV) mode of the battery charging cycle, I_{out} should be gradually reduced until the battery is fully charged. According to [17], the S-S compensation can achieve both CC and CV modes, which CV mode can be realized by stepping down V_{in} through the PFC rectifier. Lower values of the V_{AB} can be achieved by phase shifting the H-bridge inverters. Hereby, the CV mode is not included since this is not the main focus of this work and its control strategies are well-known from the literature. Additionally, for the power level of 7.7 kW, the CC mode takes place for most of the EV battery charging profile. Therefore, it is more critical to ensure high power transfer efficiency during that period to reduce the overall energy consumption.

4.5.2. MEASUREMENTS WITH COILS' MISALIGNMENT

The functionality of the V/I-D converter has been assessed for the misalignment positions shown in Figure 4.9, which parameters are listed in Table 4.4.

Table 4.4: Measured coils' parameters at the alignments in Figure 4.9.

Misalignment	L_1 (µH)	L_2 (µH)	L_3 (µH)	L_4 (µH)	M_{13} (µH)	M_{24} (µH)
Figure 4.9(a): Δy=7 cm	249.8	278.0	186.2	162.8	69.7	66.3
Figure 4.9(a): Δy=9 cm	250.8	279.2	186.5	163.0	57.6	56.6
Figure 4.9(b): tilted	247.7	276.7	185.1	162.3	79.7	50.6

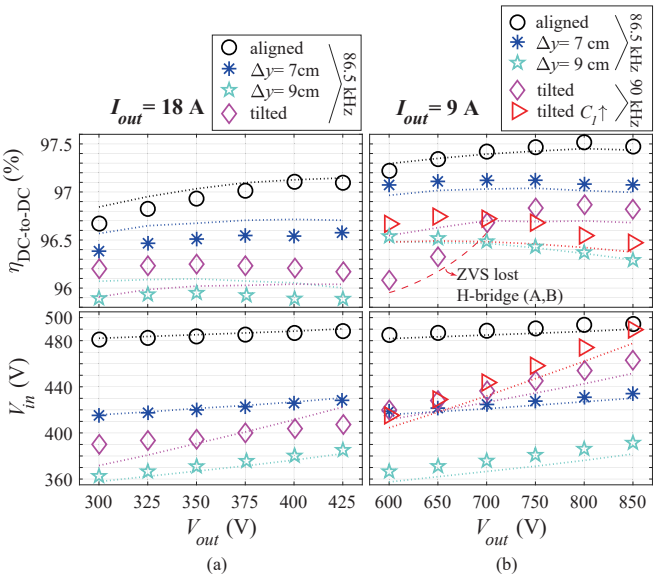

Figure 4.15: Measured DC-to-DC efficiency $\eta_{\text{DC-to-DC}}$ and input voltage V_{in} at different coils' alignments as: (a) current doubler, (b) voltage doubler. The dotted lines result from the analytical model.

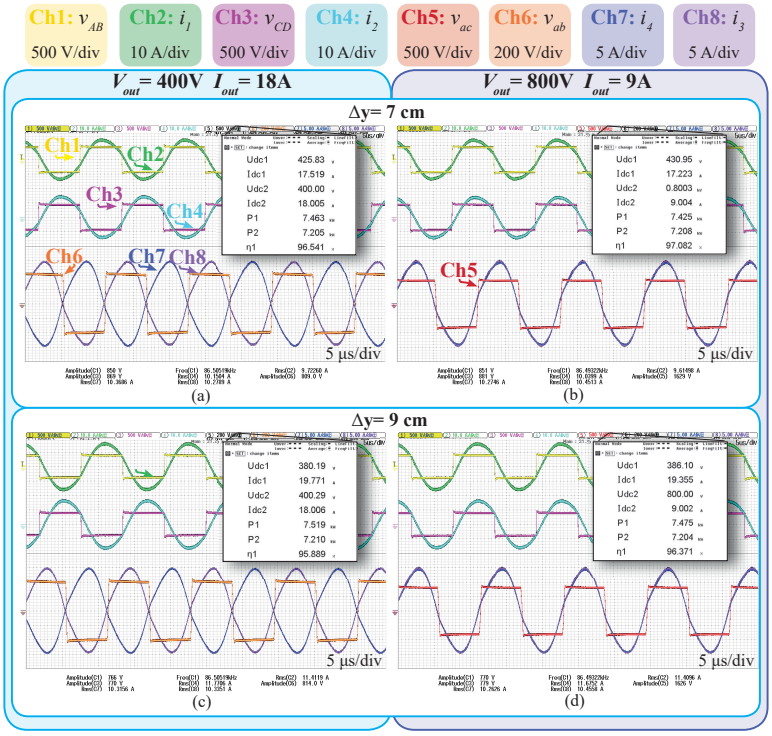

Figure 4.16: Measured circuit waveforms and DC-to-DC efficiency in the presence of lateral misalignment (see Figure 4.9(a)). Operation at 86.5 kHz and rated power for both nominal V_{out} when Δy=7 cm: (a) current doubler, (b) voltage doubler; when Δy=9 cm: (c) current doubler, (c) voltage doubler.

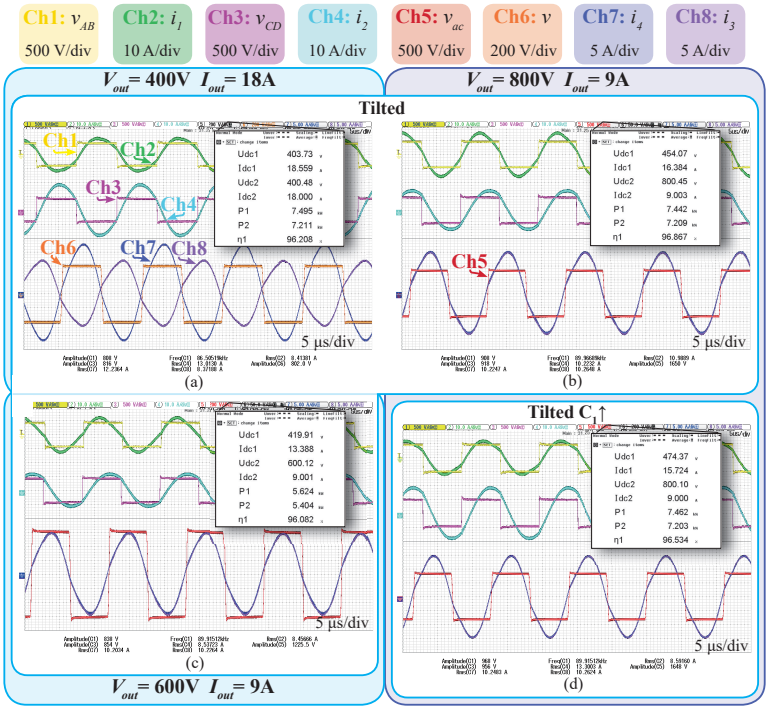

Figure 4.17: Measured circuit waveforms and DC-to-DC efficiency in the presence of tilted misalignment (see Figure 4.9(b)). Operation for both nominal V_{out}, at rated power: (a) current doubler (86.5 kHz) and (b) voltage doubler (90 kHz). (c) Voltage doubler at minimum load (V_{out}=600 V, 90 kHz). (d) Voltage doubler at rated power (90 kHz) with C_1=17.39 nF.

The overall measured $\eta_{\text{DC-to-DC}}$ and the relative V_{in} are shown in Figure 4.15. As expected from the analysis of Section 4.4.2, the DC-to-DC efficiency drops when the misalignment occurs. For the considered coils' alignments, it is possible to follow the entire CC charging using a V_{in} range that the PFC rectifier can provide.

With lateral misalignment at Δy=9 cm, the efficiency measured at the nominal V_{out} drops by 1.15% and 1.22% in the voltage doubler and the current doubler modes, respectively. This is due to higher primary currents increasing the conduction losses for the same output power. Since M_{13} and M_{24} decrease proportionally, balanced currents flow through the primary and the secondary circuits. Additionally, by operating at the same frequency of 86.5 kHz as with the aligned coils, it is possible to keep the ZVS turn-on operation for the entire CC charging. These considerations can be noticed in the measured waveforms of Figure 4.16(a)-(d).

On the other hand, when considering the tilted misalignment, M_{13} and M_{24} do not decrease proportionally. This translates into unbalanced currents within the primary and secondary circuits in both the current doubler and the voltage doubler operations, which waveforms are shown in Figure 4.17(a) and Figure 4.17(b), respectively. In the voltage doubler operation, the considerable difference between M_{13} and M_{24} would cause the hard-switching of the H-bridge inverter with A and B terminals. To mitigate this issue, the switching frequency of both inverters has been increased to 90 kHz. Neverthe-

less, at partial load, the hard-switching still occurs, causing the efficiency drop shown in Figure 4.15(b), of which the waveforms measured at V_{out}=600 V are shown in Figure 4.17(c). Considering that the operation falls slightly in the capacitive region only at partial load, this extra loss can be considered acceptable, especially in the case that the H-bridge inverters employ SiC MOSFETs with forced cooling.

An alternative solution to achieve the ZVS turn-on for the entire CC mode during the voltage doubler mode with tilted misalignment is increasing the value of C_1 to make the equivalent impedance $\boldsymbol{Z_1}$ more inductive. According to Figure 4.15(b), increasing C_1 from 14.92 nF to 17.39 nF results in higher measured $\eta_{\text{DC-to-DC}}$ at partial load. However, the $\eta_{\text{DC-to-DC}}$ drops for higher values of V_{out} due to the increase in the amplitude of I_2 visible from Figure 4.17(d). Since the capacitance must be set only once before the start of the power transfer, this could be implemented through a mechanical switch.

4.5.3. POWER LOSS ANALYSIS

The power loss breakdown of the V/I-D converter has been computed from the analytical models of Section 4.2 for the different coils' alignments, which results in Figure 4.18. The efficiency drop in correspondence of the coils' misalignment is due to the higher circulating current in the primary circuits for the same output power. Additionally, when the lateral misalignment in Figure 4.9(a) occurs, the power losses increase proportionally in both primary circuits. On the other hand, when the coils have the tilted misalignment shown in Figure 4.9(b), it is possible to notice the unbalance in the power losses. For instance, the set of coupled coils with lower mutual inductance would have higher current stress. Nevertheless, the operation of the V/I-D converter would still take place.

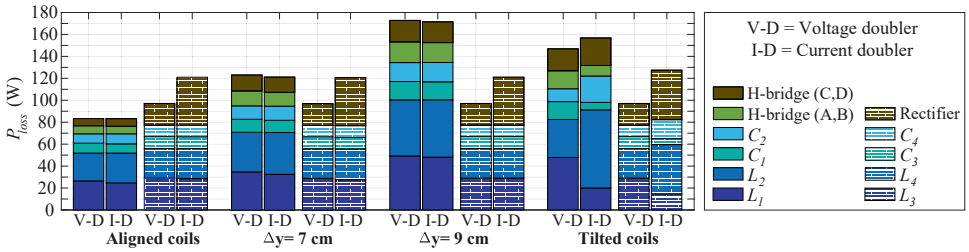

Figure 4.18: Breakdown of the computed power losses at both possible nominal battery voltages at rated power for the different coils' alignments.

4.6. CONCLUSION

This chapter has proposed a new topology defined as voltage/current doubler (V/I-D) for EV wireless charging that supplies the same power with high efficiency to both 400V and 800V batteries. The V/I-D comprises two sets of series-compensated coupled coils connected to a dedicated H-bridge converter. The control is implemented at the primary side by operating the two H-bridge inverters with the same or opposite modulation. The secondary circuit is composed of only passive devices. It has been found that the V/I-D system can be more advantageous in terms of computed power transfer efficiency (up to 1%) than the conventional 1-to-1 coil series-compensated IPT system that uses a 99% efficient DC/DC converter which is operational when the battery voltage differs

from the nominal. Furthermore, the DC/DC converter adds control complexity onboard the EV. The V/I-D system has also been found to be more efficient (up to 10%) than the conventional 1-to-1 coil series-compensated IPT system employing only input voltage control. After that, the proposed V/I-D converter was experimentally verified at 7.2 kW. Considering that the battery voltage could be either 400V or 800V, the peak DC-to-DC efficiency of 97.11% and 97.52% were measured, respectively. Additionally, by regulating the DC input voltage in the range that a power factor correction rectifier could provide, the functionality of the V/I-D converter was proved under different coils' alignments. At 9 cm lateral misalignment, the DC-to-DC efficiency dropped to 95.89% and 96.37% for the output voltage of 400V and 800V, respectively. Finally, the operation in which the axis connecting the geometrical centers of the secondary coils is tilted with respect to one of the primary coils has also been proved. The mutual inductance differs considerably between the two sets of coupled coils, resulting in an uneven distribution of power losses within the primary and secondary circuits. Nevertheless, the functionality of the V/I-D converter has been proven to be still valid.

REFERENCES

[1] R. Bosshard and J. W. Kolar, "All-sic 9.5 kw/dm^3 on-board power electronics for 50 kw/85 khz automotive ipt system", *IEEE Journal of Emerging and Selected Topics in Power Electronics*, vol. 5, no. 1, pp. 419–431, 2017. DOI: 10.1109/JESTPE.2016.2624285.

[2] J. Pries, V. P. N. Galigekere, O. C. Onar, and G.-J. Su, "A 50-kw three-phase wireless power transfer system using bipolar windings and series resonant networks for rotating magnetic fields", *IEEE Transactions on Power Electronics*, vol. 35, no. 5, pp. 4500–4517, 2020. DOI: 10.1109/TPEL.2019.2942065.

[3] W. Shi, F. Grazian, S. Bandyopadhyay, J. Dong, T. B. Soeiro, and P. Bauer, "Analysis of dynamic charging performances of optimized inductive power transfer couplers", in *2021 IEEE 19th International Power Electronics and Motion Control Conference (PEMC)*, 2021, pp. 751–756. DOI: 10.1109/PEMC48073.2021.9432541.

[4] R. Bosshard, J. W. Kolar, and B. Wunsch, "Control method for inductive power transfer with high partial-load efficiency and resonance tracking", in *2014 International Power Electronics Conference (IPEC-Hiroshima 2014 - ECCE ASIA)*, 2014, pp. 2167–2174. DOI: 10.1109/IPEC.2014.6869889.

[5] S. Bandyopadhyay, P. Venugopal, J. Dong, and P. Bauer, "Comparison of magnetic couplers for ipt-based ev charging using multi-objective optimization", *IEEE Transactions on Vehicular Technology*, vol. 68, no. 6, pp. 5416–5429, 2019. DOI: 10.1109/TVT.2019.2909566.

[6] W. Zhang and C. C. Mi, "Compensation topologies of high-power wireless power transfer systems", *IEEE Transactions on Vehicular Technology*, vol. 65, no. 6, pp. 4768–4778, 2016.

[7] H. Wu, X. Zhan, and Y. Xing, "Interleaved llc resonant converter with hybrid rectifier and variable-frequency plus phase-shift control for wide output voltage range applications", *IEEE Transactions on Power Electronics*, vol. 32, no. 6, pp. 4246–4257, 2017. DOI: 10.1109/TPEL.2016.2602545.

[8] R. L. Steigerwald, "A comparison of half-bridge resonant converter topologies", *IEEE Trans. Power Electron.*, vol. 3, no. 2, 1988.

[9] Q. Li and Y. C. Liang, "An inductive power transfer system with a high-q resonant tank for mobile device charging", *IEEE Transactions on Power Electronics*, vol. 30, pp. 6203–6212, 2015.

[10] S. Li, W. Li, J. Deng, T. D. Nguyen, and C. C. Mi, "A double-sided lcc compensation network and its tuning method for wireless power transfer", *IEEE Transactions on Vehicular Technology*, vol. 64, pp. 2261–2273, 2015.

[11] T. Kan, T.-D. Nguyen, J. C. White, R. K. Malhan, and C. C. Mi, "A new integration method for an electric vehicle wireless charging system using lcc compensation topology: Analysis and design", *IEEE Transactions on Power Electronics*, vol. 32, no. 2, pp. 1638–1650, 2017. DOI: 10.1109/TPEL.2016.2552060.

[12] F. Grazian, T. B. Soeiro, P. van Duijsen, and P. Bauer, "Auto-resonant detection method for optimized zvs operation in ipt systems with wide variation of magnetic coupling and load", *IEEE Open Journal of the Industrial Electronics Society*, vol. 2, pp. 326–341, 2021. DOI: 10.1109/OJIES.2021.3072024.

[13] W. Zhang and C. C. Mi, "Compensation topologies of high-power wireless power transfer systems", *IEEE Transactions on Vehicular Technology*, vol. 65, no. 6, pp. 4768–4778, 2016. DOI: 10.1109/TVT.2015.2454292.

[14] J. W. Kolar, J. Biela, and J. Minibock, "Exploring the pareto front of multi-objective single-phase pfc rectifier design optimization - 99.2% efficiency vs. 7kw/din^3 power density", in *2009 IEEE 6th International Power Electronics and Motion Control Conference*, 2009, pp. 1–21. DOI: 10.1109/IPEMC.2009.5289336.

[15] J. P. M. Figueiredo, F. L. Tofoli, and B. L. A. Silva, "A review of single-phase pfc topologies based on the boost converter", in *2010 9th IEEE/IAS International Conference on Industry Applications - INDUSCON 2010*. DOI: 10.1109/INDUSCON.2010.5740015.

[16] *J2954 (r) wireless power transfer for light-duty plug-in/ electric vehicles and alignment methodology*, Oct. 2020.

[17] H. T. Nguyen, J. Y. Alsawalhi, K. A. Hosani, *et al.*, "Review map of comparative designs for wireless high-power transfer systems in ev applications: Maximum efficiency, zpa, and cc/cv modes at fixed resonance frequency independent from coupling coefficient", *IEEE Transactions on Power Electronics*, vol. 37, no. 4, pp. 4857–4876, 2022. DOI: 10.1109/TPEL.2021.3124293.

5

ADVANCED AND COMPACT VOLTAGE/CURRENT DOUBLER CONVERTER USING BIPOLAR PADS

This chapter proposes an advanced and compact version of the previously defined voltage/current doubler (V/I-D), which comprises two coupled series-compensated bipolar pads (BPPs). The presented system can efficiently charge EVs with 400V and 800V battery voltage classes at the same power level without affecting the current rating of the converter's circuit components. The equivalent circuit is analyzed, focusing on the BPPs' undesired cross-coupling and its effect on the power transfer. Methods to compensate for the cross-coupling are proposed regarding the BPP design and the operating strategy. At the output power of 7.2kW and aligned BPPs, the DC-to-DC efficiency of 96.34% and 96.53% have been measured at 400V and 800V, respectively. The proposed method has also been experimentally validated for battery voltages ranging from 75% to 100% of the nominal value and in the presence of misalignment. Additionally, the interoperability of the proposed V/I-D converter is investigated. The functionality of the converter is assessed when the primary BPP is coupled with a standard secondary coil, here being the VA test station WPT2/Z2 from SAE J2954. The operation based on the misalignment is discussed through the analytical model. Then, the interoperability is verified through experimental results for the entire constant current charging mode for a rated output power of 7.2kW. Even

---

This chapter is based on:

- F. Grazian, T. B. Soeiro, P. Bauer, "Voltage/Current Doubler Converter for Electric Vehicle Wireless Charging Employing Bipolar Pads", in *IEEE Journal of Emerging and Selected Topics in Power Electronics*, 2023, (early-access).
- F. Grazian, T. B. Soeiro, P. Bauer, "Interoperability of the Voltage/Current Doubler Converter Employing Bipolar Pads with the SAE J2954 VA WPT2/Z2 for EV Wireless Charging", *2022 20th International Power Electronics and Motion Control (PEMC) Conference*, pp. 346-352.

though the functionality of the V/I-D converter is not optimal during the interoperability, the measured DC-to-DC power transfer efficiency in the considered operating range reaches the maximum at 95.22%, while the minimum is 92.86%.

5.1. INTRODUCTION

Chapter 4 proposes the converter named voltage/current doubler (V/I-D) which circuit schematic is illustrated in Figure 4.1. This is a novel universal wireless charging solution suitable for both 400 V and 800 V battery voltage classes. The V/I-D circuit employs two H-bridge inverters connected to the same DC bus, each powering one set of series-compensated coupled coils. The secondary circuits are connected to a rectification stage directly interfaced with the battery. According to Figure 4.1, the V/I-D converter employs two primary and two secondary coils which, in Chapter 4, are arranged in two physically-separated sets of rectangular coupled coils. Thereby, the distance between these two sets of coupled coils is large enough to eliminate their undesired cross-coupling. In EV wireless charging, this can be achieved by placing one set of coupled coils in correspondence with the back of the EV while the other is installed at the front. In that case, the operation of the V/I-D converter is close to the ideal one. However, this solution does not give much freedom in mounting the IPT system, and it could be significantly limiting for small-size light-duty EVs. On the other hand, the use of multicoil pads would provide a compact magnetic configuration for the V/I-D converter's coupled coils because, in that case, the two coils at each circuit side are deployed on the same ferrite layer. In EV wireless charging applications, the most common multicoil pads are the bipolar pads (BPPs) [1] and the Double-D Quadrature Pad (DDQP) [2] which, as explained in Section 1.2.3, are normally employed to achieve interoperability with rectangular and DD pads. Considering the symmetrical structure of the V/I-D converter, BPPs are preferable as multicoil pads, which geometry is qualitatively shown in Figure 5.1.

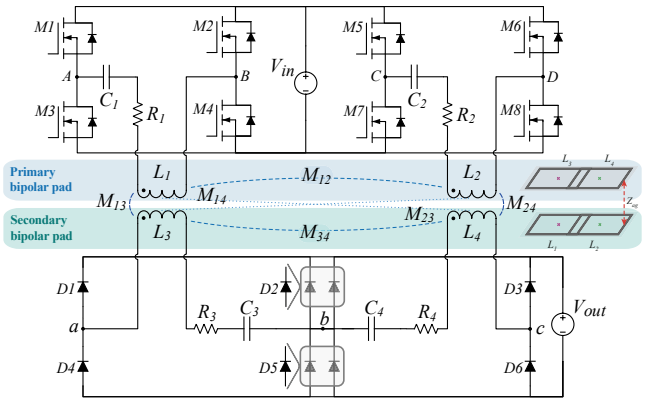

Figure 5.1: V/I-D converter for IPT systems employing series-compensated BPPs. Herein, $D2$ and $D5$ can be advantageously assembled with two parallel diodes of the same technology used in $D1$, $D3$, $D4$, and $D6$. In this case, for a given charging power independently of the voltage or current doubling operation, the current rating of the converter's circuit components is similar.

It must be noted that the proposed V/I-D converter fundamentally differs from the

voltage and current doubling circuits conventionally used in the rectification stage of resonant converters [3]. Generally, those circuits provide the advantage of limiting some components' voltage or current stress, easing their design and implementation. Voltage and current doubling circuits have also been used in IPT systems. For instance, voltage doubler rectifying circuits are employed when the output voltage is considerably greater than the input voltage [4]. On the other hand, it is advantageous to adopt current doubler rectifying circuits in IPT systems with a large output current, as explained in [5]–[7]. However, these conventional doubling circuits have a fixed voltage or current gain optimized for the specific IPT application.

Conversely, the voltage and the current gains of the proposed V/I-D converter are not fixed since 400 V and 800 V batteries can be directly charged at the same power level. This means that the V/I-D converter has a selective output doubling behavior depending on the modulation of the H-bridge inverters. The operation can assume either the voltage doubler mode (suitable for 800 V batteries) or the current doubler mode (suitable for 400 V batteries). As demonstrated in Chapter 4, the two operating modes result in approximately the same power transfer efficiency because the components ideally have the same current stress.

5.1.1. SCOPE AND CONTRIBUTIONS

This chapter explores the feasibility of employing two coupled BPPs as the magnetic arrangement of the V/I-D converter. This implementation intrinsically results in cross-coupling due to the proximity between the two sets of coupled coils, which certainly affects the power transfer of the V/I-D converter. This means that the design guidelines and operating scheme proposed in Chapter 4 would not be suitable for the V/I-D converter using BPPs. Additionally, the interoperability of the V/I-D converter is explored, evaluating the converter's performance when the primary BPP is coupled to a standardized rectangular secondary coil, i.e., the vehicle assembly (VA) test station WPT2/Z2 from SAE J2954 [8]. This is important because it demonstrates that the primary charging circuit of the V/I-D converter can also deliver wireless power to EVs that do not have the intended secondary BPP, enlarging the scope of this converter.

The main contributions are:

- Overview of BPPs in the available literature, providing insights into their main features and use.
- Investigation of the effects of the BPP unwanted cross-coupling on the V/I-D converter's functionality.
- Definition of the operating scheme and the design requirements for the coupled BPPs to mitigate the cross-coupling effects on the power transfer.
- Experimental proof that the proposed V/I-D converter employing BPPs can achieve high power transfer efficiency when charging both 400 V and 800 V at the same power level. At the output power of 7.2 kW and aligned BPPs, the DC-to-DC efficiency of 96.34% and 96.53% have been measured at 400 V and 800 V, respectively.
- Experimental proof of the V/I-D converter's functionality under different misalignment and load conditions typical of EV wireless charging.
- Experimental proof of the V/I-D converter's interoperability, where the primary charging circuit with the BPP delivers wireless power to the standardized VA test station WPT2/Z2 from SAE J2954 used as the secondary coil.

5.1.2. OUTLINE

The main features and challenges due to the undesired cross-coupling of the BPPs are explored in Section 5.2, focusing on the effects on the power transfer. Based on those results, the BPPs are designed through FEM analysis and then implemented. After that, Section 5.3 describes the 7.7 kW laboratory prototype used to verify the functionality of the proposed V/I-D converter. The expected operating points depending on the receiver pad's misalignment are analyzed from the analytical model. The experimental results in terms of DC-to-DC efficiency and circuit waveforms can be found in Section 5.4 for both aligned and misaligned BPPs. The interoperability is discussed in detail in Section 5.5 starting from the equivalent circuit modeling. After that, the operating scheme is analyzed depending on the misalignment. The analysis is proved with experimental results at the output power of 7.2 kW for the entire constant current (CC) charging mode. Finally, the main conclusions are given in Section 5.6.

5.2. BIPOLAR PADS

5.2.1. OVERVIEW: BPP AS A MAGNETIC COIL ARRANGEMENT

The BPP consists of two independent partially-overlapped rectangular coils. It was first introduced in [1] to implement a versatile EV transmitting pad that, depending on the phase of the current flowing through each coil, can work as a polarized or nonpolarized pad. Consequently, the BPP has high interoperability since it has relatively strong magnetic coupling with polarized pads such as double-D pads (DDPs) and nonpolarized pads such as circular or rectangular pads. Other examples of the BPP employed as a transmitting pad for interoperability can be found in [9]–[13]. On the other hand, [14]–[16] explore the advantages of using the BPP as receiving pad. In all these studies, the two coils in the same BPP are magnetically decoupled by appropriately selecting their overlap such that their concatenated magnetic flux approximates zero. As explained in [14], this overlapping area depends on the structure of the BPP itself and also on the configuration of the pad with which the BPP is coupled. Therefore, the overlapping area is generally chosen from the analysis of the pads through the finite element method (FEM).

However, when the BPP is used as both the transmitting and receiving pad, the cross-coupling between the coils placed at the diagonal opposite sides of the circuit would be present. Referring to Figure 5.1, this cross-coupling is denoted by M_{14} and M_{23}. In [17], it has been shown that it is possible to minimize this diagonal cross-coupling by enlarging the overlapping area at the cost of reintroducing the cross-coupling between the coils on the same BPP. This solution might be beneficial since, as shown in [16] and [18], the cross-coupling on the same BPP is relatively constant over the misalignment, which means that its effect could be compensated by adding extra compensation capacitance in the resonant circuit [16], [19], [20].

5.2.2. ANALYSIS: INFLUENCE OF BPPS' CROSS-COUPLING ON THE V/I-D CONVERTER'S FUNCTIONALITY

The V/I-D converter would assume the intended operation explained in Section 4.2.1 when the unwanted cross-coupling between the coupled coils is not present, resulting in the operating scheme illustrated in Figure 4.2. This is the case of the implementation in Chapter 4, where the two sets of coupled coils are placed far from each other. How-

ever, when considering coupled BPPs as the magnetic arrangement, cross-coupling is inevitable to a certain extent. From the Kirchhoff voltage law in (4.1) related to the voltage doubler operation, it is possible to notice that all instances of mutual inductance due to the coils' cross-coupling add up to the main functional mutual inductance. This is because the currents have the same direction in the voltage doubler mode, as shown by Figure 4.2(a). Contrarily, Figure 4.2(b) shows that the currents have opposite directions at each circuit side in the current doubler mode. This justifies the negative signs in (4.2) associated with all the mutual inductance due to the cross-coupling. Therefore, it is interesting to investigate the cross-coupling effects on the V/I-D converter's power transfer to evaluate whether the operating scheme defined in Section 4.2.1 is still valid.

For that purpose, understanding how the cross-coupling within the same BPP and the diagonal cross-coupling between opposite BPPs influence the power transfer of the V/I-D converter is fundamental to assess which of the two must be minimized by adequately designing the BPPs.

ASSUMPTIONS

The influence of the cross-coupling has been evaluated analytically for the two operating modes from (4.1) and (4.2), considering the input parameters listed in Table 5.1. Thereby, the mutual inductance M has been computed from (5.1) considering the three possible values of f_0=$\frac{\omega_0}{2\pi}$. The operating frequency of the H-bridge inverters f_{sw}=f_0 is constrained in the range allowed by SAE J2954, i.e., 79...90 kHz. To keep the analysis generic, no specific values have been chosen for the coils' inductance and the compensation capacitances. The secondary circuits are considered in resonance (X_3=X_4=0). In contrast, the primary circuits are slightly inductive (X_1=X_2 >0) to ensure the ZVS turn-on of the H-bridge inverters. Additionally, the diagonal cross-coupling from the opposite BPP and the cross-coupling within the same BPP have been studied separately to isolate their characteristics. Each of them has been swept such that M_{cross}=[1/10, 1/8, 1/6, 1/4, 1/3, 1/2]·M, while the main mutual inductances are defined as M_{13}=M_{24}=M.

$$M = \frac{8}{\pi^2}\frac{V_{in}V_{out}}{\omega_0 P_{out}} \tag{5.1}$$

In this analysis and the one of Section 5.3.2, the primary currents are computed considering the inverted output voltage from their respective H-bridge inverter as a reference. For instance, $\boldsymbol{I_1}$ has been computed with respect to $\boldsymbol{V_{AB}}$, while $\boldsymbol{I_2}$ takes $\boldsymbol{V_{CD}}$ as a reference.

Table 5.1: Input parameters used in the analysis of Section 5.2.2.

P_{out}	7.2 kW	M	[77.24, 81.79, 88.00] µH
V_{out}	[400, 800] V	R	0.5 Ω
V_{in}	360...500 V (1ϕ)	X	5 Ω
f_0	[79, 85, 90] kHz	$\boldsymbol{Z_1}$=$\boldsymbol{Z_2}$=R+jX, $\boldsymbol{Z_3}$=$\boldsymbol{Z_4}$=R	

ANALYSIS

Figure 5.2 compares the effects of the cross-coupling to the case in which M_{cross}=0·M. The comparison is made in terms of the amplitude and the phase angle of the primary currents $\boldsymbol{I_1}$ and $\boldsymbol{I_2}$, and the output current I_{out}.

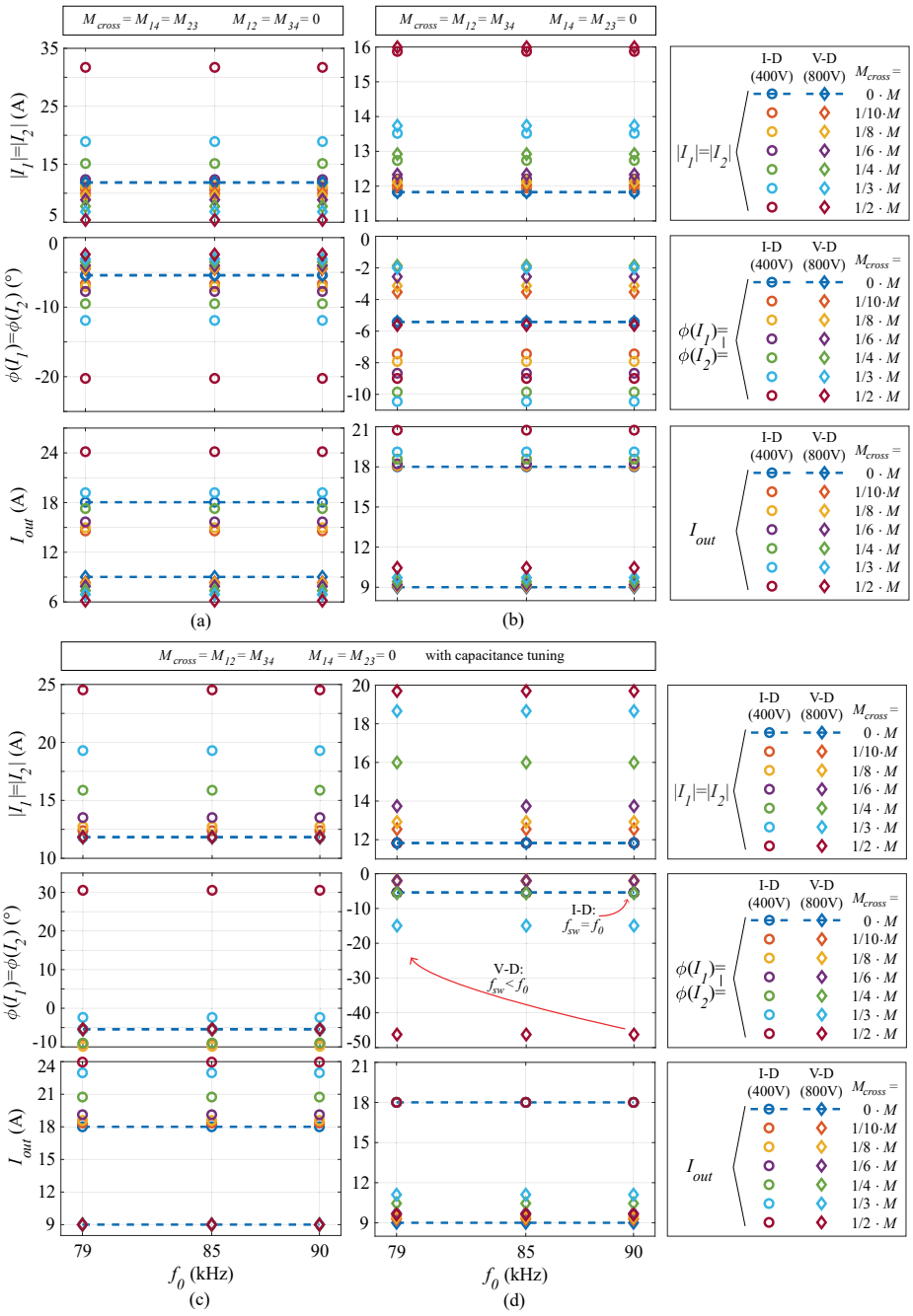

Figure 5.2: Analysis of the cross-coupling M_{cross} influence. (a) Diagonal cross-coupling M_{cross}=M_{14}=M_{23}. (b)-(d) Cross-coupling in the same BPP M_{cross}=M_{12}=M_{34}. (c) Effect of eliminating M_{cross} for the voltage doubler mode by turning all compensation capacitances according to (5.2). (d) Effect of eliminating M_{cross} for the current doubler mode by turning all compensation capacitances according to (5.3).

Figure 5.2(a) shows that the diagonal cross-coupling (M_{cross}=M_{14}=M_{23}) would still lead to inductive primary currents. However, compared to the case with no cross-coupling, the primary currents would be more inductive in the current doubling mode, while they would be less inductive in the voltage doubling mode. The diagonal cross-coupling would either add up or reduce the main mutual inductance, which is particularly clear from (4.1) and (4.2). Because this cross-coupling directly influences the power transfer, it is not possible to compensate for it by modifying the value of the compensation capacitances. Nevertheless, it is reasonable to consider M_{cross} acceptable if $M_{cross} \leq 1/4 \cdot M$ because, within this range, the variation in I_{out} can be counteracted by stepping up V_{in}. Moreover, in this range, the phase angle of the primary currents in both modes would be enough to guarantee the ZVS turn-on of the two H-bridge converters with the moderated amount of reactive current.

Similarly, Figure 5.2(b) shows that the cross-coupling in the same BPP (M_{cross}=M_{12}=M_{34}) would still lead to inductive primary currents. The variation trend in the two operating modes is similar to Figure 5.2(a). However, when considering $|I_1|$, $|I_2|$ and I_{out}, it is possible to notice that, for the same range of M_{cross}, the variations are more limited than in Figure 5.2(a). This means that it is possible to tolerate higher values of M_{cross} and compensate for their effects by stepping down V_{in}. Since, in this case, the cross-coupling is present within each BPP, it does not directly influence the power transfer between the primary and the secondary circuits. Its effects stay isolated on the two sides, and they can be treated as an extra impedance with either an inductive or capacitive nature, as shown in (4.1) and (4.2), respectively. This means that the contribution of M_{12} and M_{34} can be considered and eliminated in one of the two operating modes by selecting a suitable compensation capacitance. Examples of M_{12} and M_{34} compensation are discussed in Figure 5.2(c) and Figure 5.2(d).

In Figure 5.2(c), the cross-coupling within the same pad is compensated for the voltage doubler mode, and its impact on the current doubler mode is analyzed. This has been performed for all values of M_{cross} by adding an extra reactance to $\boldsymbol{Z_i}$ as shown in (5.2), which translates into a lower value of the compensation capacitance.

$$\text{V-Doubler}\begin{cases} \boldsymbol{Z_i} = R + j\left(X - \omega_0 M_{ih}\dfrac{|I_h^*|}{|I_i^*|}\right) \\ \rightarrow C_i = \dfrac{1}{\omega_0\left[\omega_0\left(L_i + M_{ih}\dfrac{|I_h^*|}{|I_i^*|}\right) - X\right]} \\ i,h = 1...4: \\ i{=}1 \Leftrightarrow h{=}2,\ i{=}2 \Leftrightarrow h{=}1,\ i{=}3 \Leftrightarrow h{=}4,\ i{=}4 \Leftrightarrow h{=}3 \end{cases} \tag{5.2}$$

In (5.2), $|I_i^*|$ and $|I_h^*|$ indicate the current amplitudes that would result from the case with no cross-coupling, i.e., M_{cross}=0, which can be computed from (4.1). As expected, the operation of the voltage doubling mode with cross-coupling within the same BPP coincides with the operation in the ideal case with no cross-coupling. On the other hand, with the same circuit parameters, the operation in the current doubling mode could result in the hard-switching of the H-bridge inverters if $M_{cross} > 1/3 \cdot M$.

In Figure 5.2(d), the cross-coupling within the same pad is compensated for the current doubler mode, and its impact on the voltage doubler mode is analyzed. In this case, an extra reactance has been added to $\boldsymbol{Z_i}$ as shown in (5.3) for all values of M_{cross}, which would translate into a higher value of the compensation capacitance.

$$\text{I-Doubler}\begin{cases} \boldsymbol{Z_i} = R + j\left(X + \omega_0 M_{ih}\dfrac{|I_h^*|}{|I_i^*|}\right) \\ \rightarrow C_i = \dfrac{1}{\omega_0\left[\omega_0\left(L_i - M_{ih}\dfrac{|I_h^*|}{|I_i^*|}\right) - X\right]} \\ i,h = 1...4: \\ i{=}1 \Leftrightarrow h{=}2, i{=}2 \Leftrightarrow h{=}1, i{=}3 \Leftrightarrow h{=}4, i{=}4 \Leftrightarrow h{=}3 \end{cases} \tag{5.3}$$

As expected, the operation in the current doubling mode with the cross-coupling within the same BPP coincides with the operation in the ideal case with no cross-coupling. The voltage doubling mode operation with the same circuit parameters would result in a highly inductive primary current if $M_{cross} > 1/3 \cdot M$. In that case, the power transfer efficiency would be lower due to the circulating reactive power and the relatively large turn-off current point. Nevertheless, the ZVS turn-on of the H-bridges is maintained, which would not be the case in Figure 5.2(c).

5

CHOSEN CROSS-COUPLING COMPENSATION AND OPERATING STRATEGY

The results from Figure 5.2 make it preferable to minimize the diagonal cross-coupling (M_{14} and M_{23}) by properly designing the overlap area of the coils within the same BPP. This choice cannot guarantee that the cross-coupling within the same BPP (M_{12} and M_{34}) is negligible. However, adequate compensation capacitance selection can compensate for its effect on the power transfer. From the previous analysis, it has been found that it is preferable to tune the compensation capacitances in the current doubler mode through (5.3). The tuning of the capacitors and the H-bridge inverters' switching frequency is performed at f_{sw}=f_0=90 kHz in the current doubler mode. This guarantees that, by operating the inverters at f_{sw}=79 kHz during the voltage doubler mode, the primary currents would be less inductive, reducing the circulating reactive power and the turn-off current point that can be problematic as shown in Figure 5.2(d) if $M_{cross} > 1/3 \cdot M$. This tuning and operating strategy is qualitatively shown in Figure 5.2(d). Thereby, the resulting primary currents' phase angle at 79 kHz in the voltage doubler mode cannot be computed since, in this analysis, the circuits' impedance $\boldsymbol{Z_i}$ are defined just for the resonant frequency. The advantage of this operating scheme will be proved in Section 5.3.2. Additionally, by choosing f_0=90 kHz, the required mutual inductance M is the lowest value in Table 5.1 which eases the requirement on the nominal coupling.

5.2.3. DESIGN: CROSS-COUPLING SENSITIVITY ANALYSIS THROUGH FEM

The coupled BPPs must be designed according to the cross-coupling analysis of Section 5.2.2, such that:

1. the nominal M_{13} and M_{24} are in the range of 77.24 µH;

2. the diagonal cross-coupling M_{14} and M_{23} between the two BPPs is negligible at the aligned position and for the nominal air gap. This results from selecting the overlap area between the two coils within each BPP.

The chosen BPP geometry is illustrated in Figure 5.3 of which given dimensions are listed in Table 5.2. The dimensions of the aluminum shield, the ferrite plate, and the outer sides of the winding area are chosen, given by the available physical space for the wireless charging system. Additionally, each winding consists of several turns of the chosen Litz wire having d_w as the external diameter. For simplicity, the windings are modeled as a massive planar conductor of which the total coil's spread C_{sp} is defined in Figure 5.3. Even though C_{sp} is considered to be fixed as specified by Table 5.2, there is still room to select the number of turns of each coil. This choice must guarantee that:

- the target condition $M_{13} \approx M_{24} \approx 77.24\,\mu\text{H}$ is satisfied while the air gap between the two BPPs is $Z_{ag} \approx 100\,\text{mm}$;
- the two coils within each BPP have similar parameters aiming for a symmetrical design;
- the conduction losses in the primary and secondary circuits are equal.

Table 5.2: Dimensions (in mm) valid for both coils referring to Figure 5.3.

x_a, y_a, z_a	x_f, y_f, z_f	x_l, y_c	$z_{f\text{-}c1}$, $z_{f\text{-}c2}$, $z_{f\text{-}a}$
570, 370, 2	559, 364, 4.1	545, 350	3, 10.5, 4
C_{sp}, d_w	$x_{f,unit}$, $y_{f,unit}$	Ferrite unit: 3C95, PLT43/28/4.1	
65, 2.5	43, 28	Litz wire: 600 strands, 0.071mm	

The number of turns of each coil satisfying the above-mentioned requirements results in N_1=17, N_2=18, N_3=15, and N_4=14. These have been found through the FEM analysis of the coupled BPPs with an initial overlap of $x_{overlap}$=0. It can be noticed that the coil placed closer to the ferrite in each BPP has one less turn. This choice guarantees similarity between the two self-inductance values and also between M_{13} and M_{24} considering the uneven placement of the coils in the z-direction as shown in Figure 5.3(b). The initially selected C_{sp} would be enlarged if it cannot accommodate the necessary number of turns that satisfies the requirements on the BPPs.

After selecting the number of turns, the overlap area between the two coils in the same pad must be chosen, which, in Figure 5.3, is defined in terms of $x_{overlap}$. The value of $x_{overlap}$ must result in a negligible diagonal cross-coupling. From the cross-coupling analysis in Figure 5.2, that is the case if M_{14} and M_{23} are at maximum $\frac{1}{10} \cdot M$, where $M \approx M_{13} \approx M_{24}$. According to (5.4), $x_{overlap}$ can be expressed as a function of the single coil's length x_c. In this analysis, C_{sp} and the total length occupied by the coils x_l are considered to be fixed, which values are listed in Table 5.2. On the other hand, x_c and $x_{overlap}$ can vary in the range specified by (5.5).

$$x_{overlap}(x_c) = 2 \cdot x_c - 2 \cdot C_{sp} - x_l \tag{5.4}$$

$$x_c = \left[\frac{x_l}{2} + C_{sp};\ x_l\right] \rightarrow x_{overlap} = \left[0;\ x_l - 2 \cdot C_{sp}\right] \tag{5.5}$$

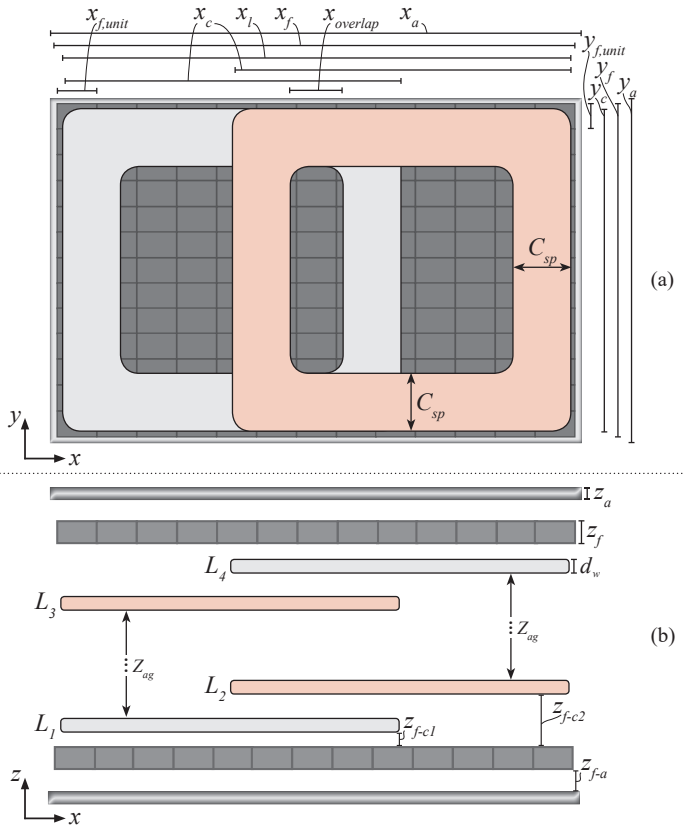

Figure 5.3: Structure and geometry of the coupled BPPs viewed from: (a) the x-y plane, (b) the x-z plane.

Several coupled BPPs configurations have been created by sweeping $x_{overlap}$ in the range 0...90 mm every 3 mm equally for both BPPs. At the same time, the self-inductance and the mutual inductance of all the coils are assessed through the FEM analysis considering Z_{ag}=101.5 mm. These results are summarized in Figure 5.4.

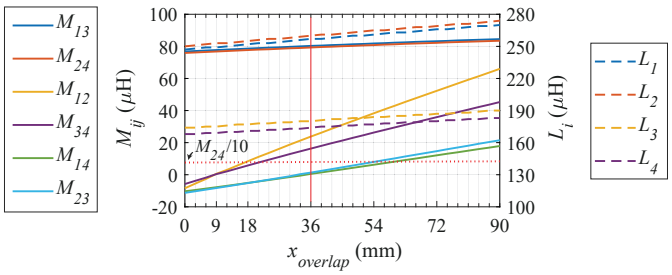

Figure 5.4: Self inductances and mutual inductances of the coupled BPPs depending on $x_{overlap}$ resulting from the FEM analysis.

It must be noted that the cross-coupling within the same pad M_{12} and M_{34} is minimized when $x_{overlap}$=9 mm. On the other hand, the diagonal cross-coupling between

opposite pads M_{14} and M_{23} is minimum for a greater value of $x_{overlap}$, being 36 mm. This result coincides with the analysis performed by [17]. The coupled BPPs with $M_{14} \approx M_{23} \approx 0$ are preferable since they result in a V-I/D converter operation close to the ideal case. However, in the case that 36 mm $\leq x_{overlap} \leq$ 54 mm, M_{14} and M_{23} can be considered negligible given the analysis performed in Figure 5.2(a).

Additionally, Figure 5.4 shows that all four cross-coupling mutual inductances are negative when there is no overlap between the coils, i.e., $x_{overlap}$=0. The physical meaning of these results can be understood by analyzing the magnetic field generated by the coils. An example is shown in Figure 5.5(a) considering two coupled BPPs with $x_{overlap}$=0. A current flows through the coil with inductance L_1 generating a magnetic field along the positive z-axis. The sign of the mutual inductance to a coupled coil depends on the direction of the total concatenated magnetic flux. For instance, the magnetic flux linking to the coil with inductance L_3 is positive since it has the same direction of the $+z$-axis. This translates into M_{13}>0. On the other hand, a negative magnetic flux concatenates to the two coils with inductance L_2 and L_4 resulting in negative cross-coupling mutual inductances, i.e., M_{12}<0 and M_{14}<0. The influence of a negative mutual inductance on the power transfer is discussed in Section 5.3.2.

On the other hand, Figure 5.5(b) shows that a positive flux might link to all three coupled coils when the two coils within each BPP are overlapped, which, according to Figure 5.4, that is the case for $x_{overlap}$>36 mm.

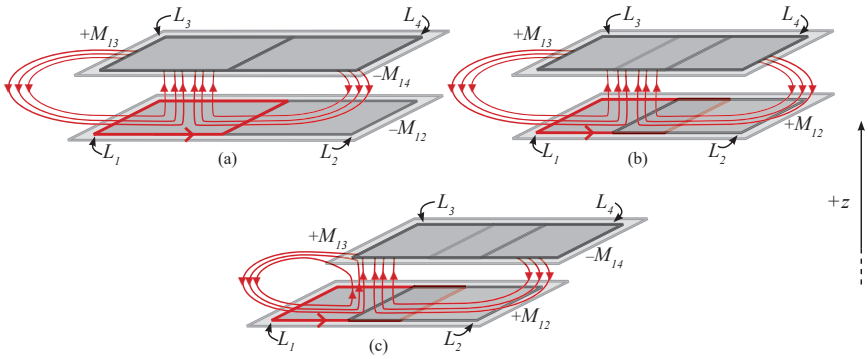

Figure 5.5: Typical magnetic flux generated by a current flowing through the coil with L_1 inductance. The mutual inductance can have either a positive or negative sign depending on the direction of the field linking to the other coils. Examples for: (a) aligned BPPs and $x_{overlap}$=0; (b) aligned BPPs and $x_{overlap}$>0; (c) BPPs misaligned in the positive x-direction and $x_{overlap}$>0.

5.2.4. IMPLEMENTATION: COUPLED BPPS FOR THE V/I-D CONVERTER

The coupled BPPs design with the minimum diagonal cross-coupling identified in Section 5.2.3 has been implemented. The overall parameters of the resulting BPPs are plotted in Figure 5.6, where the reference coordinate is chosen with respect to the implemented BPPs in Figure 5.7. The parameters of the coupled BPPs in the aligned position are listed in Table 5.3. It can be noticed that M_{13} and M_{24} differ by less than 4% from the target main mutual inductance of 77.24 µH. Even though the resulting diagonal cross-coupling M_{14} and M_{23} are larger than the values expected from Figure 5.4, these are still acceptable since they are lower than $\frac{1}{10} \cdot M_{24}$. This discrepancy is due to the manufac-

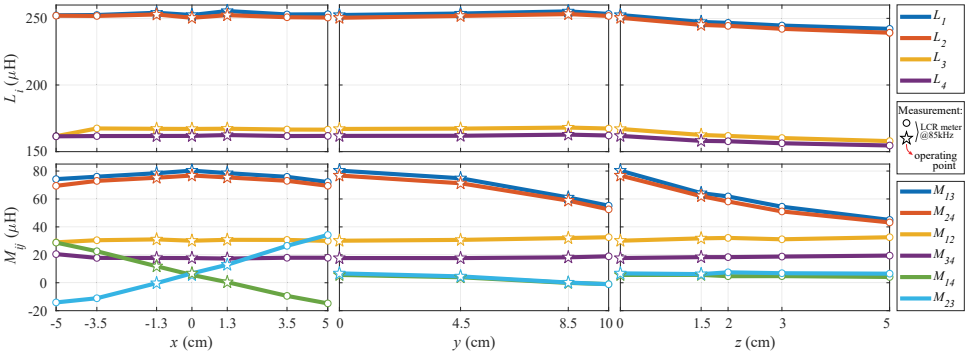

Figure 5.6: Self-inductance and mutual inductance of the coupled BPPs depending on receiving pad position, which have been measured with an LCR meter at 85 kHz. The coordinate reference system is shown in Figure 5.7. Note that the misalignment is performed only with respect to one axis at a time.

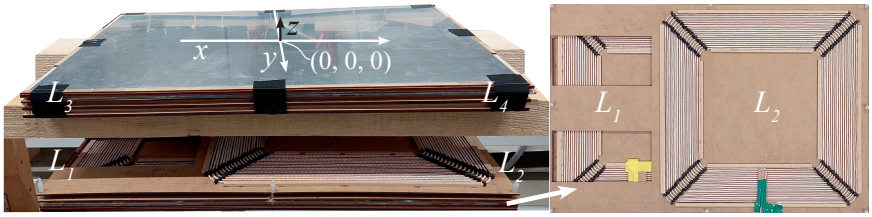

Figure 5.7: Implementation of the selected BPPs design whose parameters are listed in Table 5.3.

Table 5.3: Measured circuit parameters and coils' dimensions.

	N	L (μH)	R (mΩ)	M (μH)			(mm)
L_1	17	252.5	620	M_{13}	M_{12}	M_{14}	$x_{overlap}$
L_2	18	250.4	600	80.3	30.1	5.6	36
L_3	15	167.0	520	M_{24}	M_{34}	M_{23}	Z_{ag}
L_4	14	161.8	500	76.8	17.7	6.7	95

turing tolerances and non-idealities of the materials used for the pads' structure.

Figure 5.6 shows the variation of the coupled BPPs' parameters depending on their relative position. This considers that the receiving pad moves with respect to the three dimensions coordinate system in Figure 5.7(a). The self-inductance is approximately constant in the x- and y-direction, while it decreases by up to 5% in the z-direction. The cross-coupling within the same pad, namely M_{12} and M_{34}, stays roughly constant with any misalignment, making it suitable to use the compensation capacitance to compensate for that. This intuitively makes sense since those coils do not change their position with respect to each other. On the other hand, the diagonal cross-coupling between opposite BPPs, namely M_{14} and M_{23}, is more sensitive to misalignment. The misalignment in the y- and z-direction results in negligible M_{14} and M_{23} since they are still lower than $\frac{1}{10} \cdot M_{24}$. On the other hand, the misalignment in the x-direction influence greatly the value of M_{14} and M_{23}. For example, shifting the receiving pad along the positive x-direction results in a drop of M_{14} whereas M_{23} increases. This is because the coil with L_4 inductance moves further away from the coil with L_1 inductance while the coil with L_3 inductance becomes more aligned to the coil with L_2 inductance. For misalignment

points greater than 1.3 cm, M_{14} assumes a negative value. The physical reason for that is illustrated in Figure 5.5(c), where it is clear that a negative magnetic flux might be concatenated to the coil with L_4 inductance when the receiving pad moves in the positive x-direction. Due to the symmetry of the BPPs, similar considerations can be made for the movement of the receiving pad along the negative x-direction.

5.3. LABORATORY PROTOTYPE

The equipment and the 7.7 kW implemented laboratory prototype in Figure 5.8 have been used to prove the functionality of the V/I-D converter employing the BPPs in Figure 5.7. One bidirectional power supply has been used as the input voltage source, mimicking the voltage from a grid-connected power factor correction (PFC) rectifier. A second power supply has been employed as the load emulating the EV battery.

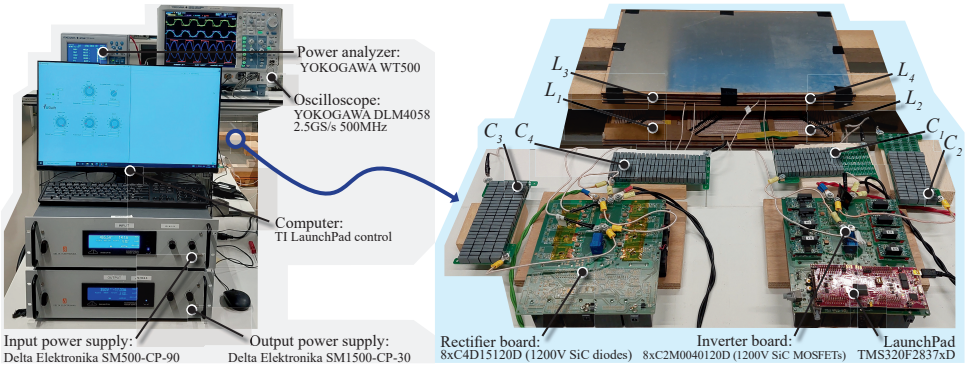

Figure 5.8: Equipment and implemented 7.7 kW laboratory prototype of the V/I-D converter employing BPPs.

5.3.1. COMPENSATION CAPACITORS' SELECTION

According to the cross-coupling compensation strategy explained in Section 5.2.2, each series compensation capacitance must be computed from (5.3) considering f_0=90 kHz such that the cross-coupling within the same BPP is compensated for the current doubler mode. The case in which the BPPs are aligned has been considered for the calculation. Additionally, the absolute value of the currents mentioned in (5.3) can be computed from (4.2) by setting all the cross-coupling terms to zero. The resulting compensation capacitances and their implementation are listed in Table 5.4.

Table 5.4: Selected compensation capacitors. The values have been measured with a LCR meter at 85 kHz.

	C_1	C_2	C_3	C_4
(nF)	14.9	14.9	20.7	21.6
(series x parallel)*	4 x 18	4 x 18	4 x 25	4 x 26
*Unit capacitor: KEMET R76TF13305050J 3.3 nF (ESR=0.22 Ω)				

5.3.2. ANALYSIS OF THE OPERATING POINTS

Before validating the proposed V/I-D converter experimentally, the operating points corresponding to the different BPPs alignments have been analyzed through the analytical

model defined in Section 4.2.1 at the rated output power of 7.2 kW. Hereby, it is assumed that V_{in} is regulated to deliver the rated output power. The range of V_{in} from 360 V to 500 V could be supplied by a single-phase grid-connected boost-like PFC rectifier in Europe (230 V RMS), which could be implemented as explained in [21] and [22].

In the following paragraphs, two analyses are executed. First, the advantages of adopting the switching frequency of 79 kHz in the voltage doubler mode are proved against the operation at 90 kHz. After that, the expected operating points are evaluated in the chosen voltage and current doubler modes.

VOLTAGE DOUBLER OPERATING AT EITHER 79 kHz OR 90 kHz

The operating points resulting from the two switching frequencies of the voltage doubler mode are summarized in Figure 5.9, where the BPPs alignments in Figure 5.6 have been considered. At the aligned position, the operating points from the two switching frequencies are similar. However, when the misalignment occurs, the phase angle of the primary currents $\phi(I_1)$ and $\phi(I_2)$ is lower when operating at 79 kHz than at 90 kHz. This translates into less circulating reactive current, lower switching losses of the H-bridge inverters, lower required V_{in}, and consequently, higher $\eta_{\text{DC-to-DC}}$. Note that the sharp decreases in $\eta_{\text{DC-to-DC}}$ correspond to transitions into hard-switching operating areas. Additionally, it must be considered that the V_{in} required from the operation at 90 kHz could be up to 600 V. Since this is considerably higher than the maximum voltage achievable from the PFC rectifier, an extra voltage boost stage would be required to supply the H-bridge inverters adding cost and complexity. These results confirm that operating the

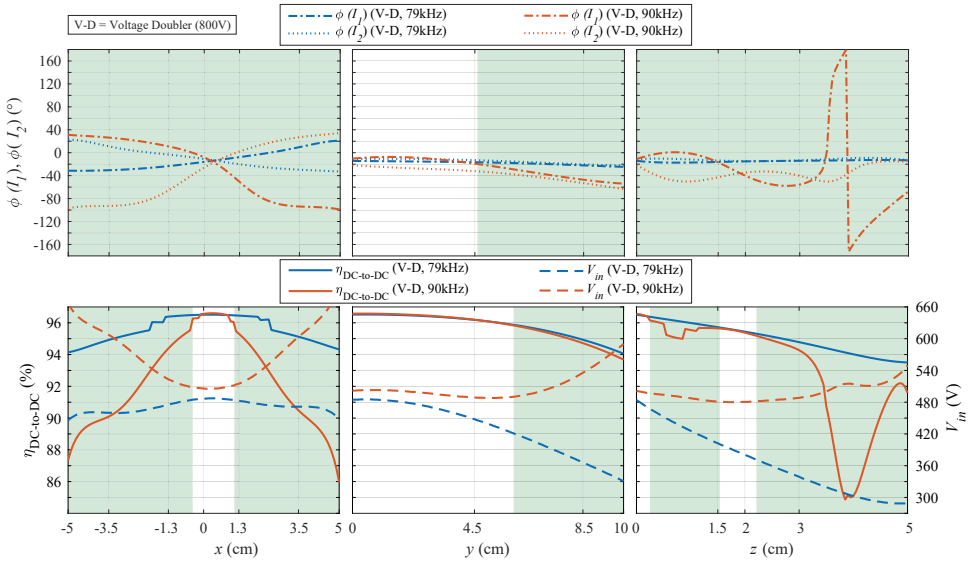

Figure 5.9: Analysis from the analytical model of the proposed V/I-D converter of the phase angle of the primary currents $\phi(I_1)$ and $\phi(I_2)$, the DC-to-DC efficiency $\eta_{\text{DC-to-DC}}$, and the required input voltage V_{in} depending on the receiving coil's misalignment in the x-, y-, z-direction. The misalignment is performed only with respect to one axis at a time. The results suppose that the output power of 7.2 kW is delivered when the V/I-D converter operates as a voltage doubler, i.e., V_{out}=800 V, while the inverters' switching frequency is either 79 kHz or 90 kHz. The green-shaded areas denote the operating regions in which 79 kHz brings a considerable advantage in terms of $\eta_{\text{DC-to-DC}}$ and ZVS turn-on capability of the H-bridge inverters.

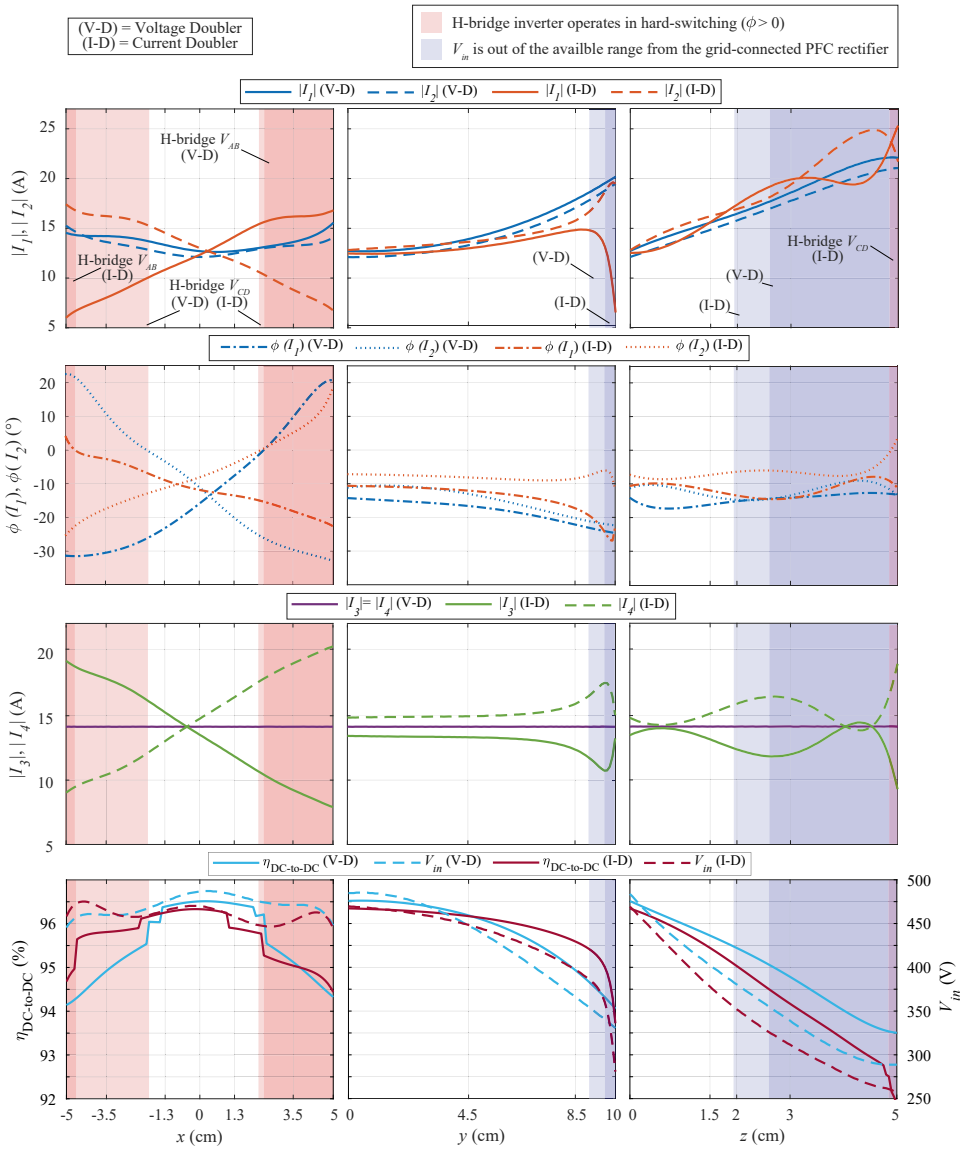

Figure 5.10: Analysis from the analytical model of the proposed V/I-D converter of the absolute value and phase angle of $\boldsymbol{I_1}$ and $\boldsymbol{I_2}$, the absolute value of $\boldsymbol{I_3}$ and $\boldsymbol{I_4}$, the $\eta_{\text{DC-to-DC}}$, and the required V_{in} depending on the misalignment in the x-, y-, z-direction. The misalignment is performed only with respect to one axis at a time. The results suppose that the output power of 7.2 kW is delivered when the V/I-D converter operates as either voltage doubler (V_{out}=800 V, 79 kHz) or current doubler (V_{out}=400 V, 90 kHz). The red-shaded areas denote the operating regions in which the hard-switching of the H-bridge inverter occurs. The blue-shaded areas indicate whether the required V_{in} is out of the available range from the grid-connected PFC rectifier.

V/I-D converter at 79 kHz is advantageous in the voltage doubler mode.

VOLTAGE DOUBLER OPERATING AT 79 kHz AND CURRENT DOUBLER OPERATING AT 90 kHz
The operating points resulting from both the voltage doubler and the current doubler modes are shown in Figure 5.10. According to $\phi(I_1)$ and $\phi(I_2)$, the misalignment of the receiving BPP in the x-direction pushes one primary current into the capacitive region leading to the hard-switching of the respective H-bridge inverter. Those operating points have been marked with red-shaded areas. At the same time, the other primary current becomes more inductive, causing higher turn-off losses. Additionally, during the current doubler mode, the current stress in the two primary and the two secondary circuits would be unbalanced. This asymmetrical behavior is due to the opposite trend of the diagonal cross-coupling M_{14} and M_{23} with respect to the misalignment in the x-direction shown in Figure 5.6. As a result, the $\eta_{\text{DC-to-DC}}$ could drop by up to 2% from the aligned case, which is still reasonable. Nevertheless, the MOSFETs of the inverting stages must be equipped with a suitable thermal management system to be able to withstand the additional power losses introduced by the hard-switching operating points. It must also be noted that the required V_{in} would still be within the available range from the grid-connected PFC rectifier. These results make the proposed V/I-D converter with BPPs more suitable for applications with a moderate misalignment profile in the x-direction. This is generally the case of EV static wireless charging since the BPPs misalignment would be constrained by the lateral size of the parking spot.

Moreover, Figure 5.10 shows that the proposed V/I-D converter with BPPs has good misalignment tolerance with respect to the y-direction since the ZVS turn-on would still be preserved. However, beyond a certain extent of misalignment, the required V_{in} is lower than the minimum available (360 V) from the PFC rectifier. This occurs in the operating points marked with the blue-shaded areas in Figure 5.10, which correspond to $y > 8.8$ cm for the voltage doubler mode, while the range $y > 9.6$ cm holds for the current doubler mode. In those operating points, lower input voltage values can be achieved by phase shifting the H-bridge inverter resulting in a lower fundamental component of $\boldsymbol{V_{AB}}$ and $\boldsymbol{V_{CD}}$. For the considered misalignment, the $\eta_{\text{DC-to-DC}}$ would drop by up to 2% since the same output power is reached with higher primary currents.

Similar phase-shift control of the H-bridge inverters is required for a certain extent of misalignment in the z-direction, which ranges are $z > 1.9$ cm for the current doubler mode and $z > 2.5$ cm for the voltage doubler mode. This is due to the relatively high sensitivity of the main mutual inductances M_{13} and M_{24} with respect to the misalignment in the z-direction. In this case, the ZVS turn-on of the inverters would be preserved in most operating points. Additionally, the $\eta_{\text{DC-to-DC}}$ could drop by up to 4% since the same output power is reached with higher primary currents.

5.4. EXPERIMENTAL RESULTS

Based on the analysis of the operating points executed in Figure 5.10, the proposed V/I-D converter in Figure 5.8 has been tested with aligned and misaligned BPPs.

5.4.1. MEASURED EFFICIENCY AND CIRCUIT WAVEFORMS

Figure 5.11 shows the measured $\eta_{\text{DC-to-DC}}$ and the applied V_{in} for the entire constant current (CC) charging profile at different alignment conditions of the coupled BPPs. The V/I-D converter operates in the current doubler mode at 90 kHz delivering an output

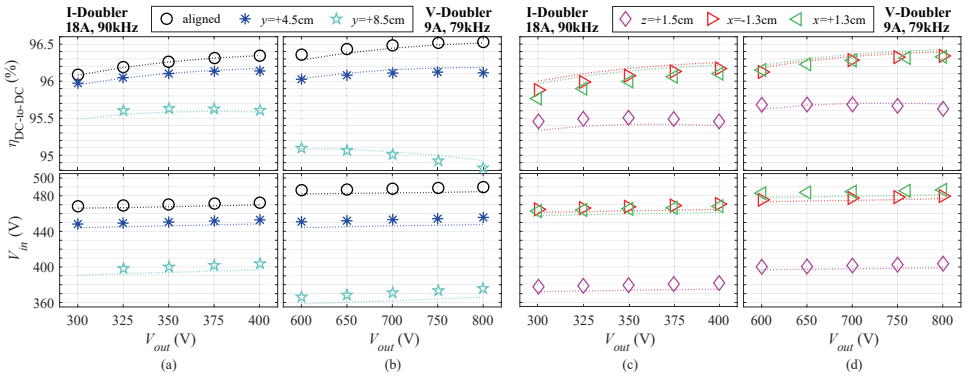

Figure 5.11: Measured DC-to-DC efficiency $\eta_{\text{DC-to-DC}}$ and used input voltage V_{in} depending on V_{out} during the CC charging mode. Measurements are performed with the coupled BPPs in the aligned and the misaligned condition in the y-direction while the V/I-D converter operates as (a) current doubler and (b) voltage doubler. Measurements performed with misaligned BPPs in either the x- or z-direction, while the V/I-D converter operates as (c) current doubler and (d) voltage doubler. Note that the misalignment is performed only with respect to one axis at a time.

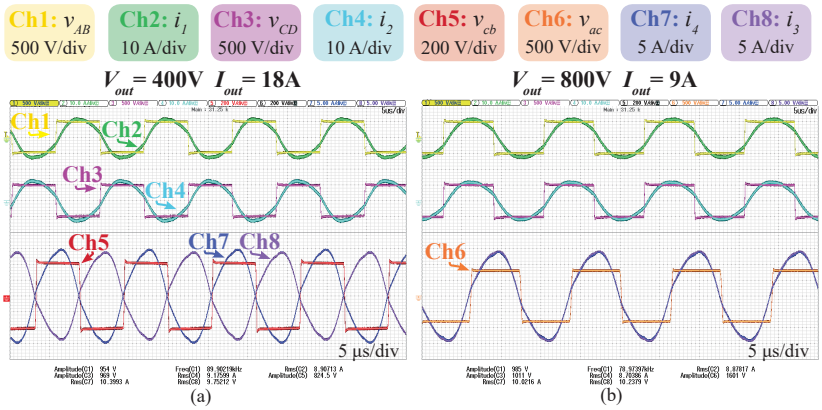

Figure 5.12: Measured circuit waveforms at the nominal V_{out} and rated P_{out} when the V/I-D converter operates with aligned BPPs as: (a) current doubler (V_{out}=400 V), and (b) voltage doubler (V_{out}=800 V).

current of 18 A while the output voltage varies from 300 V to 400 V. On the other hand, the V/I-D converter operates in the voltage doubler mode at 79 kHz delivering an output current of 9 A while the output voltage varies from 600 V to 800 V.

The highest $\eta_{\text{DC-to-DC}}$ has been measured at aligned BPPs. For instance, at the rated power, the operation in the current doubler reached 96.34% efficiency, while 96.53% was measured during the voltage doubler mode. The difference in efficiency between the two modes is mainly because two more diodes are conducting in the current doubler mode. This high efficiency is because the primary currents have the lowest amplitude while delivering the rated output power. Additionally, they have the minimum inductive behavior ensuring the ZVS turn-on of the H-bridges inverter with low turn-off losses and minimum circulating reactive current. These properties can be observed in Figure 5.12, where it is also clear that the operation in the two modes is to some extent symmetrical, resembling the ideal operation of the V/I-D converter illustrated in Figure 4.2.

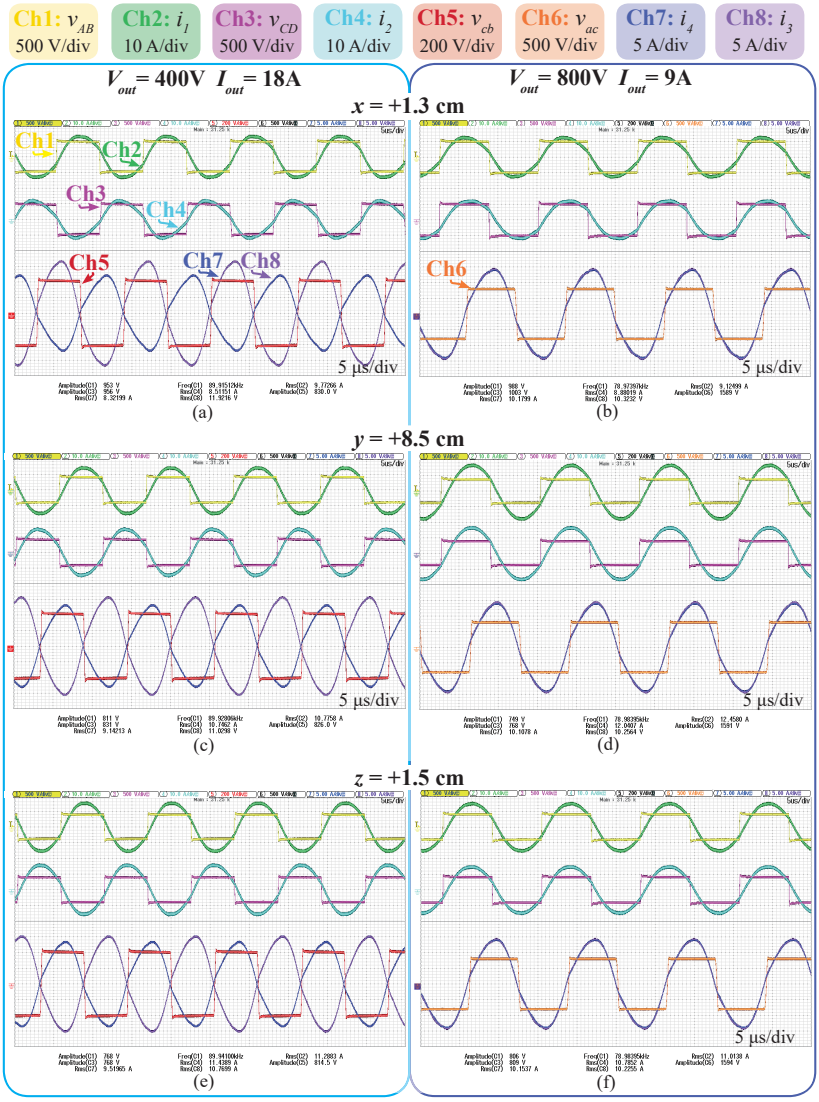

Figure 5.13: Measured circuit waveforms at the nominal V_{out} and rated P_{out} when the V/I-D converter operates with misaligned BPPs as: (a),(c),(e) current doubler (V_{out}=400 V), and (b),(d),(f) voltage doubler (V_{out}=800 V). The misalignment is: (a),(b) x=1.3 cm, (c),(d) y=8.5 cm, and (e),(f) z=1.5 cm. The misalignment is performed only with respect to one axis at a time.

When the misalignment occurs, lower values of $\eta_{\text{DC-to-DC}}$ are measured since the required V_{in} to reach the same rated output power is generally reduced, translating into higher primary currents and, consequently, greater conduction losses. Moreover, larger asymmetries in the waveforms of the primary and secondary circuits can be noticed. For example, Figure 5.13(a) and Figure 5.13(b) show that, as expected from Figure 5.10, the misalignment in the x-direction leads to a considerable difference in the phase angle of the two primary currents because of which one H-bridge is barely achieving the ZVS

turn-on. Moreover, an asymmetry in the amplitude of the secondary currents can also be observed during the current doubler mode in Figure 5.13(a). Overall, most of the measured $\eta_{\text{DC-to-DC}}$ are greater than 95.4% which makes the proposed V/I-D converter employing BPPs promising for EV wireless charging. The minimum $\eta_{\text{DC-to-DC}}$ of 94.83% has been measured during the voltage doubler mode at y=+8.5 cm. This is mainly due to the considerable circulating primary currents and the relatively high turn-off current point of the H-bridge inverters, which, as shown in Figure 5.13(c) and Figure 5.13(d), is roughly double than in the respective current doubler mode.

It must be noted that all considered operating points in Figure 5.11 use a value of V_{in} that the grid-connected PFC rectifier could provide. Moreover, the measured circuit waveforms in both Figure 5.12 and Figure 5.13 show that the ZVS turn-on is guaranteed. These results agree with the ones expected from the analytical analysis in Figure 5.10.

5.4.2. EXAMPLE OF A CC-CV CHARGING PROFILE

Figure 5.11 summarizes the measured $\eta_{\text{DC-to-DC}}$ and the applied V_{in} focusing on the CC charging profile of the EV battery since that operating mode would take place for the majority of the charging process for the rated output power level of 7.2 kW. However, the complete charging profile consisting of the CC succeeded by the constant voltage (CV) scheme can be realized by regulating the input voltage through the grid-connected PFC rectifier or by the phase-shift control of the H-bridge inverters.

Figure 5.14 shows an example of the CC-CV charging profile realized with the proposed V/I-D converter with aligned BPPs. It is assumed that V_{in} is set according to the load, which information is given by the wireless communication required from the IPT system for several features such as guided positioning, pairing, and safety. The measured $\eta_{\text{DC-to-DC}}$ increases during the CC charging mode, while it would drop slightly during the CV mode, where it is still higher than 96.2% for the considered operating points. All in all, Figure 5.14 clearly shows that the V/I-D converter is a universal solution for charging

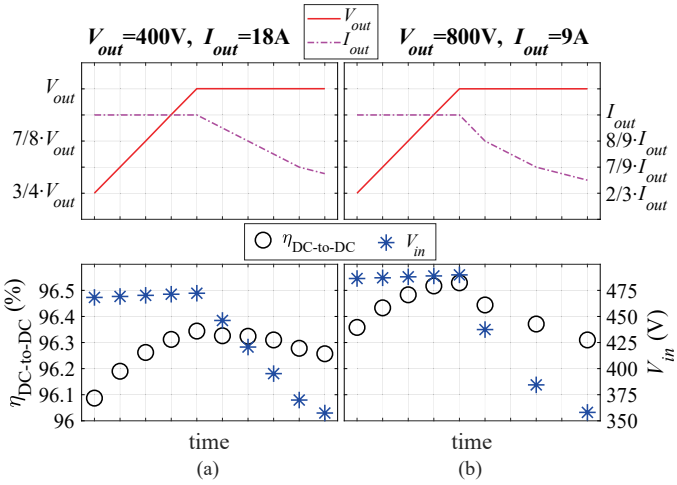

Figure 5.14: Measured $\eta_{\text{DC-to-DC}}$ and used V_{in} during a typical battery charging profile with the CC and the CV modes at aligned BPPs while the V/I-D converter operates as (a) current doubler, and (b) voltage doubler. These results summarize that the V/I-D converter is a universal solution for charging 400 V and 800 V EV batteries efficiently at the same power.

400 V and 800 V EV batteries efficiently at the same power.

5.5. INTEROPERABILITY OF THE PRIMARY BPP WITH THE TEST STATION VA WP2/Z2 FROM SAE J2954

The focus of this section is assessing the performance of the V/I-D converter when it is not working in its nominal condition. For instance, it is considered that the primary BPP is coupled to a standardized secondary coil, resulting in the circuit schematic shown in Figure 5.15.

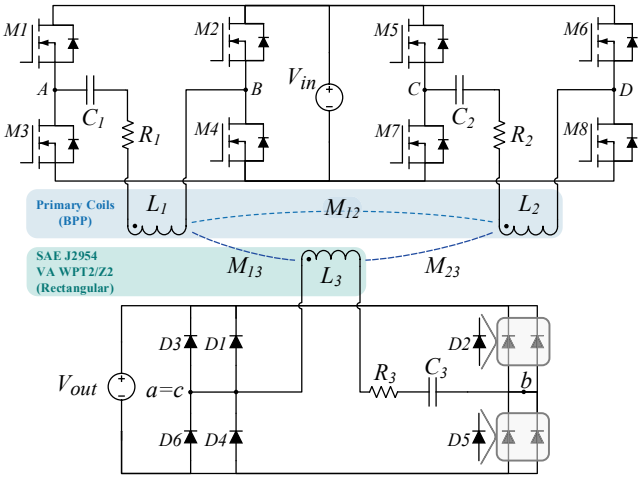

Figure 5.15: Equivalent circuit of the V/I-D converter when coupled with the standard receiving coil SAE J2954 VA WP2/Z2.

5.5.1. CIRCUIT AND ANALYTICAL MODELING

The equivalent circuit in the frequency domain is shown in Figure 5.16 where the EV battery is replaced by the equivalent load R_{ac} in (5.6) defined by [23] and [24].

$$R_{ac} = \frac{8}{\pi^2} R_L = \frac{8}{\pi^2} \frac{V_{out}^2}{P_{out}} \tag{5.6}$$

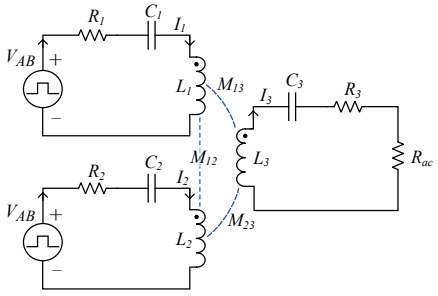

Figure 5.16: Equivalent circuit in the frequency domain for analyzing the interoperability of the V/I-D converter in Figure 5.15.

The equivalent circuit in Figure 5.16 is described by the Kirchhoff voltage law (KVL) in (5.7). Thereby, the impedance Z_i of each resonant circuit is defined in (5.8), and the

mutual inductances M_{12}, M_{13}, M_{23} are expressed in (5.9). The input $\boldsymbol{V_{AB}}$ is taken as the reference according to the phasor convention, which is defined in (5.10) through the first-harmonic approximation, where V_{in} is the DC input voltage.

$$\begin{cases} \boldsymbol{V_{AB}} = \boldsymbol{Z_1 I_1} + j\omega M_{12}\boldsymbol{I_2} + j\omega M_{13}\boldsymbol{I_3} \\ \boldsymbol{V_{AB}} = j\omega M_{12}\boldsymbol{I_1} + \boldsymbol{Z_2 I_2} + j\omega M_{23}\boldsymbol{I_3} \\ 0 = j\omega M_{13}\boldsymbol{I_1} + j\omega M_{23}\boldsymbol{I_2} + (\boldsymbol{Z_3} + R_{ac})\boldsymbol{I_3} \end{cases} \tag{5.7}$$

$$\boldsymbol{Z_i} = R_i + j\omega X_i, \quad X_i = \omega L_i - \frac{1}{\omega C_i}: \quad i = 1...4 \tag{5.8}$$

$$M_{ih} = M_{hi} = k_{ih}\sqrt{L_i L_h}: \quad i,h = 1...3 \wedge i \neq h \tag{5.9}$$

$$\boldsymbol{V_{AB}} = V_{AB,1}\angle 0° = \frac{4}{\pi}V_{in}, \quad V_{AB,1} = V_{CD,1} \tag{5.10}$$

Additionally, for a given processed power, the V/I-D resonant circuit's efficiency η_{res} is defined in (5.11).

$$\eta_{res} = \frac{R_{ac}|\boldsymbol{I_3}|^2}{V_{AB}(|\mathrm{Re}[\boldsymbol{I_1}]| + |\mathrm{Re}[\boldsymbol{I_2}]|)} \tag{5.11}$$

The total DC-to-DC efficiency $\eta_{\text{DC-to-DC}}$ also takes into account the power losses of the inverting and rectifying stages. Assuming that $X_1 > 0$ and $X_2 > 0$, the H-bridge inverters operate in zero voltage switching (ZVS) turn-on losses, meaning that the power losses can be expressed as

$$P_{inv} = 4 \cdot R_{ds,on} \cdot \left[\left(\frac{I_1}{2}\right)^2 + \left(\frac{I_2}{2}\right)^2\right] + \sum_{i=1}^{8} E_{off_{(Mi)}} \cdot f_0 \tag{5.12}$$

Additionally, since C_3 is chosen such that $X_3 \approx 0$, the rectifier's power losses are mainly due to the diodes' conduction:

$$P_{rect} = 8 \cdot \left[V_F\left(\frac{I_3}{\pi}\right) + r\left(\frac{I_3}{2}\right)^2\right] \tag{5.13}$$

The parameters of the semiconductor devices can be extrapolated from their datasheet. Finally, $\eta_{\text{DC-to-DC}}$ can be computed as

$$\eta_{\text{DC-to-DC}} = \eta_{res} \cdot \frac{P_{out}}{P_{out} + P_{inv} + P_{rec}} \tag{5.14}$$

5.5.2. MAGNETIC COUPLING AND MISALIGNMENT

Figure 5.17 shows the magnetic arrangement in which the primary BPP is coupled to the WPT2/Z2 standard rectangular coil in the aligned position. The variations of the self-inductance and the mutual inductance depending on the misalignment are shown in Figure 5.18.

When the two geometric centers are aligned, the secondary coil results in being misaligned in the x-direction with respect to both coils of the BPP. The movement along the

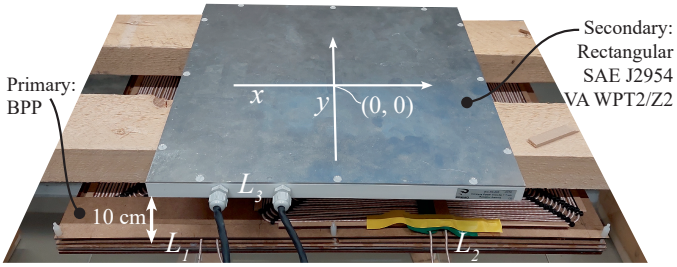

Figure 5.17: Coupled coils configuration in the aligned position. Primary (L_1 and L_2): implemented BPP for the V/I-D converter. Secondary (L_3): commercial rectangular coil manufactured by PREMO [25].

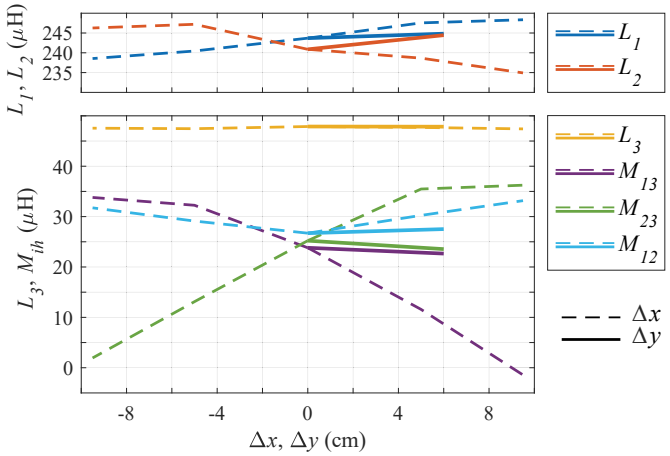

Figure 5.18: Self-inductance and mutual inductance of the BPP primary coupled to the standardized secondary depending on the misalignment, which reference is shown in Figure 5.17. Hereby, $i, h = 1...3 \wedge i \neq h$.

x-axis would improve the mutual inductance with respect to one of the primary coils, while the other one would worsen. On the other hand, the misalignment in only the y-direction causes a similar drop in M_{13} and M_{24}.

It is possible to notice that the mutual inductance between the two primary coils M_{12} is not negligible since its value might be comparable to M_{13} and M_{23}. This is because, as explained in Section 5.2.3, the coupled BPPs have been designed to minimize the diagonal cross-coupling between opposite coils while the effect of the cross-coupling within the same pad is balanced out through the compensation capacitors selection. Nevertheless, according to Figure 5.18, M_{12} is not much dependent on the misalignment compared to M_{13} and M_{23}.

The current flowing through the two coils of the BPP must have the same direction such that the primary BPP assumes the character of a non-polarized pad which is preferable when coupled to a rectangular pad. This means that the H-bridge inverters must have the same modulation as in the voltage doubler switching scheme shown in Figure 4.2(a). Considering that I_1 and I_2 have the same direction, the presence of M_{12} would push the primary currents further in the inductive region, preserving the ZVS turn-on of the MOSFETs. Therefore, M_{12} can be regarded as an extra positive reactance as shown by the KVL in (5.7). Nevertheless, based on the misalignment profile in Figure 5.18, it is important to assess the operating conditions of the circuit in Figure 5.15.

5.5.3. OPERATING CONDITIONS

ASSUMPTIONS

Since the primary circuit stays unvaried, the value of both primary compensation capacitors results from the design of the V/I-D converter. For instance, C_1 and C_2 are the ones listed in Table 5.4. Additionally, the compensation capacitance C_3=74.88 nF has been selected for the secondary rectangular coil.

The required input voltage V_{in} and the inverters' switching frequency must be selected such that the 400 V EV battery is supplied with the target output power of 7.2 kW, translating into a charging current of 18 A. Moreover, it must be guaranteed that both inverters operate in soft-switching. For these purposes, it is important to evaluate the operating points resulting from the measured self and mutual inductance conditions shown in Figure 5.18. Hereby, it is assumed that:

- V_{in} can be set in the range 360...500 V that resembles the grid-connected boost-like power factor corrector (PFC) rectifier, which could be implemented as explained in [21] and [22];
- the operating frequency of the H-bridge inverters is constrained in the range allowed by SAE J2954, i.e., 79...90 kHz;
- the H-bridge inverters can be operated independently.

ANALYSIS

Figure 5.19 summarizes the resulting operating points depending on the misalignment in the x-direction according to Figure 5.17. Specifically, the parameters that have been computed from the analytical model of Section 5.5.1 are: the absolute value and phase angle of the primary currents $\boldsymbol{I_1}$ and $\boldsymbol{I_2}$, the DC-to-DC efficiency $\eta_{\text{DC-to-DC}}$, and the required V_{in} to achieve a charging current of 18 A while the battery voltage is 400 V. Two options are investigated, i.e., whether operating either the two H-bridge inverters synchronously or only one at a time.

The results in Figure 5.19(a) are a consequence of operating both H-bridge inverters. The switching frequency of 84.5 kHz has been selected to ensure that the primary currents are inductive, i.e., they have a negative phase angle, to achieve the ZVS turn-on of the inverters while the required V_{in} is in the range covered by the PFC rectifier. When the receiver coil is placed in the aligned position (Δx=0), the current through the primary coils is relatively balanced, and the maximum $\eta_{\text{DC-to-DC}}$ is expected. On the other hand, the misalignment along either the positive or the negative direction of the x-axis would improve the mutual inductance with respect to the more proximate primary coil while worsening the other. This translates into an exponential increase of the current in the primary coil with lower mutual inductance. This considerably increases the conduction losses in one of the primary circuits, resulting in the degradation of the total $\eta_{\text{DC-to-DC}}$ up to 20%. This is not acceptable according to the minimum efficiency requirements set by SAE J2954. Moreover, the winding of the primary coils is not rated to withstand such high current densities.

On the other hand, Figure 5.19(b) shows the operating points resulting from the case in which only one H-bridge inverter is operated at the time. Specifically, $\boldsymbol{V_{AB}}$ drives the primary circuit when $\Delta x \leq 0$, while $\boldsymbol{V_{CD}}$ drives the primary circuit when $\Delta x \geq 0$. When the misalignment in the x-direction occurs, the coupling between the activated primary

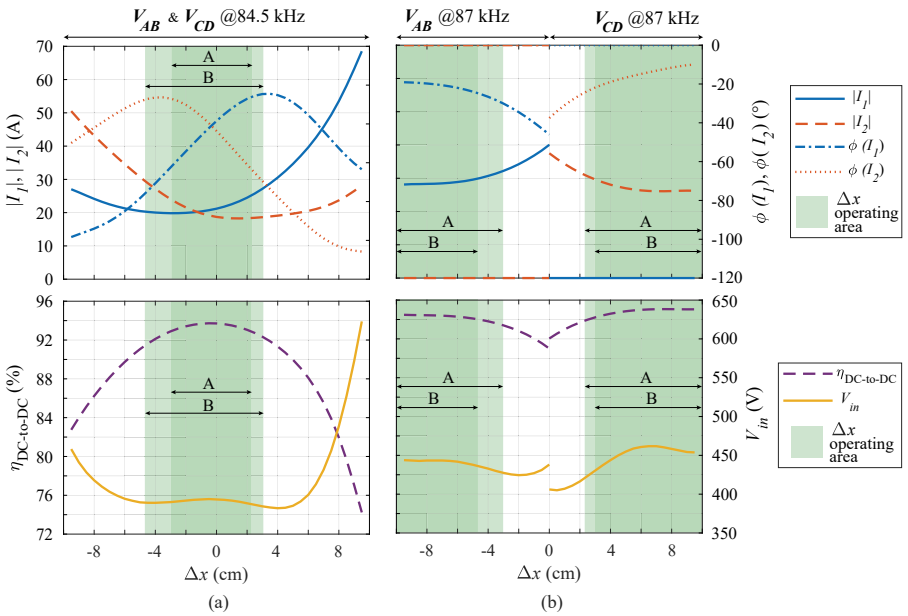

Figure 5.19: Analysis of the absolute value and phase angle of $\boldsymbol{I_1}$ and $\boldsymbol{I_2}$, the DC-to-DC efficiency $\eta_{\text{DC-to-DC}}$, and the required input voltage V_{in} depending on the receiving coil's misalignment in the x-direction. The results suppose that a 400 V battery is charged at 7.2 kW. (a) Both H-bridge inverters are operated synchronously at 84.5 kHz, resulting in the two inverted voltages $\boldsymbol{V_{AB}}$ and $\boldsymbol{V_{CD}}$ being applied to the primary circuits. (b) Only one H-bridge inverter at the time is operated at 87 kHz. Specifically, $\boldsymbol{V_{AB}}$ drives the primary circuit when $\Delta x \leq 0$, while $\boldsymbol{V_{CD}}$ when $\Delta x \geq 0$. The shaded areas denote the preferred operating regions.

coil and the secondary coil increases. This lowers the current stress in the primary circuit for the same target output power resulting in higher power transfer efficiencies. This analysis considers that, by operating one primary coil at a time, the equivalent AC resistance of the primary coil is lower than in Figure 5.19(a) since the proximity effect between the two primary coils becomes negligible. Additionally, it must be noted that, in this operating mode, the M_{12} does not contribute to the inductive behavior of the primary current. Therefore, when only one H-bridge inverter is operated, the switching frequency of the H-bridge inverter is increased to 87 kHz to ensure the ZVS turn-on of the inverter.

SELECTED OPERATING STRATEGY

One of the two operating modes in Figure 5.19 would be selected to deliver power to the secondary coil depending on the coils' alignment. When the receiver coil is placed in the aligned position, it is preferable to use both H-bridge inverters to transfer the power to the load, which results are shown in Figure 5.19(a). This choice would limit the current density through the primary coils leading to the highest achievable efficiency. This is also valid when the receiver coil is misaligned in the y-direction since, according to Figure 5.18, both M_{13} and M_{23} would drop proportionally. In that case, the output power would be regulated by controlling V_{in}. When the misalignment in the x-direction occurs over a certain threshold, only the primary coil with higher coupling to the secondary coil would be energized.

Examples of possible operating ranges are shown in Figure 5.19 by the green-shaded areas denominated as A and B. Choosing the perimeter of A as the threshold between the two operating modes ensures that the $\eta_{\text{DC-to-DC}}$ is always maximum. On the other hand, the threshold can be selected based on other criteria such as the maximum allowed current stress through the primary coils to limit their temperature rise. This is the case for the operating area B which constraints the maximum peak current to 30 A.

5.5.4. EXPERIMENTAL RESULTS

To verify the interoperability of the V/I-D converter when the coupled coils consist of the ones in Figure 5.17, the hardware in Figure 5.20 has been used operating at the rated output power of 7.2 kW. The Delta Elektronika bidirectional power supplies SM500-CP-90 and SM1500-CP-30 are used as the input and output voltage sources. The input power supply mimics the grid-connected boost-like PFC rectifier. The output power supply emulates the EV battery voltage for the whole CC charging mode. It is assumed that V_{in} is set according to the load, which information is given by the wireless communication required from the IPT system for several features such as guided positioning, pairing, and safety.

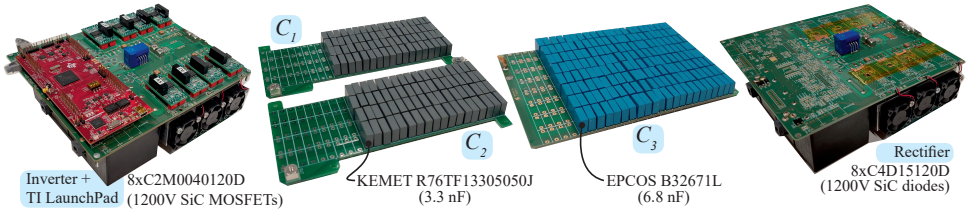

Figure 5.20: Implemented inverter, rectifier, and compensation networks with the relative devices.

Figure 5.21 and Figure 5.22 show the measured waveforms at different load and coils' alignment conditions together with the relative $\eta_{\text{DC-to-DC}}$. The measured $\eta_{\text{DC-to-DC}}$ and used V_{in} throughout the entire CC charging are plotted in Figure 5.23 resulting from different coil alignments.

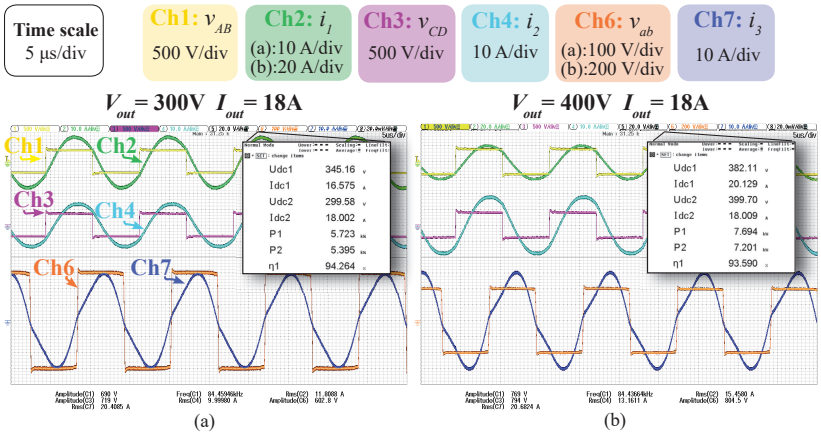

Figure 5.21: Measured circuit waveforms at I_{out}=18 A together with the relative DC-to-DC power transfer efficiency at different coils' alignments where the reference axes are shown in Figure 5.17. Aligned coils and V_{out}= (a) 300 V, (b) 400 V.

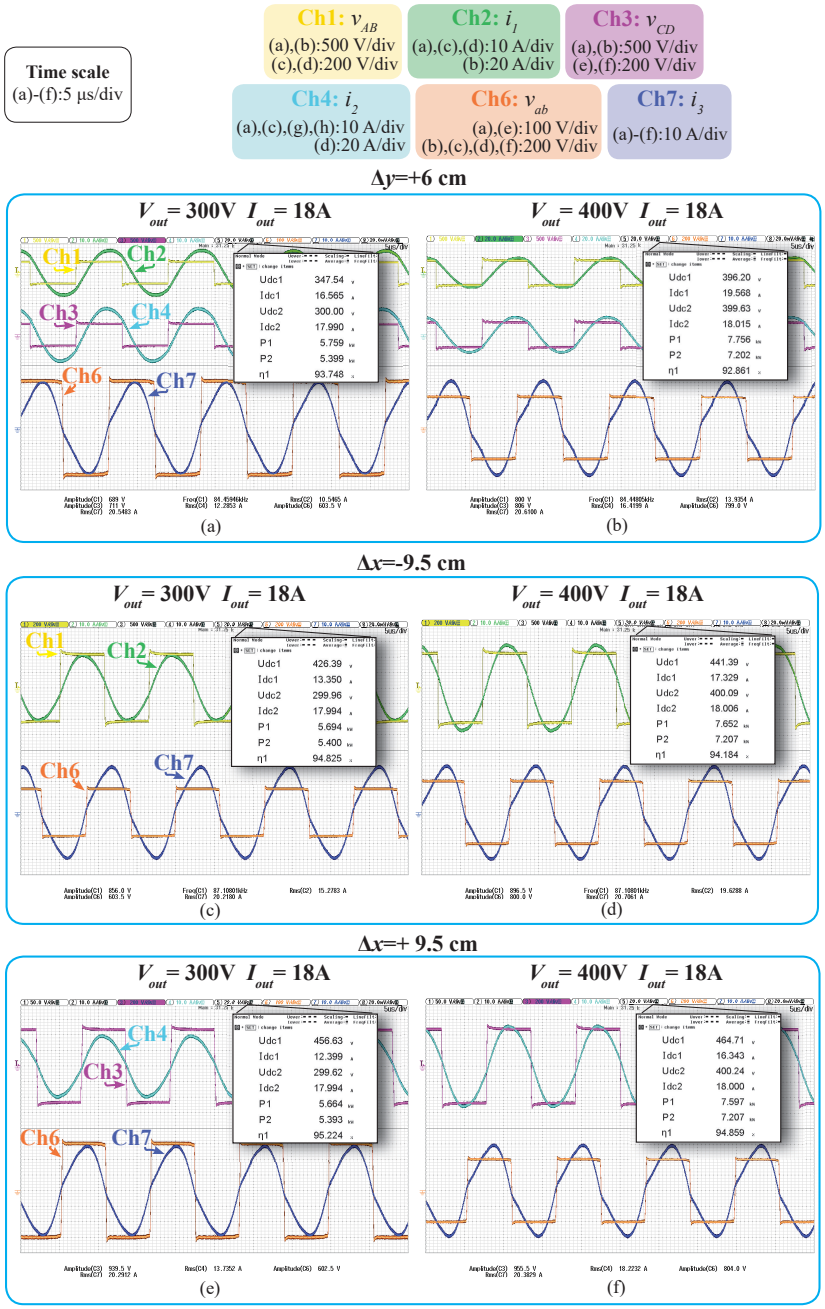

Figure 5.22: Measured circuit waveforms at I_{out}=18A together with the relative DC-to-DC power transfer efficiency at different coils' alignments where the reference axes are shown in Figure 5.17. Misalignment Δy=+6 cm and V_{out}= (a) 300 V, (b) 400 V. Misalignment Δx=-9.5 cm and V_{out}= (c) 300 V, (d) 400 V. Misalignment Δx=+9.5 cm and V_{out}= (e) 300 V, (f) 400 V.

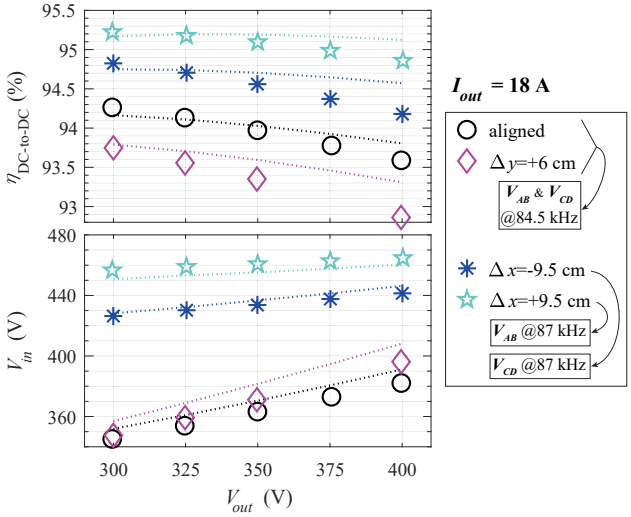

Figure 5.23: Measured DC-to-DC efficiency $\eta_{\text{DC-to-DC}}$ and used input voltage V_{in} for the entire CC charging profile and at different coils' alignments. The dotted lines show the expected results from the analytical model.

5

DISCUSSION

When the two geometric centers are aligned, the secondary coil is misaligned with respect to both primary coils causing higher primary currents for the same output power. This results in the measured $\eta_{\text{DC-to-DC}}$ being lower when the coils are aligned than when the secondary coil is misaligned along the x-axis. Additionally, the effect of M_{12} pushes the primary currents further into the inductive region, worsening the H-bridge inverters' turn-off losses. The highest $\eta_{\text{DC-to-DC}}$ has been measured when the L_3 is aligned with L_2 (Δx=9.5 cm) due to their shorter air gap, resulting in a lower input current for the same output power. For instance, efficiencies higher than 95% have been measured for most of that charging profile. Two other factors contribute to the higher measured efficiency when only one H-bridge at a time is operated. One is the lower equivalent AC resistance of the primary coil since there is a great reduction of the proximity effect between the two primary coils. The other is the reduced turn-off power losses since the H-bridge inverter operates closer to the resonant frequency. Nevertheless, all the considered operating points are achieving the ZVS turn-on of the H-bridge inverters as shown in Figure 5.21 and Figure 5.22.

It must also be noted that, with this implementation, the current density of the primary coils is considerably higher than the intended from the nominal design with the coupled BPPs. This leads to a higher winding temperature and, consequently, higher resistance. If the primary BPP has to support interoperability, it is preferable to oversize the primary coils' Litz wire to reach an overall higher efficiency.

In the CC charging profile of Figure 5.23, it is assumed that the battery voltage ranges from 300 V to 400 V. The utilized V_{in} mostly ranges from 360 V to 470 V which could be implemented in the European phase-to-neutral 230 V RMS network through a single-phase grid-connected PFC rectifier. Lower V_{in} values could be achieved by phase-shifting the inverters to decrease the fundamental component of $\boldsymbol{V}_{AB}$.

5.6. CONCLUSION

This chapter has proposed, analyzed, and experimentally verified an advanced and compact V/I-D converter using series-compensated BPPs, which can efficiently provide the same power level to both 400 V and 800 V batteries without affecting the current rating of the converter's circuit components. The power-flow control is performed only at the source side, simplifying the circuit onboard the EV. The V/I-D converter has two operating modes. The voltage doubler mode is suitable to charge 800 V batteries, while the current doubler mode is suitable to charge 400 V one. An extensive analysis of the undesired cross-coupling between the two BPPs has been performed to evaluate how it impacts the power transfer. It has been found that it is preferable to design the coils' overlap area such that the diagonal cross-coupling between opposite BPPs is negligible. On the other hand, the effect of the cross-coupling between the two coils in the same BPP can be compensated by selecting the compensation capacitances. The functionality of the converter has been tested experimentally with a laboratory demonstrator at different coils' alignments in the x-, y-, and z-direction and for load conditions typical of EV charging profiles. At 7.2 kW and with aligned BPPs, the DC-to-DC efficiency of 96.34% and 96.53% has been measured at 400V and 800V, respectively. High efficiency and the ZVS turn-on of the H-bridge inverters are maintained throughout most operating conditions. The misalignment concerning the lateral x-direction results in the most critical operating conditions since it causes an unbalance between the two diagonal mutual inductances, eventually leading to the hard-switching of one H-bridge inverter. Nevertheless, the power transfer efficiency is expected to be higher than 94% for a misalignment in the x-direction up to ± 5 cm, typical of static EV wireless charging. Additionally, the interoperability of the proposed V/I-D converter has been proved when the primary BPP is coupled with a standardized rectangular coil, e.g., the VA test station WPT2/Z2 from SAE J2954. This is important because it enlarges the usability of the proposed converter. The analytical modeling and the intended operation have been discussed. Specifically, one or both H-bridge inverters are energized depending on the coils' alignment. These conditions have been validated through experimental results for the whole CC charging mode and different alignments. The measured DC-to-DC efficiency ranges between 92.86% and 95.22%, which is relatively high considering that this is not the intended operation of the V/I-D converter.

REFERENCES

[1] G. A. Covic, M. L. G. Kissin, D. Kacprzak, N. Clausen, and H. Hao, "A bipolar primary pad topology for ev stationary charging and highway power by inductive coupling", in *2011 IEEE Energy Conversion Congress and Exposition*, 2011, pp. 1832–1838. DOI: 10.1109/ECCE.2011.6064008.

[2] M. Budhia, J. T. Boys, G. A. Covic, and C.-Y. Huang, "Development of a single-sided flux magnetic coupler for electric vehicle ipt charging systems", *IEEE Transactions on Industrial Electronics*, vol. 60, no. 1, pp. 318–328, 2013. DOI: 10.1109/TIE.2011.2179274.

[3] T.-F. Wu, C.-T. Tsai, Y.-M. Chen, and Y.-D. Chang, "Analysis and implementation of an improved current-doubler rectifier with coupled inductors", *IEEE Transactions*

on Power Electronics, vol. 23, no. 6, pp. 2681–2693, 2008. DOI: 10.1109/TPEL.2008.2005372.

[4] C. H. Kwan, J. M. Arteaga, N. Pucci, D. C. Yates, and P. D. Mitcheson, "A 110w e-scooter wireless charger operating at 6.78mhz with ferrite shielding", in *2021 IEEE PELS Workshop on Emerging Technologies: Wireless Power Transfer (WoW)*, 2021, pp. 1–4. DOI: 10.1109/WoW51332.2021.9462885.

[5] H. Z. Beh, M. Neath, J. T. Boys, and G. A. Covic, "An alternative ipt pickup controller for material handling using a current doubler", *IEEE Transactions on Power Electronics*, vol. 33, no. 12, pp. 10 135–10 147, 2018. DOI: 10.1109/TPEL.2018.2801247.

[6] Y. Wang, M. Xiong, X. Wang, *et al.*, "Research on 11kw wireless charging system for electric vehicle based on lcc-sp topology and current doubler", in *2020 IEEE Energy Conversion Congress and Exposition (ECCE)*, 2020, pp. 820–827. DOI: 10.1109/ECCE44975.2020.9235377.

[7] L. Shi, A. Delgado, R. Ramos, and P. Alou, "A wireless power transfer system with inverse coupled current doubler rectifier for high-output current applications", *IEEE Transactions on Industrial Electronics*, vol. 69, no. 5, pp. 4607–4616, 2022. DOI: 10.1109/TIE.2021.3078350.

[8] *J2954: Wireless power transfer for light-duty plug-in/ electric vehicles and alignment methodology*, Aug. 2022.

[9] A. Zaheer, H. Hao, G. A. Covic, and D. Kacprzak, "Investigation of multiple decoupled coil primary pad topologies in lumped ipt systems for interoperable electric vehicle charging", *IEEE Transactions on Power Electronics*, vol. 30, no. 4, pp. 1937–1955, 2015. DOI: 10.1109/TPEL.2014.2329693.

[10] F. Y. Lin, G. A. Covic, and J. T. Boys, "Evaluation of magnetic pad sizes and topologies for electric vehicle charging", *IEEE Transactions on Power Electronics*, vol. 30, no. 11, pp. 6391–6407, 2015. DOI: 10.1109/TPEL.2015.2419592.

[11] F. Y. Lin, G. A. Covic, and J. T. Boys, "Leakage flux control of mismatched ipt systems", *IEEE Transactions on Transportation Electrification*, vol. 3, no. 2, pp. 474–487, 2017. DOI: 10.1109/TTE.2016.2630922.

[12] F. Lin, G. A. Covic, and J. T. Boys, "A comparison of multi-coil pads in ipt systems for ev charging", in *2018 IEEE Energy Conversion Congress and Exposition (ECCE)*, 2018, pp. 105–112. DOI: 10.1109/ECCE.2018.8557369.

[13] F. Lin, G. A. Covic, and M. Kesler, "Design of a sae compliant multicoil ground assembly", *IEEE Journal of Emerging and Selected Topics in Industrial Electronics*, vol. 1, no. 1, pp. 14–25, 2020. DOI: 10.1109/JESTIE.2020.2999597.

[14] A. Zaheer, D. Kacprzak, and G. A. Covic, "A bipolar receiver pad in a lumped ipt system for electric vehicle charging applications", in *2012 IEEE Energy Conversion Congress and Exposition (ECCE)*, 2012, pp. 283–290. DOI: 10.1109/ECCE.2012.6342811.

[15] A. Zaheer, G. A. Covic, and D. Kacprzak, "A bipolar pad in a 10-khz 300-w distributed ipt system for agv applications", *IEEE Transactions on Industrial Electronics*, vol. 61, no. 7, pp. 3288–3301, 2014. DOI: 10.1109/TIE.2013.2281167.

[16] N. Rasekh, J. Kavianpour, and M. Mirsalim, "A novel integration method for a bipolar receiver pad using lcc compensation topology for wireless power transfer", *IEEE Transactions on Vehicular Technology*, vol. 67, no. 8, pp. 7419–7428, 2018. DOI: 10.1109/TVT.2018.2837348.

[17] H. Jafari, T. O. Olowu, M. Mahmoudi, and A. Sarwat, "Optimal design of ipt bipolar power pad for roadway-powered ev charging systems", *IEEE Canadian Journal of Electrical and Computer Engineering*, vol. 44, no. 3, pp. 350–355, 2021. DOI: 10.1109/ICJECE.2021.3075639.

[18] W. Zhao, X. Qu, J. Lian, and C. K. Tse, "A family of hybrid ipt couplers with high tolerance to pad misalignment", *IEEE Transactions on Power Electronics*, vol. 37, no. 3, pp. 3617–3625, 2022. DOI: 10.1109/TPEL.2021.3109639.

[19] Y. Li, R. Mai, L. Lu, T. Lin, Y. Liu, and Z. He, "Analysis and transmitter currents decomposition based control for multiple overlapped transmitters based wpt systems considering cross couplings", *IEEE Transactions on Power Electronics*, vol. 33, no. 2, pp. 1829–1842, 2018. DOI: 10.1109/TPEL.2017.2690061.

[20] R. Mai, Y. Luo, B. Yang, Y. Song, S. Liu, and Z. He, "Decoupling circuit for automated guided vehicles ipt charging systems with dual receivers", *IEEE Transactions on Power Electronics*, vol. 35, no. 7, pp. 6652–6657, 2020. DOI: 10.1109/TPEL.2019.2955970.

[21] J. W. Kolar, J. Biela, and J. Minibock, "Exploring the pareto front of multi-objective single-phase pfc rectifier design optimization - 99.2% efficiency vs. 7kw/din^3 power density", in *2009 IEEE 6th International Power Electronics and Motion Control Conference*, 2009, pp. 1–21. DOI: 10.1109/IPEMC.2009.5289336.

[22] J. P. M. Figueiredo, F. L. Tofoli, and B. L. A. Silva, "A review of single-phase pfc topologies based on the boost converter", in *2010 9th IEEE/IAS International Conference on Industry Applications - INDUSCON 2010*. DOI: 10.1109/INDUSCON.2010.5740015.

[23] R. L. Steigerwald, "A comparison of half-bridge resonant converter topologies", *IEEE Trans. Power Electron.*, vol. 3, no. 2, 1988.

[24] Q. Li and Y. C. Liang, "An inductive power transfer system with a high-q resonant tank for mobile device charging", *IEEE Transactions on Power Electronics*, vol. 30, pp. 6203–6212, 2015.

[25] PREMO. "Wc-rx-002-90k receiving antenna flexible-pad for the wireless power transfer in the electric vehicles". Accessed: 21/10/2022. (), [Online]. Available: https://www.grupopremo.com/689-wc-rx-002-90k-receiving-antenna-flexible-pad-for-the-wireless-power-transfer-in-the-electric-vehicles.

6

CONCLUSION

This thesis has explored different aspects of inductive power transfer (IPT) systems for static wireless charging of electric vehicles (EVs), where the power levels of 3.7 kW and 7.7 kW have been used for the experimental verification. This study started with the analysis of conventional IPT systems to identify their main features and advantages. After that, two main research concepts were proposed and experimentally proved. The first concept consists of a variable compensation capacitance, while the second is related to the interoperability of IPT systems with EVs having different nominal battery voltages.

6.1. REGARDING THE RESEARCH QUESTIONS

1. *Which are the most suitable compensation networks for EV wireless charging?*

According to Chapter 2, the series-series (S-S) and the double-sided LCC (DLCC) are the most suitable compensation networks among the most commonly used ones in EV wireless charging applications. The components' tuning of both compensations is independent of the mutual inductance between the coupled coils and the loading condition. Moreover, the S-S and the DLCC compensation can be directly powered by a voltage source H-bridge inverter with soft-switching capability. They also have a load-independent output current that allows a direct connection of the output high-frequency rectifying stage to the EV battery. Since the S-S compensation employs the least number of components, it can potentially reach the highest power transfer efficiency. However, its output current is inversely dependent on the coils' mutual inductance, which might be unsafe for the IPT system, especially in applications in which the mutual inductance changes in a large range, e.g., in dynamic EV wireless charging. Moreover, its power transfer characteristic strongly depends on the coupled coils' mutual inductance, meaning that, given the input constraints of the IPT system, it might not be possible to deliver the target output power without the use of additional DC/DC converters. For this reason, this thesis has proposed a design guideline for IPT systems using the S-S compensation based on the selection of coupled coils. Specifically, their nominal mutual inductance must match a target value that depends on the constraints set by the specific

application, i.e., the DC input voltage available from the grid connection, the DC output voltage set by the battery, the target output power, and the selected operating frequency. Even though the DLCC compensation can theoretically reach lower power transfer efficiencies since it employs more passive components, its power transfer capability is not limited by the coupled coils' mutual inductance. With the DLCC compensation, the nominal output power delivered by the IPT system can be advantageously selected by tuning the compensation inductances. Moreover, the load-independent output current in the DLCC compensation is directly dependent on the coils' mutual inductance resulting in an intrinsically safe IPT system over the misalignment. For this reason, it is convenient to employ the DLCC compensation in applications where the coils' mutual inductance varies in a large range, simplifying the circuit protections. Alternatively, the DLCC compensation can be used when the coils' mutual inductance is far from the target one for the S-S compensation to avoid the adoption of additional DC/DC converters to deliver the nominal output power. Furthermore, it has been shown that the opposite dependence of the S-S and the DLCC output currents with respect to the coils' mutual inductance can be used in hybrid compensation networks employing both the S-S and DLCC compensations to realize a self-balancing output power over the misalignment. Finally, it must be noted that the implemented laboratory demonstrators employing the S-S and the DLCC compensations have reached remarkable DC-to-DC power transfer efficiency for the considered power level. For instance, when using the S-S compensation, Chapter 2 shows a measured DC-to-DC peak efficiency of 96.24% at the maximum considered coupling condition for an output power of about 3.3 kW with 400 V DC output voltage. On the other hand, when considering the DLCC compensation, Appendix B shows a measured peak efficiency of 95.23% at the maximum considered coupling condition for an output power of about 3.1 kW with 400 V DC output voltage.

2. *Is it advantageous to employ variable compensation networks to mitigate the effects of misalignment on the IPT systems' performance?*

In conventional IPT systems, the available variables to control the power transfer are the input voltage, the output voltage, and the operating frequency. Employing a variable compensation component or network introduces an additional control variable, i.e., the circuit's resonant frequency. Chapter 3 has proposed and demonstrated an efficiency enhancement strategy based on variable series compensation capacitors that change the natural resonant frequency of the IPT system to make the optimum load condition that minimizes the power losses invariant of the coil's mutual inductance. This proposed method is called constant optimum load (COL). The main advantage of this solution is the elimination of voltage control at the load side. Only the input power is regulated through the grid-connected power factor correction (PFC) rectifier, ensuring that the COL condition is met while the battery voltage increases during the charging cycle. The variable series compensation capacitor has been realized at both the primary and the secondary circuits as a switch-controlled capacitor (SCC), where two implementations have been tested, namely the half-wave and the full-wave modulation. The half-wave modulation results in overall higher efficiency than full-wave modulation, with 96.30% for the input power of 3.2kW and at the maximum coils' alignment. For the same power and minimum alignment, the efficiency drops only by 0.27%. The minimum measured

efficiency is 95.68% at partial load and minimum coupling. On the other hand, at 3.2kW and maximum magnetic coupling, the full-wave modulation results in 96.18%, and the efficiency drops by 0.42% at the minimum alignment. When misalignment occurs, the system using SCCs with half-wave modulation is more efficient than the conventional S-S compensation with fixed capacitors. The efficiency gain is up to 0.68% at partial load. Additionally, the current distortion introduced by using SCCs and conventional capacitors as series compensation has been analyzed to preliminary assess the radiated magnetic field in the higher frequency domain. By computing the current's fast Fourier transform (FFT) up to 30MHz, the SCCs using the half-wave modulation have been found to introduce the highest total lumped distortion because of their asymmetrical operation. However, in correspondence to the critical frequencies of the limits set by SAE J2954 on the radiated magnetic field, the amplitude of the single harmonic components is comparable to or lower than in the other implementations. After that, the radiated magnetic field from each configuration was evaluated through finite element method (FEM) analysis. The results at 10 m distance are all far below the electromagnetic compatibility (EMC) limits from SAE J2954 up to 30 MHz. When considering the human exposure limits set by ICNIRP, a minimum distance of 25 cm from the outer sides of the coupled coils ensures a safe magnetic field level for both the general public and implanted medical devices, which has been confirmed experimentally. All in all, considering the resulting high power transfer efficiency and the compliant radiated magnetic field for a coil's misalignment range and throughout a charging cycle typical of a 3.7kW static EV wireless charger, this research has proved the suitability and advantage of the proposed COL charging method using variable compensation capacitance.

3. *How can EVs with different nominal battery voltage levels be charged efficiently at the same power class?*

Chapter 4 and Chapter 5 have proposed and demonstrated the functionality of the novel voltage/current doubler (V/I-D) converter, which consists of a universal IPT system that can efficiently charge at the same power level EVs with 400 V and 800 V battery voltages. As a result, the available power from an IPT charging station can be fully utilized when delivering wireless power to any EV, ensuring optimal interoperability with different battery voltages. The V/I-D comprises two sets of series-compensated coupled coils, i.e., two primary and two secondary coils, connected to a dedicated H-bridge converter. The power transfer control is implemented only at the primary side by operating the two H-bridge inverters with the same modulation, suitable for 800 V batteries, or opposite modulation, suitable for 400 V batteries. The power losses are ideally the same in the two operating modes since all components would conduct the same current. The secondary circuit is composed of only passive devices, resulting in a simple and cost-effective onboard circuit that does not require active control. This is a key advantage with respect to the alternative conventional solution that employs an additional output DC/DC converter that would operate when the battery voltage differs from the nominal. The proposed V/I-D converter was experimentally verified at 7.2 kW with two different coils' configurations. The first arrangement employs two physically separated sets of rectangular coupled coils, which results in a functionality close to the ideal intended one. Considering that the battery voltage could be either 400V or 800V, the peak DC-to-

DC efficiency of 97.11% and 97.52% were measured with aligned coils, respectively. Furthermore, the second arrangement consists of a more compact implementation since it employs bipolar pads (BPPs) in which the two rectangular coils at each circuit side are deployed on the same ferrite layer. The DC-to-DC efficiency of 96.34% and 96.53% has been measured with aligned BPPs at 400V and 800V, respectively. The lower efficiency resulting from the BPP magnetic arrangement is mainly caused by the power losses due to the eddy currents in the BPPs' aluminum shield, which was not used for the rectangular coils. Additionally, by regulating the DC input voltage in the range that a PFC rectifier could provide and the operating frequency within the range 79-90 kHz allowed by SAE J2954, the functionality of the V/I-D converter was proved under different misalignment profiles and loading conditions achieving overall DC-to-DC efficiencies over 94%. Finally, the interoperability of the proposed V/I-D converter has been proved experimentally when the primary BPP is coupled with a standardized rectangular coil, i.e., the VA test station WPT2/Z2 from SAE J2954. This is important because it enlarges the usability of the proposed converter by guaranteeing interoperability with different receiving coils' topologies.

4. *How does the cross-coupling affect IPT systems with multicoil magnetic pads?*

IPT systems with multicoil magnetic configurations are subjected to unwanted cross-coupling. The effects of the cross-coupling on the power transfer have been analyzed in Chapter 4 and Chapter 5, considering the two magnetic arrangements used for the V/I-D converter. Nevertheless, these conclusions can be applied to other IPT systems with similar coils' structures. Two instances of unwanted cross-coupling have been identified. The first corresponds to the cross-coupling between coils at the same circuit side, e.g., two adjacent primary coils, which is roughly constant since these two coils do not move with respect to each other. On the other hand, the second one is the diagonal cross-coupling between coils at opposite circuit sides, which is likely to vary when the misalignment occurs. Moreover, it has been found that the mutual inductance between two coils can have either a positive or a negative value depending on the direction of its concatenated magnetic flux. As a result, the effect of the cross-coupling on the power transfer highly depends on the sign of the mutual inductance. In the case of physically separated consecutive rectangular coils, it has been found that placing them next to each other with a minimum distance equal to their length would ensure that their cross-coupling would have negligible effects on the power transfer and performance of the IPT system even in the presence of a lateral misalignment ~1/3 of their distance. In the case of coupled BPPs, minimizing one of the two instances of cross-coupling is possible by selecting the overlap area of the coils within the same BPP. It has been found that it is preferable to design the coils' overlap area such that the diagonal cross-coupling between opposite BPPs is negligible since that cross-coupling directly influences the power transfer characteristic between the primary and the secondary circuits. The lateral misalignment that causes an unbalance between the two diagonal cross-coupling is the most critical since it might lead to the hard-switching of one H-bridge inverter. Therefore, applications with a moderate misalignment profile in that direction are preferred, or alternatively, the inverter's terminal management must be adequately designed to stand the switching losses in those operating conditions. On the other hand, the effect

of the cross-coupling between the two coils in the same BPP can be minimized by selecting the compensation capacitances, which is particularly beneficial considering that this cross-coupling is approximately constant over the misalignment.

6.2. FUTURE WORK

Considering the research performed in this thesis, the natural next step would be to explore whether is advantageous to employ a variable compensation capacitance in the V/I-D converter with BPPs. This could be beneficial to mitigate the effects of the cross-coupling on the power transfer, e.g., to maintain the soft-switching of the H-bridge inverters for a larger misalignment range. It would be preferable to adopt a variable compensation just at the primary circuits since there is where the proposed V/I-D converter realizes the power transfer control, and the secondary circuit can still be composed of passive components, forming a simple and cost-effective onboard circuit.

An additional challenging research direction is guaranteeing interoperability between different IPT systems used for EV charging. This is especially important when considering the commercial development of this technology, such that it can be used on a mass scale. Innovative solutions could be found that go beyond the available industrial standards on this application. Interoperability must comprise different coils' topologies and battery implementations, which becomes even more critical in dynamic wireless charging due to the extreme misalignment profiles.

Another important aspect to be researched is the scalability of IPT systems for higher power levels to allow faster battery charging cycles. At the same time, these high-power applications must guarantee compliance with EMC regulations and the safety exposure of humans to the radiated magnetic field. Eventually, for these higher power levels, improved magnetic field shielding techniques must be investigated.

Finally, other promising applications that can benefit from IPT systems can be explored further. One example could be wireless charging for ships and maritime vehicles, environments that particularly benefit from galvanic isolation. Another one could be using IPT systems to electrify rail-based transportation without the use of overhead cables, which could be used for trams or trains.

APPENDIX

A

CONSTRAINTS AND REQUIREMENTS FROM INDUSTRIAL STANDARDS AND REGULATIONS ON EV WIRELESS CHARGING

A.1. INTRODUCTION

Since 2015, standards and regulations on EV wireless charging systems have been released such that common constraints can be defined to guarantee interoperability and safety. Therefore, it is essential to be aware of these regulations to ensure that the research solutions have industrial relevance.

This appendix chapter focuses on the available regulations and standards on EV charging through WPT. At the current publication date of the thesis, these standards are IEC 61980 series, ISO 19363, SAE J2954, IEC PAS 63184, and SAE J2847/6. IEC 61980-2 and SAE J2847/6 define the requirements for the communication between the EV and the wireless charging station. Hereby they are not discussed further since the wireless communication protocol has not been used in this thesis. IEC 61980-1, IEC 61980-3, ISO 19363, SAE J2954, and IEC PAS 63184 are first explained individually from Section A.2 to Section A.5. After that, they are compared mainly in terms of the electromagnetic compatibility (EMC) and exposure of humans to the radiated magnetic field limits in Section A.6. To gain a better understanding, a quantitative and qualitative interpretation of these limits is also given. The main conclusions on the topic are given in Section A.7.

This appendix chapter is the 2022 updated version of:

- F. Grazian, W. Shi, J. Dong, P. van Duijsen, T. B. Soeiro and P. Bauer, "Survey on Standards and Regulations for Wireless Charging of Electric Vehicles", *2019 AEIT International Conference of Electrical and Electronic Technologies for Automotive (AEIT AUTOMOTIVE)*, pp. 1-5.

A

A.2. IEC 61980

The International Electrotechnical Commission (IEC) has published the standard IEC 61980 on electric vehicle WPT systems in the three following parts. Part 1 and part 3 are the most related to the content of the thesis, and they are discussed in the next sections.

- IEC 61980-1, Part 1: General requirements.
- IEC 61980-2, Part 2: Specific requirements for communication between electric road vehicle (EV) and infrastructure.
- IEC 61980-3, Part 3: Specific requirements for magnetic field wireless power transfer systems.

A.2.1. IEC 61980-1

This is an international standard released in the first edition in July 2015. At the current date of this thesis, this has been replaced by the second edition published in November 2020, which stability date is 2025 [1]. IEC 61980-1 is the first part of the IEC 61980 series that only focuses on general requirements.

IEC 61980-1 concerns generic aspects of WPT such as use cases, electrical safety, electromagnetic compatibility (EMC), and electromagnetic field (EMF) exposure, which are common for all possible wireless power transfer technologies, such as inductive power transfer (including magnetic resonance), capacitive power transfer, microwave power transfer (1-300 GHz), infrared power transfer (300 GHz-400 THz).

The transfer power classes, efficiency, interoperability, and communication are not specified here, they are part of the specific requirements for each transfer technology. The installation of the WPT charging system could be either ground mounted (in-ground, on-ground, or over-stand), vertical surface mounted, or on-roof mounted. The system can be designed either for indoor use, outdoor use, or industrial areas exposed to pollution and/or severe condition. Environmental tests must be executed to asses the WPT system compliance with IEC 61851-1 and ISO 19363.

EMC limits are defined in this standard, which are essential constraints for the development of this technology. Both immunity and disturbance requirements are specified, and each of them treats conducted and radiated perturbations. The immunity requirements refer to IEC 61000-4.

On the other hand, the disturbance requirements are divided into two groups depending on the frequency range. The low frequency (LF) range is regulated by IEC 61000-3 which sets limits for harmonics, voltage fluctuation, and flicker with respect to the AC power input port. For what concerns the radio frequency (RF) ranges, these are categorized as shown in Table A.1. Since the WPT system is classified as equipment of group 2 according to Annex A of CISPR 11:2015 and therefore, it needs to be compliant with the group 2 limits. Moreover, depending on the environment in which the WPT system is supposed to be used, that can belong to two different classes. Class A equipment is suitable for any environment other than residential, and class B equipment is suitable for residential and domestic environments.

The conducted disturbances at the AC power input port refer to the limit specified by CISPR 11, while the conducted disturbances at the wired network port refer to CISPR 32.

According to Table A.1, the limits on the radiated disturbances are divided into three frequency ranges. The radiated disturbances in the first frequency range going from

Table A.1: Categorization of EMC disturbances according to IEC 61980-1. [1]

Port	Phenomenon	Frequency range
AC power input	Conducted disturbances	150 kHz to 30 MHz
Wired network		150 kHz to 30 MHz
Enclosure	Radiated disturbances	9 kHz to 150 kHz
		150 kHz to 30 MHz
		30 MHz to 1 GHz

9 kHz to 150 kHz are regulated according to the limits in Figure A.1. These regulate the quasi-peak (QP) magnetic field strength for WPT systems measured at 10 meters distance, where differentiation is made between equipment of class A and B. Within each class, there are two limits that depend on the used input power. It is mentioned that if class B equipment with a rated AC mains power of > 3.6 kW does not satisfy the limits in Figure A.1, it should at least fulfill those limits with a greater tolerance of 15 dB. In that case, the equipment is not meant to be used in an environment with sensitive devices within 10 meters. Additionally, if the fundamental frequency of the WPT is below 150 kHz, the limits in Figure A.1 can be relaxed by 10 dB in correspondence of the second, third, fourth and fifth integer harmonics of the fundamental frequency.

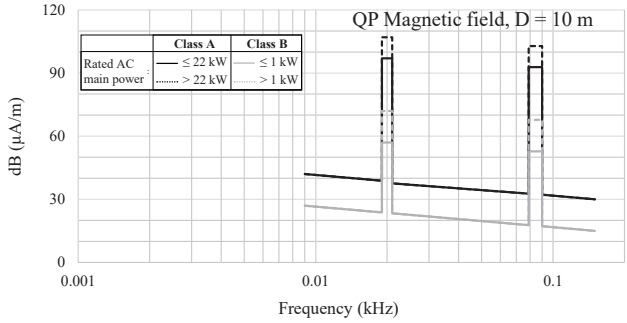

Figure A.1: IEC 61980-1 limits on the quasi-peak magnetic field strength from 9 kHz to 150 kHz for either A or B class equipment. These limits depend on the utilized AC input power. [1]

The radiated disturbances in the second frequency range going from 150 kHz to 30 MHz are regulated according to the limits in Figure A.2. These regulate the QP magnetic field strength for WPT systems measured either at 3 meters or 10 meters distance, where differentiation is made between equipment of class A and B. In this case, no distinction is made based on the input power rating.

For comparison purposes, the limits in Figure A.1 and Figure A.2 at 10 meters distance have been plotted in Figure A.3 such that the entire frequency spectrum from 9 kHz to 30 MHz is represented.

Finally, the disturbance limitations for the third frequency range from 30 MHz to 1000 MHz are proposed only in terms of the electric component of the field. These limits at 3 meters distance are reported in Figure A.4 for both classes. The limitations at 10 meters distance have the same trend as the ones in Figure A.4 with an offset of -10 dB.

For what concerns the EMF restrictions for human exposure, it is mentioned that the WPT system must not cause malfunction of cardiac implantable electronic devices

A

(CIED) present in the proximity. However, specific limits are defined in the specific parts of the WPT technologies.

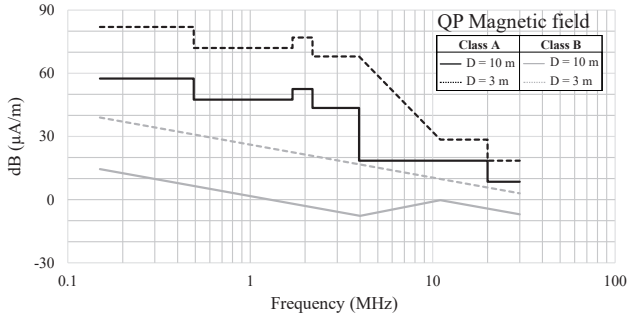

Figure A.2: IEC 61980-1 limits on the magnetic field strength from 150 kHz to 30 MHz, for both class A and B types of equipment (CISPR 11 Group 2 Class A). [1]

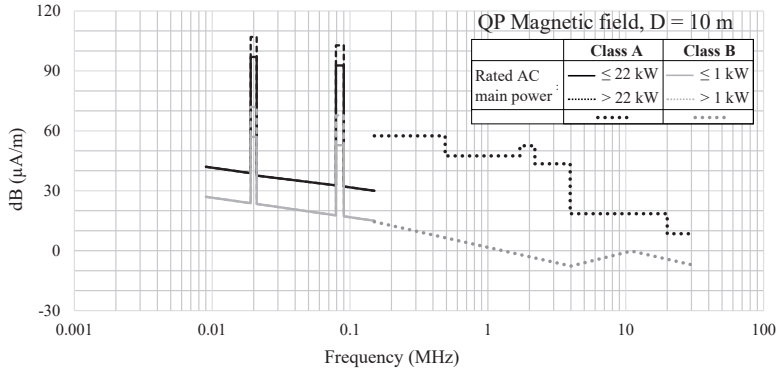

Figure A.3: IEC 61980-1 limits on the magnetic field strength from 150 kHz to 30 MHz for both class A and B types of equipment (CISPR 11 Group 2 Class A). [1]

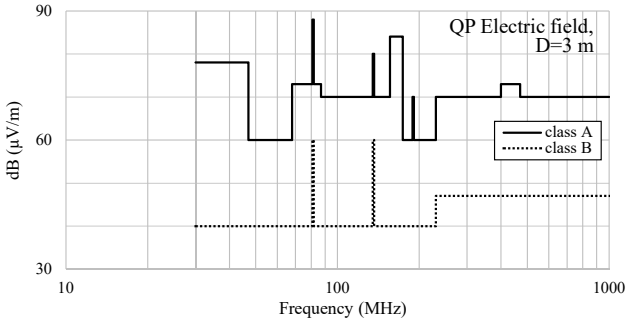

Figure A.4: IEC 61980-1 limits on the 30-1000 MHz electric field strength for both class A and B types of equipment, at 3 meters distance (CISPR 11 Group 2). [1]

A.2.2. IEC 61980-3

This is an international standard that was first released as a technical specification in June 2016. At the current date of this thesis, this has been replaced by the first edition

published in November 2022, which stability date is 2024 [2]. IEC 61980-3 concerns magnetic field wireless power transfer (MF-WPT) systems for stationary wireless charging, and the transfer power classes, Z-classes, misalignment tolerance, test conditions, and design references are the same as SAE J2954. The supply device is categorized as stationary equipment with surface or flush mounting or as non-stationary equipment. The minimum efficiency is 85% at the nominal coils' alignment and 80% under misalignment. Guidelines on the coils' positioning and interoperability are also discussed, which are in line with SAE J2954. For what concerns EMC and human exposure limits, the ones defined in IEC 61980-1 are valid. It is specified that CISPR B will be taken as a reference in the future for the radiated emission limits from 9 kHz to 150 kHz, which will be published as part of CISPR 11.

It must be noted that informative references for the wireless charging of heavy-duty EVs are also proposed, where electrical and mechanical guidelines are given. These specifications cannot be found in the other available standards. In the case of heavy-duty EVs, IPT systems consist of a multi-phase circuit, and the operating frequency of the inverter can be selected as either 20 kHz or 60 kHz.

A.3. ISO 19363

ELECTRICALLY PROPELLED ROAD VEHICLES - MAGNETIC FIELD WIRELESS POWER TRANSFER - SAFETY AND INTEROPERABILITY REQUIREMENTS

This is an intentional standard that was first released as a publicly available specification (PAS) in January 2017 by the International Organization for Standardization (ISO). After that, it was revised and replaced in April 2020 [3]. This specification is intended to be compatible with the IEC 61980 series. In particular, ISO 19363 treats magnetic field power transfer for car passengers and light-duty vehicles in stationary and unidirectional applications. An example of a WPT system structure is shown in Figure A.5. The whole transmitter system is called ground assembly (GA), and the receiver one is called vehicle assembly (VA). The WPT technology chosen is inductive power transfer using magnetic resonance. The GA and the VA are coupled through their respective coils and use wireless communication.

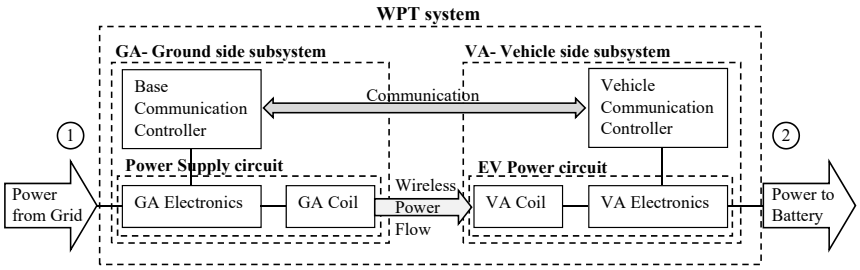

Figure A.5: Example of WPT system structure first proposed by ISO 19363. [3]

This specification has several common characteristics with IEC 61980 and SAE J2954. For what concerns EMC, ISO 19363 refers to CISPR 11 and, as mentioned in Section A.2.2, radiation limits specifically for this technology will be included in a future version of that standard. For EMF human exposure, this document refers to the Guidelines of ICNIRP

A

2010 for the general public. Requirements and validation guidelines are also provided to ensure the safety of active implantable medical devices (AIMDs). These limits will be discussed in Section A.6.2.

A.4. SAE J2954

WIRELESS POWER TRANSFER FOR LIGHT-DUTY PLUG-IN/ ELECTRIC VEHICLES AND ALIGNMENT METHODOLOGY

SAE J2954 is a standard released by the Society of Automotive Engineers (SAE) which provides specific guidelines and technical references for the design of EV WPT charging systems in the United States of America. The first edition was published in May 2016 as a technical information report (TIR), which was revised in November 2017. The second edition of SAE J2954 recommended practice (RP) was published in April 2019 as an evolution of SAE TIR J2954 based on experimental interoperability data. After that, complete revisions of SAE J2954 were released in October 2020, and, at the current date of publication of this thesis, the latest races back to August 2022 [4]. SAE J2954 aims to harmonize with the other standard developing organizations, such as ISO and IEC, seeking a worldwide 11.1 kVA WPT standard, practical to commercial applications.

SAE J2954 presents technical guidelines for wireless charging of light-duty EVs (<4545 kg), which works using stationary and unidirectional WPT charging. This WPT system is designed for EVs compliant with J1772 plug-in charging, such that the battery management system could be modified to allow both charging technologies. The WPT system schematic has been harmonized with the one of ISO 19363, shown in Figure A.5. Generally, WPT systems are composed of functional elements that have:

- a power transfer function;
- a communication function;
- safety-related functions: prevent damage from the heating of foreign objects, and protect humans from exposure to magnetic fields.

A.4.1. POWER TRANSFER

The nominal operating frequency of WPT systems is 85 kHz, with a tuning band of 79...90 kHz. The GA selects the operating frequency, and the determination must be done before the start of the charging session with a maximum of 25% of the full power. The operating frequency must be kept constant for the entire charging session. It needs to be pointed out that the lower limit of the frequency range of the previous versions of both the SAE TIR and ISO 19363 was 81.38 kHz, and currently, it has been changed to 79 kHz.

The power classes of WPT systems are organized as shown in Table A.2. SAE J2954 regulates three power classes depending on the maximum input power (Volt-Ampere) that can be drawn from the AC-utility grid. The power classes WPT1 and WPT2 align with SAE J1772 for AC levels 1 and 2 charging, while WPT3 aligns with the European three-phase outlet rating. Moreover, WPT4 and WPT5 are currently under consideration for future editions of the standard.

WPT systems are also categorized according to the Z-class, measured as the VA coil ground clearance. There are three Z-classes, as shown in Table A.3. These are defined as ranges in definite intervals such that the WPT system works when the EV is fully loaded

Table A.2: Power classes defined by SAE J2954. [1], [3], [4]

	Power classes				
	WPT1	WPT2	WPT3	WPT4*	WPT5*
Maximum input (kVA)	3.7	7.7	11.1	22	60
*under consideration					

or unloaded and independently of the tires' pressure. By now, SAE J2954 only considers the case in which the GA coil is mounted above the ground, which makes the actual air gap between the coils lower than the distance specified by the Z-class. The maximum recommended height for the GA coil is 70 mm.

Table A.3: Z-classes defined by SAE J2954. [1], [3], [4]

		Z-classes		
		Z1	Z2	Z3
VA Coil ground clearance range (mm)	from	100	140	170
	to	150	210	250

The interoperability of the GA is categorized into two classes. The interoperability class I GA is intended to operate in the entire input power range and Z-class, which is suitable for public use. On the other hand, the GA with interoperability class II is intended for specific applications, resulting in possibly limited operating ranges. According to these definitions, the interoperability between the power classes is well-defined in Table A.4. For instance, the GA interoperability class defines the maximum input power of the WPT system. Ultimately, the full power is determined by taking into account also the VA's power class.

Table A.4: Range of the WPT system's input kVA rating depending on the GA interoperability class. [4]

GA interoperability	**Minimum input kVA rating**	**Maximum input kVA rating**	**Z-classes**
Class I	1 kVA	11.1 kVA	Z1, Z2, Z3
Class II	1 kVA	From the manufacturer	

After the EV is parked in the designed spot, it is improbable that the VA coil is perfectly aligned with the GA one. Therefore, the system must allow some offset tolerances in all directions, which values are shown in Table A.5. The amount of relative positions between the GA and VA coil can be infinite, but the centered position is considered to be one that gives the maximum coupling at the target Z distance while their surfaces are parallel. In the case that the GA and the VA coils have the same magnetic configuration, which can be either polarized or non-polarized, the centered position typically coincides with the coils' geometric centers being aligned. If the coils have opposite configurations, the centered position has an offset from the aligned geometric centers. From this centered position, there are three possible degrees of freedom for the VA coil with respect to the GA which are: the direction of the travel called X, the direction perpendicular to the travel called Y, and the distance between the coils called Z. Moreover, the VA coils surface could also perform a rotation around any of these three axes. The full power must be transferred at any battery voltage at the aligned position, while a minimum of 50% of

the full power must be transferred in the misalignment tolerance area.

Table A.5: Offset misalignment tolerance of VA from the center position. [1], [3], [4]

Direction	GA: interop class I	GA: interop class II	VA
ΔX	±75 mm	±75 mm	±75 mm
ΔY	±100 mm	±100 mm	±100 mm
ΔZ	All Z-classes	From the manufacturer	From the manufacturer
Roll, Pitch, Yaw	N/A	N/A	±2°, ±2°, ±3°

SAE J2954 also defines minimum target power transfer efficiencies for the power classes, which are summarized in Table A.6. The efficiency is measured between the input and output points (1) and (2) in the schematic of Figure A.5. The efficiency test must be performed at the three reference battery voltages of 280 V, 350 V, and 420 V with the output power at its maximum rated deliverable level. It is also mentioned that some vehicle architecture might have voltages up to 900 V, which would modify the test. The efficiency test must be performed when the WPT is warmed up at a stable temperature. Multiple misalignment positions must be evaluated in any direction, including rotational misalignment.

Table A.6: Minimum efficiency requirements depending on the VA power class, the GA interoperability class, and the position between the GA and the VA coils. [4]

GA interoperability class I			GA interoperability class II	
VA power class	**Centered position**	**Misalignment area**	**Δ (GA-VA) power class**	**Any position**
WPT1	80%	75%	0	80%
WPT2	82%	77%	one power class	77%
WPT3	85%	80%	two power classes	75%

All these definitions aim to ensure electric and magnetic interoperability between coils with diverse topologies that might come from different manufacturers. Guidelines to assess electric and magnetic interoperability have been defined in detail. Moreover, SAE J2954 explains in detail the relationship between maximum coupling and alignment of coils with different magnetic configurations. In the Appendices, reference designs for GA and VA test stations are defined, which cover the first three power classes and all the Z-classes. These reference designs must be used to guarantee that GA and VA products are compliant with SAE J2954. Examples of product designs are also given. After that, guidelines on the power transfer control methods and practices to estimate the power losses are proposed. Other specifications are provided for the practical implementation of the WPT system, such as the location of the GA on the parking space, together with visual cues and markers.

A.4.2. COMMUNICATION

For what concerns the communication system, SAE J2954 relies on SAE J2836/6, SAE J2847/6, and SAE J2931/6. The communication guarantees that the alignment between the GA and the VA coils is within the tolerance area defined in Table A.5. Moreover, the communication also ensures the correct operation of a GA with interoperability class I with a product VA. The process before the start of the power transfer must be supported by bidirectional communication, and it has the following steps: WPT charging stop discovery, guidance, fine alignment, pairing, and finally, alignment check. These steps can

be supported by network-based and sensor-based positioning technologies. Typically, a combination of them is used, considering that the accuracy required by WPT systems is relatively high. Three potential alignment technologies are defined in the Appendices: low-power excitation, low-frequency RF with GA as a transmitter, or low-frequency RF with VA as a transmitter. The communication system is active during the entire charging process from the pairing stage until the end of the charge, monitoring anomalies and checking the alignment.

A.4.3. SAFETY AND EMC

Foreign object detection (FOD) is also treated by SAE J2954. In particular, if a foreign object is detected on the surface of the GA coil, the process is either not started or stopped if already running. On the other hand, in case the object is not detected, the temperature of the surface must be monitored, and the process can continue in the case that temperature does not exceed the limits of UL 2750 ($\approx 80\,^{\circ}$C). The tests to be executed with thirteen sample objects are either temperature rising or ignition tests. The concept of living object protection (LOP) is also discussed. In particular, LOP must ensure that both a living object is appropriately detected within certain boundaries and the protection system reacts fast enough such that the radiated field is not harmful. The Appendices of SAEJ 2954 also give guidelines on the LOP and its shutdown test.

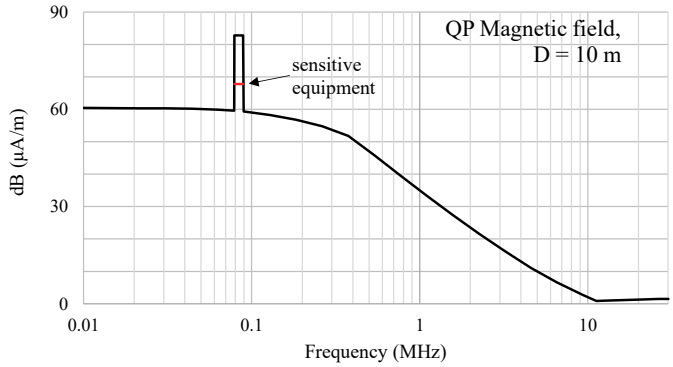

Figure A.6: SAE J2954/1 recommended limits for the radiated disturbances in residential environments below 30 MHz, for WPT1, WPT2 and WPT3. [4]

EMC limits are also recommended, classifying the WPT system as FCC part 18 below 30 MHz. Considering the entire system, i.e., the WPT system mounted on the EV, the limits of the radiated disturbances at 10 meters distance are plotted in Figure A.6. In the allowed frequency range 79-90 kHz, the radiated field must be limited to 82.8 dB, and if sensitive equipment is present within 10 meters, this limit is lowered by 15 dB. SAE J2954 is the only regulation that defines limits for EMC radiated disturbances below 150 kHz, which is not the case in IEC 61980 and ISO 19363.

EMC limits are also specified at the components level, and they can be used as a first evaluation before their integration into the WPT system. For the component-level test, the use of a metal plate (1.5 x 1.5)m with a thickness between 0.7 mm and 1 mm is recommended to mimic the EV. However, only the vehicle level measurements are the ones that determine compliance with the regulations.

A

A.4.4. EMF HUMAN EXPOSURE

The EMF exposure of both humans and cardiac implantable electronic devices (CIED) is treated extensively. For what concerns the general public and CIED, the Guidelines of ICNIRP 2010 are used as references. The EMF limits for humans with CIED are stricter. These limits are discussed in Section A.6.2. Limits for implanted medical devices (IMDs) are still under consideration for future versions of the standard. In the Appendices, guidelines on simulations and measurements of human exposure are discussed in detail. Additionally, different models for the human body are also explained.

A.5. IEC PAS 63184

ASSESSMENT METHODS OF THE HUMAN EXPOSURE TO ELECTRIC AND MAGNETIC FIELDS FROM WIRELESS POWER TRANSFER SYSTEMS - MODELS, INSTRUMENTATION, MEASUREMENT AND NUMERICAL METHODS AND PROCEDURES (FREQUENCY RANGE OF 1 KHZ TO 30 MHZ)

This is an IEC publicly available specification (PAS) released in May 2021, which applies to both stationary and dynamic WPT systems for assessing the human safety of the radiated fields from 1 kHz to 30 MHz. Different assessment methods and test procedures are explained. An example of these is provided based on results obtained from a heavy-duty

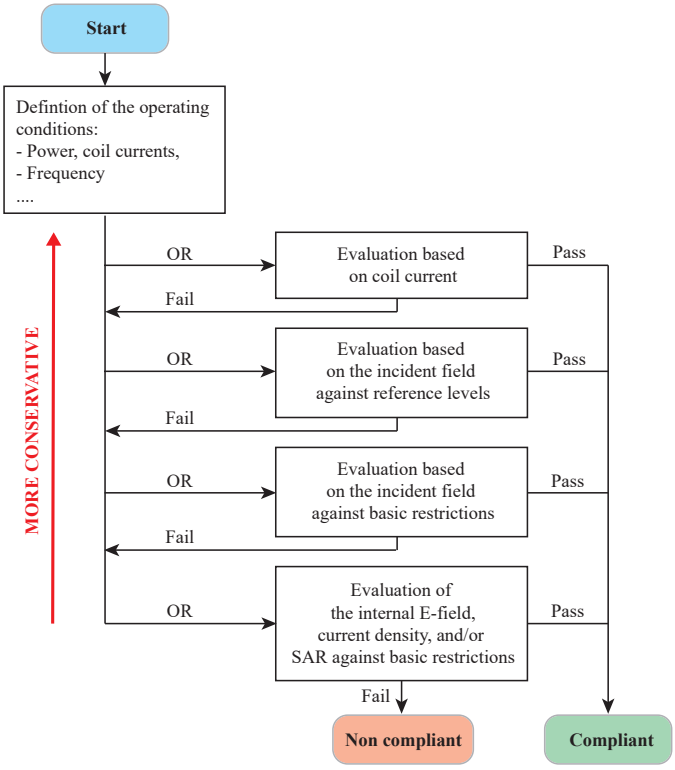

Figure A.7: Flowchart of the assessment procedure considering the direct effect defined by IEC PAS 63184.

EV WPT system. For assessing the human exposure to magnetic field radiations, any of the steps in Figure A.7 can be used. These methods are based on the coil current, external electric and magnetic fields, specific absorption rate (SAR), and internal electric fields. It must be noted that the flowchart in Figure A.7 starts with the most conservative method, and, in the case that it is not satisfied, a less conservative one can be used to evaluate the assessment. Additionally, the definition and difference between reference levels and basic restrictions are discussed in Section A.6.2.

A.6. COMPARISON AND DISCUSSION

The available standards and regulations on EV charging through WPT have been discussed singularly in the previous sections. Since they define constraints on the same application, it is reasonable that they agree with each other. However, it is interesting to compare these regulations for what concerns EMC and EMF human exposure to verify to which extent they agree.

A.6.1. EMC

To guarantee the unperturbed operation of electronic devices in the WPT charging system surroundings, EMC limits are imposed by standards and regulations without considering the safety limits for humans. Figure A.8 compares the EMC limits of the QP magnetic field strength in dB at 10 meters distance. According to SAE J2954 RP, in the operating frequency range 79-90 kHz, the field limit peaks up to 82.8 dB. This higher field value is allowed because the operating frequency range is chosen on purpose for this application, which means that the radiated field at this frequency would not interfere with the operation of any other electronic device. It is reasonable to assume that the amount of radiation allowed in the operating frequency range would be determined by the EMF human exposure limits. This assumption is discussed and evaluated in Section A.6.3.

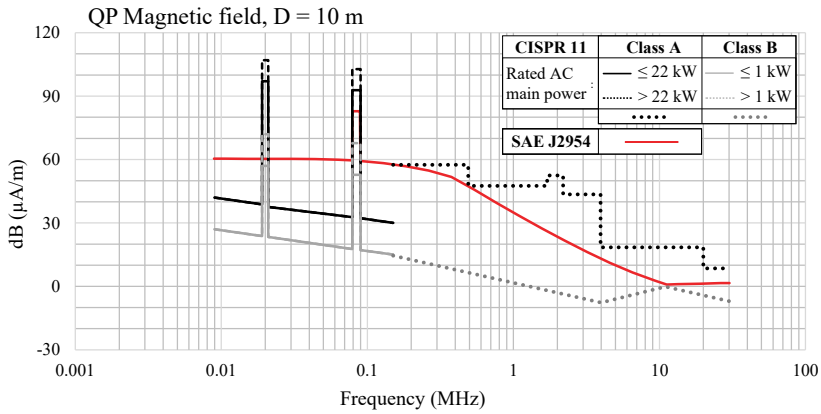

Figure A.8: Limits of the magnetic field strength at 10 meters distance.

A.6.2. HUMAN AND CIED EXPOSURE TO RADIATED EMF

To guarantee that EMF radiations are not dangerous to the EV passengers and the people in the surroundings, limits for the EMF are defined, taking into account both the

intensity and the frequency of the radiated EMF. A high-frequency EMF could interfere with some biological functions inside the human body if its intensity is relatively high because it can induce an electric field and currents in the body's tissues. Therefore, it is important to ensure that these have an intensity within the safety limits for humans. Measurements at different coils' alignments must be performed such that the worst-case measurement can be recorded and compared with the regulations. All regulations limit the EMF in three regions with respect to the EV with the WPT system.

- Region 1: area underneath the vehicle.
- Region 2: area around the vehicle
- Region 3: area inside the vehicle.

Manufacturers need to make sure that the EMF human exposure in all regions does not exceed the limits in Table A.7 when living beings are in the surroundings of the WPT system. This means that region 1 must have fast detection and shutdown systems.

ICNIRP has extensively studied the biological effects of EMF on human tissues, depending on both the field intensity and frequency. Therefore, in the ICNIRP Guidelines 2010, *basic restrictions* on the maximum allowed EMF inducted inside the human body are defined for different tissues. However, since it is impossible to measure the EMF directly inside the body, *reference levels* are defined for the EMF outside the human body, such that if these conservative levels are also met the limits inside the body would be within the basic restrictions. The reference levels for general public exposure are shown in Table A.7, for the frequency range of interest 3 kHz-10 MHz. These guidelines apply to all regions surrounding the wireless charger but do not necessarily preclude interference with CIEDs.

Table A.7: Reference levels for general public exposure in the frequency range 3 kHz-10 MHz (RMS values). [5]

Electric field strength - E	**Magnetic field strength - H**	**Magnetic flux density - B**	**Touch current**
83 V/m	21.5 A/m	27 μT	0.2* f (kHz) =17 mA @85 kHz

In Table A.8, stricter limits are defined such that the WPT system's radiation is safe for a wider range of people.

Even if the RMS values of the field are reported in Table A.7 and A.8, the peak values are considered as normative limits. These EMF limits concern only the operating frequency range because the contribution of higher harmonics can be neglected if their amplitude is at least 30 dB below the fundamental.

Table A.8: CIED EMF exposure limits (RMS values) for region 2 and region 3.

Region	**Magnetic filed strength - H**	**Magnetic flux density - B**
2, 3	11.9 A/m	15 μT
	from 79 to 90 kHz	

A.6.3. EMC AND EMF: QUANTITATIVE AND QUALITATIVE INTERPRETATION

Table A.7 and A.8 clearly show the limits of the EMF exposure in the allowed frequency range. However, it is difficult to evaluate them without using any other term of compar-

ison. For gaining a better understanding of their meaning, they are compared first with another radiation phenomenon and, after this, with the EMC limits in Figure A.8.

The most tangible example is to consider the natural magnetic field of the Earth as a term of comparison. According to [5], the magnetic flux density of the geomagnetic field varies in the range 30-70 μT, depending on the distance of a certain location from the geomagnetic poles. This natural magnetic field can be considered to be static and, consequently, its frequency is 0 Hz. Therefore, the geomagnetic field does not interfere with the human biological function inside the body, because it has low intensity and it is static. On the other hand, the magnetic field produced by the WPT system for EV charging is time-varying, which means that it is potentially able to induce an electric field and currents inside the human body. However, these are negligible in case their intensity is kept at a low level. To achieve so, in Table A.7 and A.8, the radiated magnetic field by the WPT system has the same order of magnitude as the geomagnetic one. Moreover, the limits of EMF human exposure to the magnetic field strength and flux density are expressed, respectively, in A/m and μT. Nevertheless, the EMC magnetic field limits in Figure A.8 are expressed in $dB_{(\mu A/m)}$ which makes it difficult to directly compare them to the human exposure limits. Assuming that the limits of Table A.8 are taken as reference, the magnetic flux density must be within 15 μT in the allowed frequency range, which intensity is less than the typical value of the geomagnetic field. This value can be transformed in $dB_{(\mu A/m)}$ to be able to compare it directly to the EMC limits. The procedure is divided into two steps. Firstly, the magnetic flux density is converted in magnetic field strength (see Table A.8) and then, its peak value is converted in $dB_{(\mu A/m)}$ as in (A.1).

$$20 \cdot \log\left(\frac{\overbrace{\sqrt{2} \cdot 11.9 \cdot 10^6 \mu A/m}^{\text{peak value}}}{\mu A/m}\right) = 144.52 \text{ dB}_{(\mu A/m)} \tag{A.1}$$

According to (A.1), the amount of magnetic field allowed in the surrounding of the vehicle is 144.52 dB considering the most conservative case. From Figure A.8, in the same frequency range, the EMC limit recommended by the SAE RP is up to 82.8 dB at a distance of 10 meters from the vehicle. This limit seems to be reasonable since it is lower than the limit for human exposure. However, it would be interesting to derive the value of the magnetic field in the surroundings of the vehicle knowing that at 10 meters distance, its value is 82.8 dB, and evaluate if that value would be still lower than 144.52 dB.

A.7. CONCLUSION

Since 2015, standards and regulations on EV charging through WPT have been released. Currently, the available ones are the IEC 61980 series, ISO 19363, SAE J2954, IEC PAS 63184, and SAE J2847/6 which have many common points. However, they are not entirely in agreement in terms of EMC. From Figure A.8, it is clear that the limits currently adopted by IEC 61980-1 are on average 15 dB larger than the ones in SAE J2954. Since the human exposure to magnetic fields is also well-regulated in the operating frequency range 79-90 kHz, it would be convenient to define EMC limits for that frequency range that also ensure a safe magnetic field around the vehicle for the humans. Additionally, the propagation of the magnetic field would also depend on the coils' topology. Con-

A

cluding, wireless charging is a technology still in its early stages and new regulations are now under development. In the future, other aspects will also be regulated such as dynamic, vehicle-to-grid, and wireless charging of high-duty EVs.

REFERENCES

[1] *Iec 61980-1: Electric vehicle wireless power transfer (wpt) systems - part 1: General requirements*, IEC, Nov. 2020.

[2] *Iec 61980-1: Electric vehicle wireless power transfer (wpt) systems - part 3: Specific requirements for magnetic field wireless power transfer systems*, IEC, Nov. 2023.

[3] *Iso 19363:2020: Electrically propelled road vehicles - magnetic field wireless power transfer - safety and interoperability requirements*, ISO, Apr. 2020.

[4] *J2954: Wireless power transfer for light-duty plug-in/ electric vehicles and alignment methodology*, Aug. 2022.

[5] *Icnirp guidelines for limiting exposure to time-varying electric and magnetic fields (1hz - 100 khz)*, Health Physics 99(6):818-836, International Commission on Non-Ionizing Radiation Protection, 2010.

B

MODELING OF THE CURRENT DISTORTION IN THE DOUBLE-SIDED LCC COMPENSATION

B.1. INTRODUCTION

The equivalent circuit of IPT systems employing the double-sided LCC (DLCC) compensation is shown in Figure B.1. The DLCC compensation has been analyzed widely in the literature [1]–[6]. The first paper modeling the DLCC compensation is [2], which defines the parameter tuning method and analyzes the circuit through the first harmonic approximation (FHA). Additionally, [3] and [4] propose a compact DLCC in which the compensation inductor is integrated with the coupled coil. It must be noted that these papers consider that the primary and the secondary circuits are symmetrical, which simplifies the parameters' selection of the DLCC. Contrarily, [5] explains a DLCC design method for maximum efficiency considering asymmetry between the coupled coils.

In IPT systems, it is important to predict the inverter's turn-off current to assess whether the zero voltage switching (ZVS) turn-on can be achieved. However, [2] has acknowledged that the inverter's current can be heavily distorted due to the low-pass filter characteristic of the input LC circuit consisting of L_{f1} and C_{f1}. Because of those high-order harmonic components, the analytical prediction of the turn-off current would not be accurate by simply using the FHA analysis. Therefore, the inverter's current is assessed by considering the high-order harmonic components, and, based on those, the

---

This appendix chapter is based on:

- F. Grazian, G. Yu, G. Zhu, C. Riekerk, J.Dong, T. B. Soeiro, P. Bauer, "Modeling of the Inverter Current Distortion in the Double-sided LCC Compensation for Inductive Power Transfer Systems", *submitted*.

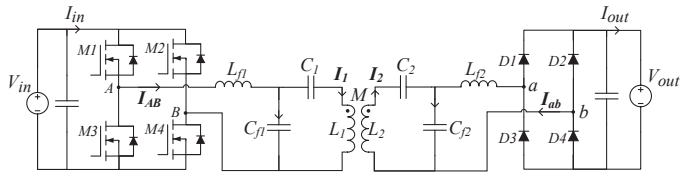

Figure B.1: Equivalent circuit of an IPT system employing the DLCC compensation network.

inverter's turn-off current has been estimated. As a result, this analytical estimation of the turn-off current is relatively accurate when the diode rectifier operates in continuous conduction mode (CCM), but large errors are found in discontinuous conduction mode (DCM). Using a similar approach, [3] and [4] defined guidelines on the selection of C_2 are given to achieve the inverter's turn-off current that guarantees the ZVS turn-on operation. However, detailed modeling of the turn-off current is not provided. Likewise, no detailed analytical analysis of the inverter's turn-off current has been performed in [1] and [5]. All in all, no analytical model has been proposed yet that can accurately predict the inverter's current flowing through L_{f1} valid for any loading condition.

This work defines an analytical method to predict the distortion of the H-bridge inverter's current when the diode rectifier is operating in both CCM and DCM. This method is beneficial to assess if the inverter would achieve the ZVS turn-on in any operating conditions without performing circuit simulations. Section B.2 defines the parameters' tuning and the analytical circuit modeling of the DLCC based on the FHA. Thereby, two different load modeling are considered. The first is based on the equivalent resistive load and the other is the square wave voltage source model that takes into account the diodes rectifier and the battery. After that, the proposed method for the prediction of the inverter's current distortion is explained in Section B.3. This proposed method has been experimentally verified in Section B.4 using a 3.7 kW IPT system which coupled coils are the ones of Section 2.4. Finally, the main conclusions are discussed in Section B.5.

B.2. DLCC CIRCUIT MODELING

COMPENSATION TUNING

The parameters' tuning for the DLCC compensation network in Figure B.1 generally follows the approach used in [2], which has been explained in Section 2.5.2. This is summarized in (B.1), where $\omega_0 = 2\pi f_0$ is the angular resonant frequency. As a result of (B.1), at both the primary and the secondary circuit, the compensation inductor resonates with the parallel capacitor at the same ω_0 as the coupled coil with the series compensation capacitor. Moreover, the mutual inductance M between the coupled coils is defined in (B.2) depending on the coupling factor k.

$$L_{fi}C_{fi} = \frac{1}{\omega_0^2}, \quad L_i - L_{fi} = \frac{1}{\omega_0^2 C_i} \qquad i = 1,2 \tag{B.1}$$

$$M = k\sqrt{L_1 L_2} \tag{B.2}$$

PHASOR CONVENTION BASED ON THE FHA

The equivalent circuit of an IPT system using the DLCC compensation is shown in Figure B.2, including the components' equivalent series resistance. The operating points

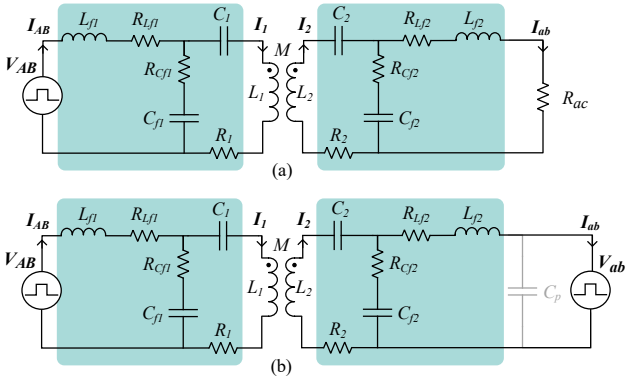

Figure B.2: Equivalent circuit of the DLCC compensation for the analysis in the frequency domain which load is modeled as (a) equivalent resistance R_{ac} defined in (B.8), (b) voltage source $\boldsymbol{V_{ab}}$ defined in (B.9).

of the circuit in Figure B.2 can be computed in terms of voltages and currents through the Kirchhoff voltage law in (B.3). Thereby, the used circuit impedances are defined in (B.4)-(B.6).

$$\begin{bmatrix} \boldsymbol{V_{AB}} \\ 0 \\ 0 \\ \boldsymbol{V_{ab}} \end{bmatrix} = \begin{bmatrix} \boldsymbol{Z_{L_{f_1}}} + \boldsymbol{Z_{C_{f_1}}} & -\boldsymbol{Z_{C_{f_1}}} & 0 & 0 \\ -\boldsymbol{Z_{C_{f_1}}} & \boldsymbol{Z_1} + \boldsymbol{Z_{C_{f_1}}} & j\omega M & 0 \\ 0 & j\omega M & \boldsymbol{Z_2} + \boldsymbol{Z_{C_{f_2}}} & -\boldsymbol{Z_{C_{f_2}}} \\ 0 & 0 & \boldsymbol{Z_{C_{f_2}}} & -\boldsymbol{Z_{L_{f_2}}} - \boldsymbol{Z_{C_{f_2}}} \end{bmatrix} \begin{bmatrix} \boldsymbol{I_{AB}} \\ \boldsymbol{I_1} \\ \boldsymbol{I_2} \\ \boldsymbol{I_{ab}} \end{bmatrix} \tag{B.3}$$

$$\boldsymbol{Z_{L_{f_1}}} = R_{L_{f1}} + j\omega L_{f1}, \quad \boldsymbol{Z_{C_{f_1}}} = R_{C_{f1}} + \frac{1}{j\omega C_{f1}} \tag{B.4}$$

$$\boldsymbol{Z_{L_{f_2}}} = R_{L_{f2}} + j\omega L_{f2}, \quad \boldsymbol{Z_{C_{f_2}}} = R_{C_{f2}} + \frac{1}{j\omega C_{f2}} \tag{B.5}$$

$$\boldsymbol{Z_1} = R_1 + j\omega L_1 + \frac{1}{j\omega C_1}, \quad \boldsymbol{Z_2} = R_2 + j\omega L_2 + \frac{1}{j\omega C_2} \tag{B.6}$$

The input voltage source $\boldsymbol{V_{AB}}$ defined in (B.7) is used according to the FHA [7]. $\boldsymbol{V_{AB}}$ uses the phasor convention, and it is specified in terms of its absolute value and phase angle. $\boldsymbol{V_{AB}}$ is taken as the reference, i.e., $\phi_{V_{AB}}$. The circuit in Figure B.2(a) models the load as the equivalent resistance R_{ac} in (B.8), as explained in [7]. In this case, $\boldsymbol{V_{ab}}$ in (B.3) should be replaced with $\boldsymbol{V_{ab}}$=$R_{ac}\boldsymbol{I_{ab}}$. Alternatively, the circuit in Figure B.2(b) models the load as the voltage source $\boldsymbol{V_{ab}}$ defined in (B.9). This representation is closer to reality if the battery is directly connected to the rectifier circuit, as shown in Figure B.1.

$$\boldsymbol{V_{AB}} = V_{AB}\angle 0° = \frac{4}{\pi} V_{in} \tag{B.7}$$

$$R_{ac} = \frac{8}{\pi^2} R_L = \frac{8}{\pi^2} \frac{V_{out}}{I_{out}} = \frac{V_{ab}}{I_{ab}} \tag{B.8}$$

$$\boldsymbol{V_{ab}} = V_{ab}\angle\phi_{ab} = \frac{4}{\pi} V_{out}\angle\phi_{V_{ab}} \tag{B.9}$$

Moreover, another useful parameter is the input impedance $\boldsymbol{Z_{in}} = \boldsymbol{V_{AB}}/\boldsymbol{I_{AB}}$ defined in (B.10) which describes the equivalent impedance of the IPT system seen from the input source $\boldsymbol{V_{AB}}$. Similarly to the approach used in [8] and explained in Section 2.2.1, $\boldsymbol{Z_{in}}$ is computed through the reflected impedance $\boldsymbol{Z_r}$ in (B.11).

$$\boldsymbol{Z_{in}} = \boldsymbol{Z_{L_{f_1}}} + \frac{\boldsymbol{Z_{C_{f_1}}}(\boldsymbol{Z_1} + \boldsymbol{Z_r})}{\boldsymbol{Z_{C_{f_1}}} + \boldsymbol{Z_1} + \boldsymbol{Z_r}} \tag{B.10}$$

$$\boldsymbol{Z_r} = \frac{\omega^2 M^2}{\boldsymbol{Z_2} + \frac{(\frac{\boldsymbol{V_{ab}}}{\boldsymbol{I_{ab}}} + \boldsymbol{Z_{L_{f_2}}})\boldsymbol{Z_{C_{f_2}}}}{\frac{\boldsymbol{V_{ab}}}{\boldsymbol{I_{ab}}} + \boldsymbol{Z_{L_{f_2}}} + \boldsymbol{Z_{C_{f_2}}}}} \tag{B.11}$$

EQUIVALENT LOAD: RECTIFIER AND BATTERY

According to the FHA, the load modeling in the DLCC compensation considers either the equivalent resistance R_{ac} defined in (B.8) or the voltage source model $\boldsymbol{V_{ab}}$ in (B.9) considering that $\phi_{V_{ab}}$=$-\pi/2$. Efforts to model analytically the equivalent load in the DLCC have been made in [9] and [10]. However, they consider the major assumption that the diode rectifier always operates in CCM. Moreover, [9] defines a model valid for a resistive load type, while [2] and [10] consider the load based on the voltage source model with $\phi_{V_{ab}}$=$-\pi/2$. These load modeling strategies might result in large approximations since two main instances are neglected.

The first factor is the conduction mode of the diode rectifier, which typical operating waveforms are shown in Figure B.3. The top plots result from a rectifier using the ideal diode model, while the bottom ones result from a rectifier that considers the physical diode characteristics. The current i_{ab} would flow through L_{f2} only when $v_{Cf2} > v_{ab}$. If this condition is always satisfied during the switching cycle, the diode rectifier will operate in continuous conduction mode (CCM), which examples are illustrated in Figure B.3(a). On the other hand, if $v_{Cf2} > v_{ab}$ is not satisfied for the entire switching cycle, the diode rectifier will operate in discontinuous conduction mode (DCM), which examples are illustrated in Figure B.3(b). Especially in DCM, it is clear that the load characteristic fundamentally differs from the case using the equivalent resistive load.

The second factor is the parasitic capacitance of the diode rectifier, which lumped equivalent value can be modeled as the capacitor C_p shown in Figure B.2(b), connected in parallel to the output voltage source $\boldsymbol{V_{ab}}$. This capacitance must be discharged and charged as $\boldsymbol{V_{ab}}$ inverts polarity. From the zoom in Figure B.3(c), its capacitive behavior results in a delay of v_{ab} with respect to the case of an ideal diode rectifier. The peak current $\hat{I}_{Cp}$ in Figure B.3(c) is defined as $\hat{I}_{Cp} = i_{ab}(\theta_c)$. Around the current zero-crossing, $i_{ab}(\theta)$ can be approximated as

$$i_{ab}(\theta) = I_{ab}\sin(\theta - \theta_b) \tag{B.12}$$

where $\phi_{V_{Cf2}}$ is taken as a reference and, according to the FHA, $I_{ab} = \frac{\pi}{2} I_{out}$ assuming that I_{out} is defined by the battery charging cycle.

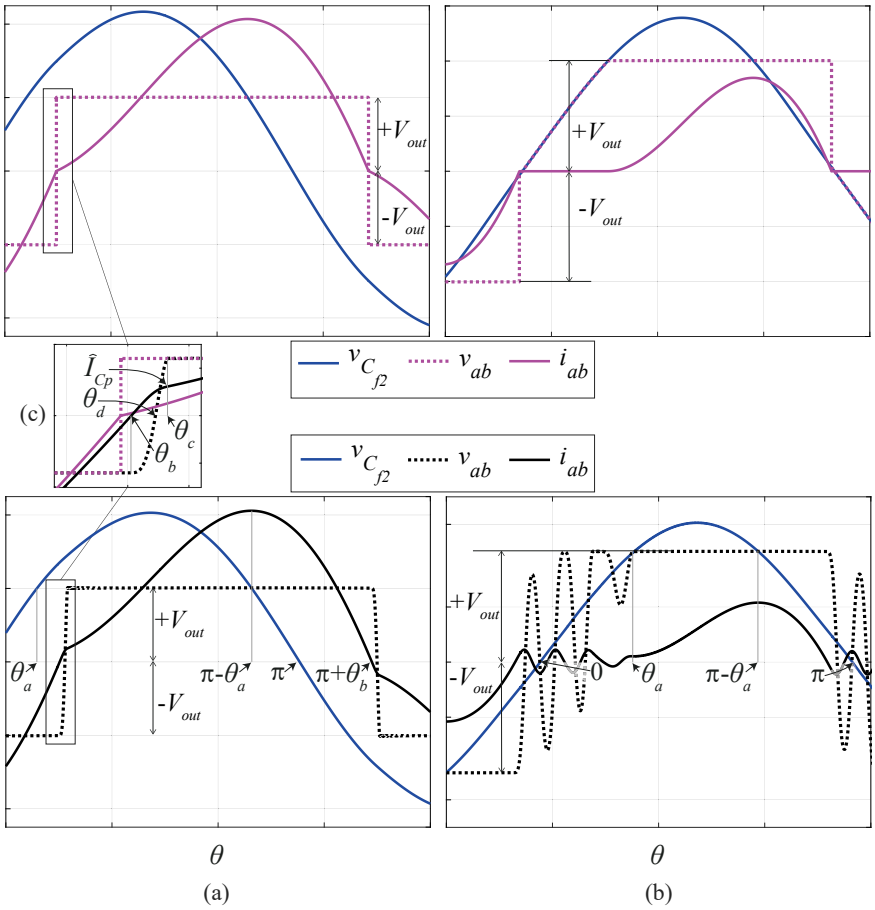

Figure B.3: Conduction of the diode rectifier depending on the voltage across C_{f2}: (a) CCM, (b) DCM. The top plots result from ideal diode models, while the bottom plots result from the physical diode characteristics. (c) Zoom on the turn-on transition of the diodes D1 and D4 in Figure B.1. It must be noted that the phase angle of $v_{C_{f2}}$ is considered as the reference, i.e., $\phi_{V_{Cf2}}$=0, and θ is considered as the x-axis such that θ=$\omega_0 \cdot t$.

During the interval $[\theta_b;\theta_c]$, $v_{ab}(\theta)$ can be written as (B.13). Specifically, for θ=θ_c, (B.14) can be found, which results in (B.15).

$$v_{ab}(\theta) = -V_{out} + \frac{1}{\omega_0 C_p}\int_{\theta_b}^{\theta} I_{ab}\sin(\theta-\theta_b)\,d\theta \tag{B.13}$$

$$2\cdot V_{out} = \frac{1}{\omega_0 C_p}\int_{\theta_b}^{\theta_c} I_{ab}\sin(\theta-\theta_b)\,d\theta \tag{B.14}$$

$$\theta_{C_p} = \theta_c - \theta_b = \cos^{-1}\left(1-\frac{2V_{out}\omega_0 C_p}{I_{ab}}\right) \tag{B.15}$$

Finally, $\hat{I}_{Cp}$=$I_{ab}\sin(\theta_c-\theta_b)$ can be computed.

B.3. PREDICTION OF THE INVERTER CURRENT DISTORTION

The distortion of i_{AB} can not be estimated only by considering the circuit analysis based on the fundamental harmonic components. The higher-order harmonics introduced by the square wave voltage sources must be taken into account.

B

METHODOLOGY

From the Fourier series of a square wave, the input and output voltage sources in Figure B.2(b) can be expressed in the time domain as

$$v_{AB}(t) = \sum_{n=1,3,5...}^{\infty} \frac{4}{\pi}\frac{1}{n} V_{in} \cdot \sin(n\omega_0 t) \tag{B.16}$$

$$v_{ab}(t) = \sum_{n=1,3,5...}^{\infty} \frac{4}{\pi}\frac{1}{n} V_{out} \cdot \sin(n\omega_0 t + \phi_{V_{ab}}) \tag{B.17}$$

where the amplitude and phase angle are chosen according to the fundamental component in (B.7) and (B.9). Furthermore, the Fourier series of i_{AB} can be written as

$$i_{AB}(t) = \sum_{n=1,3,5...}^{\infty} I_{AB,n} \cdot \sin(n\omega_0 t + \phi_{I_{AB,n}}) \tag{B.18}$$

where the amplitude $I_{AB,n}$ and phase angle $\phi_{I_{AB,n}}$ can be calculated through the circuit analysis in the frequency domain of Section B.2 for each harmonic component, i.e., imposing $\omega{=}n{\cdot}\omega_0$. This means that $I_{AB,n}$ and $\phi_{I_{AB,n}}$ can be computed as depicted in (B.19). As a result, the inverter switch-off current $I_{OFF}{=}i_{AB}(T_0/2)$, where $T_0{=}1/f_0$.

$$\boldsymbol{I_{AB,n}} = I_{AB,n}\underline{/\phi_{I_{AB,n}}} = \frac{\boldsymbol{V_{AB,n}}}{\boldsymbol{Z_{in,n}}} = \frac{\frac{4}{\pi}\frac{1}{n}V_{in}}{Z_{in,n}\underline{/\phi_{Z_{in,n}}}} \tag{B.19}$$

The computation of $\boldsymbol{I_{AB,n}}$ depends on the input impedance $\boldsymbol{Z_{in,n}}$ which, according to (B.11) and (B.10), depends on the loading condition. The equivalent load can be modeled as the equivalent resistance $R_{ac,n}$ which circuit is shown in Figure B.2(a). Alternatively, it can be modeled as the output voltage source $\boldsymbol{V_{ab,n}}$ which circuit is shown in Figure B.2(b).

It is interesting to assess whether the two equivalent load models in Figure B.2 result in the same estimation of $i_{AB}(t)$. From (B.17), it can be found that $\boldsymbol{V_{ab,n}}{=}\frac{4}{\pi}\frac{1}{n}V_{out}\underline{/\phi_{V_{ab}}}$. Therefore, the comparison between the $i_{AB}(t)$ resulting from modeling the load as $R_{ac,n}$ or $\boldsymbol{V_{ab,n}}$ can be made only if $\phi_{V_{ab}}$ is known. Based on the fundamental component analysis, the output voltage source $\boldsymbol{V_{ab}}$ results in leading $\boldsymbol{V_{AB}}$ of $-\pi/2$, meaning that $\boldsymbol{V_{ab,n}}{=}\frac{4}{\pi}\frac{1}{n}V_{out}\underline{/-\pi/2}$. However, Figure B.3 shows that this might be a considerable assumption since $\phi_{V_{ab}}$ also depends on the rectifier conduction.

PROPOSED ESTIMATION METHOD FOR $\phi_{V_{ab}}$

Figure B.3 shows that the voltage across C_{f2} and the amplitude of v_{ab}, i.e., V_{out}, influence the conduction of the diode rectifier and, consequently, v_{ab} and i_{ab}. In this analysis, it is considered that V_{out} is set by the battery, and the output power P_{out} is set by the battery charging cycle. To compute $\phi_{V_{ab}}$ at the chosen operating conditions, it is essential to find $v_{C_{f2}}$.

1) COMPUTATION OF $v_{C_{f2}}$ FROM THE FHA

As a first approximation, the amplitude and phase angle of $V_{C_{f2}}$ can be found from the circuit analysis of Section B.2 performed using the FHA, i.e., at ω=ω_0. Since V_{out} and P_{out} are given, hereby the load is modelled as R_{ac}=$\frac{8}{\pi^2}\frac{V_{out}^2}{P_{out}}$. According to Figure B.3, $v_{C_{f2}}$ is taken as the reference in the analysis of the rectifier conduction, meaning that the phase angle $\phi_{V_{Cf2}}$=0. Therefore, $v_{C_{f2}}$ results in

$$v_{C_{f2}}(\theta) = V_{C_{f2}} \sin\theta \tag{B.20}$$

where θ=$\omega_0 \cdot t$.

The estimation of $\phi_{V_{ab}}$ is first performed considering the CCM of the diode rectifier. If the solution is not a rational positive number, the diode rectifier operates in DCM and the estimation is performed for that case. This process is summarized in the flowchart of Figure B.4.

2) CCM

According to Figure B.3(a), the phase angle of v_{ab} with respect to $\phi_{V_{C_{f2}}}$ is $\phi_{V_{ab}}$=θ_d, where θ_d satisfies (B.13) such that $v_{AB}(\theta_d)$=0. As a result,

$$\theta_d = \theta_b + \cos^{-1}\left(1 - \frac{\omega_0 C_p V_{out}}{I_{ab}}\right) \tag{B.21}$$

The unknown θ_b can be found by solving (B.23), which consists of integrating (B.22) in the intervals $[\theta_b; \theta_c]$ and $[\theta_c; \theta_b + \pi]$ of Figure B.3(a), also considering (B.13).

$$i_{ab}(\theta) = \int [v_{C_{f2}}(\theta) - v_{ab}(\theta)]\, d\theta \tag{B.22}$$

$$\begin{cases} \hat{I}_{Cp} = \dfrac{1}{\omega_0 L_{f2}} \int_{\theta_b}^{\theta_c} [V_{C_{f2}} \sin(\theta) - v_{ab}(\theta)]\, d\theta \\ 0 = \hat{I}_{Cp} + \dfrac{1}{\omega_0 L_{f2}} \int_{\theta_c}^{\theta_b+\pi} [V_{C_{f2}} \sin(\theta) - V_{out}]\, d\theta \end{cases} \tag{B.23}$$

The system of equations in (B.23) is nonlinear and, to simplify its computation, θ_{C_p} is considered to be known as defined in (B.15). The solution of (B.23) is shown in (B.24). If the diode rectifier operates in CCM as shown in Figure B.3(a), (B.24) will have a rational numerical solution. Conversely, if i_{ab} decreases from $\hat{I}_{Cp}$ to zero while $v_{Cf2} < v_{ab}$, (B.24) will not output a valid solution meaning that the diode rectifier operates in DCM as shown in Figure B.3(b).

$$\theta_c = \cos^{-1}\left[\frac{\pi V_{out} - 2\omega_0 L_{f2}\hat{I}_{Cp} + \dfrac{\hat{I}_{Cp} - I_{ab}(\theta_{C_p})}{\omega_0 C_p}}{2V_{C_{f2}}}\right] \tag{B.24}$$

Assuming that the rectifier operates in CCM, θ_b can be computed as θ_b=$\theta_c - \theta_{C_p}$, which θ_{C_p} and θ_c result from (B.15) and (B.24), respectively. At this point, θ_d can be

computed according to (B.21). Finally, considering the convention in (B.3) where the input voltage source $\boldsymbol{V_{AB}}$ is the reference, the phase angle of V_{ab} results in

$$\phi_{V_{ab}} = \theta_d - \phi_{V_{Cf2}} \tag{B.25}$$

B

3) DCM

If the diode rectifier operates in DCM, i_{ab} would be approximately zero as long as $v_{Cf2} < v_{ab}$, which examples are shown in Figure B.3(b). In this case, (B.24) would not result in a rational numerical solution. According to Figure B.3(b), the phase angle of v_{ab} with respect to $\phi_{V_{C_{f2}}}$ is $\phi_{V_{ab}}$=θ_b.

The unknown θ_b can be found by solving (B.26), which consists of integrating (B.22) over the interval $[\theta_a; \theta_b + \pi]$ according to Figure B.3(b).

$$\begin{cases} \theta_a = \sin^{-1}\left(\dfrac{V_{C_{f2}}}{V_{out}}\right) \\ 0 = \dfrac{1}{\omega_0 L_{f2}} \int_{\theta_a}^{\theta_b+\pi} [V_{C_{f2}} \sin(\theta) - V_{out}]\, d\theta \end{cases} \tag{B.26}$$

where θ_a is the phase angle correspondent to $v_{C_{f2}}(\theta_a)$=V_{out}.

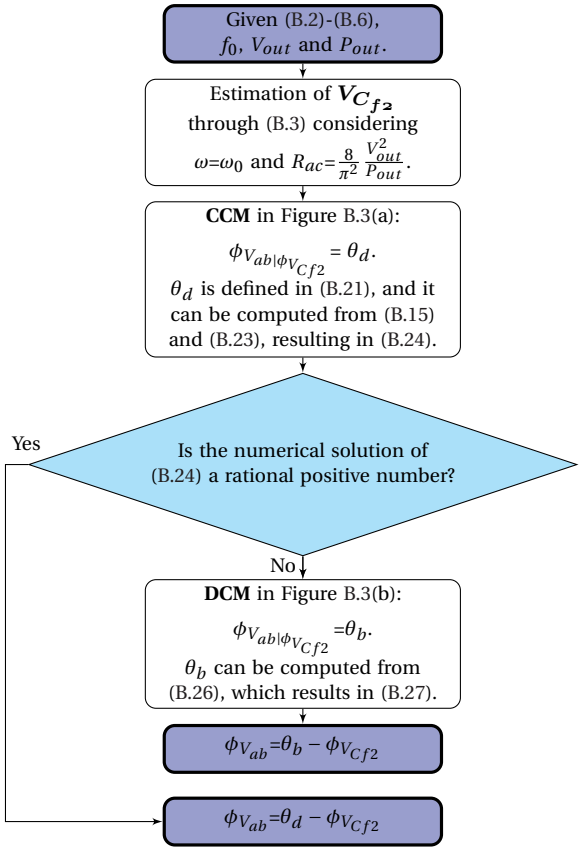

Figure B.4: Flowchart of the proposed estimation method for $\phi_{V_{ab}}$.

The solution of (B.26) is

$$V_{C_{f2}} \cos\theta_b - V_{out}\theta_b = V_{out}(\pi - \theta_a) - V_{C_{f2}} \cos\theta_a \tag{B.27}$$

Since (B.27) is not linear, the numerical solution for θ_b can be found through a parametric sweep. Finally, considering the convention in (B.3) where input voltage source $\boldsymbol{V_{AB}}$ is the reference

$$\phi_{V_{ab}} = \theta_b - \phi_{V_{Cf2}} \tag{B.28}$$

B.4. EXPERIMENTAL VERIFICATION

This section verifies the analytical model proposed in Section B.3 to estimate the harmonic components of i_{AB}.

3.7 kW LABORATORY DEMONSTRATOR

Figure B.5 shows the laboratory prototype used for the experimental verification. The value of the circuit parameters is listed in Table B.1. The Delta Elektronika bidirectional power supplies SM500-CP-90 and SM1500-CP-30 are used as the input and output voltage sources.

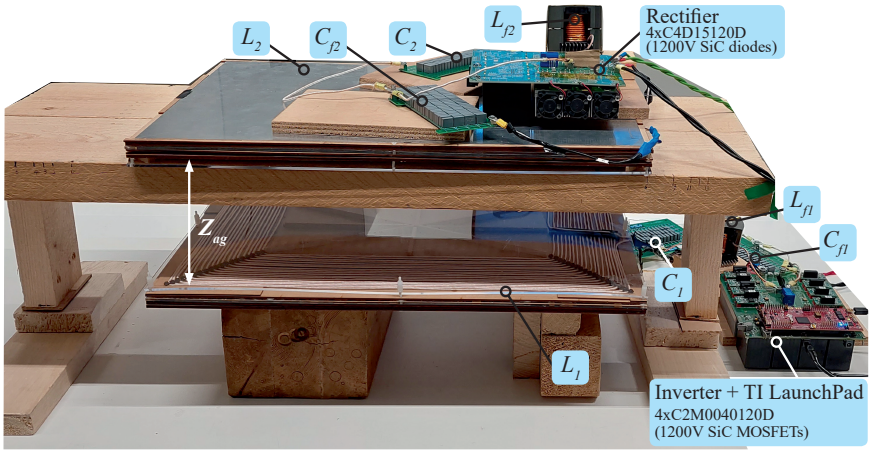

Figure B.5: 3.7 kW laboratory demonstrator of the implemented IPT system using the DLCC compensation.

Table B.1: Circuit parameters of the 3.7 kW laboratory demonstrator in Figure B.5.

	Coupled coils				**Compensation Network**		ESR (mΩ)
	M=M_{max}	M=M_{mid}	M=M_{min}				
	M=96.35 µH	M=68.25 µH	M=50.50 µH	ESR	L_{f1} (µH)	101.1	45
	Z_{ag}=10.6 cm	Z_{ag}=13.8 cm	Z_{ag}=17.0 cm	(mΩ)	L_{f2} (µH)	83.8	45
L_1 (µH)	337.4	331.5	328.1	650	C_1 (nF)	14.4	55
L_2 (µH)	223.9	218.0	215.3	440	C_2 (nF)	27.7	31
Compensation inductors' core PM/74/59, ferrite material N87					C_{f1} (nF)	36.0	25
Capacitor unit: KEMET R76TF13305050J 3.3 nF (ESR=0.22 Ω)					C_{f2} (nF)	41.7	23

B

MEASUREMENTS

The inverter voltage v_{AB}, current i_{AB} and the DC-to-DC power transfer efficiency $\eta_{\text{DC-to-DC}}$ have been measured at several operating points by sweeping both the DC input and the output voltages. Moreover, three values of mutual inductance have been considered which are specified in Table B.1. From these measurements, the inverter switch-off current I_{OFF} has been recorded and compared in Figure B.6 to the computed values resulting from three different analytical models, which respectively consider the load as:

- the equivalent resistance R_{ac};
- the voltage source $\boldsymbol{V_{ab}}$ with $\phi(V_{ab})$=$-\pi/2$;
- the voltage source $\boldsymbol{V_{ab}}$ of which $\phi(V_{ab})$ has been computed according to the proposed method in Section B.3.

According to Figure B.6, the proposed estimation method can predict I_{OFF} for a wide range of operating conditions more accurately than the method using a conventional

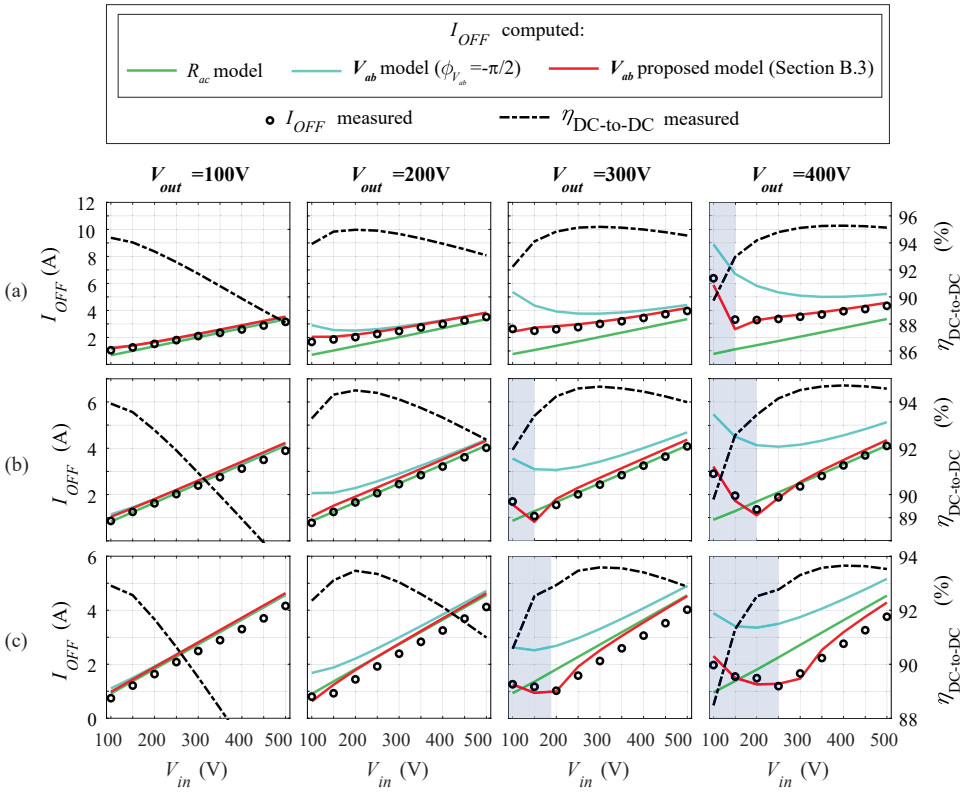

Figure B.6: Comparison between the measured and computed the inverter switch-off current I_{OFF}. The measured DC-to-DC power transfer efficiency $\eta_{\text{DC-to-DC}}$ has also been included. Measurements performed at: (a) M=M_{max}, (b) M=M_{mid}, (c) M=M_{min}. The shaded areas indicate the operating points in which the diode rectifier operates in DCM.

load modeling strategy. The proposed method is also effective when the diode rectifier operates in DCM. These results confirm that it is fundamental to model the conduction of the diode rectifier to accurately estimated I_{OFF}.

Additionally, the computed and measured inverter voltage v_{AB} and current i_{AB} have been plotted in the time domain in Figure B.7, which results from V_{in}=500 V and V_{out}=400 V at the three considered mutual inductance values. The measured and estimated signals are in agreement. The differences are reasonable considering the assumption of the proposed model and the circuit parameter variations that might occur during the operation. The proposed model could be improved further if the dead time of v_{AB} were considered, which would undoubtedly add more complexity. It must also be noted from $(i_{AB})_1$ that the estimation of I_{OFF} considering only the first harmonic component would lead to large errors.

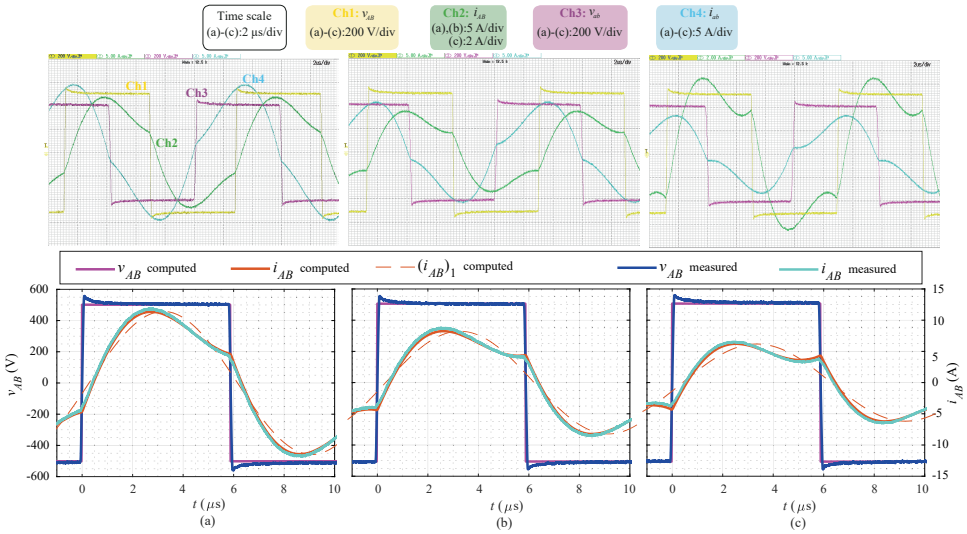

Figure B.7: Plot in the time domain of the computed and measured inverter voltage v_{AB} and current i_{AB} at V_{in}=500 V, V_{out}=400 V, and: (a) M=M_{max}, (b) M=M_{mid}, (c) M=M_{min}.

B.5. CONCLUSIONS

An estimation method for the inverter current distortion has been proposed for IPT systems that use the DLCC compensation. This is fundamental to assess analytically whether the inverter operates in ZVS turn-on. The proposed model has been proven effective for a wide range of operating conditions. It has been demonstrated that modeling the diode rectifier's conduction is fundamental to achieving an accurate inverter switch-off current estimation.

Additionally, the implemented prototype's high DC-to-DC power transfer efficiency must be noted, which is remarkable for the considered power level. For instance, the efficiency of 95.23% has been measured at the maximum considered coupling condition for an output power of around 3.1 kW with 400 V DC output voltage.

B

REFERENCES

[1] W. Li, H. Zhao, J. Deng, S. Li, and C. C. Mi, "Comparison study on ss and double-sided lcc compensation topologies for ev/phev wireless chargers", *IEEE Transactions on Vehicular Technology*, vol. 65, no. 6, pp. 4429–4439, 2016. DOI: 10.1109/TVT.2015.2479938.

[2] S. Li, W. Li, J. Deng, T. D. Nguyen, and C. C. Mi, "A double-sided lcc compensation network and its tuning method for wireless power transfer", *IEEE Transactions on Vehicular Technology*, vol. 64, pp. 2261–2273, 2015.

[3] W. Li, H. Zhao, S. Li, J. Deng, T. Kan, and C. C. Mi, "Integrated *LCC* compensation topology for wireless charger in electric and plug-in electric vehicles", *IEEE Transactions on Industrial Electronics*, vol. 62, no. 7, pp. 4215–4225, 2015. DOI: 10.1109/TIE.2014.2384003.

[4] T. Kan, T.-D. Nguyen, J. C. White, R. K. Malhan, and C. C. Mi, "A new integration method for an electric vehicle wireless charging system using lcc compensation topology: Analysis and design", *IEEE Transactions on Power Electronics*, vol. 32, no. 2, pp. 1638–1650, 2017. DOI: 10.1109/TPEL.2016.2552060.

[5] Y. Chen, M. Li, B. Yang, *et al.*, "Variable-parameter t-circuit-based ipt system charging battery with constant current or constant voltage output", *IEEE Transactions on Power Electronics*, vol. 35, no. 2, pp. 1672–1684, 2020. DOI: 10.1109/TPEL.2019.2920948.

[6] W. Li, G. Wei, C. Cui, X. Zhang, and Q. Zhang, "A double-side self-tuning lcc/s system using a variable switched capacitor based on parameter recognition", *IEEE Transactions on Industrial Electronics*, vol. 68, no. 4, pp. 3069–3078, 2021.

[7] R. L. Steigerwald, "A comparison of half-bridge resonant converter topologies", *IEEE Trans. Power Electron.*, vol. 3, no. 2, 1988.

[8] C.-S. Wang, G. Covic, and O. Stielau, "General stability criterions for zero phase angle controlled loosely coupled inductive power transfer systems", in *27th Annual Conference of the IEEE Industrial Electronics Society (IECON)*, 2001.

[9] Y. Guo, L. Wang, Y. Zhang, S. Li, and C. Liao, "Rectifier load analysis for electric vehicle wireless charging system", *IEEE Transactions on Industrial Electronics*, vol. 65, no. 9, pp. 6970–6982, 2018. DOI: 10.1109/TIE.2018.2793260.

[10] Y. Guo, Y. Zhang, W. Zhang, and L. Wang, "Battery parameter identification based on wireless power transfer system with rectifier load", *IEEE Transactions on Industrial Electronics*, vol. 68, no. 8, pp. 6893–6904, 2021. DOI: 10.1109/TIE.2020.3003549.

ACKNOWLEDGEMENTS

I would like to express my deep gratitude to the people who have supported and accompanied me throughout my Ph.D. research journey. Without their help, this project would not have been possible.

First, I would like to sincerely thank my promotor, professor Bauer, who gave me the opportunity to start this project and provided all support needed along the way. I am very grateful for all the experiences I had. Thank you for believing in me. I want to thank my co-promotor, Jianning, who was always there to help me and has the natural ability to give the right advice at the right time. I wish all the best to you and the wireless power transfer team. A special thank goes to Peter and Bart, who supervised and inspired me during my Master's thesis project, persuading me to continue the academic research path. You have opened a bright door for me.

Thiago, I'm truly grateful to have had you as my supervisor. I feel incredibly lucky to have been mentored by someone with such impressive expertise in both academia and industry. Your knowledge has constantly inspired me. Every day, I have learned invaluable lessons, including how to write high-quality scientific publications, develop new concepts, troubleshoot problems, and prove these ideas in the laboratory. Thank you for sharing your expertise with me - I will always carry these experiences with me.

In my research, I have spent long hours in the lab. My work would not be the same without the help of the technicians, who are always ready to help. It was a great pleasure to work with you, and thank you for the fun chat between one experiment and the other. Heel erg bedankt, Bart, Joris, Harrie and Mladen! Sharmila, you are the soul of the DCES group. Thank you for all the precious help, the wise and kind pieces of advice, and the wonderful yoga classes. I want to take the chance to thank also the ESE assistant professors Laura, Zian, Gautham, Babak, Mohamad, Aditya, and Patrizio. It was always a pleasure to exchange ideas and catch up when our paths crossed on the third floor. I would like to thank the EEMCS Diversity and Inclusion Team (EDIT) for keeping me motivated during the hardest times. While working with you, I have realized that improving our faculty environment and culture is equally important to solving technical problems. Keep it going, you are great! Thank you, Lucia, for sharing this journey with me it would not have been the same without you. I had the pleasure of advising some MSc students, which made me grow professionally. Thank you, Gautam, Swaminathan, Calvin, Yawen, and Pooja, for putting your trust in me. When I started, I had the pleasure of having as senior Ph.D. student colleagues Pavel, Soumya, Aditya, Udai, Nils, Mladen, and Nishant. Thank you for setting an example!

I was lucky to share my office with the best mates I could wish for. The four of us started our Ph.D. journey at the same time, and it was great to go through it together, knowing that we could rely on each other. We will never forget the conferences and the magical summer school in Gaeta of 2019! Marco, thank you for always being there for me during the hard moments and the fun times. It was great to come to the office every

morning knowing that I would find a good friend there. Wiljan, how beautiful it is that we shared the same TU Delft path since our first days in the MSc, exploring our passion for power electronics. Time went so fast, and growing side by side has been so special. I hope we will work together again one day. Who knows! Wenli, I was very lucky to have you as my wireless charging buddy. I learned a lot from you and am so proud of what we have achieved. Furthermore, I have collaborated on wireless charging with other brilliant researchers. Thank you, Guangyao, Calvin, Gangwei, Wenli, Kevin, and Yi. It was a pleasure working with you. I shared my Ph.D. journey with many amazing colleagues. Thank you, Dhana, for being the friend I could open up to. I miss so much our coffee breaks. Thank you, Sachin, for being a great bro. It is always nice to see you. Yang, I have always enjoyed our talks, and I am glad I got to know you better in Gaeta and PEMC! Lyu, thank you for always bringing a positive vibe. It helped me so much during stressful times! I will never forget our great music sessions. Thank you, Miad, for all the laughs. PEMC would not have been so much fun without you. Thank you, Joel, Dario, Alvaro, Christian, and Alejandro, for enhancing my Latin spirit, I always enjoy so much meeting you guys. Thank you, Gautam, Djurre, Nikos, Farshid, Zhengzhao, Yawen, Robin, Sohrab, Adnan, Junji, Yunhe, Ria, David, Siddhesh, Reza, Cristi, Lu, Faezeh, Weichuan, Xuliang, Yun, and Tianming. It was a pleasure to spend our lunch and coffee breaks together. It is always very nice talking to you, people!

Ibra and Lucia, we met as colleagues, but in a short time, we became much more than that. I cannot wait for our next trip together! Ibra, our love dramas brought us closer during our confessional sessions on the hidden stairs to the fourth floor. After that, you made my days in and outside the office special. How could I forget all the chicory coffees, fancy haver lattes, the pasta cooking, the conferences/honeymoon, the trips to Prato, the parties I dragged you to, the many confessional sessions, and the life in den Haag? Thank you for always being there for me! Lucia, thanks for being the friend who gives the right advice at the right time. It is always so much fun when we meet. I love how we go from deep discussions to ending up partying spontaneously. Let's never change this, please!

At the beginning of my Ph.D., I moved into the mythical house of Hof van Delftlaan with Benni, Titi, and Priya. There, we had our home far from home. Thank you, girls, for all the italian-spanish-indian dinners, legendary parties with the police, Santa Cristina, board games, and much more. We all left that house now, but I know we have built unforgettable memories. I am looking forward to our next trip!

My Italian family in the Netherlands made me feel closer to home. Jack, Fra, and Isa, you are the first people I met in the introduction program, and I feel that we literally have grown up together in these past years. I know that we will always be there for each other. Franz, you were adopted into the Italian gang, and thank you for joining in many adventures. I heard you are a pizza master now, and I cannot wait to try it in Berlin. Ireen, thank you for being a great friend and for always following me anywhere: from the first day at the Millers to the hostel and Flixbus in Berlin. Now we need to find another good excuse to go to Tenerife again! Edo, thank you for all the parties, laughs, talks from the heart, and ladies' nights. Jacopino, thank you for your energy and always bringing happiness to the room! Caspi, you are phenomenal, a legend. I am so glad I have met you and got the chance to be your neighbor on the fabulous canal, separated by Zuidwal Latino.

I will never forget the pain in my cheeks after every night we spent together. Rochi, you are a ray of sunshine. The espresso martinis together are never enough! Thank you, Lara and Daniele, for always making me feel at home when I see you!

I feel so blessed that I have met special people who have become my closest friends in the last few years. Anika, I miss so much the times we were living in front of each other in Delft. You were my greatest support when I was feeling low in motivation. You still make my days so bright! Counting the days to our next adventure. Annebob, our friendship was blessed by limoncello, and from there, we became inseparable. I enjoy so much spending time with you! Thank you for always making me feel loved. You and David made our time in Den Haag so special. I hope one day we will have our lasagna house. Luisa, meeting you was a blessing. Your selflessness and kindness are so inspiring! I am so lucky to have you in my life.

This journey in the world of electrical engineering started in beautiful Bologna with amazing people. We have the best time together, and every time we see each other is like time has never passed. Thank you, Ila, Alessia, Lisa, Sachi, LB, AleAlbe, Epi, Giovi, Basit, Gabri, and Lucke.

Thank you to my babes, whom I also call figliole. We have known each other since we were literally babies, and it is beautiful to think that we still support each other after so many years. I am sure that this will never change! Thank you, Giuli, Chicco, Chiara and Benni. And Chicco, thank you for understanding me better than I often do myself. Our phone calls bring me pure happiness! I am also very lucky to have Bea, Anna, Cami, and Cate in my life, who are always there for me after so many years. The time spent together is never enough. I cannot wait to see you again!

Thank you to my family for always believing in me. I am so lucky for all the opportunities you gave me. Thanks to my brothers Raffi and Giovi for all your support. I will always be there for you. Benni, it was great to share part of my time in Delft with you, my sister. Thanks for always being there when I need it! Mum, thank you for following me in any direction I wanted, always there, ready to support me without any hesitation. You are the best. Dad, I dearly keep all our memories in me because you still live in them. Nonni Sidi, it is not easy to express how thankful I am to you. Thank you for giving me all the love possible, the kind of love that does not need words.

Fili, you encouraged me from the first moment to take this Ph.D. research opportunity. Thank you for always wanting what is best for me. I am so happy and grateful for the life we built together. We are a formidable team. When I look back at all these years together, my heart swells with joy and love. When I look at you, I see my future, and I am so excited about it.

LIST OF PUBLICATIONS

JOURNAL PAPERS

1. F. Grazian, T. B. Soeiro, P. van Duijsen, P. Bauer, "Auto-Resonant Detection Method for Optimized ZVS Operation in IPT Systems With Wide Variation of Magnetic Coupling and Load", in *IEEE Open Journal of the Industrial Electronics Society*, vol. 2, pp. 326-341, 2021.

2. F. Grazian, T. B. Soeiro, P. Bauer, "Inductive Power Transfer based on Variable Compensation Capacitance to Achieve an EV Charging Profile with Constant Optimum Load", in *IEEE Journal of Emerging and Selected Topics in Power Electronics*, vol. 11, no. 1, pp. 1230-1244, Feb. 2023.

3. F. Grazian, T. B. Soeiro, P. Bauer, "Voltage/Current Doubler Converter for an Efficient Wireless Charging of Electric Vehicles with 400V and 800V Battery Voltages", in *IEEE Transactions on Industrial Electronics*, vol. 70, no. 8, pp. 7891-7903, Aug. 2023.

4. F. Grazian, T. B. Soeiro, P. Bauer, "Voltage/Current Doubler Converter for Electric Vehicle Wireless Charging Employing Bipolar Pads", in *IEEE Journal of Emerging and Selected Topics in Power Electronics*, (early-access), 2023.

5. F. Grazian, G. Yu, G. Zhu, C. Riekerk, J.Dong, T. B. Soeiro, P. Bauer, "Modeling of the Inverter Current Distortion in the Double-sided LCC Compensation for Inductive Power Transfer Systems", *submitted*.

As a co-author:

1. G. R. Chandra Mouli, P. Van Duijsen, F. Grazian, A. Jamodkar, P. Bauer, O. Isabella, "Sustainable e-bike charging station that enables AC, DC and wireless charging from solar energy", *Energies*. 2020; 13(14):3549.

2. W. Shi, J. Dong, T. B. Soeiro, C. Riekerk, F. Grazian, G. Yu, P. Bauer, "Design of a Highly Efficient 20-kW Inductive Power Transfer System With Improved Misalignment Performance", in *IEEE Transactions on Transportation Electrification*, vol. 8, no. 2, pp. 2384-2399, June 2022.

3. G. Zhu, J. Dong, F. Grazian, P. Bauer, "A Parameter Recognition Based Impedance Tuning Method for SS-Compensated Wireless Power Transfer Systems", *submitted*.

CONFERENCE PAPERS

1. F. Grazian, P. van Duijsen, T. B. Soeiro, P. Bauer, “Advantages and tuning of zero voltage switching in a wireless power transfer system”, *2019 IEEE PELS Workshop on Emerging Technologies: Wireless Power Transfer (WoW)*, 2019, pp. 367-372.

2. F. Grazian, W. Shi, J. Dong, P. van Duijsen, T. B. Soeiro, P. Bauer, "Survey on Standards and Regulations for Wireless Charging of Electric Vehicles", *2019 AEIT International Conference of Electrical and Electronic Technologies for Automotive (AEIT AUTOMOTIVE)*, 2019, pp. 1-5.

3. F. Grazian, P. van Duijsen, B. Roodenburg, T. B. Soeiro, P. Bauer, “Auto-resonant Control of the H-Bridge Resonant Converter for Inductive Power Transfer Applications”, *2020 IEEE 29th International Symposium on Industrial Electronics (ISIE)*, 2020, pp. 1593-1598.

4. F. Grazian, W. Shi, T. B. Soeiro, J. Dong, P. van Duijsen, P. Bauer, “Compensation network for a 7.7 kW wireless charging system that uses standardized coils”, *2020 IEEE International Symposium on Circuits and Systems (ISCAS)*, 2020, pp. 1-5.

5. F. Grazian, W. Shi, T. B. Soeiro, J. Dong, P. Bauer, “Electric Vehicle Charging Based on Inductive Power Transfer Employing Variable Compensation Capacitance for Optimum Load Matching”, *IECON 2020 The 46th Annual Conference of the IEEE Industrial Electronics Society*, 2020, pp. 5262-5267.

6. F. Grazian, W. Shi, T. B. Soeiro, J. Dong, P. van Duijsen, P. Bauer, “Quality Factor Based Design Guideline for Optimized Inductive Power Transfer”, *2020 IEEE PELS Workshop on Emerging Technologies: Wireless Power Transfer (WoW)*, 2020, pp. 178-183.

7. F. Grazian, T. B. Soeiro, P. Bauer, “Design Trade-Offs Between the Coupled Coils’ Inductance and the Series-Series Compensation Capacitance for EV Wireless Charging Systems”, *2022 International Symposium on Power Electronics, Electrical Drives, Automation and Motion (SPEEDAM)*, 2022, pp. 270-276.

8. F. Grazian, T. B. Soeiro, P. Bauer, “Coils’ Current Distortion Due to Variable Series Compensation Capacitance in EV Wireless Charging for a Constant Optimum Load”, *2022 Wireless Power Week (WPW)*, 2022, pp. 54-59.

9. F. Grazian, T. B. Soeiro, P. Bauer, “Interoperability of the Voltage/Current Doubler Converter Employing Bipolar Pads with the SAE J2954 VA WPT2/Z2 for EV Wireless Charging”, *2022 IEEE 20th International Power Electronics and Motion Control Conference (PEMC)*, 2022, pp. 346-352.

As a co-author:

1. W. Shi, J. Dong, S. Bandyopadhyay, F. Grazian, T. B. Soeiro, P. Bauer, "Comparative Study of Foreign Object and Misalignment in Inductive Power Transfer Systems", *IECON 2019 - 45th Annual Conference of the IEEE Industrial Electronics Society*, 2019, pp. 2634-2639.

2. W. Shi, F. Grazian, J. Dong, T. B. Soeiro, P. Bauer, "Analysis of Magnetic Field Emissions in Inductive Power Transfer EV Chargers Following Reference Designs in SAE J2954/2019", *2020 IEEE International Symposium on Circuits and Systems (ISCAS)*, 2020, pp. 1-5.

3. W. Shi, F. Grazian, J. Dong, T. B. Soeiro, P. Bauer, "Detection of Metallic Foreign Objects and Electric Vehicles Using Auxiliary Coil Sets for Dynamic Inductive Power Transfer Systems", *2020 IEEE 29th International Symposium on Industrial Electronics (ISIE)*, 2020, pp. 1599-1604.

4. W. Shi, F. Grazian, S. Bandyopadhyay, J. Dong, T. B. Soeiro, P. Bauer, "Analysis of Dynamic Charging Performances of Optimized Inductive Power Transfer Couplers", *2021 IEEE 19th International Power Electronics and Motion Control Conference (PEMC)*, 2021, pp. 751-756.

5. C. Riekerk, F. Grazian, T. B. Soeiro, J. Dong, P. Bauer, "Study on Soft Start-Up and Shut-Down Methods for Wireless Power Transfer Systems for the Charging of Electric Vehicles", *2021 IEEE PELS Workshop on Emerging Technologies: Wireless Power Transfer (WoW)*, 2021, pp. 1-6.

PATENTS

1. F. Grazian, T. B. Soeiro, P. Bauer, “An inductive power transfer system for wirelessly charging a battery with either half or double the nominal battery voltage for the same output power as well as a corresponding method”, Dutch patent application No. 2031085.

CURRICULUM VITÆ

Francesca GRAZIAN

05-05-1994	Born in Prato, Italy.

EDUCATION

2018-2023	Ph.D. candidate Delft University of Technology, the Netherlands
2016–2018	MSc in Electrical Engineering Delft University of Technology, the Netherlands
2013–2016	BSc in Electrical Engineering Alma Mater Studiorum – University of Bologna, Italy

WORK EXPERIENCE

2023-ongoing	Electrical Engineer Laser Precision Solutions, Amsterdam, the Netherlands
2018-2023	Ph.D. candidate, researcher in Power Electronics Delft University of Technology, the Netherlands
2017-2018	Power Electronics Intern Huawei Technologies, Nuremberg, Germany

AWARDS

2022	Best paper award - 2022 IEEE International Conference on Power Electronics and Motion Control (PEMC)
2022	Best poster award - ECPE European PhD School
2019	NENnovation award - 3rd place,


TU Delft